## *Specular and diffuse X-ray scattering studies of surfaces and interfaces*

Hudson, John Matthew

# Specular and Diffuse X-ray Scattering Studies Of Surfaces And Interfaces

by

John Matthew Hudson B.Sc.

A thesis submitted in partial fulfilment of the requirements for the degree of Doctor Of Philosophy

The University Of Durham

June 1994

## Abstract

The behaviour of thin film semiconducting and magnetic devices depends upon the chemical and physical status of the as-grown structure. Since the dimensions of many devices can be in the Angstrom and nanometre region, characterisation techniques capable of measuring chemical and physical parameters in this regime are necessary if an understanding of the effect of specimen structure on observed properties is to be achieved. This thesis uses high resolution x-ray scattering techniques to characterise sub-micron layered structures of semiconducting and magnetic materials.

Double crystal diffraction is routinely employed in the semiconductor industry for the on-line inspection of sample quality. While material parameters such as sample perfection and layer composition may be rapidly deduced, the non-destructive measurement of layer thickness is more difficult (particularly for multilayered samples) and lengthy simulation procedures are often necessary to extract the thickness information from a double crystal diffraction profile. However, for semiconductor structures which act as Bragg case interferometers, oscillations (known as thickness fringes) appear in the diffracted profile. The period of these fringes can be directly related to layer thickness. Attempts to Fourier transform diffraction data, in order to automatically extract the frequency of thickness fringes, have previously been only partially successful. It is shown that the relatively weak intensity of the thickness fringes and the presence of the substrate peak in the analysed diffraction data, drastically reduce the quality of the subsequent Fourier transform. A procedure for the manipulation of diffraction data is suggested, where an "average" envelope is fitted to the thickness fringes and used to normalise the data. The application of an auto-correlation is shown to further increase the quality of the Fourier transform of the normalised data. The application of Fourier transform techniques to the routine analysis of double crystal diffraction data is discussed

A novel technique for the measurement of absolute lattice parameters of single crystals is presented, which is capable of determining lattice constants with an absolute accuracy of around 2 parts in $10^5$. The technique requires only the use of a conventional triple crystal diffractometer with motorised $2\theta$ circle movement and the provision for a fine, precise rocking motion of the analyser. To demonstrate the technique, exemplary measurements on GaAs and InAs crystals are presented.

Triple crystal diffraction analysis has been performed on three material systems of current technological interest; the $Hg_{1-x}Mn_xTe$ on GaAs, the $Cd_{1-x}Hg_xTe$ on $CdTe/Cd_{1-x}Zn_xTe$ and the low temperature grown GaAs systems. Studies on the $Hg_{1-x}Mn_xTe$ on GaAs system reveal that the principal contribution to the rocking curve widths of layers grown using the direct alloy growth (DAG) method, arise from the tilt (i.e., mosaicity) of layer sub-grains. This finding is confirmed by double crystal topography which shows that the layers are highly mosaic with a typical grain size of (130±5)μm. Topographic studies of $Hg_{1-x}Mn_xTe$ on GaAs, grown using the interdiffused multilayer process (IMP), show that sample quality is significantly improved with single crystal material being produced using this growth method. Triple crystal diffraction studies of the $Cd_{1-x}Hg_xTe$ on $CdTe/Cd_{0.96}Zn_{0.04}Te$ systems reveal several findings. These are that the main contribution to rocking curve widths is from lattice tilts and that the tilt distribution increases as the layer thickness decreases. Further, the quality of the $Cd_{0.96}Zn_{0.04}Te$ substrate analysed is superior to that of the CdTe and that $Cd_{1-x}Hg_xTe$ layers grown on $Cd_{0.96}Zn_{0.04}Te$ substrates are generally of a higher quality than those grown on CdTe. Triple crystal analysis of MBE and ALE grown GaAs films, deposited at low growth temperatures, show that, at equivalent temperatures, superior quality films are grown by the ALE technique. Narrow lattice dilation and tilt distributions are reported for GaAs films grown at temperatures as low as 300°C by the ALE method.

While diffraction techniques are highly suitable for the study of relatively perfect crystalline material, they are not appropriate to the analysis of heavily dislocated or even amorphous specimens. This is not the case for the Grazing Incidence X-Ray Reflectivity (GIXR) technique, whose sensitivity is not dependent upon sample structure. The GIXR technique is currently attracting increasing interest following the development of commercial instruments. In this thesis, GIXR has been used to probe the layer thickness and interfacial roughness of a series of magnetic multilayer samples and $Si/Si_xGe_{1-x}$ superlattices. The technique is shown to be capable of measuring layer thickness to an accuracy of one monolayer. Modelling of specular GIXR data for the $Si/Si_xGe_{1-x}$ superlattices has shown that the magnitude of interfacial roughness is different for the two types of interface within the high Ge content superlattice samples, the $Si_xGe_{1-x} \rightarrow Si$ interface possessing a long range sinusoidal roughness of (0.9±0.3)nm, in addition to the short range roughness of (0.5±0.2)nm present at all interfaces. By collecting the diffuse scatter from a GIXR experiment, conformal, or correlated, roughness has been observed in both the multilayer and superlattice samples.

## Acknowledgements

Financial support for this work from the Science and Engineering Research Council, and from Bede Scientific Instruments Ltd. and Epitaxial Products International Ltd. (EPI Ltd.) through the provision of a C.A.S.E. award is gratefully acknowledged. I am grateful to Prof. A.D.Martin for allowing me use of the facilities of the Physics Department of the University of Durham.

I wish to express my warm thanks to Prof. B.K.Tanner for his supervision of this project. Gratitude is also due to Mr. R.Blunt, my industrial supervisor at E.P.I. Ltd., particularly for the provision of a seemingly endless supply of samples and the best pair of tweezers I ever used.

Much of the work presented in this thesis has resulted from collaboration with other workers and Dr.A.R.Powell, Dr.C.R.Li, Dr.C.C.R.Watson and Dr.S.K.Halder are thanked. Thanks are extended to the many friends and staff at Durham University who have made my period of study there so enjoyable. In particular, past and present members of the Solid State Group are thanked for their friendship and bad jokes, especially Mr C.M.Friend, Dr. C.I.Gregory, Mr. T.D.Hallam, Mr.R.Luscombe, Mr.H.Ramsbottom , Dr A.G.Turnbull, Mr. C.C.R.Watson and Dr S.M.Westwood. This list is in alphabetical order so as to offend none of the above and the fact that Stephen Westwood appears last does not mean that names are listed (in descending order) according to looks.

Particular mention must be made to all the staff of Bede Scientific Instruments Ltd. for provision of equipment and friendly assistance in moments of need. My thanks are also due to Paul Foley and the technical staff of the Electronics, Student and Main Workshops of the Durham Physics Department, the reprographic staff (Mr.M.Lee, Miss V.Greener and Mrs.P.Russell) for their advice on photography (and endless repairs to the photocopier) and the secretarial staff of the Physics Department. The number of people who have assisted, directly or indirectly, to the production of this thesis is long and I apologise that I cannot name them all. However, the staff of the Company Research Laboratory, British Nuclear Fuels Plc. deserve special mention for their highly treasured friendship and support over the latter stages of the writing of this thesis. Thanks are also due to Mr.K.Keegan for spiritual guidance and Mr.T.Butcher for moments of hilarity.

My parents are warmly thanked for their unstinting support over the previous six years. Finally, I wish to thank Miss S. Pooley, to whom this thesis is dedicated, whose endless encouragement and support has contributed significantly in the production of this thesis.

## List Of Publications

Hudson J.M, Powell A.R., Bowen D.K., Wormington M., Tanner B.K., Kubiak R.A. and Parker E.H.C., Proc. Mat. Res. Soc., 239, 455 (1992).

Powell A.R., Bowen D.K., Wormington M., Kubiak R.A., Parker E.H.C., Hudson J.M. and Augustus P.D., Semicond Sci.&Technol. V7, 627 (1992).

Powell A.R., Bradler J., Thomas C.R., Kubiak R.A., Bowen D.K., Wormington M. and Hudson J.M., Proc. Mat. Res. Soc., 238, 653 (1992).

Tanner B.K. and Hudson J.M., IEEE Trans. On Magnetics, V28(5), 2736 (1992).

Hallam T.D., Halder S.K., Hudson J.M., Li C.R., Funaki M., Lewis J.E., Brinkman A.W. and Tanner B.K., J. Phys. D: Appl. Phys., 26, A161, (1993).

Hudson J.M., Tanner B.K. and Blunt R., Advances In X-Ray Analysis, 37, 135 (1993).

Bowen D.K., Tanner B.K., Hudson J.M., Pape I., Loxley N. and Tobin S., *To be published in Advances In X-Ray Analysis.*

## Declaration

I declare that this thesis is original. No part of it has been submitted previously for a degree at any other University. Aside from the TEM micrographs and defect selective etching data presented, for which I thank P.D.Augustus (GEC Marconi) and C.C.R.Watson (Durham University) respectively, all work shown is my own unless stated otherwise. Work done in collaboration with other groups is duly acknowledged at the appropriate section.

**The samples analysed in this thesis were obtained from the following sources;**

Chapter V : **Epitaxial Products International Ltd, Cardiff, U.K. (all HEMT samples)**

Chapter VI : **Bede Scientific Instruments Ltd., Durham U.K. (GaAs and InAs single crystals)**

Chapter VII : **M.Funaki, Durham University, U.K. ($Hg_{1-x}Mn_xTe$), GEC Marconi Infra-Red, Southampton, U.K. ($Cd_xHg_{1-x}Te$ on $CdTe/Cd_{1-x}Zn_xTe$), University of Crete, Crete (Low temperature grown GaAs).**

Chapter VIII : **Warwick University, Warwick, U.K. ($Si/Si_{1-x}Ge_x$ superlattice samples), Leeds University (Au/Co magnetic multilayers).**

# Contents

# Chapter I

# Growth, Use And Characterisation Of Thin Film Semiconductor And Magnetic Materials.

## 1.1 Introduction

Few aspects of modern life remain untouched by the presence of semiconducting and magnetic devices. In applications ranging across communications, data processing, computing, data storage and consumer goods, the evolution of electrical and magnetic systems has had great impact on both the technological and economical expansion of the developed world. By 1996 the value of the world market dealing in the fabrication of integrated circuits alone, is expected to exceed 150 billion dollars[1]. Significant research and development efforts are being directed into further developing semiconductor technology, with scientists from many disciplines involved in improving materials fabrication methods, devising material characterisation techniques and extending device applications.

Much of the current attention devoted to these high technology materials revolves around the deposition and properties of thin films grown on crystalline substrates. Thin layered materials often exhibit novel electrical, magnetic and other physical properties, which are not observed in the bulk material. The actual behaviour of thin film semiconducting and magnetic devices strongly depends upon the chemical and physical status of the as-grown structure. Since the dimensions of many devices can be in the Angstrom and nanometre region, characterisation techniques capable of measuring chemical and physical parameters in this regime are necessary if an understanding of the effect of specimen structure on observed properties is to be achieved. This thesis uses x-ray scattering techniques to characterise sub-micron, layered structures of semiconducting and magnetic materials. Many of the systems analysed have thin epitaxial layers deposited on to their surface, where the term "epitaxial" refers to the formation of an extended single crystal layer on top of a crystalline substrate. The following sections give a brief overview of the material systems analysed in this thesis, with a discussion on the various thin film growth techniques. The discussion is by no means a comprehensive one and the reader is referred to the references quoted for a deeper treatment of the subjects covered.



## 1.2 Semiconductor Devices

Prior to the growth of thin film semiconducting and magnetic films, substrates of high crystalline quality must be prepared if good quality layer growth is to be achieved. Substrates most commonly used for semiconductor growth are Si, GaAs and InP. Two methods of mass producing single crystal silicon have evolved; the crucible-free floating zone technique (FZT) and the crucible-pulling or Czochralski method. In both techniques, crystallisation takes place on an (001) or (111) oriented seed crystal which is pulled at a slow rate to a thin crystal neck, eliminating dislocation line defects at the beginning of the growth process. The techniques differ in the choice of starting material, with crack free (poly)silicon rods providing the feed stock in the floating zone method, while crushed pieces of polysilicon constitute the starting material in the Czochralski process. Floating zone silicon growth occurs by creating a small molten region in the silicon rod with RF heating, allowing small grains of silicon to recrystallise as a single crystal product (figure 1.1(a)). In the Czochralski method (figure 1.1(b)), the crushed Si pieces are stored in a crucible, with a rod of single crystal silicon being slowly drawn away from the melt.

The Czochralski technique must be further refined if III-V semiconductors are to be grown, since the group V element dissociates upon melting of the semiconducting compound. By using a sealed, or encapsulated, system the problem of group V dissociation can be circumvented. In the liquid encapsulated Czochralski technique (LEC), first proposed by Mullin[2] et al., a pellet of solid boron trioxide glass overlies the crucible charge (figure 1.1(c)), forming a liquid encapsulation over the melt during growth. LEC grown GaAs is commonly used as a high purity, undoped substrate for epitaxial growth.

As implied by their name, III-V semiconductor compounds are alloys combining elements from groups III and V of the periodic table. The III-V binary compounds crystallise in the zinc blende (or sphalerite) structure, which is equivalent to the diamond lattice adopted by silicon and germanium except that the basis consists of two different atomic types[3], with a group III atom at the origin and a group V atom at co-ordinate position (1/4, 1/4, 1/4). Alternatively, this can be visualised as a face centred cubic lattice of group III atoms interpenetrated by a face centred cubic

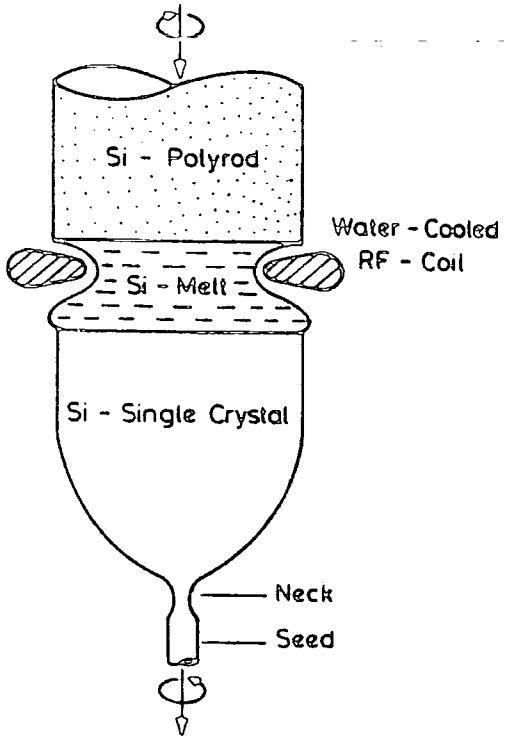


Figure 1.1(a) : The floating zone technique (FZT) used for the growth of single crystal silicon. After Moss and Ledwith[1].

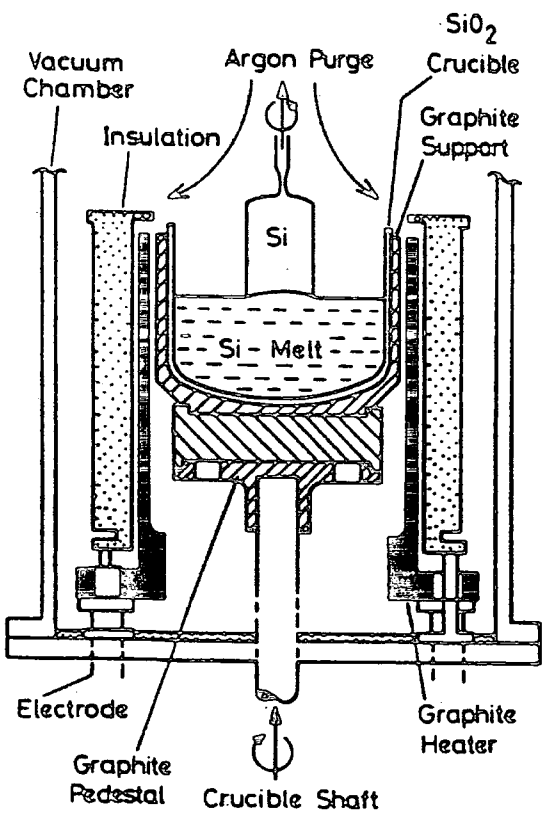


Figure 1.1(b) : The Czochralski technique for single crystal silicon growth from a crucible. After Moss and Ledwith[1].

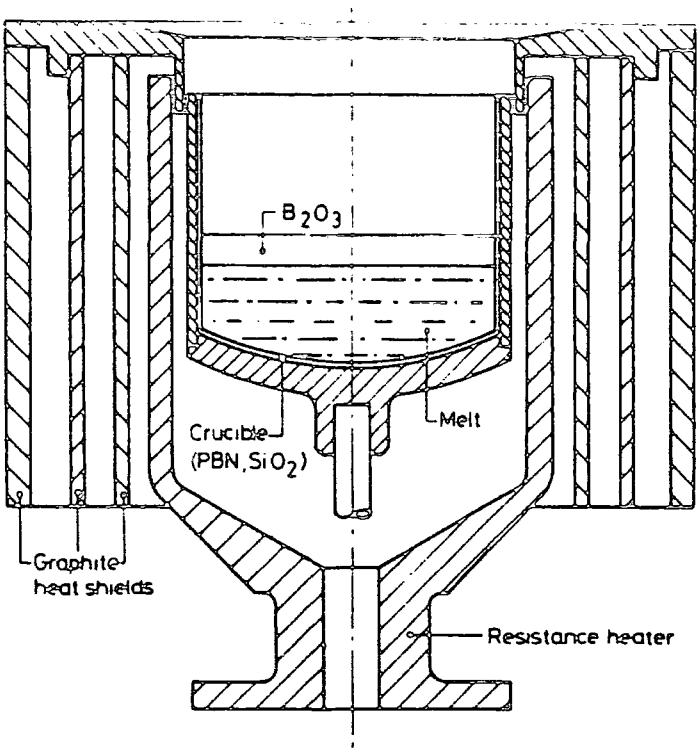


Figure 1.1(c) : The Liquid Encapsulated Czochralski method (LEC) for growth of single crystal III-V semiconductors. After Moss and Ledwith[1].

lattice of group V atoms, the group V atoms being displaced relative to the group III atoms by the vector (1/4, 1/4, 1/4).

Even though silicon can be melt grown with an extremely high degree of crystal perfection, the indirect bandgap of silicon has resulted in wide scale use of III-V and II-VI compound semiconductors, despite the high quality growth of such materials being significantly more difficult than in the case of silicon. In semiconductors with direct band-gaps (e.g., GaAs and InP), carrier transitions between the valence and conduction bands occur with no change in momentum. Thus in a graph of electronic energies versus wave vector (the parabolic E-k curve), emission of light occurs by a vertical descent from the minimum conduction band level to the maximum vacant level in the valence band. For indirect band-gap semiconductor materials (e.g., Si and Ge), the transition occurs with a change in momentum. This momentum change is accommodated by excitation of lattice vibrations and heating of the crystal lattice, making electron hole recombination (and thus photonic emission) much less probable. In general, direct gap semiconductors are more efficient by several orders of magnitude at emitting light, compared with indirect band-gap materials.

By manufacturing semiconducting compounds with three or more elemental components the bandgap (and hence wavelength of photonic emission) of the semiconductor can be tailored to a particular value. This is the situation with III-V semiconducting alloys which are extensively used in the telecommunications industry for the long range transmission of information along optical fibres[4]. Figure 1.2 shows the range of wavelengths available from various semiconductor material systems. The light signal carrying the information originates from semiconducting lasers and is attenuated as it passes along the fibre. The absorption of a typical silica optical fibre varies as a function of the transmitted wavelength[5,6], as demonstrated by figure 1.3[7], displaying minima in the absorption spectrum corresponding to wavelengths of 1.3μm and 1.55μm. An optical fibre transmission system contains many repeater units (basically detector-amplifier-transmitter combinations) used periodically to boost the attenuated light signal. By operating at wavelengths corresponding to minimum attenuation within the optical fibre, the spacing of the repeater unit can be increased to a large distance, allowing considerable savings in capital cost. Solid state lasers emitting at 1.55μm, allow the transmission of high bit rates (> $1Gbs^{-1}$), with a repeater spacing of over 100 km. At these high bit rates, the main factor affecting repeater spacing is no longer signal attenuation but chromatic

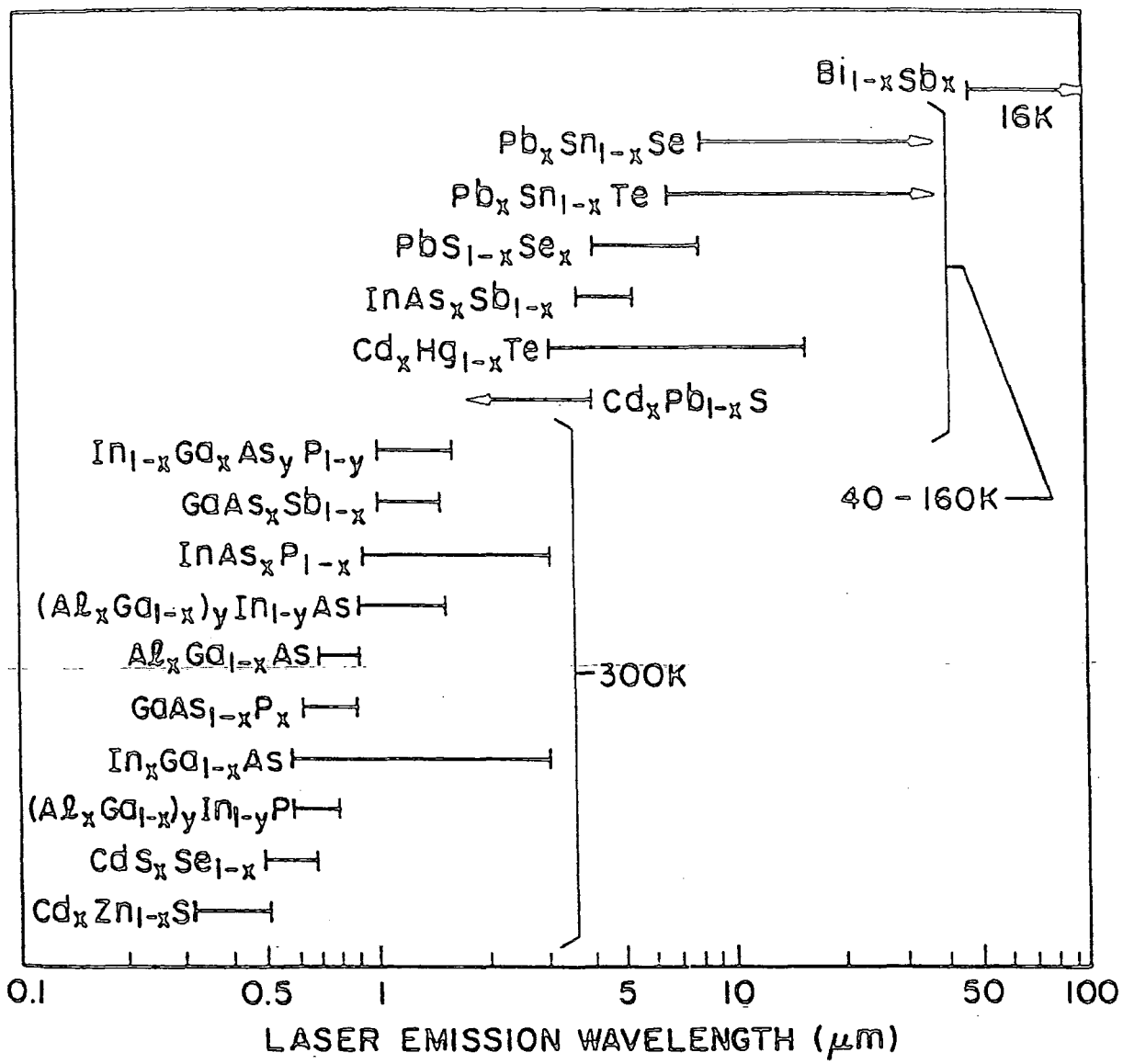


Figure 1.2 : The wavelength range of semiconductor lasers covered by different material systems. After Agrawal and Dutta[10].

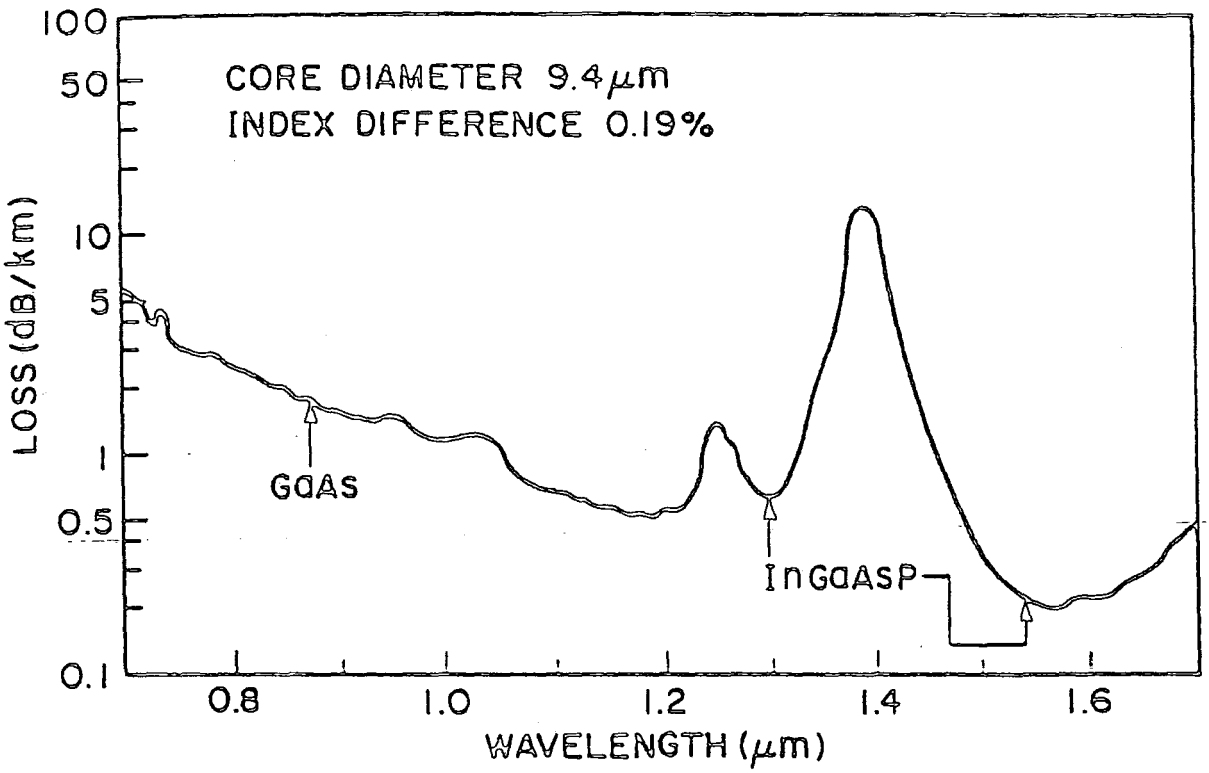


Figure 1.3 : Attenuation of the light signal in an optical fibre as a function of wavelength. The positions of minimum attenuation are indicated by the arrows. After Miya et al.[7].

dispersion within the fibre, a problem which can be addressed by limiting the spectral width of the laser source[8], or by modification of the fibre characteristics[9].

The semiconductor laser consists of a forward biased diode formed from the junction between two direct gap semiconductors. The applied voltage "injects" electrons from the n-type material conduction band across the junction to the p-type material conduction band, where they combine with holes resulting in the emission of a photon with energy approximately equal to the band gap energy. If this "injection current" is increased beyond a particular threshold value, photons arising from electron-hole recombinations stimulate further photonic emissions and laser action results. If the two ends of the diode perpendicular to the layer/substrate interface are made flat and polished, so as to act as partially reflecting mirrors, then light is reflected back across the region of recombination in the p-type material, causing amplification of the stimulated emission. An intense laser beam emerges from the crystal, whose output power can be tens of milliwatts, where the overall laser efficiency can approach 10%. A more comprehensive review of semiconducting lasers covering their growth, application and operation has been given by Agrawal and Dutta[10].

Compound semiconductors made from combining group II elements (e.g., Cd, Zn, Hg) with elements from group VI (e.g., S, Se, Te) are finding increasing applications, particularly with regard to design of LED's and injection lasers operating in the blue portion of the visible spectrum[11]. II-VI compounds have direct energy band gaps ranging from a fraction of a volt in Hg containing compounds to over 3.5 eV in ZnS, with low temperature mobilities approaching $10^6$ $cm^2V^{-1}s^{-1}$. If the group II element is substituted by a magnetic transition ion such as Mn, a new class of materials known as dilute magnetic semiconductors results (e.g., Cd(Mn)Te and Zn(Mn)Se) in which the semiconducting properties of the pure compound are largely retained. However, the localised magnetic moment of the magnetic transition ion (arising from the unfilled 3d shell) leads to magneto-optical effects which have been exploited in, for example, optical isolator devices.

Superlattice structures have generated much recent excitement in scientific research and technology development circles. The term superlattice refers to a structure with many thin layers, deposited in a regular, periodic manner onto a substrate. These structures thus exhibit one dimensional periodicity in the growth direction (i.e.

perpendicular to the substrate interface). The periodicity can be obtained by either regularly varying the sequence of deposited layers (i.e. A-B-A-B-A-B-A-B etc., where A and B are layers of differing composition) or by introducing "modulation" doping into a superlattice in order to create energy wells. In this definition, the term "thin" implies that the layers are of such small thickness that the wave functions of charge carriers in adjacent layers overlap interfacial boundaries and couple together. Epitaxial structures, by definition, involve coherent ordering of a crystal lattice across the boundary between two layers of different composition. For systems where the coherence across the interface is significantly worse, the crystalline quality is diminished by the presence of defects in the layers themselves and at interfaces (e.g., as in the case of metallic layers), and the term "superlattice" is no longer strictly appropriate, as the quality of the "artificial" lattice is degraded. Such structures are instead termed multilayers, although, in practice, the terms "superlattice" and "multilayer" are frequently interchanged. The excitement surrounding superlattice technology has been generated by the novel quantum effects which have been observed as a result of the coupling of electron wavefunctions across interfacial boundaries. Charge carriers are confined within a periodic band structure, exhibiting quantised energy levels, which can be engineered through selection of different layer materials and values of repeat period.

Excellent reviews detailing the growth, theory of operation and applications of semiconductor devices exist in the literature and the reader is referred to the work of Sze[12], Jaros[13] and others for a more comprehensive description.

## 1.3 Magnetic Multilayer Structures

Thin ferromagnetic films have found extensive applications in the production of audio, video and data storage devices (such as computer disks). Ferromagnetic materials have been long known to exhibit an anisotropic resistivity in a magnetic field[14]. This anisotropy has been used[15] to make magneto-resistors using thin films of alloys such as permalloy ($Ni_xFe_{1-x}$). This dependence of the film resistivity on the magnetisation of the thin layer forms the basis for magnetic recording media.

Two forms of recording media can be distinguished by considering the direction of the magnetisation relative to the thin film surface. In longitudinal media the magnetisation vector lies in the plane of the thin film, while in perpendicular devices

the magnetisation points perpendicular to the film surface, i.e., in the growth direction. The advantage of perpendicularly magnetised media is that a higher density of magnetic information can be stored.

Recently, great interest has been shown in the use of magnetic multilayer systems, with regard to their potential as high density recording media[16], this interest being sparked by the discovery of "Giant negative MagnetoResistance (GMR)" in Fe/Cr superlattice systems by Baibach[17] et al.. Magnetic multilayer systems consist of alternate layers of magnetic and non-magnetic materials. In the absence of an applied magnetic field the magnetic moments of adjacent magnetic layers can be spontaneously aligned either ferromagnetically or antiferromagnetically, depending upon the thickness of the layers. The polarity of this alignment varies periodically with the thickness of the non-magnetic layer[18]. When the magnetic layers are aligned antiferromagnetically, the resistance of the structure is greater than when they are aligned ferromagnetically due to the spin dependence of the electron scattering.

The magnetic properties of thin film recording media depend strongly on the grain size, thickness, film composition, perfection, impurity content and interfacial roughness of their constituent layers. In order to understand how each of these features affect multilayer magnetic properties, it is necessary to be able to characterise each of these physical and chemical properties. While methods exist which are capable of measuring film composition and impurity content, very few characterisation techniques are able to yield information on the surface and interfacial roughness of multilayered samples. This problem is addressed in Chapter VIII, which describes the use of grazing incidence x-ray reflectivity techniques (GIXR) to probe the interfacial structure within magnetic multilayers.

### 1.4.1 Epitaxial Growth

The growth of high quality, crystalline sub-micron devices has only been made possible by the development of sophisticated epitaxial growth techniques. Three main growth methods are commonly used in the fabrication of sample structures and these are liquid phase epitaxy (LPE), vapour phase epitaxy (VPE) and molecular beam epitaxy (MBE). A variety of alternate methods have also been

developed but these are all essentially loosely based around these three common "core" techniques.

### 1.4.2 Liquid Phase Epitaxy

Liquid phase epitaxy (LPE) is a popular technique used in the growth of semiconductor samples (in particular, low cost LED's) and is particularly suited to the growth of relatively thick (2 to 10μm) layers of high crystalline quality[19]. The rate of deposition of LPE is high, with layer growth rates of around 1μm per minute not uncommon. LPE involves the precipitation of a crystalline film from a supersaturated melt onto the parent substrate, which serves as both a template for the epitaxy and as a physical support for the heterostructure. One of the most common experimental arrangements is the multibin furnace[20], shown in fig.1.4[10].

At growth temperatures above 350°C, the difference in evaporation rates of indium and phosphorus mean that phosphorus is lost more quickly from InP substrates leading to the formation of indium rich InP droplets on the substrate surface, which have a detrimental effect on the morphology and quality of subsequent epitaxial layers[21]. To circumvent this problem, growth has been carried out in a phosphine ($PH_3$) rich environment[22], although this is expensive and tends to contaminate epitaxial layer materials in adjacent silos. A better solution is to close off particular silos with caps of carbon and pellets of a tin, indium and InP mixture[23]. As the temperature is increased, thermal decomposition of the pellet occurs and an overpressure of phosphine results. This technique allows LPE growth of InP to be carried out at up to 700 °C.

The limitations of LPE growth include poor thickness uniformity and rough surface morphology, particularly for thin epitaxial layers.

### 1.4.3 Metal-Organic Vapour Phase Epitaxy

Vapour phase epitaxy (VPE) concerns the growth of epitaxial material from gaseous sources[24]. Growth of material from the vapour phase (VPE) is most commonly practised using the metal-organic vapour phase epitaxy (MOVPE) technique[25], which is also known in a more general context as metal-organic chemical vapour deposition (MOCVD). A schematic arrangement of an MOCVD reactor is shown in

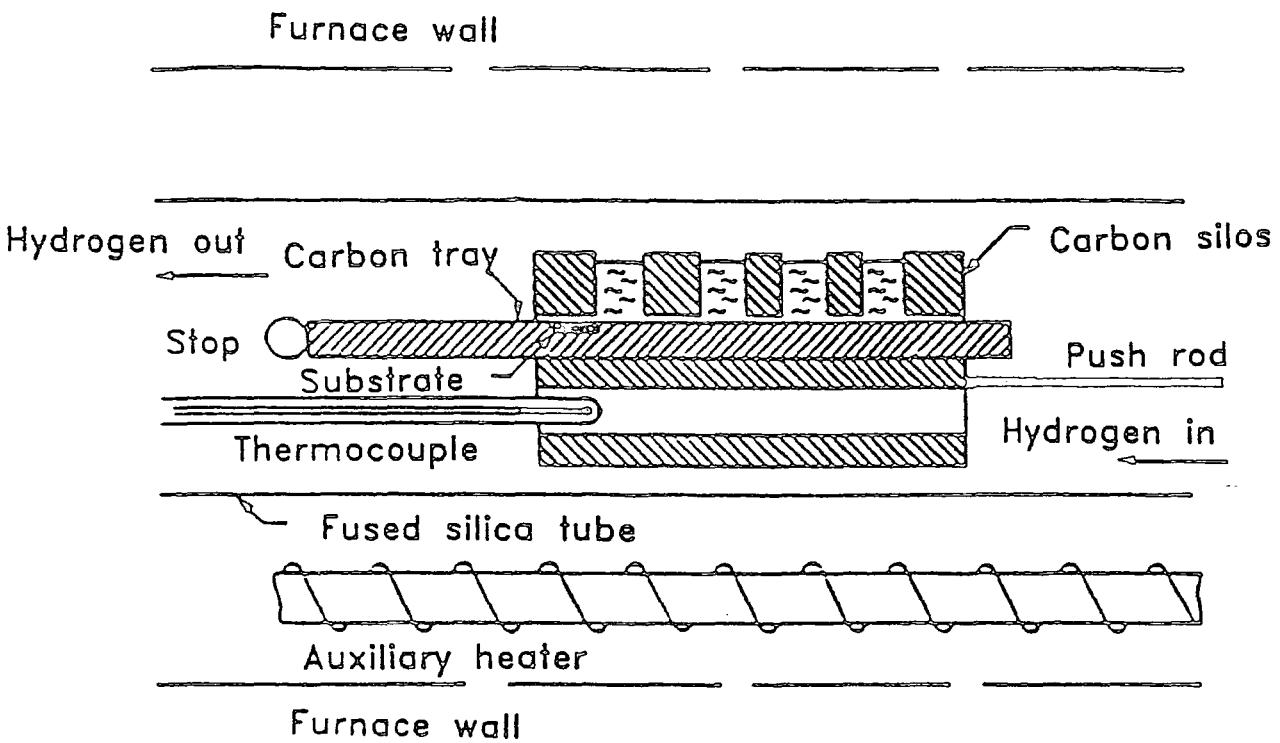


Figure 1.4 : The multibin liquid phase epitaxy (LPE) furnace. After Agrawal and Dutta[10].

fig.1.5[26]. In the case of epitaxial growth of III-V semiconductor compounds, group V elements (e.g., As, P) are introduced into the reactor chamber in the form of trihydrides (e.g., $AsH_3$, $PH_3$) while group III elements are introduced in the form of covalent alkyls (e.g., $In(CH_3)_3$, $Ga(CH_3)_3$). The gases flow over the susceptor (on which the substrate is placed), which is heated (by infra red lamps or RF coils) to around 500°C. At these elevated temperatures, pyrolitic cracking of the gases occurs, and the group III and group V elements are deposited epitaxially onto the heated substrate. The actual mechanism of atomic deposition is not fully understood, though it is known empirically that the amount of group III material present is the sole determinant of the resulting layer deposition rate. Typical pressures within the reaction chamber are between 0.1 and 0.5 atmospheres with a through gas flow of 1 to 15 cm per second. Doping can be introduced into the deposited layer by mixing hydrogen sulphide (n-type) or dimethyl zinc (p-type) with the group III and group V containing gases, within the reaction chamber. Computer control of the temperature and pressure of the injected gases allows the final composition of the epitaxial layer to be accurately determined.

### 1.4.4 Molecular Beam Epitaxy

Molecular beam epitaxy essentially involves controlled evaporation in an ultra high vacuum system ($10^{-10}$ torr). The reaction of one or more evaporated beams of atoms or molecules with the single crystal substrate yields the desired epitaxial film. The independent control of beam sources, coupled with a slow growth rate enables the fabrication of thin films with a precision on the atomic level. Deposition of thin films from a fraction of a micron in thickness, down to a single monolayer are possible. For GaAs materials, MBE growth progresses with a typical rate of around 1μm per hour. A cross sectional view of a typical MBE system, illustrating the major components, is shown in fig.1.6[27]. In MBE the physical surface migration of adsorbed molecules determines the properties of the films grown. For chemical vapour deposition processes (CVD), the chemical interaction between gas phase and solid surface plays an important role in the subsequent growth rate, stoichiometry and impurity concentration of thin films.

A recent advance in MBE techniques has seen As and P used to provide a gas source. Organometallics used for this purpose are thermally cracked, releasing the group V element as a molecular beam into the system, yielding excellent epitaxial

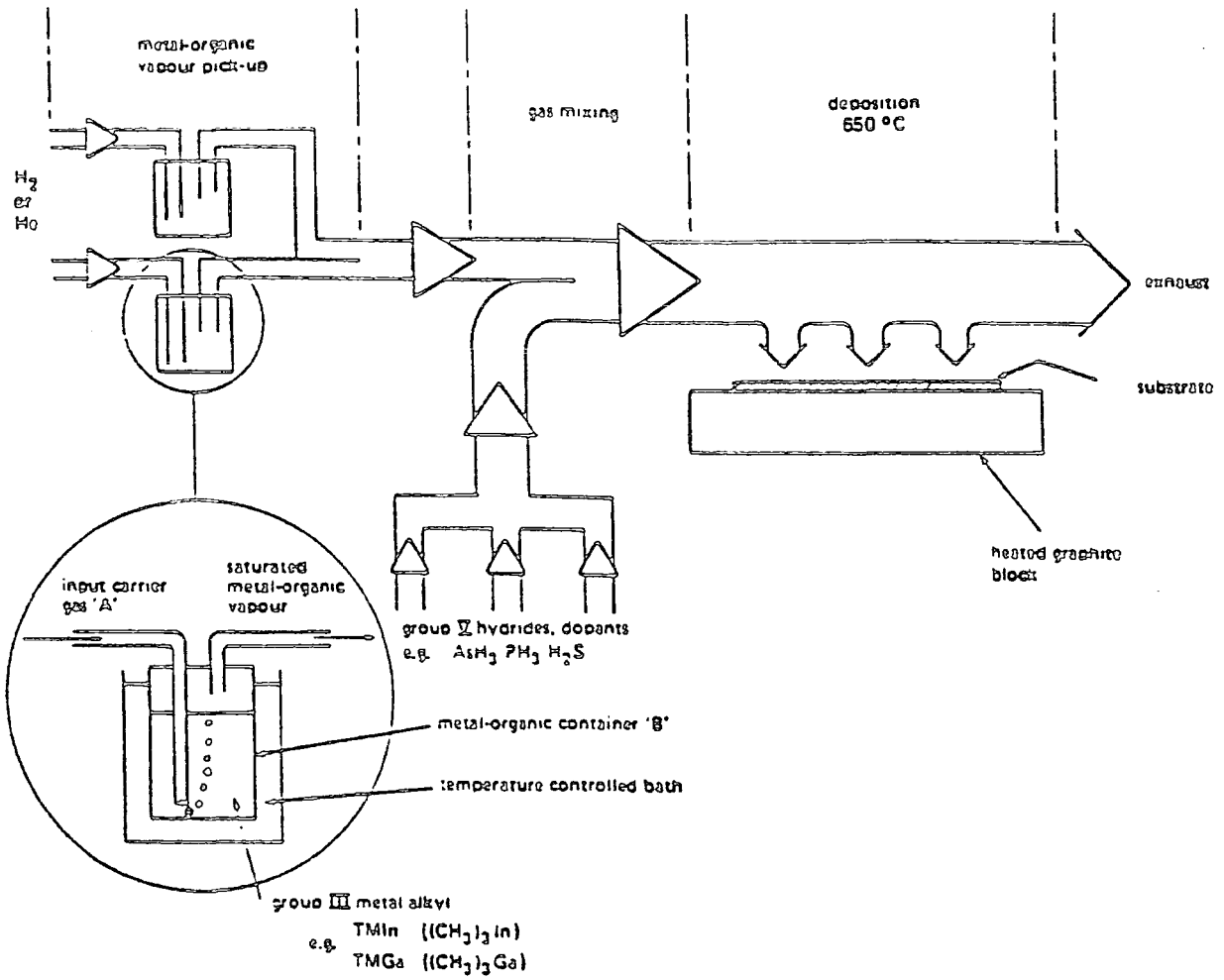


Figure 1.5 : The MOVPE growth Process. After Nelson et al.[26].

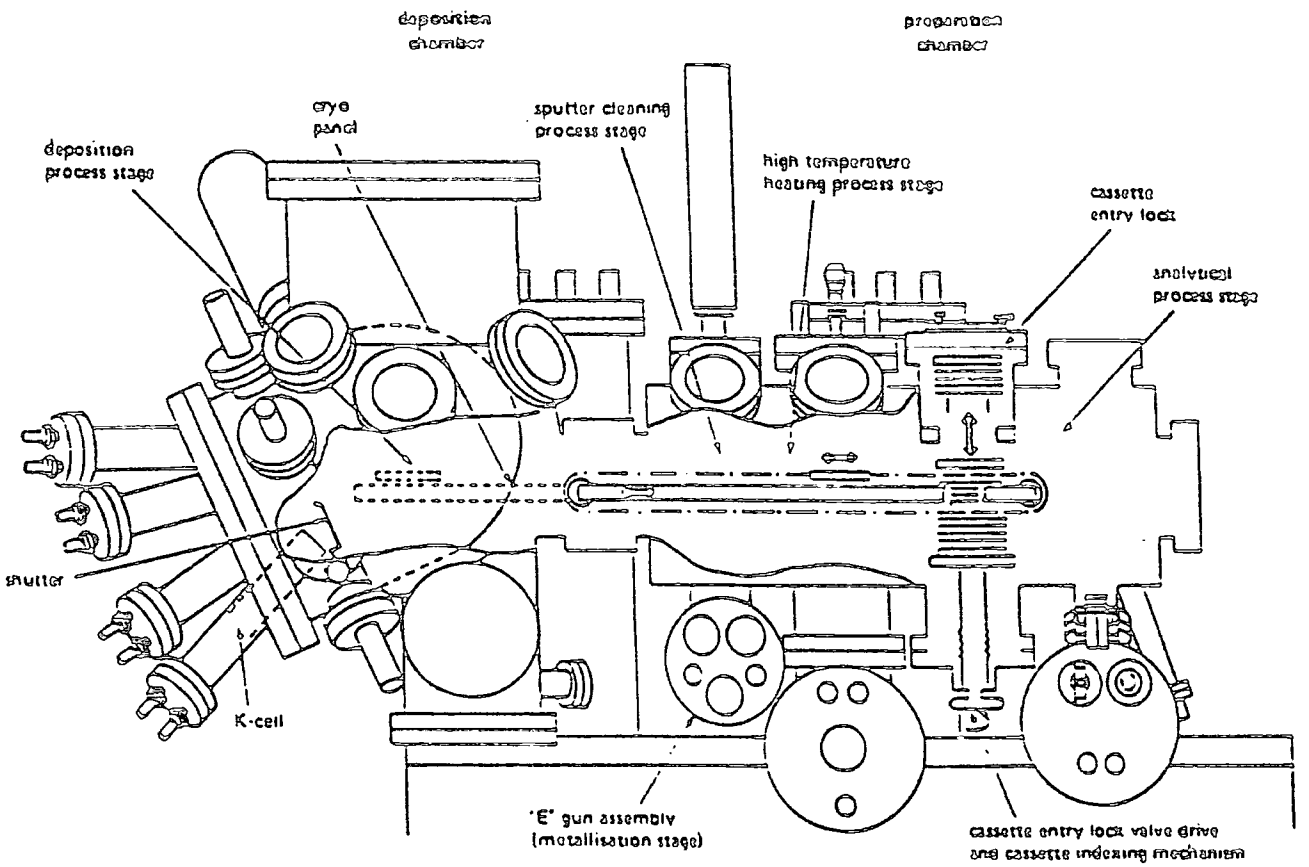


Figure 1.6 : Cross sectional view of a typical MBE system. After Davies and Andrews[27].

film growth. Growth using this technique is known by the acronym MOMBE (Metal-Organic Molecular Beam Epitaxy)[28,29,30]. Another variant of the MBE method is the Atomic Layer Epitaxy technique (ALE)[31,32]. In ALE, growth at the sample surface is self limiting and complete monolayers are sequentially deposited as the growth process progresses. The growth rate is thus proportional to the number of reaction cycles rather than the intensity of the reactant flux or the time of growth. The original application of ALE techniques was in the growth of II-VI materials and dielectric thin films for electroluminescent display devices[33], although it has recently attracted significant interest from the III-V field. This is due to ALE's potential for achieving atomic layer controlled ultra-thin film heterostructures, which are rapidly being developed for applications in high speed devices, optoelectronic integrated circuits and sophisticated quantum confinement structures. The work peresented in Chapter VII uses high resolution x-ray scattering techniques to characterise a series of ALE grown epitaxial GaAs layers.

## 1.5 Sputtering Techniques

Another common technique employed in the deposition of thin films is sputtering. The quality of layers deposited using this method is worse than in the case of epitaxial techniques, with poor crystalline quality being typical of many sputtered systems. However, sputtering has the advantage of very high growth rates and is applicable to situations where thick layers are required with no great demand on crystalline quality.

A simplified sputtering system is shown in fig.1.7[34]. The target is a plate of the material from which the thin film is to be synthesised, and, since a negative potential is often applied, the target forms the cathode of the electrical system, with typically a negative bias of some several kilovolts applied to the cathode. After evacuation of the chamber, a gas is introduced which serves as the medium in which a discharge is initiated and maintained. The gas introduced is typically argon, and gas pressures can range from a few to 100 mtorr. Upon producing a visible glow discharge, a thin film of the target material is built up upon the substrate. Positive ions in the discharge strike the cathode plate and eject, amongst other products, neutral target atoms through momentum transfer. These atoms enter and pass through the discharge region eventually to condense upon the substrate, producing the desired thin film. Sputtering has been likened[35] to "atomic pool" where the positive

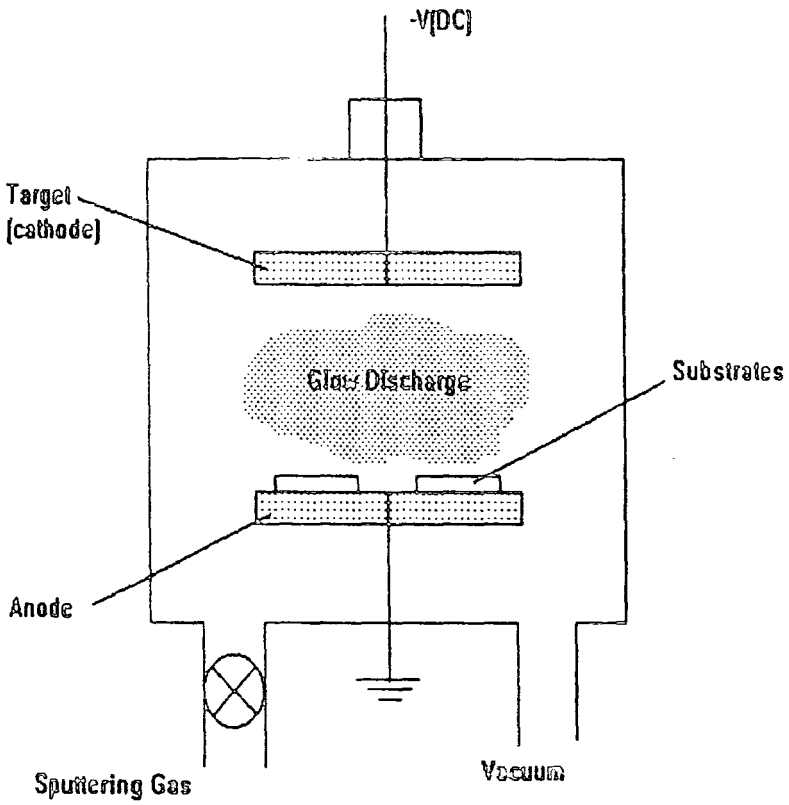


Figure 1.7 : Schematic diagram of a sputtering system[34].

discharge gas ions (the cue ball) break up the close packed rack of atoms (billiard balls), scattering some backward (toward the player). The most fundamental parameter characterising sputtering is the sputter yield, S, which is defined as the number of atoms or molecules ejected from a target surface per incident ion and is a measure of the efficiency of the sputtering process. Sputtering processes can be divided into four main categories; dc methods where the target (cathode) is kept at a steady negative potential; RF methods where an ac signal is applied to the electrodes (used to deposit insulating thin films); magnetron sputtering, which employs magnetic fields to contain electrons within the plasma region (and thus enhance the probability of ion collisions and increase the sputter deposition rates) and reactive sputtering in which deposition occurs in the presence of a reactive gas (e.g., oxygen mixed with argon, if an oxide layer is to be deposited). Magnetron sputtering is currently the most common commercial technique, mainly due to its high sputter rates, typically 1μm per min for Al. This deposition rate is around an order of magnitude higher than that found for conventional sputtering methods.

## 1.6 Epitaxial Layer Growth

Three processes have been proposed by which epitaxial layer growth is thought to occur. The type of growth observed is dependent upon the enthalpy of bonds present at the substrate/film/vacuum interfaces. In the so-called Frank van der Merwe mode the layer/vacuum interfacial energy is less than that of the substrate/vacuum interface and energy considerations mean that a layer is preferentially deposited onto the substrate. If the bond enthalpies of the epitaxial layer continually decrease as the thickness of the deposited layer increases, then planar film growth will continue (i.e. a thicker layer would lead to a less energetic, more stable layer/vacuum interface).

The second growth mode, known as the island (or Volmer-Weber) growth mode, occurs when the layer/vacuum interfacial energy exceeds that of the substrate/vacuum interface. This occurs in highly mismatched systems (e.g., CdTe on GaAs and GaAs on Si) or where the deposited layer has a different crystallographic structure to the substrate material. In this instance, layer growth does not proceed in a planar manner but rather three dimensional islands of layer material are formed on the substrate surface, which eventually coalesce to form the epitaxial layer. The boundaries between these islands can be heavily dislocated and

tilted with respect to each other, resulting in more imperfect layers (i.e. greater defect content) than in the case of Frank van der Merwe type growth.

A final growth mode (the Stranski-Krastanov mode) exists where the scenario is somewhere between the Frank van der Merwe and island growth modes. Initial epitaxial growth is planar (i.e. van der Merwe) but a perturbation in bond enthalpies of the layer material is observed as the layer thickness increases, resulting in a transition from two dimensional planar growth to three dimensional island (or Volmer-Weber) growth.

In coherent epitaxial growth, the lattice parameter of the layer parallel to the interface matches that of the substrate, i.e. the substrate acts as a "template" for the deposited layer. In the case where the bulk lattice parameters of the substrate and layer materials are different, then a "mismatch" is said to exist between the substrate and layer crystal structures. The lattice mismatch (or misfit), m, is quantitatively defined by equation (1.1),

$$m = \frac{(a_l - a_s)}{a_s} \tag{1.1}$$

where $a_s$ is the substrate lattice parameter and $a_l$ the bulk layer lattice parameter.

For substrate/layer systems which are mismatched, epitaxial growth proceeds with the lattice mismatch of the substrate and layer materials being accommodated by tetragonal distortion (elastic strain) of the layer lattice, in order to maintain coherency of the substrate and layer unit cells across the interface[36,37]. An increase in the layer thickness is accompanied by a corresponding increase in the total strain energy within the crystal lattice until a critical point is reached, where the total strain energy is so large that the lattice mismatch can no longer be accommodated by elastic strain of the layer material. At this particular layer thickness, known as the critical thickness, $h_c$, misfit dislocations are formed which reduce the total strain energy in the epitaxial layer. The layer lattice parameter parallel to the interface moves back toward its bulk value, and the lattice of the layer material in the region of the interface is said to "relax". The relaxation, R, is defined as the proportion of the misfit strain which is reduced by the nucleation of misfit dislocations near to the interface between the substrate and the epitaxial layer[38],

$$R = \frac{(c - a_l)}{(a_s - a_l)} \tag{1.2}$$

where the lattice constants parallel to the interface of the totally unstrained epitaxial layer, the partially strained epitaxial layer and the substrate are denoted by the parameters $a_l$, $c$ and $a_s$ respectively.

Thus in epitaxial growth of a mismatched system three different situations are possible, as illustrated in fig.1.8. The layer can exhibit no coherency with the substrate (and deposit, or "relax" with a unit cell with the bulk layer lattice parameter), grow with full coherence maintained parallel to the interface (i.e., epitaxial growth) or grow in a manner somewhere between these two situations and exhibit partial coherence/relaxation.

The point at which a layer material will begin to "relax" depends upon the absolute value of the substrate/layer mismatch as well as the thickness of the epitaxial layer. Theoretical models for calculating the critical thickness (i.e., the point at which relaxation begins) of an epitaxial layer have been developed[39] but matching of predicted to experimentally measured critical thicknesses has, in general, been only approximate (see Chapter VII). While misfit dislocations lying in the interface between the layer and the substrate are the most efficient means by which misfit strain is relaxed, other types of dislocation are also present within the system. Dislocations extending from the substrate into the epitaxial layer are known as threading dislocations. When a lattice strain is present, the vertical segments of the threading dislocations in the substrate and epitaxial layer move in opposite directions, leaving a segment of misfit dislocation lying in the plane of the interface.

The generation of misfit dislocations has a significant bearing on device behaviour, as they have been found to degrade seriously device performance. In quantum well laser systems dislocations act as centres for non-radiative recombination of electron/hole pairs, leading to a reduction in the luminescence quantum efficiency of over two orders of magnitude for only a small increase over the critical thickness[40]. Measurements of threshold voltage variations in Field Effect Transistor (FET) arrays have been strongly correlated with the dislocation distribution density across wafers.

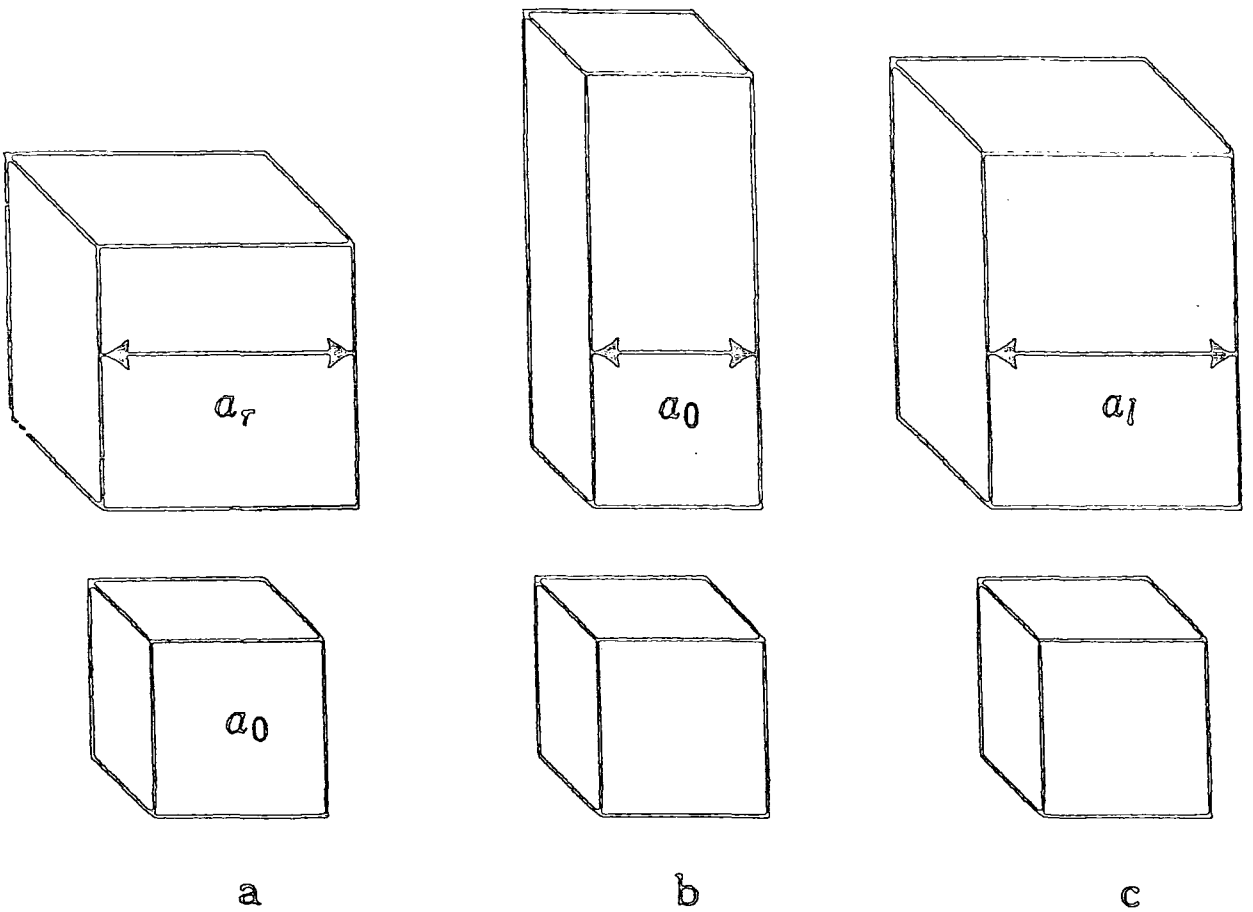


Figure 1.8 : Configurations of the epitaxial layer unit cell. After Halliwell[38].

(a) full relaxation (i.e. bulk state), (b) coherently strained,
(c) partially relaxed.

Measurement of the lattice constant of epitaxial layers is of great use in the semiconductor industry as the lattice parameter of ternary alloys can be directly related to their composition by the use of Végard's law. This states that the lattice parameter of a ternary or quartenary alloy varies linearly with the composition[41,42], i.e., it can be deduced by linearly interpolating between the lattice parameters of the constituent binary components. Végard's law is extensively used in the high resolution x-ray diffraction characterisation of ternary semiconductor structures, where a measured lattice mismatch is used to calculate the composition of strained, heteroepitaxial alloys. Since the observed mismatch in an x-ray diffraction experiment relates to the lattice parameter of the *strained* layer material, the tetragonal distortion of the layer lattice must be taken into account if the *real* mismatch is to be determined (i.e. the mismatch of the substrate and layer bulk lattice parameters). The real mismatch, m, is related to the effective mismatch, $m^*$, by equation (1.3),

$$m^* = m \times \frac{(1+\nu)}{(1-\nu)} \tag{1.3}$$

where $\nu$ is the Poisson ratio, which is related to the elastic constants $C_{11}$ and $C_{12}$ by equation (1.4)[43].

$$\nu = \frac{C_{12}}{C_{11} + C_{12}} \tag{1.4}$$

Theoretical treatments of layer strain have been described by several authors[44,45,46] using classical elasticity theory, where sharply defined interfaces, a rigid substrate and an isotropic layer subjected to a state of plane stress are assumed. For growth on (001) oriented substrates, the strained layer lattice parameter perpendicular to the interface, c (i.e. in the growth direction) has been shown to be,

$$(c - a_s) = \frac{(1+\nu)}{(1-\nu)}(a_l - a_s) \tag{1.5}$$

where $a_l$ and $a_s$ are the bulk lattice parameters of the layer and substrate respectively.

## 1.7 Characterisation Methods For Semiconductor Materials

The ever decreasing dimensions of thin layered semiconductor and magnetic systems, together with the strong dependence of sample behaviour with as-grown structure, demand that the physical and chemical structural parameters are grown to within a tight tolerance by the grower. Many analytic techniques have been developed with which the physical and chemical status of materials can be determined and mention will be given here to only those methods most commonly employed in industrial and academic research laboratories.

In general, the sample is probed with some form of wave or particle generating a signal or product which is then collected and analysed in an attempt to deduce a specific specimen parameter. As has been found by many other authors and reviewers of characterisation methods, it is convenient to group the various techniques according to the nature of the incident probing radiation. In general, the experimental probe can be classified as an optical probe, an x-ray probe, an electron beam or a particle beam. Following the approach of Shaffner[47], figure 1.9 outlines the capabilities of the more commonly used characterisation techniques employed in the semiconductor industry, grouped according to the state of the incident probe. Rarely does a single characterisation technique provide the investigator with all of the desired structural information, and a combination of complementary techniques is needed to fully characterise the physical and chemical state of the specimen. Characterisation techniques may also be classified as destructive (where the probing radiation permanently damages the specimen structure) or non-destructive (where the sample state is left unchanged). Non-destructive testing methods are of obvious benefit, particularly in a large scale production context where routine quality checking of high value samples is employed.

Techniques employing optical probes include interferometry[48,49] (used for layer thickness measurements) ellipsometry[50] and vibrational spectroscopy[51]. In ellipsometry, a beam of polarised light is directed at oblique angles to the layer surface and the reflected beam monitored. The signal is generated by interference of the components of the probing radiation, which undergo multiple reflection from the interfaces between the substrate and different layers. Information is obtained on the optical constants of materials, thicknesses of overlying layers and the presence of disturbed and roughened layers.

| | Optical Microscopy | Fourier Transform Infrared (FTIR) | Photo Luminescence (PL) | Infrared and Ultra-Violet (IR & UV) | Raman Micro-Probe | Photo-Neutron Activation |
|---|---|---|---|---|---|---|
| Depth Analyzed | > 1-3 μm | 1-10 mm | 1-3 μm | 1 mm IR<br>1 μm UV | 1 μm | 0.5 cm |
| Diameter of Analysis Region | ~ 1 cm | 2 mm | > 5 μm | 1 mm | 2 μm | 0.5 cm |
| Detection Limit (atoms/cm$^3$) | visual inspect | $1\times10^{11}$ | $1\times10^{11}$ | $5\times10^{10}$ | $5\times10^{10}$ | $5\times10^{15}$ |
| Detection Limit (ppm) | visual inspect | $2\times10^{-6}$ | $2\times10^{-6}$ | 100 | 1000 | 0.1 |
| In-depth profiling resolution | none | none | none | none | none | none |
| Time for Analysis | < 1 hour | 2 hours | 2 hours | < 1 hour | < 1 hour | 2 hours |
| Comments | In-depth profiling achieved by angle-lap cross section | Performed at 10-15°K temperatures | Performed at 4°K temperatures | Performed at room temperature | | Built measurement only |

(a) Optical probe techniques.

| | Scanning Electron Microscopy (SEM) | Auger Electron Spectroscopy (AES) | Scanning Auger Microprobe (SAM) | Electron Microprobe (EMP) | Analytical Electron Microscopy (AEM) | High Voltage TEM (HVTEM) |
|---|---|---|---|---|---|---|
| Depth Analyzed | ~ 1000 Å | 20 Å | 20 Å | 1 μm | < 1000 Å | < 1000 Å |
| Diameter of Analysis Region | 50 Å - 5 mm | 100 μm | 1000 Å | 1 μm | 10 μm | 10 μm |
| Detection Limit (atoms/cm$^3$) | surface image | $5\times10^{19}$ | $1\times10^{21}$ | $5\times10^{19}$ | defect imaging | lattice imaging |
| Detection Limit (ppm) | surface image | 1,000 | 20,000 | 1000 | defect imaging | lattice imaging |
| In-Depth Profiling Resolution | stereo microscopy | 20 Å | 20 Å | none | stereo microscopy | none |
| Time for Analysis | < 1 hour | < 1 hour | < 1 hour | < 1 hour | 1-3 days | 1-3 days |
| Comments | In-depth profiling achieved by angle-lap cross section | Profiling achieved by argon sputtering | Profiling achieved by argon sputtering | Wave-length & energy dispersive analysis | sample preparation requires specialized techniques and is time consuming | |

(b) Electron probe techniques.

Figure 1.9 : Characterisation techniques used for the analysis of epitaxial thin films and surfaces. Techniques are classified according to the status of the experimental probe. After Shaffner[47].

| | Rutherford Backscattering Spectroscopy (RBS) | Neutron Activation Analysis (NAA) | Ion Microscope (IMS,SIMS) | High Energy Ion Channeling | Charged Particle Activation Analysis (CPA) |
|---|---|---|---|---|---|
| Depth Analyzed | 200 Å - 1 μm | 1 μm | 50 Å | 100 Å | 300 μm |
| Diameter of Analysis Region | 2 mm | > 1 cm | > 5 mm | 1 mm | 5 mm |
| Detection Limit (atoms/cm$^3$) | $5x10^{19}$ | $5x10^{11}$ - $5x10^{10}$ | $5x10^{15}$ - $5x10^{10}$ | $5x10^{19}$ | $5x10^{13}$ |
| Detection Limit (ppm) | 1000 | 0.00001 - 100 | 0.1 - 100 | 1.0 | 0.001 |
| In-depth Profiling Resolution | 200 Å | 1 μm | 50 Å | surface technique | 25 μm |
| Time for Analysis | 1 hour | 2-5 days | 1 hour | 2 hours | 2 hours |
| Comments | No standards needed | In-depth profiling by chemical etching | Spatial Resolution near 1 μm | crystalline substrate required | In-depth profiling by chemical etching |

(c) Particle probe techniques.

| | Powder X-ray Diffraction (XRD) | Thin Film Analysis (Seeman-Bohlin) | Lang X-ray Topography (Lang) | Double Crystal Topography (DCT) | X-ray Fluorescence (XRF) | X-ray Photoelectron Spectroscopy (XPS,ESCA) |
|---|---|---|---|---|---|---|
| Depth Analyzed | 10-50 μm | 100 Å - 1 μm | 500 μm | 5-100 μm | 1-3 μm | 20 Å |
| Diameter of Analysis Region | > 1 mm | 1x5 mm | > 1 cm | > 1 cm | > 5 mm | 5 mm |
| Detection Limit (atoms/cm$^3$) | $5x10^{19}$ | $5x10^{19}$ | $1x10^{-3}$ in Δd/d | $1x10^{-7}$ in Δd/d | $1x10^{19}$ | $5x10^{19}$ |
| Detection Limit (ppm) | 1000 | 1000 | — | — | 200 | 1000 |
| In-depth Profiling Resolution | none | none | stereo topography | none | none | 20 Å |
| Time for Analysis | < 1 hour | 2 hours | 1 hour | 4 hours | 10 min | < 1 hour |
| Comments | sample cannot be amorphous | grazing incidence beam used | whole slice survey | whole slice survey | rapid & quantitative | In-depth profiling by argon sputtering |

(d) X-ray probe techniques.

Vibrational spectroscopic methods used for the study of molecules at surface include infra-red (IR), Raman[52] and electron energy loss spectroscopy (EELS). Raman spectroscopy is a long established technique in which the inelastic scattering of photons is used to determine vibrational transitions within molecules. EELS is a related technique to the Raman method, except that the photon probe is replaced by a beam of electrons. In addition to giving molecular identification, vibrational spectroscopy can yield information on the mode and strength of attachment of the layer atoms to the substrate, by comparison of changes in the vibrational spectra of atoms in their free and absorbed state. Furthermore, since Raman and infra-red spectroscopy are optical techniques, measurements are not confined to systems under high vacuum and *in situ* analysis may sometimes be performed.

Perhaps the most wide spread method for analysing thin epitaxial films is the technique of scanning electron microscopy (SEM). In SEM, a beam of electrons of energies up to 50 keV, sourced from a hot filament, is focused to a very fine spot size (~ 50Å) and rastered across the specimen surface. Upon striking the surface, the electrons decelerate, giving up energy in inelastic collisions with the sample atoms. Electronic excitations occur and secondary electrons are emitted from the specimen, together with Auger and elastic back scattered electrons. In addition to these products, target characteristic x-rays, heat, light and specimen currents are produced, which can all be detected with appropriate instrumentation. The choice of the particular SEM mode which is employed, depends upon which product is actually detected and subsequently imaged. The most common SEM mode relied upon collection of the low-energy, secondary electrons. The low energy of these particles means that they originate from a subsurface depth of only a few tens of angstroms, giving excellent surface structure information. Non-planar surfaces yield significant contrast variations allowing three dimensional images of high quality to be obtained with excellent depth of focus. In semiconductor samples the incidence of the primary electron beam on the specimen surface generates electron/hole pairs which constitute a current which can be detected and used to modulate the intensity of the signal displayed on the cathode ray tube. This is the basis of the EBIC (Electron Beam Induced Current) technique where subsurface defects and failure sites can be spatially separated within the sample image.

Compositional information can be obtained by collection of the characteristic x-rays emitted from the sample due to the impingement of the high energy primary beam, using the electron microscope in the EDX mode (Energy Dispersive X-ray analysis). By sorting the x-rays as a function of energy, elemental analysis can be performed with the intensity of the x-ray peaks being directly related to the concentration of the element.

If structural information is required from a layered structure which is sufficiently thin to transmit electrons, then the technique of transmission electron microscopy (TEM) can be applied. Here, the primary electron beam travels through the sample, with electrons being scattered at ion cores and defect sites. Electrons scattered elastically from the crystalline lattice give rise to diffraction patterns which can be analysed in order to correlate specimen structure with an observed pattern. The TEM can be operated in two modes; the so-called "bright field" image in which apertures are used to block the diffracted images, allowing only the central intense beam to be detected, and the "dark field" image, where only one of the diffracted beams is selected out to contribute to the formation of the final image, with the central beam being blocked out. TEM has been extensively used in the characterisation of epitaxial systems, some examples being the work of Chang[53] et al. and Alavi[54] et al. who have studied compositional variations and misfit dislocations in strained layers, Carey[55] (the investigation of defects in MOVPE InGaAs ), Schaus[56] et al. (analysis of quantum well heterostructures in order to optimise growth conditions) and Dupius[57] et al. (a study of the dislocation behaviour upon thermal processing of Ge layers grown on Si). TEM is often combined with other characterisation techniques, which provide complementary information (e.g. x-ray analysis, photoluminescence), in order to fully characterise sample structure/composition[58,59,60,61].

To monitor layer growth *in situ*, electron diffraction techniques are commonly employed. In LEED[62] (Low Energy Electron Diffraction) a low energy electron beam (< 1keV) is directed normally to the layer surface, with electrons penetrating to only a few angstroms below the layer surface. In RHEED (Reflection High Energy Electron Diffraction)[63] the incident electron beam strikes the layer at a grazing angle (the incidence angle is no more than a few degrees). The electron energy is much greater than in the case of LEED, with energies ranging from 5keV to 100 keV. This high electron energy results in a large Ewald sphere. Since the reciprocal lattice points and Ewald sphere have a finite width, intersection of the two

occurs for some distance along the height of the reciprocal lattice point, and a streaky rather than sharp spot diffraction pattern results. The low energy of electrons (and hence small Ewald sphere radius) in LEED means that a sharp spot diffraction pattern is produced. An important feature of RHEED, is that the intensity of the reflected electron beam depends upon the step density of the growing film. During deposition of an epitaxial layer, the intensity varies sinusoidally as successive monolayers are grown, the period of oscillation being equal to the monolayer formation time. The type of pattern observed can also be related to the mode of epitaxial growth, with three dimensional "island" growth being characterised by "spotty" diffraction patterns and streaks indicating smooth layered, planar growth (i.e. 2D growth). Reflection electron microscopy techniques are very sensitive to surface perfection and have been applied, for example, in the surface reconstruction of Si[64] and the study of atomic height steps in metals[65].

Two of the most popular techniques which employ particle probes are secondary ion mass spectroscopy (SIMS)[66,67] and Rutherford back scattering (RBS)[68,69]. In SIMS, the specimen surface is bombarded by a source of ions resulting in the sputtering of neutral and charged ions from the outermost regions of the thin film. Once in the gas phase, the ions are mass analysed in order to identify the species present as well as determine their abundance. The SIMS technique is of particular use when measuring the composition of epitaxial films, particularly as a function of depth. It has the disadvantage of being destructive and no complete theory yet exists to describe fully the sputtering process (i.e. an accurate description of ion yields taking into account escape velocities and dependence on ion projectile and target materials). While SIMS is of great use when determining near-surface compositions, RBS is often used if compositional information is required from regions well into the sample. High energy (MeV) beams of low mass ions are fired at the specimen and penetrate thousands of angstroms, or even several microns deep into the thin film, with a negligible signal being generated from surface sputtering. Projectile ions lose their energy through electronic excitation and ionisation of target atoms. Some of the fast moving projectile ions (usually $^4He^+$) penetrate the electron cloud shield and undergo collisions with the nuclei of the more massive stationary target atoms. Coulomb repulsion occurs between the incident ions and atomic nuclei resulting in Rutherford backscattering. Backscattered ions are analysed with respect to their energy in order to determine elemental information on the target composition. RBS

can detect concentration levels of around 1 atomic percent and is often applied in determining the stoichiometry of thin film binary compounds.

The materials characterisation described in this thesis utilises x-ray scattering techniques to determine sample structure. Discussion of the specific experimental techniques used will be presented in Chapter IV. Subsequent chapters will then present examples of the applications of these techniques to the analysis of material systems of current technological importance. The work presented in Chapter V concerns the automated extraction of layer thickness information from the high resolution diffraction profiles of High Electron Mobiltity Transistors (HEMT's). Chapters VI and VII utilise high resolution diffraction techniques to analyse samples, in order to determine their lattice constants and defect structure, respectively. Chapter VIII will discuss the application of grazing incidence x-ray reflectivity to the study of layer thickness and interface roughness in multilayer and superlattice structures. Prior to a description of the principles and applications of x-ray scattering, a theoretical discussion of the interaction of x-rays with solids (both crystalline and amorphous), and the theory of high resloution diffraction will be presented in the following two chapters.

# CHAPTER II

# Theory Of X-Ray Scattering

## 2.1 Introduction

X-ray analysis of material structure is based on the concept of directing x-rays onto a sample and studying the direction, energy or intensity of scattered or emitted radiation in order to deduce structural information about the specimen itself. As x-rays have a wavelength comparable with an atomic spacing they can be used to probe sample structure with a sensitivity on a sub-nanometre scale in a non destructive manner. Several different types of scattering experiments can be employed (as will be discussed in Chapter IV) with the choice of experimental configuration adopted being dependent upon both the kind of information sought and the type of material to be analysed (e.g. whether crystalline or amorphous).

Most x-ray characterisation methods can be classified into three main areas; those of flourescence, reflectivity and diffraction techniques. Fluoresence techniques are concerned with the absorption of incident x-rays and their subsequent re-emission as radiation with a characteristic energy. By equating the energy of the emitted x-rays to an electronic transition between two energy levels the type of atom involved in the absorption process can be identified. In this way the presence of individual elements within a sample of unknown composition can be detected and this phenomena is utilised in x-ray fluorescence analysis techniques such as EXAFS (Extended X-ray Absorption Fine-Structure). The use of such methods is beyond the scope of this study and the reader is referred to a number of texts for a review of fluorescence techniques[1,2,3].

The work discussed in this thesis is concerned with the use of the other two types of x-ray characterisation probes mentioned above; reflectivity and diffraction. These techniques are similar in that they both involve studying the scattered radiation (usually as a function of angle) from a sample and have found use within research and industrial laboratory environments. In order to interpret the results of an x-ray scattering experiment a detailed theoretical knowledge of the interaction of the x-ray beam with the sample under investigation is necessary.

### 2.2.1 X-Ray Reflectivity

One of the simplest x-ray characterisation techniques is that of grazing incidence x-ray reflectivity. The technique makes use of the fact that the refractive index of x-rays in materials is just less than unity which implies that the incident x-ray beam is totally externally reflected for incidence angles below some critical angle, $\theta_c$. Since the value of $\theta_c$ is typically small (a fraction of one degree) then the x-ray beam is incident at exceedingly acute angles, hence the name grazing incidence x-ray reflectivity (GIXR). For incidence angles increasing past $\theta_c$ the x-ray beam propagates increasingly more deeply into the sample, with a corresponding reduction in the strength of the reflected beam. From a knowledge of how the intensity of the reflected beam changes as the incidence angle is varied, structural information on the sample under illumination can be obtained. One way of extracting this structural data is by simulating a reflected profile to match an experimental result. A theory is therefore needed from which it is possible to model the reflected beam intensity as a function of incidence angle. This problem has been addressed by several workers, including Pomerantz[4], Névot and Croce[5] and Parratt[6] and the treatment of Parratt is followed here.

### 2.2.2 The Parratt Model For Specular Reflection Of X-Rays

The analysis of GIXR profiles as a method of studying certain structural properties was proposed by Parratt in 1954. Parratts initial work[6] concerned the oxidation of thin copper layers grown on glass substrates and his theoretical modelling of the reflected x-ray profile began by considering a system of two homogenous media only.

Consider a system of two media (e.g. medium 1 could be air, medium 2 the sample bulk). The Fresnel coefficient for reflection, $F_{1,2}$, from the interface btween the two media is given by[7],

$$F_{1,2} = \frac{E_1^R}{E_1} \tag{2.1}$$

where the superscript , R, denotes the reflected beam (see fig.2.1)..

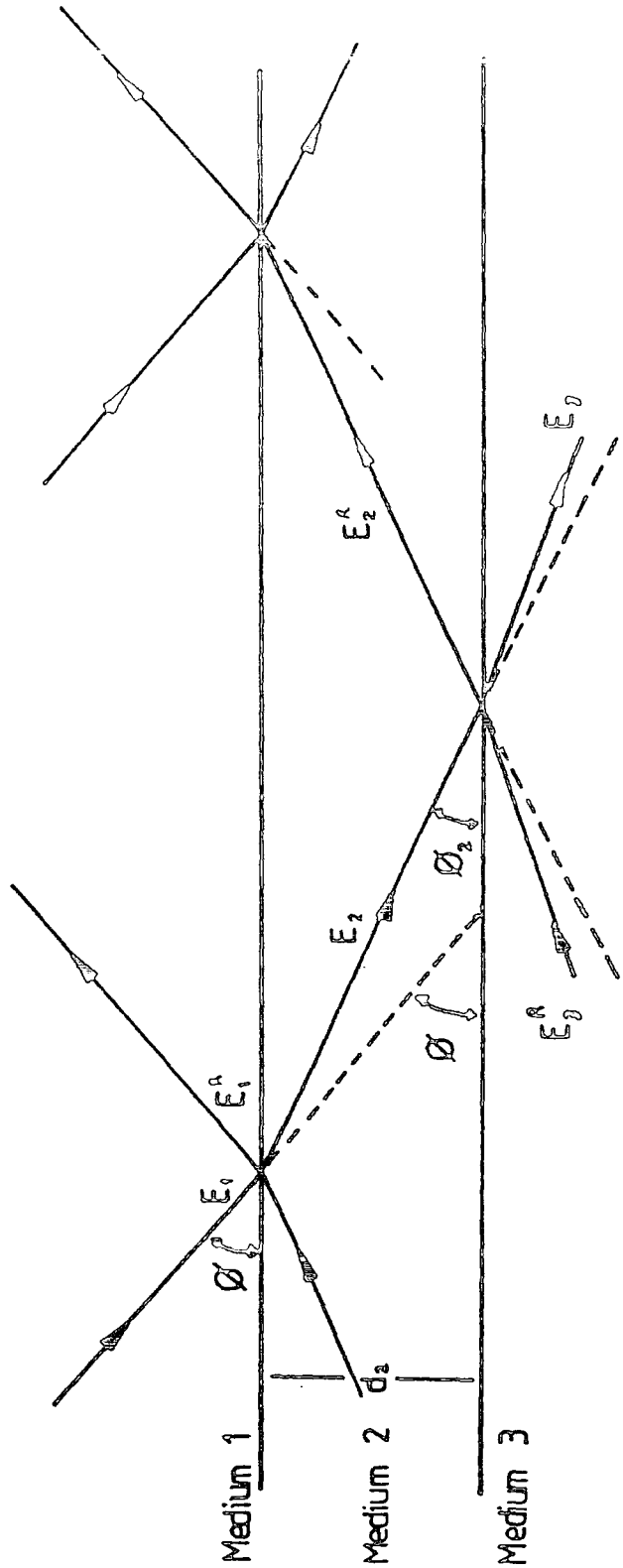


Figure 2.1 : A Diagram showing reflected and refracted beams at the interfaces of stratified, homogeneous media. After Parratt[6].

The expressions for the electric vectors of the incident beam $E_1(z_1)$, reflected beam $E_1^R(z_1)$ and refracted beam $E_2(z_2)$ at a perpendicular distance z from the surface are:

$$E_1(z_1) = E_1(0)\exp\{i[\omega t - (k_{1,x}x_1 + k_{1,z}z_1)]\} \tag{2.2}$$

$$E_1^R(z_1) = E_1^R(0)\exp\{i[\omega t - (k_{1,x}x_1 - k_{1,z}z_1)]\} \tag{2.3}$$

$$E_2(z_2) = E_2(0)\exp\{i[\omega t - (k_{2,x}x_2 + k_{2,z}z_2)]\} \tag{2.4}$$

where $\omega$ is the angular frequency and $k_1$ and $k_2$ are the propagation vectors outside and inside the material respectively. The z-direction is taken as positive into the sample with the y-direction parallel to the sample surface, the x-z plane contains the incident, reflected and refracted beams and the x-ray incidence angle is denoted by $\phi$.

For x-rays the incident angle is small and we can write,

$$k_{2,x}^2 + k_{2,z}^2 = k_2^2 = r_2^2 k_1^2 = r_2^2(k_{1,x}^2 / \cos^2\phi) \cong k_{1,x}^2(1 - 2\delta_2 - 2i\beta_2 + \phi^2) \tag{2.5}$$

Here $r_1$ is the refactive index of air or vacuum (and is set equal to one) and $r_2 = (1 - \delta_2 - i\beta_2)$ is the refactive index of the sample (medium 2). $\beta_2$ is given by $\lambda\mu_2 / 4\pi$ where $\mu_2$ is the linear (incoherent) absorption coefficient of the specimen. Since $\delta_2$ and $\beta_2$ are both of the order of $10^{-5}$ or less , second and higher powers of these can be neglected.

As the x-ray beam is grazing the approximation $k_{1,x} \approx k_1$ can be employed and from the condition for continuity of the tangential compoments, $k_{2,x} = k_1$, it follows that,

$$k_{2,z} \approx k f_2 \tag{2.6}$$

where $f_2 = (\phi^2 - 2\delta_2 - 2i\beta_2)^{\frac{1}{2}}$.

The electric vector of the refracted beam becomes,

$$E_2(z_2) = E_2(0)\exp\{i[\omega t - (k_{2,x}x_2)]\}\exp[-ik_1 f_2 z_2] \tag{2.7}$$

and the Fresnel coefficient may be rewritten as,

$$F_{1,2} = \frac{E_1^R}{E_1} = \frac{\sin\phi - r_2\sin\phi_2}{\sin\phi + r_2\sin\phi_2} = \frac{\phi - f_2}{\phi + f_2} = \frac{f_1 - f_2}{f_1 + f_2} \tag{2.8}$$

with $f_1 = (\phi^2 - 2\delta_1 - 2i\beta_1)^{\frac{1}{2}} = \phi$.

### 2.2.3 Extension To Systems Of N Layers

Parratt's theoretical description can be extended to any number of stratified, homogeneous media. For a system with N lamina, where the thickness of each layer is denoted by $d_n$ $(n \le N)$, the tangential components of the electric vectors, as shown in Fig .2.1 can be expressed as,

$$a_{n-1}E_{n-1} + a_{n-1}^{-1}E_{n-1}^R = a_n^{-1}E_n + a_n E_n^R \tag{2.9}$$

$$(a_{n-1}E_{n-1} - a_{n-1}^{-1}E_{n-1}^R)f_{n-1}k_1 = (a_n^{-1}E_n - a_n E_n^R)f_n k_1 \tag{2.10}$$

where the vector amplitudes $E_{n-1}$, $E_{n-1}^R$, and $E_n$, $E_n^R$ refer to the values midway through medium n-1 and n respectively. The variable $a_n$ is the amplitude factor for half the perpendicular depth $d_n$ and (using Eqn. 2.7) may be written as,

$$a_n = \exp(-ik_1 f_n \frac{d_n}{2}) = \exp(-\frac{i\pi}{\lambda} f_n d_n) \tag{2.11}$$

The reflectivity at the surface of each lamina may be obtained by solving equations (2.9) and (2.10). This is done by dividing their difference by their sum and expressing the result as a recursion relation (Eqn. 2.12). This gives the reflected amplitude, $R_{n-1,n}$, at the ideally abrupt interface between laminae n-1 and n in terms of the reflected amplitude, $R_{n+1,n}$, at the similarly abrupt interface between layers n and n+1 (i.e. the interface below).

$$R_{n-1,n} = a_{n-1}^4\left(\frac{R_{n,n+1} + F_{n-1,n}}{R_{n,n+1}F_{n-1,n} + 1}\right) \tag{2.12}$$

where,

$$R_{n,n+1} = a_n^2\left(\frac{E_n^R}{E_n}\right) \tag{2.13}$$

and,

$$F_{n-1,n} = \frac{f_{n-1} - f_n}{f_{n-1} + f_n}. \tag{2.14}$$

Equation (2.12) is initially solved for the bottom medium (the substrate) where $R_{n,n+1}$ is taken to be zero (the substrate is assumed to be semi-infinite and therefore contains no reflected wave). It is then applied successively to each interface, working from the substrate up to the sample surface. The ratio of reflected to incident intensities is obtained by separating Eqn.(2.12) into its real and imaginary terms and multipling by the complex conjugate,

$$\frac{I_R}{I_0} = \left|\frac{E_1^R}{E_1}\right|^2 \tag{2.15}$$

The angular dispersive reflectivity profile for the sample is generated by performing this calculation for each setting of the incidence beam angle.

### 2.2.4 Reflectivity From Rough Interfaces/Surfaces

The previous theoretical description has been achieved by considering all surfaces and interfaces to be smooth and ideally abrupt. Of course, real samples will deviate significantly from this model and the reflected x-ray intensity is extremely sensitive to roughness at the top surface and buried interfaces. The theory of reflection from statistically rough surfaces has been developed by several authors[8,9,10,11].

If we assume a Gaussian distribution of interface heights about a mean position with standard deviation, $\sigma_n$, the specular reflection coefficient, $F_{n-1,n}$, of the interface between layers (n-1) and n, becomes,

$$F_{n-1,n} = \frac{f_{n-1} - f_n}{f_{n-1,n} + f_n}\left\{\exp\left[-\frac{1}{2}\left(\frac{4\pi\sigma_n}{\lambda}\sin\phi\right)^2\right]\right\} \tag{2.16}$$

The effect of surface and interface roughness is to reduce the magnitude of the reflected intensity and any interference fringes present in the reflectivity profile. This point will be further discussed in Chapter 8.

### 2.3.1 X-Ray Diffraction

X-ray reflectivity studies can be applied to any system as there is no dependence of the reflected amplitude upon the crystal structure of the sample. The situation is different when using diffraction techniques to characterise materials, as the existence of a regular crystal structure is required for a diffracted beam to exist. In a crystalline material the atoms are arranged in a regular three dimensional array known as the crystal lattice. As an x-ray wavelength is roughly similar to an interplanar spacing the crystal lattice acts as a three dimensional diffraction grating. Constructive interference will occur between x-rays diffracted from successive atomic planes at particular incidence angles given by the famous Bragg equation below,

$$n\lambda = 2d_{hkl} \sin \theta_B \tag{2.17}$$

where n is the order of diffraction, $\lambda$ the x-ray wavelength and $\theta_B$ the Bragg angle, the value of incidence angle at which diffraction occurs. The variable $d_{hkl}$ is the interplanar spacing for an *hkl* reflection from an orthorhombic cell whose planes are separated by *a*/*h*, *b*/*k* and *c*/*l* in the three axial directions and is given by,

$$d_{hkl} = \frac{1}{\sqrt{h^2/a^2 + k^2/b^2 + l^2/c^2}} \tag{2.18}$$

The diffraction of x-rays from a crystalline material is described by two general theories, the kinematical theory and the dynamical theory. The simplest of these, the kinematical theory, has been discussed previously by several authors[12,13,14,15] and is often invoked as a first approximation when trying to understand qualitatively the diffraction process.

### 2.3.2 The Kinematical Theory

In the kinematical theory intensity formulae are derived by assuming that the amplitudes of the scattered waves are small compared with the incident wave amplitude and that each wavelet is scattered only once. Since the probability of multiple scattering events increases with crystal size and perfection, only small or highly imperfect crystals are described adequately by this theory.

Consider the scattering from two points within an atom where the incident and scattered wave vectors are defined as $\underline{k}$ and $\underline{k}'$, respectively. The phase difference ($\delta_j$) between waves scattered at points O and P is given by $2\pi(\underline{k}-\underline{k}').\underline{r}_j$ where $\underline{r}_j$ is the vector connecting O and P. The amplitude, A, scattered from an atom is;

$$A = \sum_j A_e \exp(i\delta_j) \tag{2.19}$$

where $A_e$ is the amplitude scattered by one electron and j takes the value of 1 up to the atomic number (Z). The atomic scattering amplitude, $f$, is then defined as the amplitude scattered by an atom divided by the amplitude scattered by a single electron, i.e.,

$$f = \sum_j \exp(i\delta_j) = \sum_j \exp[i2\pi(\underline{k}-\underline{k}').\underline{r}_j] \tag{2.20}$$

The aim here is to calculate the scattering from a single unit cell and then to sum the contributions from all unit cells within the crystal. If we define the atoms within a unit cell to have positions denoted by $\underline{R}_1, \underline{R}_2 .... \underline{R}_t$ with respect to the origin of the unit cell, and the unit cells themselves to have origins with position vectors $\underline{r}_1, \underline{r}_2 .... \underline{r}_i$ , then the total scattered amplitude is given by;

$$A = \sum_i \sum_t f_t \exp[-i2\pi(\underline{r}_i + \underline{R}_t).\underline{K}] \tag{2.21}$$

where $\underline{K} = (\underline{k}-\underline{k}')$. This can be rewritten as;

$$A = F_K \sum_i \exp[-i2\pi\underline{r}_i.\underline{K}] \tag{2.22}$$

where the term $F_K$ is known as the geometrical *structure factor* and is given by equation (2.23).

$$F_K = \sum_t f_t \exp[-i2\pi \underline{R}_t . \underline{K}] \qquad (2.23)$$

Since the amplitude of the scattered radiation, $A$, is related to the total scattered intensity, $I$, by $I = A^* A$, where $A^*$ is the complex conjugate, it can be seen that the kinematical theory predicts that the intensity of a Bragg reflection is proportional to the square of the structure factor, $F_K$.

### 2.3.3 The Dynamical Theory

For large perfect crystals the amplitudes of the diffracted and incident waves become comparable as the probability of multiple scattering becomes large. In this case there is a coherent coupling between the incident and diffracted radiation with a continual transference of energy as the beams pass through the crystal and kinematical theory no longer adequately describes the diffraction process.

In order to allow for the effects of multiple scattering the dynamical theory of x-ray diffraction must be employed. The first dynamical treatment of the x-ray scattering processes was given by Darwin[16] in 1914 with an alternative treatment presented by Ewald[17] soon after. In the theory proposed by Ewald, each lattice point was represented by a dipole, set into oscillation by an electromagnetic field within the crystal. These oscillating dipoles, in turn, emit radiation forming a radiation field within the crystal. Von Laue[18] reformulated the Ewald treatment as a problem requiring the simultaneous solution of Bragg's law and Maxwell's equations in a material with a periodic electric susceptibility. His approach was to propose a localised positive charge at each lattice point, sitting in a continuous distribution of negative charge. The electromagnetic field associated with the x-ray radiation causes polarisation within the crystal proportional to the local electric field. Both approaches achieved success in interpreting experimentally observed scattering phenomena, but the derivation of Laue will be followed here. A full treatment of dynamical scattering leads to a complete description of all allowed wave vectors and field amplitudes within the crystal. Detailed accounts and

reviews of dynamical theory are available in the literature[19,20,21,22,23], and only a brief outline will be presented here.

### 2.3.4 Allowed Wave Vectors Within The Crystal

The problem reduces to solving Maxwells equations in a triply periodic medium. Assuming the magnetic permeability to be unity and the electric conductivity to be zero, Maxwells equations reduce to,

$$\nabla \times \nabla (1-\chi)\underline{D} = -\frac{1}{c^2}\frac{\partial^2 \underline{D}}{\partial^2 t^2} \tag{2.24}$$

where $\chi$ is the electric susceptibility and $\underline{D}$ the electric displacement amplitude. The electric susceptibility is given by 2.25,

$$\chi = \frac{e^2\lambda^2}{\pi mc^2} g(\underline{r}) \tag{2.25}$$

with e the electronic charge, m the electron mass, c the velocity of light, $\lambda$ the x-ray wavelength and $g(\underline{r})$ the electron density in the scattering volume, V, expanded as a Fourier sum over the reciprocal lattice (2.26),

$$g(\underline{r}) = \frac{1}{V}\sum_{\underline{h}} F_{\underline{h}} \exp(-2\pi i \underline{h}\cdot\underline{r}) \tag{2.26}$$

Since the electron density reflects the periodic nature of the crystal lattice it also may be expressed as a Fourier series[15],

$$\chi = \sum_{\underline{h}} \chi_{\underline{h}} \exp(-2\pi i \underline{h}\cdot\underline{r}) \tag{2.27}$$

so that, by comparison of terms the susceptibility may be related to the Structure Factor as shown below,

$$\chi_{\underline{h}} = -\frac{e^2\lambda^2}{\pi mc^2 V} F_{\underline{h}} \tag{2.28}$$

The effect of absorption is taken into account by making the susceptibility a complex quantity, comprising of the sum of real, $\chi^r$, and complex, $\chi^i$, components.

The solution of the wave equation given in Eqn.2.24 can be expressed as a Bloch wave,

$$\underline{D} = \sum_{\underline{h}} \underline{D}_{\underline{h}} \exp(-2\pi i \underline{K}_{\underline{h}} \cdot \underline{r}) \tag{2.29}$$

where the wave-field is considered to consist of an infinite number of plane waves, $\underline{K}_{\underline{h}}$. The set of wave vectors, $\underline{K}_{\underline{h}}$, are linked by the Laue condition,

$$\underline{K}_{\underline{h}} = \underline{K}_0 + \underline{h} \tag{2.30}$$

where $\underline{K}_0$ and $\underline{h}$ represent the incident wave vector and reciprocal space vectors respectively. This condition can be visualised by the Ewald sphere construction where a sphere of radius $|\underline{K}_0|$ is drawn in reciprocal space whose surface contains the origin and reciprocal lattice point corresponding to the {hkl} reflection. In x-ray diffraction the Ewald sphere radius is of the order 1 $Å^{-1}$ and the curvature of the sphere is large in comparison to the spacing between reciprocal lattice points. Thus the possibility of two or more reflections being excited simultaneously is very small. The problem then reduces to the two beam case where only the refracted and diffracted beams need be considered, i.e., those x-rays with wave vectors parallel to either the incident beam, $\underline{K}_o$, or the diffracted beam, $\underline{K}_{\underline{h}}$. Substitution of equations (2.27) and (2.29) into equation (2.24) gives,

$$\sum_{g} \{\chi_{h-h'}(\underline{K}_{\underline{h}} \cdot \underline{D}_{\underline{h}'})\underline{K}_{\underline{h}} - \chi_{h-h'}(\underline{K}_{\underline{h}} \cdot \underline{K}_{\underline{h}})\underline{D}_{\underline{h}'}\} = (k^2 - \underline{K}_{\underline{h}} \cdot \underline{K}_{\underline{h}})\underline{D}_{\underline{h}} \tag{2.31}$$

where $k = \omega/c$ is the wave vector in vacuum and $h'$ ranges over all the wave vectors in the reciprocal space of the crystal. By applying the two beam situation this can be expanded out to form ,

$$\begin{aligned} \chi_{\underline{h}}(\underline{K}_{\underline{h}} \cdot \underline{D}_0)\underline{K}_{\underline{h}} - \chi_{\underline{h}}(\underline{K}_{\underline{h}} \cdot \underline{K}_{\underline{h}})\underline{D}_0 + \chi_0(\underline{K}_{\underline{h}} \cdot \underline{D}_{\underline{h}})\underline{K}_{\underline{h}} - \chi_0(\underline{K}_{\underline{h}} \cdot \underline{K}_{\underline{h}})\underline{D}_{\underline{h}} \\ = (k^2 - \underline{K}_{\underline{h}} \cdot \underline{K}_{\underline{h}})\underline{D}_{\underline{h}} \end{aligned} \tag{2.32}$$

which describes the interaction between the diffracted x-ray beam, $\underline{K}_h$, and the incident x-ray beam, $\underline{K}_0$, and,

$$\chi_{\bar{h}}(\underline{K}_0 \cdot \underline{D}_h)\underline{K}_0 - \chi_{\bar{h}}(\underline{K}_0 \cdot \underline{K}_0)\underline{D}_h + \chi_0(\underline{K}_0 \cdot \underline{D}_0)\underline{K}_0 - \chi_0(\underline{K}_0 \cdot \underline{K}_0)\underline{D}_0 = (k^2 - \underline{K}_0 \cdot \underline{K}_0)\underline{D}_0 \tag{2.33}$$

which represents the interaction of x-rays multiply scattered back into the incident beam. By taking the scalar product of Eqn.(2.32) with $\underline{D}_h$ and the scalar product of Eqn.(2.33) with $\underline{D}_0$, and remembering that electromagnetic waves are transverse (i.e. $\underline{K}_0 \cdot \underline{D}_0 = \underline{K}_h \cdot \underline{D}_h = 0$), we obtain,

$$k^2 C\chi_{\bar{h}}\underline{D}_h + [k^2(1+\chi_0) - \underline{K}_0 \cdot \underline{K}_0]\underline{D}_0 = 0 \tag{2.34}$$

$$[k^2(1+\chi_0) - \underline{K}_h \cdot \underline{K}_h]\underline{D}_h + k^2 C\chi_h \underline{D}_0 = 0 \tag{2.35}$$

where,

$C = \underline{D}_0 . \underline{D}_h = 1$ for $\sigma$ polarisation

$C = \cos 2\theta_B$ for $\pi$ polarisation

For a non trivial solution to exist to equations (2.34) and (2.35) their determinant must be equal to zero, viz.

$$\begin{vmatrix} k^2 C\chi_{\bar{h}} & k^2(1+\chi_0) - \underline{K}_0 \cdot \underline{K}_0 \\ k^2(1+\chi_0) - \underline{K}_h \cdot \underline{K}_h & k^2 C\chi_h \end{vmatrix} = 0 \tag{2.36}$$

from which, by writing,

$$\alpha_0 = \frac{k}{2}[\underline{K}_0 \cdot \underline{K}_0 - k^2(1+\chi_0)]$$
$$\alpha_h = \frac{k}{2}[\underline{K}_h \cdot \underline{K}_h - k^2(1+\chi_0)] \tag{2.37a,b}$$

the fundamental equation of dynamical theory, that of the dispersion surface, can be obtained (Eqn.(2.38)).

$$\alpha_0 \alpha_h = \frac{k^2}{4} C^2 \chi_h \chi_{\bar{h}} \tag{2.38}$$

### 2.3.5 The Dispersion Surface

The dispersion surface is a graphical representation of Eqn.(2.38) and describes the set of wave vectors, $\underline{K}_0$ and $\underline{K}_h$, which are allowed to exist within the crystal. The dispersion surface can be constructed[24] by first drawing a sphere of radius $k$ around the origin of reciprocal space and the reciprocal lattice point $\underline{h}$, as illustrated in Fig.2.2. For an incident wave defined by the line OL, Braggs Law is satisfied and a strong diffracted beam results with direction given by Lh. Since this is merely a graphical representation of the Laue condition (eqn. 2.30) the point L is known as the Laue point. One of the main differences between the kinematical and the dynamical theory arises in their treatment of the refractive index. The kinematical theory assumes a refractive index of unity whereas the dynamical theory accounts for wave field interactions which produce an anisotropic refractive index. In the dynamical case, if no diffracted wave exists (i.e. $\underline{D}_h = 0$) then, from equation 2.34, the wave vector, $\underline{K}_0$, is given by,

$$|\underline{K}_0| = k(1+\frac{\chi_0}{2}) \tag{2.39}$$

far from the Bragg condition. This implies that the wave vector in the crystal is given by the product of the wave vector in vacuum with the refractive index. A second pair of spheres, of radius $k(1+\chi_0/2)$ is then drawn around the points O and h. Far from the Laue point the tail of the wave vector, $\underline{K}_0$, lies upon the sphere about O. When a strong diffracted beam occurs then the relation between $\underline{K}_0$ and $\underline{K}_h$ is defined by equation (2.38), and the wave vector tail no longer lies upon the spheres. The area contained within the region of intersection of the two spheres contains points which represent the pairs of wavevectors which satisfy Eqn.(2.39). Thus near the exact Bragg angle a range of wave vector solutions are possible, all of which satisfy the Laue condition. Fig 2.3 shows the region of intersection of the two spheres at a much greater magnification, where the tails of the wave vectors $\underline{K}_0$ and $\underline{K}_h$ lie on the solid line. As the radius of the spheres is large in comparison to the region highlighted in Fig 2.3 the spheres may be approximated as planes, and the equation describing the dispersion surface (eqn. 2.38) becomes a hyperboloid of revolution with axis Oh. The dispersion surface has four branches, two each for the two polarisation states. The amplitudes and wave vectors of the waves $\underline{K}_0$ and $\underline{K}_h$, satisfying the Bragg condition, are

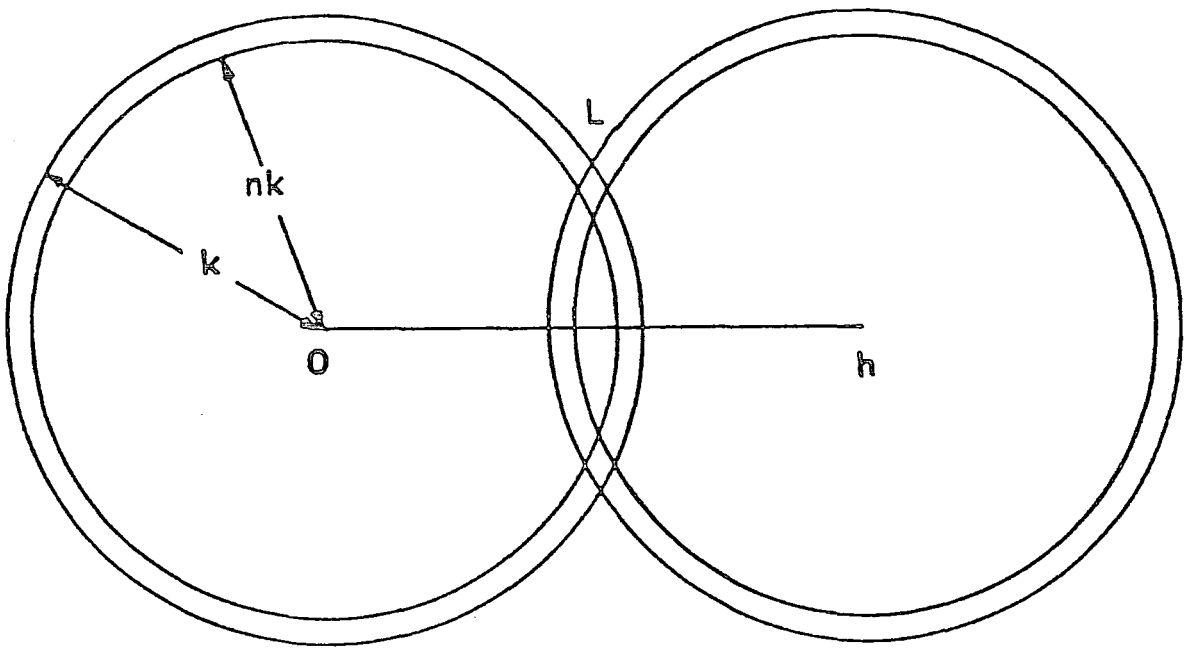


Figure 2.2 : Spheres in reciprocal space about the origin, O, and reciprocal lattice point, h. The point, L, is known as the Laue Point. After Tanner[24].

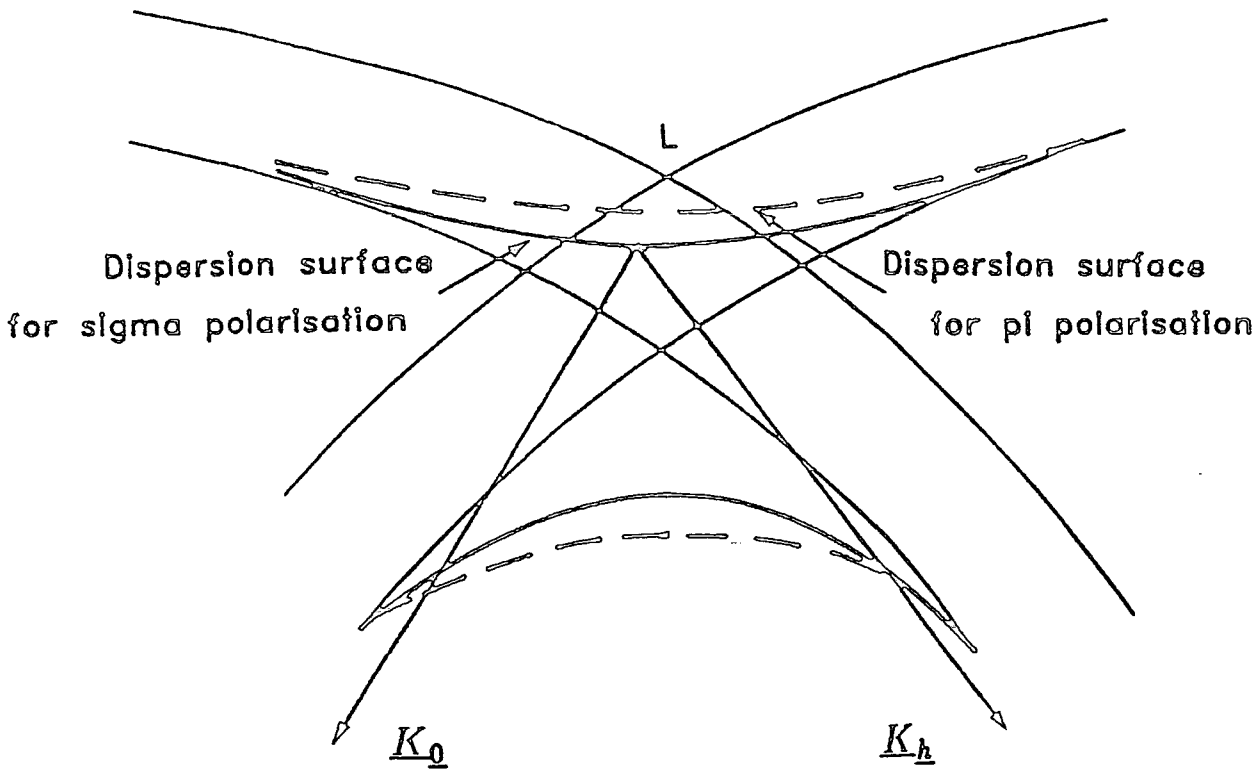


Figure 2.3 : A magnified view of the region around the Laue Point, L, showing the dispersion surface. After Tanner[24].

determined from their tie point, i.e. their particular position on the dispersion surface. Whether or not a particular tie point is excited is determined by the boundary conditions. Some of these conditions are imposed by the particular experimental situation and the need to match the tangential components of the wave electric and magnetic field vectors across the crystal surface. These constraints mean that the incident and diffracted wave vectors may only differ by a vector normal to the crystal surface. Once the boundary conditions have been applied to the problem then the above analysis allows the wave vectors and amplitude of the incident and diffracted waves to be determined.

### 2.3.6 Important Results Arising From Dynamical Theory

A dynamical treatment of the x-ray diffraction processes occurring within highly perfect crystalline samples allows several relations concerning the diffracted beam to be obtained, and are quoted here. Darwin derived the fractional integrated intensity of the Bragg diffracted peak to be,

$$\frac{\delta I}{I_0} = \frac{8|C|}{3} \frac{\chi_h}{\sin 2\theta_B} \sqrt{\frac{|\gamma_h|}{\gamma_0}} \qquad (2.40)$$

where $I_0$ is the incident intensity, $\gamma_0$ and $\gamma_h$ the direction cosines of the incident and diffracted beams respectively. Thus the dynamical theory predicts the integrated intensity from a perfect crystal to be linearly dependent upon the structure factor. This contrasts with the kinematical theory which predicts an integrated intensity which is proportional to the square of the structure factor. A comparison, therefore, between the two theories gives significant discrepancies. Values for the integrated intensity based on the kinematical theory are always much greater than those predicted by the dynamical theory, or those measured experimentally. This is symptomatic of a major deficiency in the kinematical theory, the exclusion of primary extinction effects.

The full width of the diffraction peak at half maximum intensity (FWHM), which is often used as a guide to the perfection of the scattering material, is given by,

$$\Delta\theta_{\frac{1}{2}} = \frac{2C(\chi_h\chi_{\bar{h}})^{\frac{1}{2}}}{\sin 2\theta_B}\sqrt{\frac{|\gamma_h|}{\gamma_0}} \tag{2.41}$$

Finally, dynamical theory predicts that, if thin layers are present on the sample, then interference fringes will be observed in the diffraction profile. These arise from the continual energy exchange occurring within the crystal between the refracted and diffracted waves, and are known as Pendellösung fringes. The period of these fringes, $\Delta\theta$, can be directly related in the Bragg geometry to the layer(s) thickness(es) by,

$$\Delta\theta = \frac{\lambda \sin(\theta+\phi)}{t \sin 2\theta_B} \tag{2.42}$$

where $\lambda$ is the x-ray wavelength, $\theta_B$ the Bragg angle for the reflection used, $\theta$ the angle subtended between the incident beam and diffracting planes and $\phi$ the angle between the diffracting planes and sample surface. The measurement of Pendellösung fringe spacing in order to extract layer thickness information will be further discussed in Chapter V.

### 2.3.7 The Takagi-Taupin Equations

Having established an understanding of the diffraction processes occurring within the crystal, this knowledge can be applied in writing simulation programs to predict the diffraction profile from a crystal lattice. The use of simulation techniques has become widespread in x-ray diffraction analysis. By matching a simulated profile against an experimental measurement many of the samples' structural parameters may be determined. For the analysis of thin or imperfect layers, routines which employ the kinematic assumptions of weak scattering and little absorption are often invoked as a first approximation[25]. This has the disadvantage that should the layer have been grown on a "perfect" substrate then the kinematical theory does not apply to the substrate itself where multiple scattering effects occur. This will result in the predicted relative integrated intensities being incorrect. One appealing aspect of kinematical simulation is the speed of analysis, with the time required to carry out a dynamical simulation being several orders of magnitude greater A semi-kinematical approach has also been

attempted where a simulation routine treats the scattering from the thin layer as kinematic but that from the substrate as dynamical[26]. However, simulation routines which fully utilise the dynamical theory have been written by several authors[27,28,29] and have enjoyed great success in matching experimental profiles. The simulation work conducted in this thesis utilises the RADS (Rocking Curve Analysis by Dynamical Simulation) software package provided by Bede Scientific Instruments Ltd., and is based upon solving differential equations to determine the amplitude of the incident and diffracted beams at each interface within the sample, an approach adopted by Takagi[30] and Taupin[31]. Takagi proposed that the Fourier components, $\underline{D}_h$, in equation (2.29) be allowed to vary slowly with position across the x-ray beam thus accounting for variations in the wavefield induced by lattice distortions. The analysis was then reduced to the solution of two partial differential equations linking the total wavefield amplitudes, $\underline{D}_0$ and $\underline{D}_h$, in the forward and diffracted beam directions ( $\underline{s}_0$ and $\underline{s}_h$ respectively), known as the Takagi-Taupin equations,

$$\frac{i\lambda}{\pi}\frac{\partial \underline{D}_0}{\partial \underline{s}_0} = \chi_0 \underline{D}_0 + C\chi_{\bar{h}}\underline{D}_h \tag{2.43}$$

$$\frac{i\lambda}{\pi}\frac{\partial \underline{D}_h}{\partial \underline{s}_h} = (\chi_0 - \delta_h)\underline{D}_h + C\chi_h \underline{D}_0 \tag{2.44}$$

with $\delta_h$ representing the deviation of the incident x-ray beam from the exact Bragg condition.

By splitting the epitaxial layer into many thin laminae parallel to the interface, within which a constant composition, thickness and crystal structure is assumed, the Takagi-Taupin equations can be solved analytically. The x-ray reflectivity at the top of each laminae is calculated in terms of the reflectivity at the bottom. By calculating the reflectivity from the substrate first it is possible to work iteratively upwards determining the reflectivity at each interface of the laminae until the total reflectivity from the whole epitaxial layer is obtained. This process is repeated for a whole series of incidence angles in order to obtain the sample diffraction profile. The double crystal rocking curve is finally acquired by correlating this generated diffraction profile with the profile of the Bragg reflection from the first (reference)

crystal, with the entire calculation being performed for both states of x-ray polarisation.

# Chapter III

# Multiple Crystal X-Ray Diffraction

## 3.1 Introduction

In essence, angular dispersive x-ray diffraction experiments involve illumination of a sample with a monochromatic x-ray beam, where the beam incidence angle is varied around the sample Bragg angle, in order to obtain the diffraction profile. As the complete diffraction curve is obtained by moving or "rocking" the sample the resulting plot of angle versus diffracted intensity is known as the "rocking curve". Should the sample contain epitaxial layer(s) with a different lattice parameter to that of the substrate then the layer(s) and the substrate will satisfy the Bragg condition at different angular settings resulting in several peaks in the rocking curve. The angular separation of these maxima can be directly related to their difference in lattice parameter. Hence, for materials which obey Vegards law, the material composition may be deduced. A study of the peak shapes and relative intensities allows information on layer thicknesses and crystal perfection to be obtained.

The resolution of the x-ray diffraction technique is highly dependent upon the quality of the incident beam in terms of both its angular and spectral distribution. Single crystal diffraction, where no pre-conditioning of the x-ray beam occurs, is dominated by effects such as beam divergence, x-ray source size and wavelength dispersion which all broaden the widths of rocking curve peaks. Consequently, the single crystal technique is appropriate only for the study of material systems where large differences in the lattice parameter of the substrate and layer(s) exist (and hence large peak angular separations). In practice, this means that single crystal techniques are employed only when the lattice mismatch ($\Delta d / d$) , where d is the substrate lattice parameter and $\Delta d$ the difference between the layer and substrate lattice parameters, is $10^{-4}$ or greater[1].

Where greater resolution is needed, i.e., for the study of systems with closely matched lattice parameters, then the resolution degrading effects associated with the incident x-ray beam must be reduced. A method of achieving this was first demonstrated by Compton[2], who introduced a first (or reference crystal) to pre-

condition the x-ray beam. By using Bragg reflection from this first crystal to select out a narrow angular band the angular divergence of the beam prior to striking the sample crystal is greatly diminished. Thus the beam is conditioned so that the angular divergence is defined by the quality and curvature of the reference crystal and no longer by the divergence arising from the x-ray source itself. This principle is utilised in the double crystal (or double axis) diffractometer, which is capable of routinely studying systems with lattice mismatches of a few parts in $10^6$ (or, in exceptional circumstances[3], even mismatches as low as a few parts in $10^{-8}$).

## 3.2 The Double Crystal Diffractometer

The concept of double crystal diffractometry (DCD), also known as double axis diffractometry, was developed by several authors and the reader is referred to the papers by Scwarzchild[4], Allison and Williams[5], Allison[6], Compton and Allison[7] and Du Mond[8] for a complete description. Although the concept was first developed in the 1930's the lack of suitably perfect crystals meant that its use did not become widespread until the advent of highly perfect, monocrystalline epitaxial layer growth in the past three decades. Double crystal diffractometers are now routinely used, particularly in the semiconductor industry, to provide structural analysis of epitaxial material, and the theory of operation of these instruments is presented below.

The double crystal (or double axis) diffractometer utilises two crystals, a reference crystal and the sample crystal itself, which are both set to satisfy the Bragg condition. Three different relative orientations as shown in Fig 3.1., are generally applied for the study of perfect crystals. In Fig.3.1(a) the crystals are positioned so that the outward normals from the diffracting planes are parallel and pointing in opposite directions and is called the parallel (+n,-n) configuration. Fig.3.1(b) represents the situation where the outward normals are both pointing down the page, i.e., the sample crystal is "turned around" with respect to Fig.3.1(a), and is known as the antiparallel (+n,+n) geometry. A third situation arises when the sample material (or reflection used) differs from the reference crystal and this is depicted in Fig. 3.1(c) as the (+n,-m) setting. Before a mathematical description of the various diffractometer settings is presented the diffraction conditions can best be visualised in a graphical manner by the use of "Du Mond" diagrams.

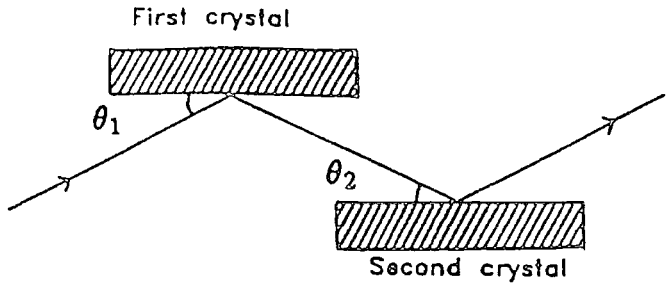


a) The parallel (+n, -n) setting. $\theta_1 = \theta_2$.

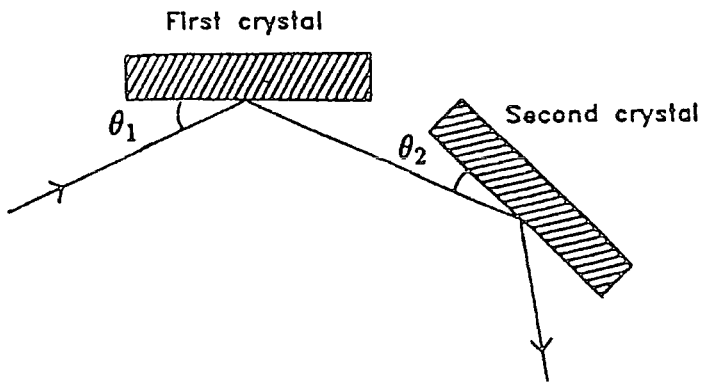


b) The antiparallel (+n, +n) setting. $\theta_1 = \theta_2$

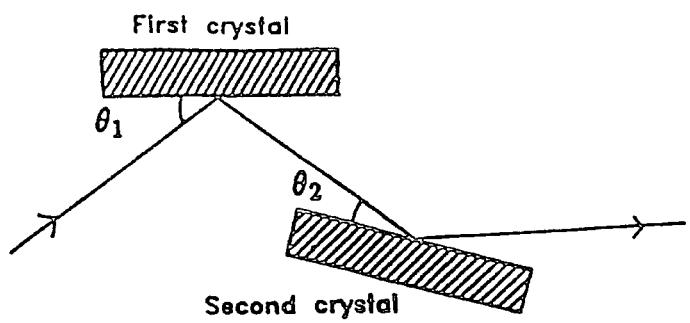


c) The parallel (+n, -m) setting. $\theta_1 \neq \theta_2$.

Figure 3.1 : Possible settings of the Double Crystal Diffractometer.

## 3.3 Du Mond Diagrams

The Du Mond diagram is a graphical representation of Braggs law and shows, for a given lattice spacing, at which angles Bragg diffraction occurs for various wavelengths. This is demonstrated in Fig.3.2 which shows Braggs law for the first three orders, n, of a reflection. Here the relation connecting wavelength with angle is shown as a line, though in practice the Du Mond diagram possesses a finite width, that of the perfect crystal reflecting range. The real power of Du Mond diagrams arises when describing multiple crystal diffraction. In the case of the double crystal diffractometer, by including the Du Mond diagrams for both reference and first crystals on the same graph then the diffraction condition for successive Bragg diffraction from both crystals may be investigated. The rocking of the sample crystal can be modelled in the Du Mond diagram by moving the curve corresponding to the sample across that of the reference crystal. Where the two curves overlap then simultaneous diffraction occurs. The diffracted intensity at a particular angle corresponds to the area of overlap of the two Du Mond diagrams and mathematically this corresponds to the convolution of the two crystal reflecting ranges.

The Du Mond analysis of the diffracted profile for the three diffractometer geometries shown in Fig.3. helps greatly to simplify understanding. The case of the (+n,-n) geometry, shown in Fig.3.1(a), can be represented by the Du Mond diagrams in Fig.3.3(a). Here the two crystals are of similar material with the same reflection (and hence Bragg angle) applicable to both. As the crystals are parallel, all wavelengths diffracted at the first crystal will also be diffracted at the second crystal. The two Du Mond diagrams exactly overlap and a large diffracted intensity results. Since all wavelengths are diffracted at the same relative setting of the crystals then the parallel (+n,-n) geometry is seen to be non-dispersive in wavelength. If the sample curve is misplaced only slightly from the reference crystal curve (which is equivalent physically to rocking the sample) then the area of intersection rapidly falls to zero and no wavelength is doubly diffracted. As the angular range over which diffraction occurs is thus very narrow it is possible to obtain rocking curves with widths given by the convolution of the two perfect crystal reflecting curves. In this geometry the double crystal diffraction technique is particularly sensitive to lattice distortions or misorientations. To reduce angular divergence a collimator, positioned before the first crystal, and set of slits, placed

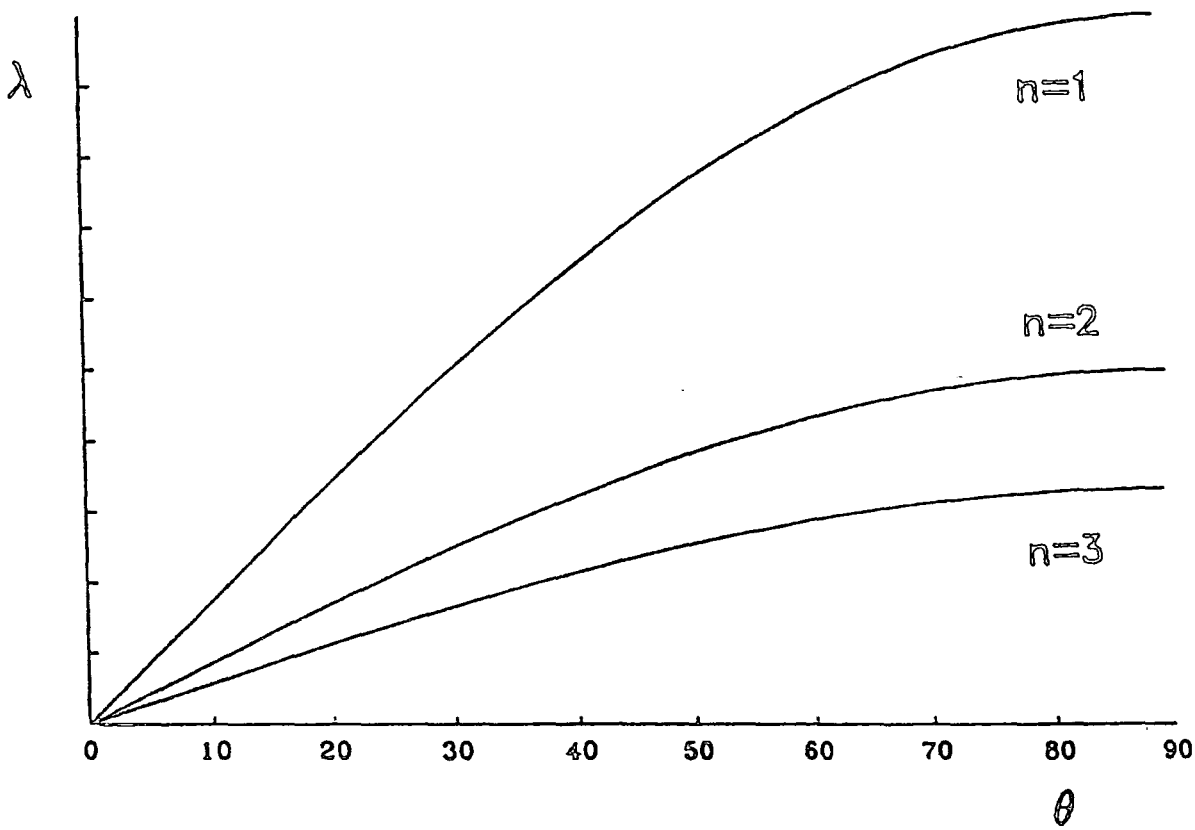


Figure 3.2 : The Bragg law for the first three orders of diffraction.

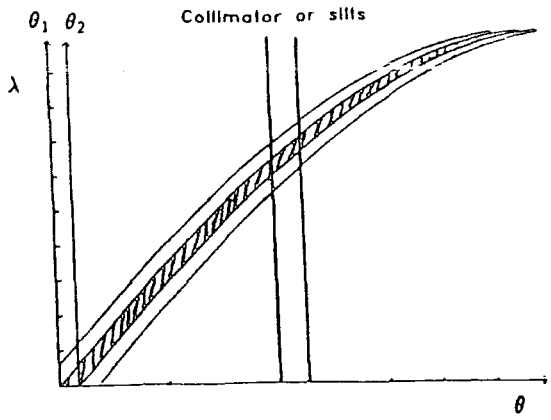


a) The parallel (+n, -n) setting. $\theta_1 = \theta_2$.

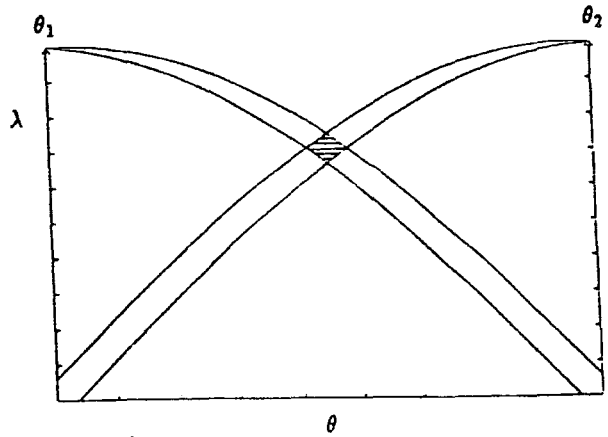


b) The antiparallel (+n, +n) setting. $\theta_1 = \theta_2$

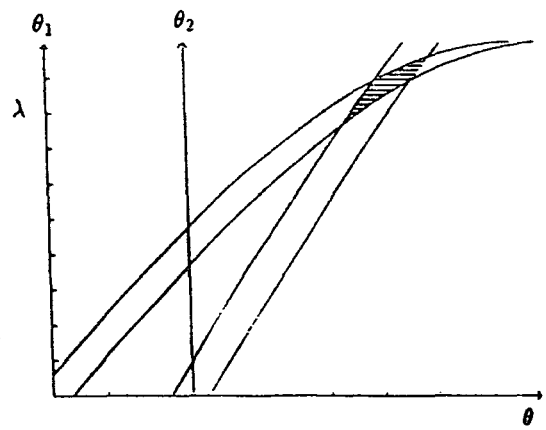


c) The parallel (+n, -m) setting. $\theta_1 \neq \theta_2$.

Figure 3.3 : Du Mond diagrams for the various diffractometer settings shown in Figure 3.1.

between the two crystals, are often employed. The range of incidence angles passed by these is represented in Fig.3.3(a) as a pair of lower and upper limits.

For the situation represented by Fig.3.1(b), the antiparallel (+n,+n) setting, diffraction from the "other" side of the sample crystal is shown by reversing the direction of the sample Du Mond diagram, Fig.3.3(b). In this case, as the sample curve is moved across the reference curve, different wavelengths in turn satisfy the Bragg condition. The antiparallel (+n,+n) setting is thus seen to be highly dispersive in wavelength. Further, the angular range over which simultaneous diffraction will occur is now large and the resulting rocking curve peak will be significantly broadened. This setting is relatively insensitive to lattice distortions as misorientations no longer cause a drastic reduction in the diffracted intensity (as in the (+n,-n) configuration). For this dispersive geometry the diffraction peak width contains a contribution from the intrinsic width of the incident radiation. The extent of the rocking curve peak broadening, $\delta\Theta$, is given by,

$$\delta\Theta = \left|\delta\phi_1 + \delta\phi_2\right| = \frac{\delta\lambda}{\lambda}\left|\tan\theta_2 + \tan\theta_1\right| \qquad (3.1)$$

where $\delta\lambda$ is the bandwidth of the incident x-ray radiation (usually the CuK$\alpha_1$ line), $\delta\phi_1$and $\delta\phi_2$ are the full widths at half height maximum (FWHM ) and $\theta_1$ and $\theta_2$ the Bragg angles of the reference and sample crystals respectively.

The third setting, (+n,-m), with the two crystals in the so-called parallel setting, but where either the two crystals are either of different material or utilise different Bragg reflections is described by Fig.3.3(c). As the sample is rocked then the area of intersection of the two curves moves up and down with respect to the wavelength axis. Thus the (+n,-m) setting also is dispersive in wavelength and the rocking curve peak width is broadened. However, the extent of this broadening is less than in the case of the (+n,+n) setting, and is given by equation (3.2),

$$\delta\Theta = \left|\delta\phi_1 - \delta\phi_2\right| = \frac{\delta\lambda}{\lambda}\left|\tan\theta_2 - \tan\theta_1\right| \qquad (3.2)$$

Although the parallel, non-dispersive (+n,-n) setting has the highest sensitivity, the dispersive (+n,+n) and (+n,-m) settings are often used in some experimental

situations, in particular double crystal x-ray topography, where the introduction of a dispersive geometry reduces angular sensitivity and inhibits the formation of multiple images[9].

## 3.4 Theoretical Description Of Double Crystal Diffractometers

While Du Mond demonstrated graphically the operation of the double crystal diffractometer its behaviour has been described mathematically by several authors. A summary of the more salient points, as discussed by Compton and Allison[7] and Pinsker[10] is presented below, including a verification of the non-dispersive properties of the (+n,-n) setting.

Since the refractive index of x-rays in matter is different to that in vacuum, the x-ray beam is bent slightly upon entering the sample, by an amount, $\Delta$, given by Snell's law of refraction, and the angular setting of a crystal at the centre of its diffraction peak, $\theta$, will differ slightly from the angular setting given by the kinematic Bragg angle, $\theta_0$. Thus the first (reference) crystal is aligned such that a central ray in the incident beam makes an angle,

$$\theta = \theta_0 + \Delta \tag{3.3}$$

with the diffracting planes, corresponding to the centre of the diffraction peak. The deviation, $\Delta$, from the exact Bragg angle is generally small (of the order of a few arc seconds), although this increases for grazing incidence, asymmetric reflections. For double crystal rocking curve analysis of III-V semiconductors, where electron densities and thus refractive indexes are similar, the angular deviation from the kinematic Bragg angle is roughly equivalent for layer and substrate materials. Hence, while peak positions may shift slightly the angular splitting between them can be assumed to remain constant. For systems where a significant electron density change does occur across the interface between two media, then the refractive index effect may again become considerable. Pietsch and Borchard[11] have studied the lattice matched $Ca_xSr_{1-x}F_2$ on GaAs system and found that, for reflections with low angles of incidence, the peaks from the layer and substrate are resolved as a consequence of the difference in the refactive index correction for the two materials.

In general, a ray incident upon the reference crystal may be characterised in terms of three quantities, its vertical and horizontal divergence (as measured from the central ray) and its wavelength. The extent of the vertical and horizontal divergence can be controlled by the introduction of a collimating system prior to the x-ray beam reaching the first crystal. In the paper of Compton and Allison[6] it is shown that the deviation of an arbitrary ray from the central ray can be expressed as,

$$\alpha - \frac{1}{2}\psi^2 \tan\theta(\lambda_0, n_1) - (\lambda - \lambda_0)\frac{\partial\theta}{\partial\lambda_0}(\lambda_0, n_1) \qquad (3.4)$$

where $\alpha$ and $\psi$ represent the horizontal and vertical components of divergence respectively. The glancing angle made by the central ray (for which the divergence is, by definition, zero) with the reference crystal is denoted by $\theta(\lambda_0,n_1)$ where $n_1$ is the order of reflection and $\lambda_0$ the wavelength corresponding to the centre of the spectral line of the incident radiation. Physically, the middle term in equation (3.4) describes the deviation due to the vertical divergence and the final term deals with the spread of wavelengths in the incident x-ray beam. The mathematical analysis is extended to include the presence of the sample crystal, and the angular deviation, $\beta$, of an arbitrary ray from the position of the central ray on the second crystal (whose incidence angle is denoted by $\theta(\lambda_0,n_2)$) is given by equation (3.5).

$$\pm\beta \text{ m}\alpha - \frac{1}{2}\psi^2 \tan\theta(\lambda_0, n_2) - (\lambda - \lambda_0)\frac{\partial\theta}{\partial\lambda_0}(\lambda_0, n_2) \qquad (3.5)$$

Here the upper signs correspond to the (+n,+n) geometry and the lower signs to the (+n,-n) setting. The intensity of the sample diffracted beam, for all angles of incident rays, is obtained by considering the power in an element of the incident beam characterised by vertical and horizontal divergences of $\psi$ and $\alpha$, whose wavelength lies in the range $\lambda$ to $(\lambda+d\lambda)$. This power is given by, $G(\alpha,\psi)J(\lambda-\lambda_0)d\alpha d\lambda d\psi$, where the function, J, gives the distribution of energy in the incident spectrum and the function, G, is a geometric instrumental factor. The total integrated intensity from the sample crystal is expressed as,

$$P(\beta)=\int_{-\psi_m}^{\psi_m}\int_{\lambda_{min}}^{\lambda_{max}}\int_{-\alpha_m}^{\alpha_m} C_1\left[\alpha-\frac{1}{2}\psi^2\tan\theta(\lambda_0,n_1)-(\lambda-\lambda_0)\frac{\partial\theta}{\partial\lambda_0}(\lambda_0,n_1)\right]$$

$$\times C_2\left[\pm\beta\mp\alpha-\frac{1}{2}\psi^2\tan\theta(\lambda_0,n_2)-(\lambda-\lambda_0)\frac{\partial\theta}{\partial\lambda_0}(\lambda_0,n_2)\right]G(\alpha,\psi)J(\lambda-\lambda_0)d\alpha d\lambda d\psi \tag{3.6}$$

where the functions $C_1$ and $C_2$ describe the reflection curves of the first and second crystals respectively. The limits for the divergence are taken as some maximum value (m or -m) on either side of the central ray. By evaluating P(β) as a function of angle the x-ray rocking curve can be generated. Physical results can be obtained from this rather cumbersome expression by assuming the following simplifications,

i) that in the limiting case where the diffraction pattern is extremely narrow the effective value of the functions $C_1$ and $C_2$ is negligible unless its argument is nearly zero,

ii) the power distribution of the x-ray source is constant over the crystal reflecting range,

iii) the vertical divergence is small.

In this case, where the reference crystal and sample are of the same material, the expression for P(β) can be described in the form below.

$$P(\beta)\propto\int_{-\infty}^{\infty}C(\alpha)C(\alpha-\beta)d\alpha \tag{3.7}$$

Equation (3.7) represents the correlation of the two crystal reflecting ranges and the resulting intensity distribution is thus symmetric even if the constituent curves $C_1$ and $C_2$ are not.

By returning to equation (3.6), in the limit of the arguments of $C_1$ and $C_2$ becoming zero (i.e. setting equations (3.4) and (3.5) to be zero) and eliminating α from the pair of equations so produced, equation (3.8) is formed.

$$\beta - \frac{\psi^2}{2}\{\tan\theta(\lambda_0, n_1) \pm \tan\theta(\lambda_0, n_2)\} - (\lambda - \lambda_0)\left\{\frac{\partial\theta}{\partial\lambda_0}(\lambda_0, n_1) \pm \frac{\partial\theta}{\partial\lambda_0}(\lambda_0, n_2)\right\} = 0 \tag{3.8}$$

If we define D to be,

$$D = \frac{\partial\theta}{\partial\lambda_0}(\lambda_0, n_1) \pm \frac{\partial\theta}{\partial\lambda_0}(\lambda_0, n_2) \tag{3.9}$$

and use the differential form of Bragg's law to obtain,

$$D = \frac{1}{\lambda_0}\{\tan\theta(\lambda_0, n_1) \pm \tan\theta(\lambda_0, n_2)\} \tag{3.10}$$

then some mathematical manipulation yields the result,

$$\beta = \frac{1}{2}D\lambda_0\psi^2 + D(\lambda - \lambda_0) \tag{3.11}$$

The importance of this result is demonstrated by the fact that the dispersion of the double crystal diffractometer is given by $\partial\beta/\partial\theta$ and thus the differential of equation (3.10) is,

$$\frac{\partial\beta}{\partial\theta} = D \tag{3.11}$$

Hence, for the (+n,-n) setting of the diffractometer, where the bottom (-) sign applies in equation (3.9), the dispersion is seen to be zero, a result in agreement with that predicted by the use of Du Mond diagrams.

## 3.5 Incident Beam Divergence And Diffractometer Misalignment

The most common type of x-ray source used experimentally is a sealed filament type x-ray tube possessing, typically, a copper target. The output from such a tube will consist of Brehmmstrahlung radiation spread over a wide range of wavelengths superimposed on which will be intense characteristic spectral lines. The most intense of these will be the CuKα doublet and the CuKβ lines. Use of a collimation system prior to the first crystal will reduce the angular divergence so

that simultaneous diffraction of the Kα and Kβ lines will not occur. However, the close separation of the $CuK\alpha_1$ and $CuK\alpha_2$ lines results in both lines being diffracted by the reference crystal. The less intense $K\alpha_2$ component can then be removed by a slit placed between the reference and sample crystals and this slit also has the effect of further reducing the beam angular divergence. For the non-dispersive geometry the component of angular divergence in the diffraction plane has no effect on the width of the rocking curve but broadens the peak in the dispersive settings. However, for the component of divergence normal to the diffraction plane rocking curve broadening occurs for all three diffractometer configurations. The effect of angular divergence on the rocking curve was examined by Yoshimura[12] and further developed by Xu and Li[13]. These workers incorporated the component of divergence normal to the diffraction plane as a third dimension on the Du Mond diagram. Thus, in addition to an axis representing wavelength, two other axes, θ and ψ, are drawn to denote the components of divergence in and normal to the diffraction plane respectively. By describing the diffraction conditions in this way, Xu and Li were able to derive a resolution function for the double crystal diffractometer.

Thus far it has been asssumed that the incident x-ray beam is normal to the diffracting planes of both the first and second crystals. In practice this is unlikely to be exactly true with the normals of both reflecting planes tilted with respect to the diffraction plane itself. The effect of this tilt is to broaden the double crystal diffraction curve and change slightly the measured sample Bragg angle. This increase in peak width results in a decrease in peak height, although the total integrated intensity beneath the rocking curve stays constant.

In his 1928 paper, Shwarzchild derived an order of magnitude expression for the FWHM of the rocking curve in terms of a tilt misalignment angle, χ, and component of divergence normal to the diffraction plane, $\psi_n$, as shown below.

$$\begin{aligned} \theta_{\frac{1}{2}} &= 2\chi\psi_n && \text{for} \quad \chi \rangle \psi_n(\tan\theta_1 \pm \tan\theta_2) \\ \theta_{\frac{1}{2}} &= M\psi_n^{\,2} + \chi\psi_n + \frac{\chi^2}{4M} && \text{for} \quad \chi \langle 2M\psi_n \end{aligned} \tag{3.12}$$

Here, $M = \frac{1}{2}(\tan\theta_1 \pm \tan\theta_2)$ where the + sign applies for the dispersive settings and the - sign for the non-dispersive geometry. For the (+n,-n) setting, M is thus equal to zero and the peak FWHM is equal to $\chi\psi_n$, i.e. the width varies linearly with the tilt angle. Since wavelength dispersion is very small for the (+n,-n) setting, tilt misalignment is the dominant broadening mechanism. Conversely for the dispersive diffactometer configurations the broadening due to dispersion is significantly greater than that due to tilt.

## 3.6 Triple Crystal Diffractometers

For bent or mosaic crystals Bragg diffraction will occur over a larger range of incidence angles for a given lattice spacing, d, than for an ideally "flat" specimen. Since the double axis system utilises an open detector, the scattering from a sample is integrated over all incidence angles within the detector aperture. As sample curvature is an inherent feature of lattice mismatched epitaxial specimens then peak broadening within the rocking curve is often an unavoidable aspect of double crystal analysis, even for the non-dispersive (+n,-n) diffractometer setting. Even if this peak broadening can be tolerated, fine structure present in the diffraction profile, such as Pendellösung fringes, can be significantly blurred or even lost. In addition, as well as recording the dynamically diffracted beam the open detector will also collect the thermal diffuse scatter from the sample, further degrading the sensitivity of the double crystal technique.

One way to eliminate this problem is by using a third crystal to investigate the angular distribution of the scattered radiation. This technique is employed in the triple crystal diffractometer, first proposed by Renninger[14], which uses an analyser crystal to Bragg select out scattered radiation as a function of angle. Radiation scattered from the sample is only passed through the analyser if its direction lies within the angular width of the analyser diffraction condition. Scattering from a curved, or misoriented, region of the sample will satisfy the Bragg law at only one setting of the analyser crystal. Further, since scattering from defects will occur in a different direction to that from the perfect crystal, the analyser may be used to separate out these two components of scatter. One of the main features of the triple crystal diffractometer is that it is able to distinguish the scattering from tilted, or misoriented, regions of the sample from that arising as a result of lattice

dilations. How the technique achieves this will be discussed in Chapter IV. Cowley[15] has derived the resolution function of a triple crystal diffractometer, for both conventional and synchrotron sources, by assuming that the resolution is controlled by the properties of the first and analyser crystals. The wavelength dispersion of the triple crystal diffractometer has been expressed by Ryan as[16],

$$\frac{d\Phi}{d\lambda} = \frac{1}{\lambda}\left[\tan\theta_1 - 2\tan\theta_2 + \tan\theta_3\right] \tag{3.13}$$

where $\theta_1, \theta_2$ and $\theta_3$ are the Bragg angles of the first, sample and analyser crystals respectively, $\lambda$ the wavelength and $\Phi$ the angular setting of the analyser. The most common setting of the diffractometer is (+n,-n,+n) and if all crystals are chosen to be the same so that $(\tan\theta_1) = (\tan\theta_2) = (\tan\theta_3)$, then the dispersion is seen to become zero.

## 3.7 Multi-Reflection Beam Conditioners

The previous discussion has demonstrated the benefits which may be obtained by using a third crystal to Bragg analyse the scattered radiation. The triple crystal diffractometer has a significantly better angular resolving power compared to that of the double axis system. However, it does not offer any great improvement in spectral resolution. The (+n,-n,+n) geometry is non-dispersive in wavelength only if similar materials and Bragg reflections are used for each of the three crystals. Employment of different crystals, reflections or even other geometries (e.g. the (+n,-n,-n) setting) results in significant peak broadening[17]due to wavelength dispersion effects. This presents a problem experimentally in that if the diffractometer is to be employed in its highest mode of resolution, then each time a different sample material or reflection is used, the first and analyser crystals must be re-aligned to match the conditions of the sample crystal.

This drawback may be overcome by using multi-reflection systems to "monochromate" the beam. Previously the x-ray beam is initially incident upon the first crystal which conditions the beam in terms of its angular distribution only. Since this first crystal diffracts both lines in the Kα doublet it does not act as a monochromator. By utilising a "beam conditioner" before the first crystal then the x-ray beam can be truly monochromated before hitting the sample crystal. The

minimum requirement in order to eliminate dispersion effects is to use at least a two reflection beam conditioning system in the (+n,+m) geometry, where the second reflection monochromates the beam[18]. In practice, the most popular form of beam conditioning is achieved by employing a four reflection monochromator. The four reflections may originate from the same single crystal or, as was originally employed, from four separate crystals as illustrated in Fig 3.4(a). The corresponding Du Mond diagrams for this situation are presented in Fig.3.4(b). The principle of operation may best be understood by considering the diagram in three stages. The first two crystals, taken as a pair, act as a double crystal diffractometer in the (+n,-n) geometry. Hence, when both are aligned to diffract the dispersion is zero and the full spectral range is passed to the third crystal. However, the third crystal is oriented in an antiparallel manner and the direction of its Du Mond diagram is reversed with respect to the first two crystals (fig. 3.4(b)). This crystal, therefore, diffracts only a small range of wavelengths as represented by the area of intersection of the Du Mond diagrams. This arrangement alone is sufficient to deliver a monochromatic beam to the sample but a fourth reflection is commonly used[19,20] to diffract the monochromatic beam back into its original direction, i.e., co-linear with the input beam. This system of beam conditioning has been studied in a five crystal diffractometer by Bartels[21] and Slusky and Macrander[22], for both possible settings of the fifth crystal (the sample), and is illustrated in Figs.3.5(a,b). The area of intersection (shaded) of the du Mond diagrams is seen to be small, resulting in a low diffracted intensity reaching the detector. However, due to the decrease in the intensity of the tails in the rocking curve the diffractometer signal to noise ratio is significantly improved allowing study of small angle scattering effects[23]

An alternative method of beam conditioning is by using four successive reflections from a channel cut within a single crystal (+n,-n,+n,-n) as in the Bede Scientific Channel Cut Collimator (C.C.C.), which consists of a single, highly perfect silicon crystal aligned for the symmetric (022) reflection. The choice of four reflections means that the emerging beam is highly conditioned in terms of angular divergence with greatly diminished Bragg tails. Monochromation of the beam is achieved by diffraction from a further crystal in the non-parallel setting. The narrow intrinsic width of the (022) reflection results in a high resolution device although for cases where less sensitivity is acceptable C.C.C.'s using asymmetric (022) reflections yield diffracted peaks of greater intensity.

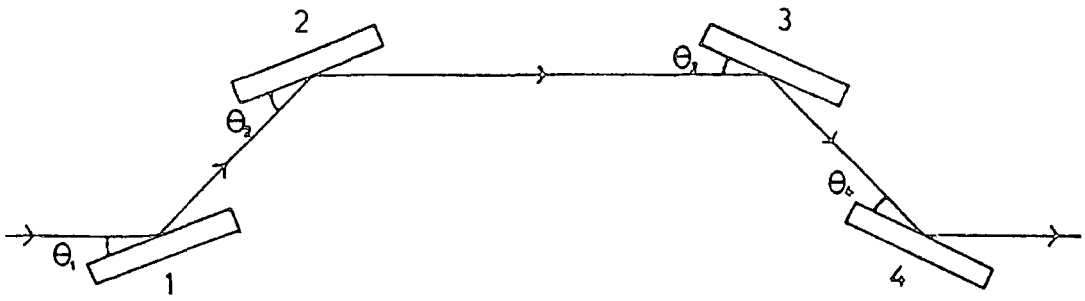


a) A monochromating system employing four separate crystals in the (+n, -n, -n, +n) configuration.

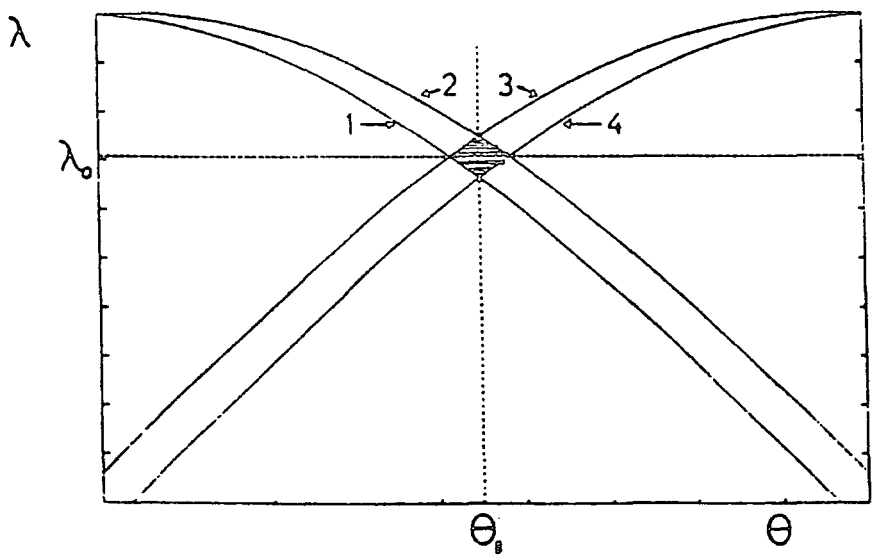


b) The Du Mond diagram for the above arrangement. At the diffraction condition, curves 1&2 and 3&4 overlap.

Figure 3.4 : A four crystal monochromator.

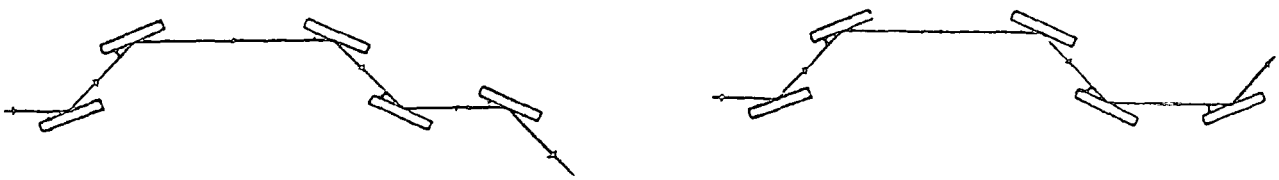

(+n, -n, -n, +n, -n) (+n, -n, -n, +n, +n)

a) Five crystal diffractometer arrangements.

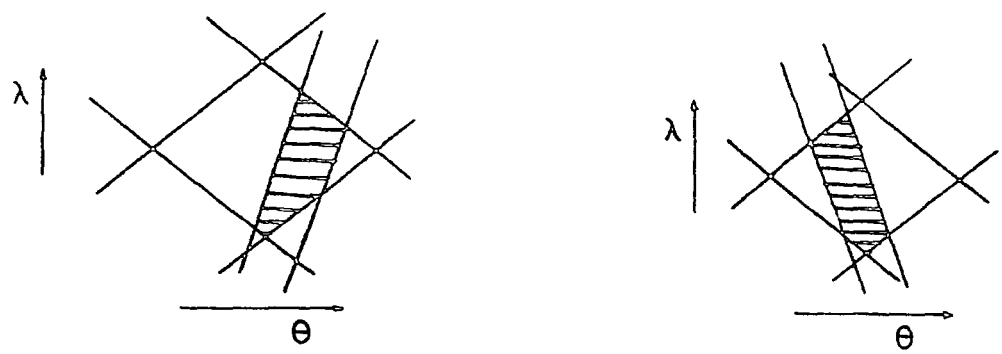


(+n, -n, -n, +n, -n) (+n, -n, -n, +n, +n)

b) Du Mond diagrams for the above diffractometer settings.

Figure 3.5 : A five crystal diffractometer.

By incorporating the two or four reflection beam conditioner as a "bolt-on" block, housed directly in front of the x-ray tube exit hole, the angular and spectral dispersive problems of the double crystal diffractometer may be greatly diminished. This arrangement is demonstrated in fig.3.6 which shows the schematic beam path of the x-ray beam though the diffractometer. Thus no restrictions apply to the choice of material or reflection and it is no longer necessary to change the reference crystal when studying different systems. Just as the benefits of crystal monochromators are enjoyed by double axis users, similar advantages are utilised by triple crystal diffraction workers. Fewster[24] has used a (n,-n,-n,+n) monochromating system, together with an analyser crystal, to produce a six crystal diffractometer which eliminates the effects of sample curvature in addition to angular and spectral dispersion. The triple axis diffactometer used in this thesis employs a four reflection channel cut collimator and monochromating crystal to provide dispersion free diffraction conditions.

The use of beam conditioning systems has found applications in the fields of dispersion free double axis diffractometry, high resolution triple axis diffraction, ultra low angle scattering and grazing incidence x-ray reflectometry (GIXR). Indeed, a conventional double axis diffractometer, fitted with a Bede C.C.C., has been shown to provide adequate beam conditioning in order to analyse thin film thicknesses[25] using the GIXR technique.

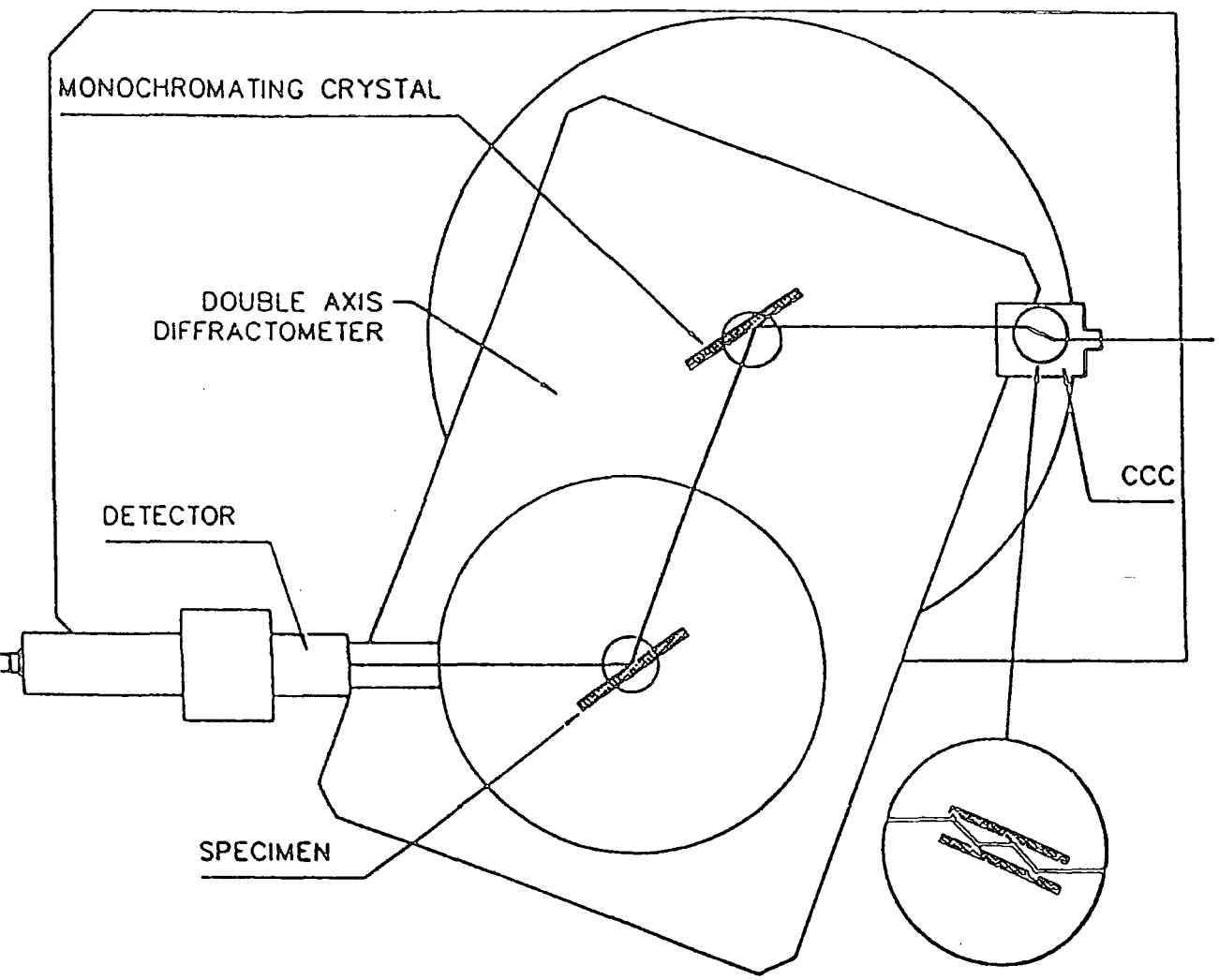


Figure 3.6 : The path of the x-ray beam through a double crystal diffractometer fitted with a four reflection channel cut collimator.

Courtesy of Bede Scientific Instruments Ltd.

# Chapter IV

# Experimental Techniques Of X-Ray Scattering

## 41. Introduction

A wealth of different x-ray scattering techniques are available to the experimentalist with which to study the structural properties of materials. The particular method chosen is dependent upon the type of information sought about the material and the crystalline quality of the sample itself. Broadly speaking the various methods can be classified as diffraction or non-diffraction techniques and applications of these methods have been found in both industry and the research laboratory. As an example, the previous two decades have seen extensive use of the double crystal diffractometer in the semiconductor industry, for routine analysis of crystal structure. The recent development of a commercial reflectometer is expected to lead to increasing use of the grazing incidence reflectivity technique by device fabrication institutions. With the advent of synchrotron radiation and the drive toward smaller device structures (many in the nanometre region) x-ray characterisation techniques have been continually developed and refined to meet the needs of the crystal grower. For a complete description of the techniques available in x-ray scattering analysis, the reader is referred to a number of texts[1,2,3,4]. The remainder of this chapter will discuss only those methods used in the production of this thesis, with particular emphasis given to the alignment procedures and experimental configurations used.

## 4.2 Double Crystal Diffractometry

One of the most popular x-ray characterisation techniques is that of double crystal diffraction (DCD), also known as high resolution diffraction (HRD). A theoretical description was presented in Chapter III. The instrumentation necessary for rapid routine analysis has evolved to a high degree with double crystal diffractometers now an integral feature of many industrial characterisation laboratories. Commercial instruments, equipped with sample rotation, rocking and X-Y mapping motions, allow both symmetric and asymmetric sample reflections to be collected. Highly mismatched layers may become partially or completely relaxed (by the introduction of misfit dislocations at the growth interface) and the

recording of asymmetric reflections allows the lattice parameters of incoherent layers to be determined[5,6]. Double crystal experiments described in this thesis were performed in the University of Durham, on a prototype Bede model 150 diffractometer, whose construction is based upon a design first proposed by Hart[7] in 1969. The term 150 arises from the separation between the two crystal axes which is 150mm. The instrument is automatically controlled by an IBM compatible computer using the Bede DCC software control package and Minicam electronics interface.

The Bede model 150 diffractometer provides automated rotation of two crystal axes, allowing fine, calibrated motion of the reference and specimen crystals. The whole diffractometer itself may be rotated about an axis co-axial with the reference (or first) crystal axis, although this rotation must be performed manually. Diffractometer alignment is aided by the use of machined tools which fit into the collar of the two diffractometer axes. During initial alignment, the diffractometer base is rotated so that the collimator pinhole (from which the x-ray beam emerges) and the pointers placed in the two axes are co-linear. The diffractometer body is then manually rotated to twice the Bragg angle of the reference crystal reflection. Thus when the first crystal is mounted and aligned to its Bragg condition (within a scatter shield) the diffracted beam should pass over the second crystal axis. This can be checked by insertion of an alignment tool with a vertical slit into the second axis. By placing the detector (scintillation or proportional) behind this alignment tool the coincidence of the beam path and the vertical slit can be verified. Should the two not be in coincidence, i.e. not all of the diffracted intensity passes through the slit, then the base position of the diffractometer is changed slightly (and the peak from the reference crystal re-found) until the full diffracted beam passes through the alignment tool to the detector. To ensure that the reference crystal diffracted beam passes parallel to the diffractometer surface, a second alignment tool with a machined horizontal slit set at the appropriate height, is placed into the second axis. The first crystal is tilted until the full diffracted beam passes through this horizontal slit. The x-ray beam now being delivered to the second axis contains two major wavelength components, the $CuK\alpha_1$ and $CuK\alpha_2$ characteristic lines. To remove the less intense $K\alpha_2$ component a slit is introduced between the first and second axes. The $K\alpha_2$ line is diffracted on the high angle side of the $K\alpha_1$ component, and is approximately 50% less intense. Practically, the removal of this line can be achieved by bringing the slit on the high angle side in until a reduction

of one third in the total intensity is measured. However, this technique presumes linear performance of the x-ray detector in the region of the diffracted x-ray beam intensity (or prior calibration of the detector performance), which may not be true for all detectors even at low generator power settings. A much better method, though more time consuming, is to increase the generator power, and place a piece of dental film at the second axis to detect if the $K\alpha_2$ component is present. Successive dental film images are recorded until the slit is positioned to eliminate the $K\alpha_2$ line. Having aligned the diffractometer to this stage, no further movement of the diffractometer base, reference crystal or slits should be necessary unless the diffractometer is accidentally knocked, or a different crystal is to be used as the reference. Routine use of the double crystal instrument should now involve positioning of the sample crystal only. To record the sample rocking curve, the sample is positioned at the second axis and rocked until the Bragg peak is found. Once this has been achieved the sample tilt is adjusted to bring the diffraction planes of the reference and sample crystals coplanar. The integrated intensity under the double crystal rocking curve stays constant as the sample tilt is varied. However, the effect of non-parallelism of the reference and sample crystal diffraction planes is to reduce the height of the peak maximum, and thus broaden the width of the diffraction profile. Hence, an easy method of locating the correct sample tilt position is to find the tilt adjustment which yields the most intense Bragg peak upon rocking of the sample. This technique is not the sole procedure used to tilt optimise samples and various other methods have been described by other workers[8,9].

Once the sample rocking curve has been recorded, then the positions and intensities of peaks in the diffraction profile are analysed to deduce sample structure. One of the prime uses of DCD is in the measurement of alloy composition, a capability which is well exercised industrially in the characterisation of III-V semiconductor heterostructures. Halliwell[10] has shown the measurement of lattice mismatch using a DCD to be more precise than any other technique, with an accuracy of 20ppm (parts per million) for both the 004 and 115 reflections from InGaAs and InGaAsP on InP using a DCD. Much of the rocking curve analysis can be carried out manually although, for complicated structures, comparison with a simulated model is necessary to extract the full information content of the recorded profile.

### 4.3.1 X-Ray Topography

While rocking curves can provide a great deal of structural data, particularly on compositional variations, the data is averaged spatially over an area corresponding to the size of the incident beam (0.25 to 2mm$^2$). X-ray topographical methods allow the strain variations in a crystal to be mapped on the micron scale and a very large literature[3,11,12,13,14] exists on their application to electronic materials, principally for the study of dislocation density and configuration, dislocation mobility and the investigation of strains at the edges of films and devices. X-ray topography relies on the fact that the strain fields associated with crystal defects cause local distortions of the crystal lattice, which change the diffraction condition in the region of the defect. By setting the sample crystal to the perfect crystal Bragg condition and imaging the diffracted beam on a photographic medium, specimen defects are imaged on the film as regions of different contrast within the uniform image of the surrounding crystal. For effective misorientations greater than the width of the double crystal rocking curve a complete loss of intensity is recorded locally (i.e. within the region of the defect). Use of a large area incident beam allows the crystal perfection and defect distribution of a large section of the sample to be determined.

X-ray topographic techniques can be grouped as either single or multiple crystal methods. For single crystal techniques, the wavelength spectrum incident upon the specimen crystal is determined by the x-ray source. For laboratory based experiments where a conventional fixed target x-ray tube, with relatively large angular divergence, is used as the radiation source then single crystal topographic methods are sensitive only to short range strain fields such as those found in the immediate vicinity of a crystal defect. Multiple crystal techniques, of which the double crystal method[15,16] is the most popular, employ one or more perfect crystals to pre-condition the beam before it strikes the sample. By limiting the angular divergence of the x-ray source with a reference crystal reflection, the wavelength spectrum incident upon the sample crystal is determined by the perfect crystal reflecting range of the first crystal. As a result the multiple crystal technique is sensitive to much larger range strain fields. The topographic results presented in this thesis (Chapter VII) were collected using a specially adapted Bede 150 diffractometer, in the dispersive double crystal setting.

### 4.3.2 Double Crystal Topography

Double crystal diffractometry is similar to double crystal diffraction analysis except that a spatially large incident beam is used and the x-ray radiation detector is replaced by a photographic plate. While the large flux rates, small angular divergence and wavelength tunability of synchrotron radiation sources make them ideal for double crystal topography[17], topographic analysis can still be conducted using a conventional fixed target x-ray tube (although typical exposure times are long). In the laboratory, double crystal diffractometry should be performed in the dispersive geometry where the reference and sample crystals differ. The DuMond diagrams of the two crystals will then overlap for only a limited angular range and it is possible to select a sample image from the $K\alpha_1$ line only. In the non-dispersive geometry, where all wavelengths are diffracted, doubling of the sample image occurs due to the presence of both $K\alpha_1$ and $K\alpha_2$ components.

Before selecting a particular experimental geometry, the experimentalist must decide upon the resolution necessary in the topographic image and the extent of sample coverage by the incident x-ray beam. Use of a large area incident beam will allow full sample coverage, thus allowing defects from all parts of the specimen to be imaged. Selection of an asymmetric reflection with grazing incidence angle for the reference crystal allows the beam width to be expanded by a factor of up to 20. The expansion limit of the incident beam is then set by the critical angle for total external reflection, limiting the incidence angle to be greater than about 0.5°. If the collimator slit is machined to be around 1-2mm wide and extended some 30mm in the vertical direction, then by using the line source of the x-ray tube, samples of dimension 1" by 1" (or more) may be fully imaged. The disadvantage of employing extreme beam expansion optics is that the $CuK\alpha_1$ and $CuK\alpha_2$ components are no longer spatially separated and may not be resolved by use of a shielding slit. The resolution of the final topograph is then reduced.

An alternative approach is to achieve large sample coverage by employing a (grazing incidence) asymmetric reflection on the sample crystal. This allows a more intense, symmetric reflection to be used at the first axis, e.g., the (004) reflection from (001) oriented Si, where the $CuK\alpha_2$ component may be removed by a slit. The diffracted beam incident upon the sample is now narrow (1-2mm) but by choosing a suitable asymmetric sample reflection, with an extremely small

incidence angle, the entire surface of the specimen can be covered by the reference crystal beam.

It should be noted that full sample coverage in topography experiments does not necessarily mean that the entire specimen surface is imaged. This depends to a great extent upon the sample curvature. For many samples, where the presence of mismatched layers leads to a "bowing" of the specimen with misorientations considerably greater than the rocking curve width, only a small "band" may actually diffract. By recording topographs at various sample crystal settings, "contours" of equal effective misorientation may be obtained[18,19]. By rotating the specimen 180° about the diffraction vector and repeating the experiment, lattice tilts and dilations may be separated[20]. An alternative method of distinguishing between tilts and lattice parameter variations is by using a triple crystal diffractometer[21]. As in the case of double crystal topography, triple axis analysis can be thought of as an extension of DCD methods, with the spatial distribution of the scattered radiation being determined.

### 4.4.1 Triple Crystal Diffractometry

The triple crystal diffractometer utilises Bragg reflection from a third crystal to investigate the scattered radiation as a function of scattering vector, $\underline{k}$. Some commercial triple crystal diffractometers are available although many workers have developed their own instrumentation. The multi-reflection nature of the triple crystal technique means that an intense x-ray source is preferable if an appreciable final signal is to be obtained. Due to this, triple crystal analysis can easily be performed with synchrotron radiation[22] or rotating anode generators[23,24] although it is possible to record high quality data with a conventional x-ray tube[25,26]. The triple crystal data presented in this thesis was collected with a Bede model 200 diffractometer, which is essentially a double crystal instrument with an attachable third crystal stage. This model differs from the Bede 150 diffractometer in that the separation between the two axes is larger (200mm), and provision is made for motorised, computer controlled movement of the diffractometer base (co-axial with the first crystal axis) and of the detector circle (co-axial with the second crystal axis), on which the analyser stage is mounted. A schematic diagram of the Bede 200 diffractometer, with triple crystal stage, is shown in fig.4.1. The analyser crystal can be used to investigate the sample diffracted beam either by

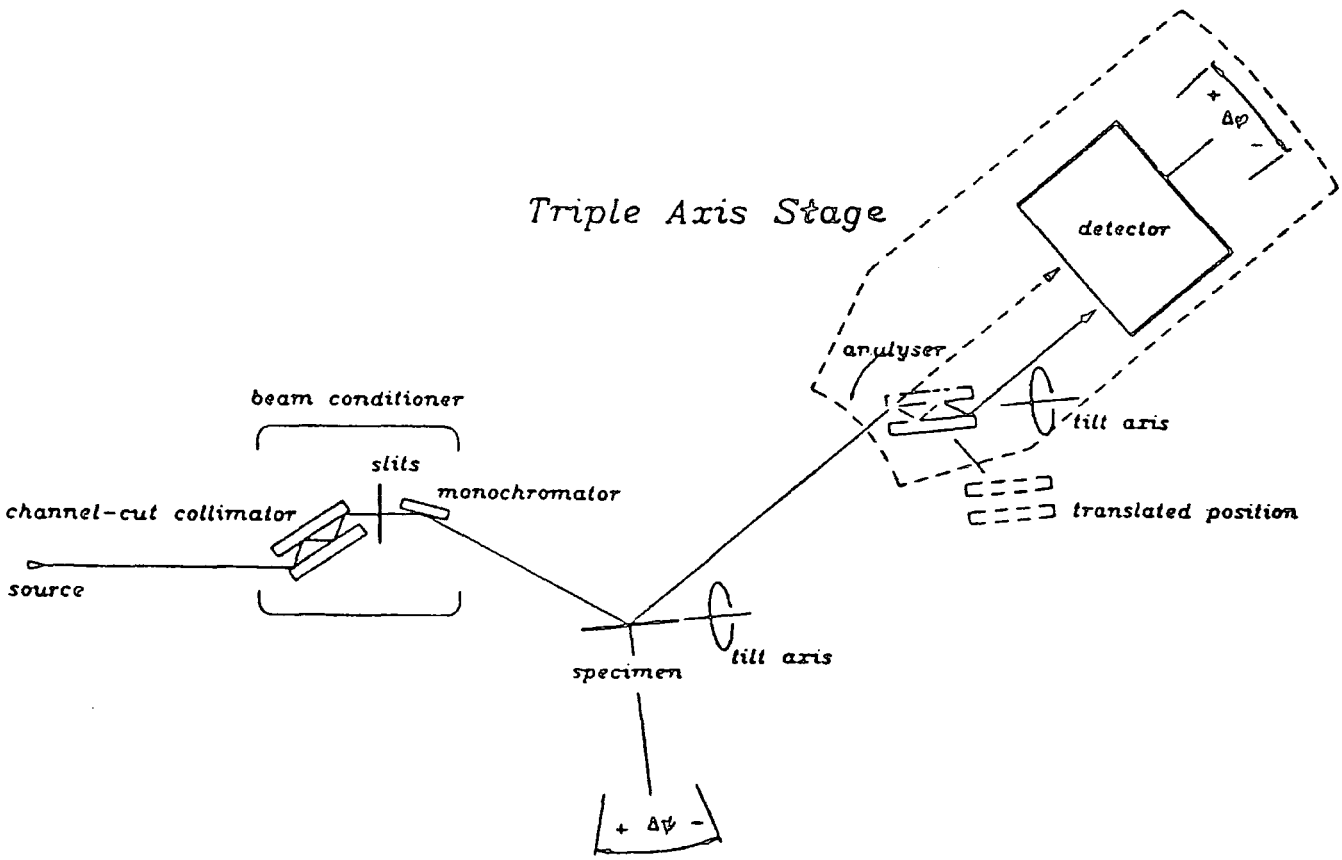


Figure 4.1 : Schematic geometry of the Bede 200 diffractometer with triple crystal stage. Courtesy of Bede Scientific Instruments Ltd.

rotating the entire analyser stage around the detector circle or by rocking the analyser crystal about its own axis (known as Axis 3). The facility to translate the analyser tangentially to the detector circle (i.e. across the specimen diffracted beam) and to tilt the third crystal is also available (the so-called Xscan motion). While, at first sight, triple crystal diffraction may seem complicated and difficult to set up, the experimental procedure may be broken down into a series of small steps. The following section describes how triple crystal data may be collected on the Bede 200 diffractometer.

### 4.4.2 Alignment Procedure In Triple Crystal Diffractometry

Prior to the following steps been carried out, it is assumed that the channel cut collimator and monochromating crystal have been adjusted to give an intense Bragg diffracted beam over the second (sample) crystal axis, travelling parallel to the diffractometer surface. For a conventional x-ray tube source, use of a pinhole sized beam is unlikely to provide adequate x-ray intensity to the second axis and it is recommended that an incident beam size of at least 2mm square is used. The procedure for setting up the "double crystal" section of the diffractometer alignment is slightly different to that described in section 4.2. The incorporation of a four bounce beam conditioner means that the x-ray beam reaching the first axis has sufficiently small angular divergence for simultaneous diffraction of the CuK$\alpha_1$ and K$\alpha_2$ components not to occur. The separation of their diffracted peaks from the first axis is some 300" and the first crystal is positioned so as to diffract the intense K$\alpha_1$ line only. It should be noted that in this geometry the first (reference) crystal is acting as a true monochromator. The position and tilt of the monochromating crystal is varied until the diffracted beam is parallel to the diffractometer surface and travels directly over the second axis. To maximise intensity, the CCC is rotated gently until the diffracting planes of the beam conditioner and monochromator are parallel. The diffractometer is now set up into "double crystal" mode and dispersion free double axis experiments may be performed. Before triple axis measurements are carried out, it is helpful to set the analyser crystal to its Bragg condition and adjust its tilt to match those of the beam conditioner and monochromating crystals. By doing this at this point the analyser tilt need never be adjusted again, and only a fine tuning of the analyser position will be later required to find the triply diffracted beam. The only major task in the

triple axis experiment will then be to find the (tilt optimised) Bragg diffracted beam from the sample crystal itself.

As mentioned above, for the Bede model 200 diffractometer controlled by the DCC software package, two methods are available by which to rotate the third crystal. The entire third crystal stage can be rotated around a circle concentric with the second crystal axis, known as the detector circle. This is achieved in the control software by moving the motor labelled as "detector" and use of this motor is not to be confused with movement of the actual detector (the scintillation/proportional counter). Diffractometer alignment then proceeds as follows:

1. With no sample crystal in position and the slits in front of the analyser wide open, the entire third crystal stage is rotated to the zero degree position on the detector axis. While set at zero on its manually adjustable scale, the analyser is translated sideways (using the XScan motor) until the diffracted beam from the first crystal travels straight down the channel of the analyser crystal.

2. The analyser crystal is set to the approximate Bragg position (23.65° for the Si(220) reflection) and locked in place. This will now mean that the beam from the reference crystal no longer passes down the analyser channel and a small correction in the Xscan position of the third crystal must be made. This correction is determined geometrically and, for the analyser used in this thesis, corresponds to a translation of 3.05 mm.

3. By fine tuning the angular position of the third crystal (Axis3), the Bragg peak from the analyser is found. The intensity of this peak is then maximised by optimising the tilt of the analyser crystal. Having done this, then the analyser is moved around the detector circle to twice the Bragg angle of the specimen.

Having found, and tilt optimised the Bragg reflection from the third crystal, the diffracting planes of the CCC, monochromating crystal and third crystal are co-planar. No further adjustment to the tilt angles of these crystals need be performed unless the diffractometer is knocked out of alignment.

4. The sample crystal is placed on the second axis and, with the analyser crystal translated away from in front of the detector, the sample Bragg reflection is found (Axis 2). The diffracting planes of the specimen are brought co-planar with all other diffracting crystals by tilt optimising.

At this stage a standard double crystal experiment can be performed.

4. With the sample set at its Bragg peak, the slits in front of the analyser are reduced to the size of the diffracted beam. In particular, care must be taken that no sample scatter is allowed to travel over the top of the analyser crystal, thus introducing a constant intensity background.

5. To find the peak from the analyser crystal, it must be ensured that the sample diffracted beam strikes the opening of the channel cut into the third crystal. This is best achieved by translating the analyser (Xscan) until its edge half cuts the diffracted beam. Translation of the analyser by a further 3.05mm into the x-ray beam should bring the diffracted beam to the centre of the channel entrance.

6. The analyser is rocked about its axis (Axis 3) until the Bragg peak is found.

The diffractometer is now aligned to carry out triple axis analysis. Three types of scan may now be carried out, each giving different, but complimentary, information on the sample defect structure.

### 4.4.3 Scanning Modes In Triple Crystal Diffractometry

Three scan types may now be carried out, two of which require only single scans to be taken and are at least as rapid as the recording of double crystal rocking curves.

Measurement of lattice tilts

Consider the triple axis arrangement depicted in fig 4.2. Here all crystals are set to their diffraction condition and an intense diffracted beam, wave vector $\underline{k}$, is incident upon the detector face. Assuming the sample crystal to be perfect, with a narrow intrinsic Bragg width, then any rotation of the specimen axis (Axis 2) will

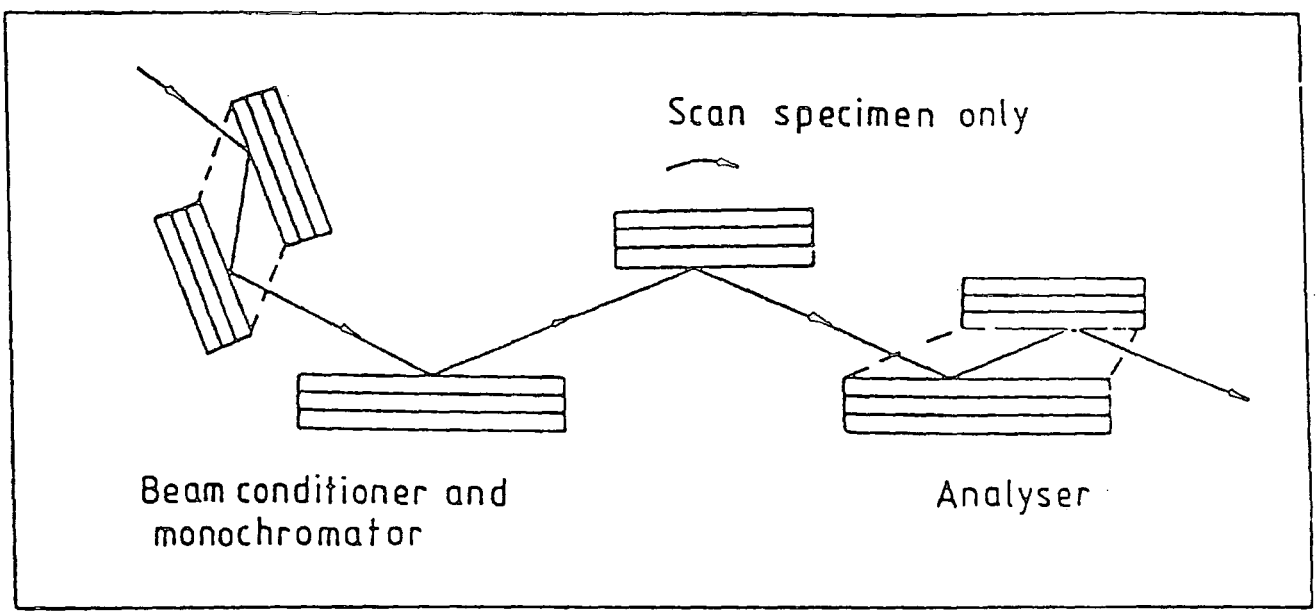


Figure 4.2 : Path of the diffracted beam in a triple crystal experiment.
Courtesy of Bede Scientific Instruments Ltd.

rapidly result in no Bragg diffracted beam reaching the detector. If the sample contains regions which are tilted with respect to each other (i.e. it has sub-grains or a mosaic spread) then, as the sample is rotated, these regions will satisfy the Bragg condition in turn, diffracting x-rays of wave vector, $\underline{k}$, onto the analyser. The angular range over which the sample can be rocked, and still deliver an x-ray beam to the analyser crystal, is thus an indication of the tilt distribution within the crystal. Any sample region with a different lattice parameter will diffract x-rays of wave vector $\underline{k'}$ onto the third crystal. Since the analyser is set to diffract x-rays of wave vector $\underline{k}$, no diffracted intensity arising from regions of lattice dilation will reach the detector. Rocking of the sample crystal only, in the triple crystal arrangement, thus measures the lattice tilt distribution only.

Measurement of lattice parameter distribution

Suppose that, in fig.4.2, the analyser is now scanned at twice the angular rate of the sample crystal. Initially a region of the specimen of lattice parameter, d, is set to diffract, with the analyser crystal positioned so that a diffracted beam reaches the detector. As the sample is rocked, regions of the specimen with a lattice parameter, $d'$, will satisfy the Bragg condition. Since the analyser is set at twice the angular position of the specimen, a diffracted beam will also result from the analyser and be recorded at the detector. Each time a region of different lattice parameter is rotated to the Bragg position the analyser will always be set to pass the diffracted beam onto the counter. The $\theta/2\theta$ scan thus measures the distribution of lattice parameters within the crystal. It remains undistorted by variations in lattice tilt, such as those caused by mosaic spread or long range curvature of the specimen. Tilted regions of the sample (diffracting wave vector, $\underline{k}$), will not contribute to the scattering recorded by the detector, as the analyser position will no longer be correct in order to "pass" radiation of this wave vector..

Measurement of Diffuse Scatter

If the surface region of the sample is distorted then the scattering is no longer governed by the dynamical scattering in the bulk of the crystal, and diffuse scattering, governed by kinematical theory, will occur. A full map of the diffuse scattering from the specimen can be made by recording a series of scans, for different specimen and analyser positions, coupled so as to trace out a grid in

reciprocal space centred around the reciprocal lattice point of the Bragg reflection. Although such a scan is time consuming (it can require collection of around 50 separate scans) the recorded scatter can contain much information. Diffuse scattering appears as a broad central hill around the reciprocal lattice point. The presence of tails or asymmetry in the total scatter (which can give information on the types of crystal defect) may also be highlighted by construction of a full reciprocal space map. The benefit of using a set of shielding slits in front of the analyser crystal is demonstrated by fig.4.3(a,b). This shows the scattering from a GaAs substrate recorded as a series of transverse scans for different analyser settings (Axis 3). The effect of air scatter, particularly over the top of the analyser crystal, introduce streaks of recorded intensity in reciprocal space (fig.4.3(a)). The introduction of shielding slits successfully eliminates this extra scatter (fig.4.3(b)).

### 4.4.4 Transforming From Real To Reciprocal Space

When carrying out triple crystal reciprocal space mapping, the variables recorded are the intensity of scatter collected and the angular positions of the sample ($\psi$) and analyser ($\varphi$) crystals. As the scattering is more easily interpreted from its distribution in reciprocal space, these real space variables must be transformed into the reciprocal domain. The angular position of the specimen defines the position of the diffracting planes whose scattering is being measured at this scattering angle. Fig.4.4 shows schematically the scattering from a triple crystal experiment in reciprocal space. The points O and h, define the origin and reciprocal lattice point of the Bragg reflection, respectively. The scattering is being measured from a small volume surrounding the point $[\Delta Q_y, \Delta Q_z]$. The scattering vector, $\underline{K}$, not shown directly in fig.4.4 may be considered as the sum of the "ideal" scattering vector from the origin to point $\underline{h}$, plus a deviation $\Delta\underline{Q}$ such that $\underline{K} = \underline{h} + \Delta\underline{Q}$. The deviation vector $\Delta\underline{Q}$ has two components, $\Delta Q_y$ and $\Delta Q_z$. It can be shown geometrically[27] that these components are related to the deviation of the specimen ($\Delta\psi$) and analyser crystals ($\Delta\varphi$) from their zero positions (at the nominal Bragg angle) by:

$$\Delta Q_z = \Delta\varphi \cos\theta_B / \lambda \tag{4.1}$$

$$\Delta Q_y = (2\Delta\psi - \Delta\varphi) \sin\theta_B / \lambda \tag{4.2}$$

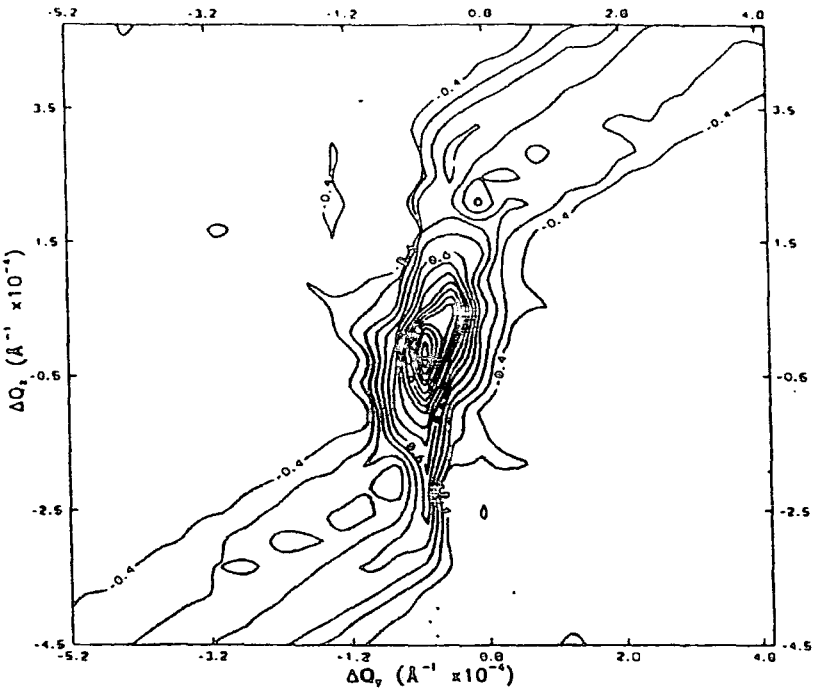


Figure 4.3(a) : The reciprocal space map of the scatter from an undoped GaAs substrate. No shielding slits in front of the detector.

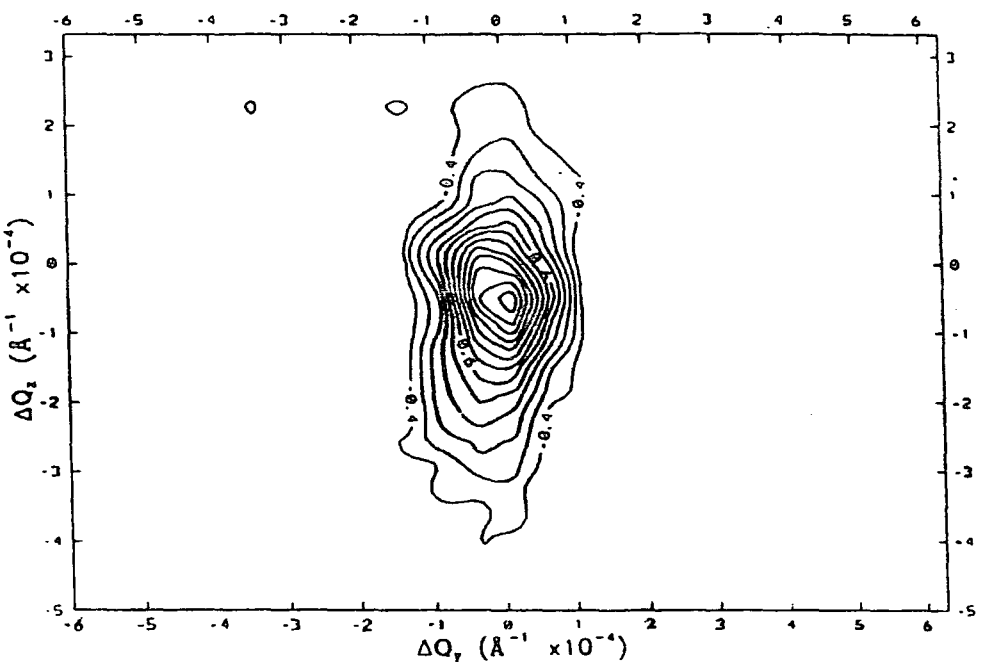


Figure 4.3(b) : The reciprocal space map of the scatter from an undoped GaAs substrate. A set of shielding slits have been placed in front of the detector.

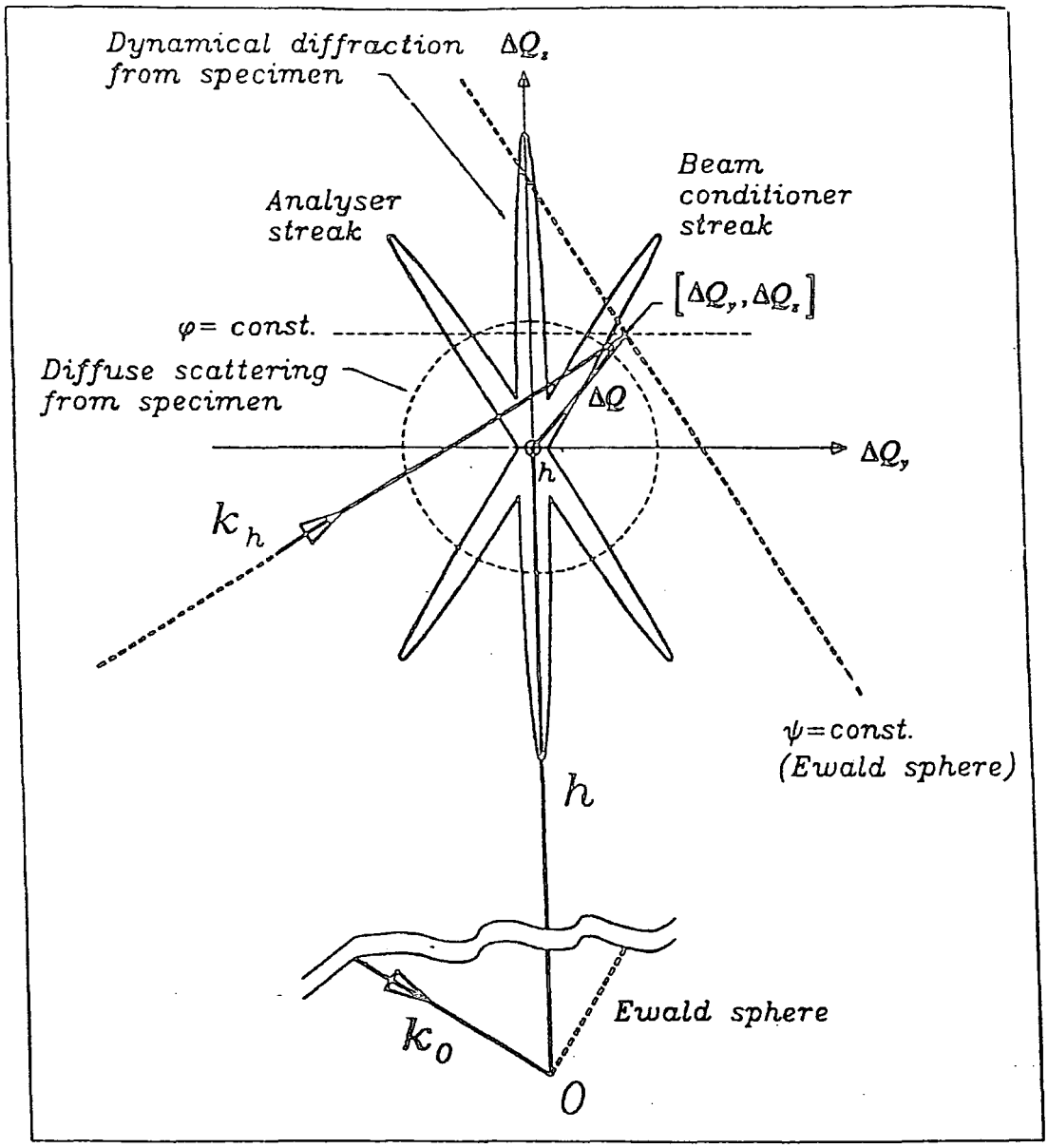


Figure 4.4 : A scattering map in reciprocal space. Equal intensity contours are shown schematically, and the Ewald sphere is approximated as a plane near reciprocal lattice points O and h.

Courtesy of Bede Scientific Instruments Ltd.

Thus a scan of specimen only ($\Delta\psi$) affects only $\Delta Q_y$, and provides a scan from left to right (i.e. transversely) in reciprocal space. A scan of the analyser crystal affects both $\Delta Q_y$ and $\Delta Q_z$ and, in fact, sweeps along the Ewald sphere. A scan of $\Delta Q_z$ alone may be achieved by setting

$$(2\Delta\psi - \Delta\varphi) = 0 \qquad (4.3)$$

i.e. scanning the analyser at twice the rate of the specimen crystal (often termed a $\theta$ /2$\theta$ scan). It is also worthy of note to recognise that the double crystal rocking curve corresponds to scanning with a line inclined at $\theta_B$ to the horizontal axis, with the measured intensity given by the integral of all the scatter beneath that line.

The presence of streaks can be observed at $\pm\,\theta_B$ to the vertical axis. These result from the finite angular resolution of the beam conditioner and analyser crystals and would be absent if these crystals had zero width rocking curves. A practical method of reducing these streaks (as implemented in this thesis) is to employ multiple reflections in the beam conditioner and analyser crystals. This is demonstrated in fig.4.5, which shows the measured scatter with no beam conditioner crystal for the undoped GaAs substrate whose scatter distribution with a four bounce beam conditioner was shown in fig.4.3. However, the introduction of additional reflections further attenuates the magnitude of the original x-ray beam as it passes through the diffractometer, placing limitations on the intensity of the sample diffracted beam if triple crystal analysis is to be successfully performed. In real terms the magnitude of the overall diffracted beam is related to the quality of the sample under investigation. For (relatively) perfect III-V semiconductor samples the high reflected intensity means that triple crystal analysis can be performed easily, even with multi-bounce beam conditioner and analyser systems. In the case of II-VI semiconductors, which typically have a much poorer crystalline quality, it is often necessary to eliminate many of the beam conditioner/analyser reflections in order to maintain a reasonable (or at least detectable) triply diffracted intensity. Thus a compromise must be achieved between having adequate experimental resolution and a sufficiently intense diffracted signal. This point will be further discussed in Chapter VII

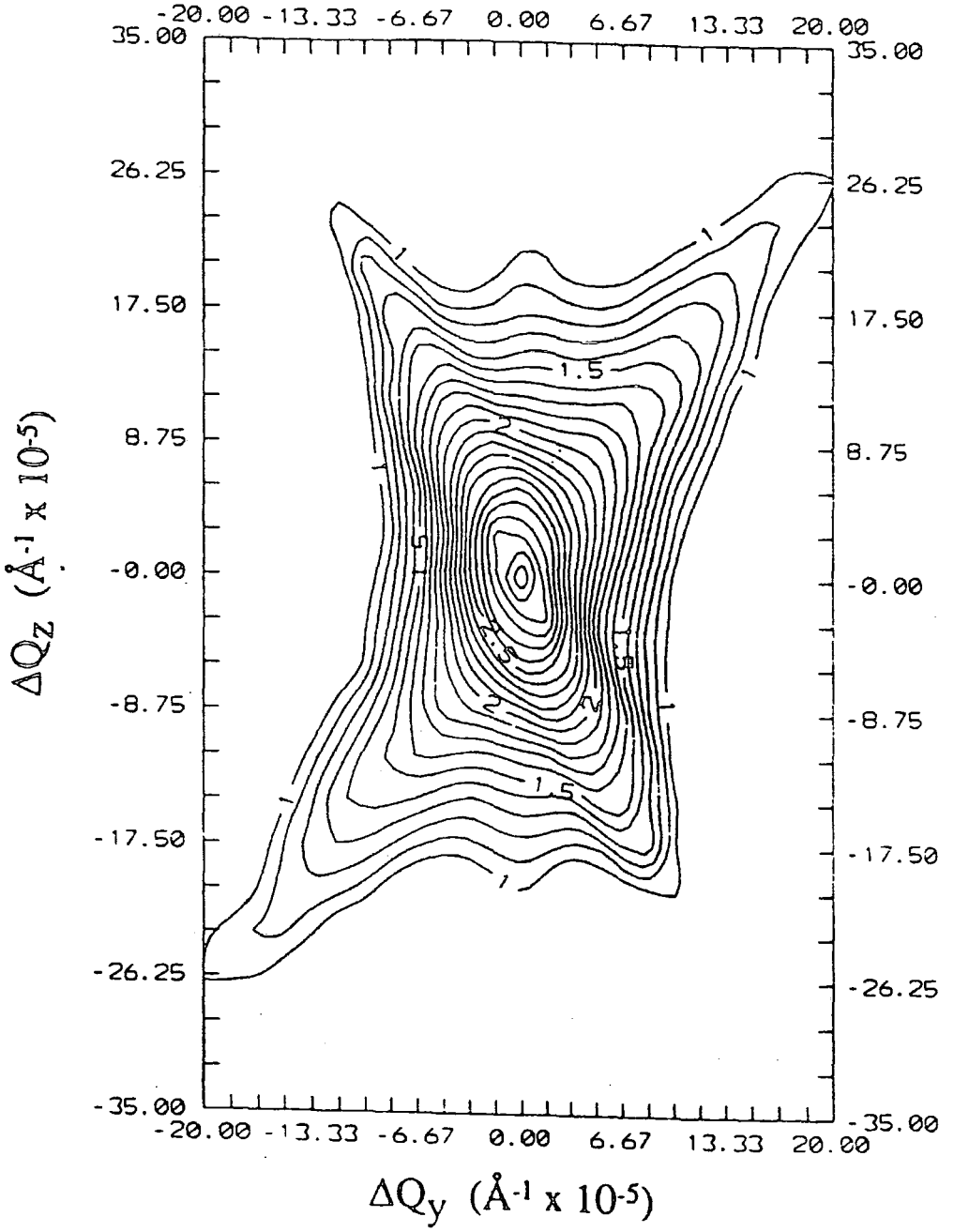


Figure 4.5 : The reciprocal space map of the scatter from an undoped GaAs substrate, with no beam conditioning crystal used. Contrast the characteristic "star" shape of the scatter with that recorded from the same crystal using a beam conditioner (fig.4.3).

### 4.5.1 Grazing Incidence X-Ray Reflectometry (GIXR)

The use of diffraction based techniques is limited to the analysis of highly perfect crystalline structures. For samples which have a high defect density, or which are even amorphous, near surface information such as thickness and abruptness of surface layers may be obtained by using the Grazing Incidence X-ray Reflectivity method (GIXR). Since the refractive index of x-rays in material is just less than unity, total external reflection occurs for glancing incidence angles below some critical value, $\theta_c$. The manner by which the reflected intensity varies as the incidence angle is increased above $\theta_c$ (at which point the incident beam begins to penetrate into the uppermost region of the sample), can be used to derive much structural information. The reflected amplitude falls sharply with incidence angle (as the inverse fourth power of the scattering vector) and thus useful sample information is only recorded over a few degrees before the sample signal becomes indistinguishable from the experimental noise. Hence, an intense x-ray source is advantageous in GIXR experiments. While conventional x-ray diffractometers can be adapted in order to take reflectivity data the use of a dedicated reflectivity instrument[28] to record GIXR measurements simplifies greatly the experimental alignment while offering high incident beam intensities. The reflectivity data presented in this thesis was collected on the prototype of the Bede Scientific GXR1 reflectometer, and a schematic of the scattering geometry is shown in fig.4.6. The prototype GXR1 used two Si crystals to precondition the incident beam. At the first, a simple symmetric reflection delivered an intense diffracted beam to the second beam-conditioning crystal. At the second crystal, a highly asymmetric Bragg reflection was used not only to compress the x-ray beam in the plane of incidence, but also to reduce the angular divergence of the x-ray beam. A low divergence reduced the linewidth of the incident beam as well as improving the angular resolution of the instrument. The resulting beam emerging from the beam conditioner block had a height of only 80μm and an angular divergence of around 30 arc seconds. This incident beam was coincident on the sample at exactly the centre of specimen rotation (i.e. the $\theta$ axis) so that the beam did not move across the sample surface as the specimen is rocked. By using novel, high precision bearings, the axes of rotation of the sample ($\theta$) and detector ($2\theta$) on the GXR1 are designed to be accurately co-axial. Complete specimen manipulation is provided by kinematically supporting the sample table on three independent goniometers. Movement of all three goniometers by an equal amount allows the sample height

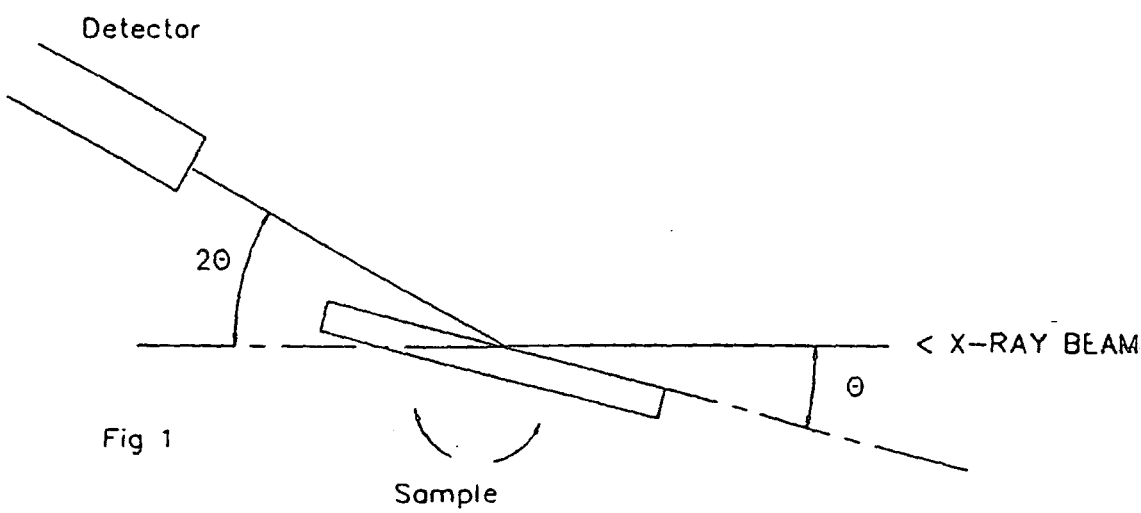


Figure 4.6 : Schematic arrangement of the scattering in a GIXR experiment.

to be varied, while, by driving opposing goniometers in opposite directions, the sample stage may be tilted in directions parallel and perpendicular to the incident beam, maintaining the height of the centre of the table. In order to ensure the maximum possible signal to noise ratio for large scattering angles, it is essential that a very low background detector (~ 0.2 c.p.s.) is used to collect the scattered radiation.

To aid alignment the Bede GXR1 reflectometer is fitted with an automatic, computer controlled alignment system, consisting of a low power laser and quadrant optical detector. The height and tilt of the sample is adjusted so that, as the sample is rotated, precession of the reflected laser beam is eliminated, at which point the specimen is "flat" with respect to the incidence beam and axes of rotation of the sample ($\theta$) and detector ($2\theta$) axes. For systems with no optical alignment facility, the sample position must be manipulated manually and a typical working procedure is presented below.

### 4.5.2 Alignment Procedure In GIXR

The height of the incident beam is made to be coincident with the axis of rotation of the reflectometer with the use of a machined alignment tool. The CuK$\alpha_2$ component of the x-ray beam emerging from the beam conditioner is spatially separated from the CuK$\alpha_1$ component and is removed with a slit. This procedure is simplified greatly by use of an x-ray camera to directly image the two wavelength components passing through the slit. With no sample stage in place the detector axis is scanned to record the angular profile of the incident beam. This has two purposes, the first being to locate the centre of the incident beam which defines the zero of the detector ($2\theta$) axis. Secondly, the shape of the beam profile is used to determine if stray scatter is emerging from the beam conditioner or if some fraction of the CuK$\alpha_2$, component is escaping past the edge of the slit system. Once the preceding steps have been carried out, and a monochromatic, intense x-ray beam is incident upon the centre of rotation of the reflectometer, no further alignment of elements in front of the sample stage need take place.

The main aim when aligning samples in GIXR experiments is to have the sample surface initially co-planar with both the incident beam and axes of rotation of the sample($\theta$) and detector ($2\theta$) motions. Any tilt of the sample out of this plane can

be resolved into two components, parallel and perpendicular to the incident x-ray beam. A specimen tilt in the forward direction will result in an offset error in the measured incidence angle ($\theta$). A tilt in the perpendicular direction will lead to the specularly reflected beam falling away from the narrow detector slit and a smaller reflected intensity being recorded. Approximate alignment of the sample stage itself is often best achieved by use of a clock gauge to set the sample "flat" with respect to the incident beam and the axis about which the sample stage and detector arm are rotated. The reflectometer alignment procedure then proceeds as follows:

1. The sample is placed onto the specimen table and placed centrally into the x-ray beam path. Positioning of the sample with respect to the incident beam can usually be judged by eye although a more exact method is as follows. The (unloaded) specimen stage is raised/lowered to half cut the x-ray beam and then translated away from the beam toward the sample loading window (using the "Trans" axis). The specimen is then mounted on the stage, which is translated back across the incident beam. The positions at which a change in the recorded intensity occur correspond to the edges of the specimen, and the position of the sample stage on the ("Trans") axis is adjusted to be the midway point.

2. Care must be taken to ensure that the sample surface intercepts the incident x-rays and is parallel to the x-ray beam. This is achieved by moving the sample up into the narrow x-ray beam (by changing the z position), and varying the sample tilt in the forward direction (Tilt 1), until a maximum intensity is recorded at the detector. If the alignment of the sample stage has been pre-set with a clock gauge, then the correction needed to bring the sample surface parallel to the incidence beam should be small unless the specimen is distinctly wedge-shaped. Once the sample is "flat" with respect to the x-ray beam, the sample is raised until it half cuts the incident beam. The sample is now aligned in one of the two (perpendicular) tilt directions.

3. The orientation of the specimen in the other tilt direction must now be adjusted to bring the sample surface co-planar with the incident x-ray beam and the axis of rotation of the sample ($\theta$) and detector ($2\theta$) rotations. This task is simplified by the provision of a rotary stage on the GXR1 reflectometer. By rotating the sample by 90°, so that the uncorrected tilt is now in the forward

direction a procedure similar to that described in step (2) may be adopted. The sample is tilted (Tilt 2 motor) until the recorded intensity is a maximum (some further refinement of the sample height may be required).

Steps 2 to 3 are iteratively carried out until the experimentalist is confident that both tilt components have been eliminated and that the sample is half cutting the incident beam.

4. In theory, the sample surface should now be flat with respect to the incident beam and reflectometer axis. This can be checked by rocking the sample axis, $\theta$, to an incidence angle of (say) 1000" and moving the detector axis, $2\theta$, to the nominal specular position (2000"). If the sample is correctly aligned then the maximum reflected intensity should be recorded within 50" of the nominal specular position. If the sample is then rotated by a further 90°, while set at the specular condition, then the magnitude of the reflected beam should not change by a large fraction as the sample rotates. If the sample is not correctly aligned, then as the specimen rotates, the specular beam will fall away from the narrow slits and no intensity will be recorded by the detector.

### 4.5.3 Scanning Modes In GIXR

The most common mode of scan employed in reflectivity experiments is the specular scan, where a coupled $\theta/2\theta$ motion is used to record the reflected radiation. This type of scan, which is useful for the determination of thin layer thicknesses, can be extremely rapid, provided the sample is of high quality, due to the intense nature of the specular beam. On the GXR1, where the incident x-ray beam intensity can be over 1.5 million c.p.s., a typical specular scan can be recorded in only a few minutes. While interface roughness information may also be extracted, the use of specular profiles to measure interface abruptness is limited[29]. The specular technique is not able to distinguish between interface roughness and interdiffusion nor give information on the roughness correlation length. To achieve this, so called "diffuse" scans must be employed. The presence of roughness at interfaces causes x-rays to be scattered out of the specular condition and into the diffuse component of the total scatter. Two types of scan, the transverse and longitudinal diffuse modes, are commonly used to investigate this diffuse component.

Transverse Scans

The transverse scan records the scattered radiation as the sample position (θ) is varied for a fixed detector setting (2θ). In reciprocal space, (fig.4.7), this corresponds to varying the incident wave vector, $\underline{k}_0$, while keeping the scattered wave vector, $\underline{k}_h$, constant. To a good approximation this is equivalent to allowing the tip of the scattering vector to move horizontally through reciprocal space (i.e. parallel to the y-axis in fig.4.7), thus explaining the origin of the term "transverse scan".

Longitudinal Scans

In longitudinal scans a coupled θ/2θ scan is performed with an initial sample offset from the specular peak. In reciprocal space this corresponds to increasing the length of the scattering vector while maintaining its direction parallel to the vertical axis (i.e. moving longitudinally in reciprocal space).

A complete map of the sample reflected scatter can be constructed by carrying out a series of transverse or longitudinal scans. The resulting "scatter map" can be plotted in terms of intensity versus sample (θ) and detector (2θ) positions, or plotted directly into reciprocal space by transformation of the recorded motor positions.

### 4.5.4 Transforming From Real To Reciprocal Space

Figure 4.7 shows the region of the reciprocal lattice near the origin, O, where the scattering is being sampled from a point (volume element), Q. The absolute angles of the specimen and detector positions with respect to their true zero settings are ψ and φ, respectively. The angle, δ, measured between the scattering vector Q and the vertical x-axis indicates how far from the specular condition the scattering occurs. Since $|\underline{k}_0| = |\underline{k}_h| = \lambda^{-1}$, then the magnitude of the scattering vector can be written as (from fig.4.7):

$$|Q| = \left(\frac{2}{\lambda}\right)\sin\left(\frac{\varphi}{2}\right) \tag{4.4}$$

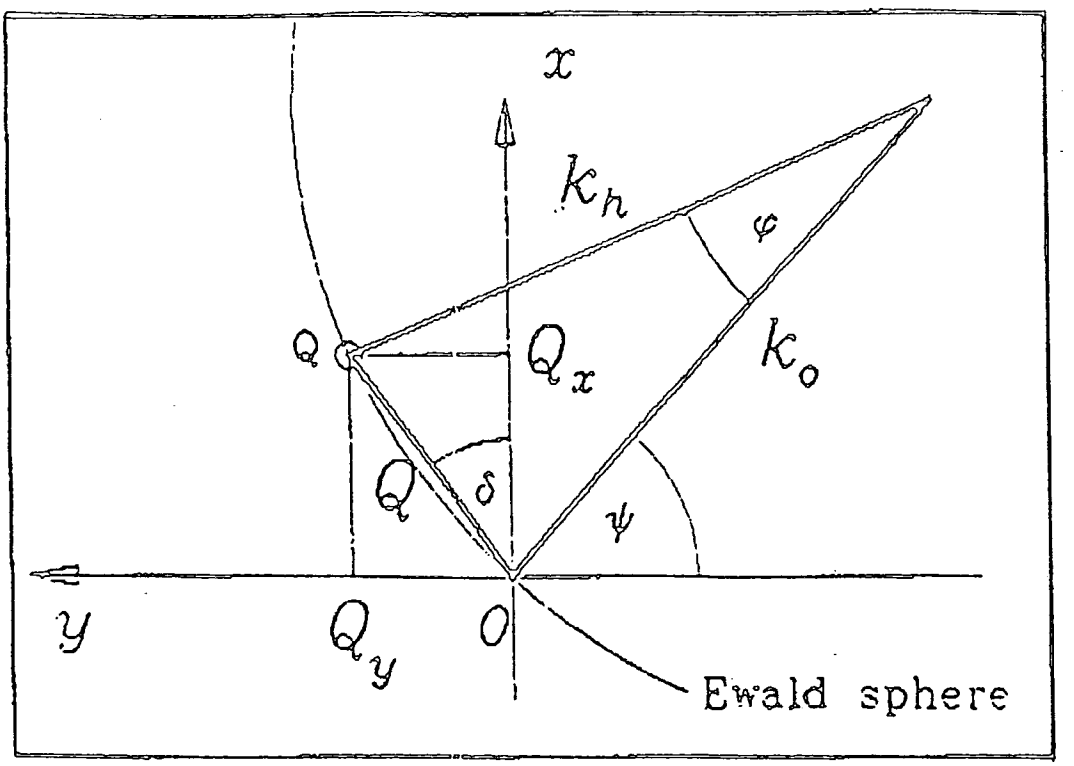


Figure 4.7 : Reciprocal lattice in the neighbourhood of the origin, showing the case of grazing incidence reflection.

Courtesy of Bede Scientific Instruments Ltd.

The scattering vector itself may be resolved into two components, parallel to the x and y axes. By noting that,

$$\delta = \psi - \varphi/2 \tag{4.5}$$

these components may be expressed as

$$Q_x = |Q|\cos\delta = \left(\frac{2}{\lambda}\sin\left(\frac{\varphi}{2}\right)\right)\cos\delta \tag{4.6}$$

$$Q_y = |Q|\sin\delta = \left(\frac{2}{\lambda}\sin\left(\frac{\varphi}{2}\right)\right)\sin\delta \tag{4.7}$$

Equations 4.6 to 4.7 may be used to transform a series of longitudinal or transverse diffuse scans into reciprocal space. Since they are without approximation their use can be applied to even the smallest scattering vectors. As for the analysis of triple crystal data, by feeding a series of recorded longitudinal or diffuse scans into a contour mapping program (such as the Golden Software SURFER package) a pseudo three dimensional map of the sample reflectivity can be constructed. This is of particular use when investigating long range features present in the diffuse scatter, as will be shown in Chapter VIII.

# Chapter V

# Layer Thickness Determination In High Electron Mobility Transistors Using Fast Fourier Transform Analysis

## 5.1 Introduction

Routine high resolution x-ray diffraction has now become a widely used characterisation tool in many semiconductor fabrication companies. The design of some commercial double axis diffractometers has allowed this technique to be used by semi skilled operators in a production line environment, with a high throughput of samples. While material parameters such as perfection and composition of heteroepitaxial layers can be rapidly deduced, measurement of layer thicknesses, particularly for systems with multiple layers, can be complicated and time consuming. Indeed, the structure of multiple layer systems can often only be determined by the use of a simulation program. When thin layer thickness determination only is required, the presence of oscillations in the rocking curve, known as thickness fringes (or sometimes called Pendellösung fringes), can negate the need for recourse to lengthy simulation processes, as the period of these fringes can be directly related to layer thickness. Such fringes are pronounced in rocking curves taken from Bragg case interferometers, which consist of a thin layer of composition B sandwiched between two thicker layers of composition A. This sample structure is common to several industrially important semiconductor devices, including High Electron Mobility Transistors (HEMT's). If these fringes are to be used to gain information on layer thicknesses then the experimental challenge is to ensure that their visibility in the rocking curve be made as high as possible, either by increasing the diffractometer signal to noise ratio or improving upon the photon counting statistics by employing longer count times. Obviously, with regard to employing the technique to routine analysis within a large scale fabrication environment, demands upon an increase in the total data collection time should be kept minimal. A more detailed discussion upon experimental requirements will follow later in this chapter.

## 5.2 Thickness Fringes

The presence of thin epitaxial layers of uniform composition leads to oscillations in the diffracted intensity profile known as thickness fringes[1,2,3]. The period of these oscillations can be directly related to the layer thickness (t) by the inverse relationship given below[4,5].

$$\Delta\theta = \frac{\lambda \sin(\theta + \phi)}{t \sin 2\theta_B} \tag{5.1}$$

with $\phi$ the angle between the sample surface and the Bragg planes, $\lambda$ the x-ray wavelength, $\theta_B$ the Bragg angle and $\Delta\theta$ the thickness fringe period in radians.

The measurement of thickness fringe spacing in order to extract layer thicknesses has been used before by several workers, in both symmetric[6,7,8,9] and asymmetric[10] scattering geometries. For single layer systems it is sufficient to measure by hand the thickness fringe period and convert this directly to a layer thickness by use of equation (5.1). The situation is complicated somewhat by the presence of more than one layer as the superposition of frequencies occurs. Tanner and Halliwell[11] have reported an observed fringe spacing in rocking curves of double layer heterostructures which appears to deviate from the true thickness fringe period in particular cases, an effect attributed by Miles[12] to complex interference effects arising in each layer.

## 5.3 Fourier Analysis

If a data set contains one or more harmonic components then the application of a Fourier Transform (FT) to the data yields a function with maxima corresponding to each frequency present in the original function. The size of the peak in the FT for a given frequency depends upon the amplitude of oscillation in the initial data. It is important therefore that the amplitudes of the harmonic elements in the data set are made as relatively large as possible. This may involve using the logarithm of the data or employing some other method to artificially increase the amplitude of periodic components. The presence of a constant background level, in addition to reducing the relative size of the oscillations, will be interpreted by the FT as

existence of a very long period oscillation leading to a low frequency peak in the final transform. Any d.c. level should thus be subtracted from the data particularly if this level is high.

The resolution of the FT is dependent upon the number and step size of the data points. If high frequency components are to be sampled then a small step size is necessary in the original rocking curve. Should the sampling size be too large then aliasing may occur, where a frequency lower than that which actually exists will be recorded. The range of the FT x-axis is inversely proportional to the rocking curve step size. Since the number of points in the initial data set is equal to the number of points in the FT, collection of data over a large range will lead to a small step size in the FT and hence more accurate determination of frequency (and layer thickness).

### 5.4.1 Application To Rocking Curve Analysis

Double axis diffraction experiments on interferometer structures yield profiles with thickness fringes containing, in principle, information upon each individual layer thickness. The previous discussion would suggest that Fourier transformation of the rocking curve data would give the frequency spectrum, which could then be converted (using equation (5.1)) to corresponding layer thicknesses. Attempts have been made to Fourier transform diffraction data[13], but with only limited success. The work of Miles[12] was motivated by the desire to reduce the number of variables when simulating experimental data. The aim of this study is to investigate whether or not the use of Fourier analysis can be used within a production line environment for the rapid measurement of layer thicknesses in HEMT structures, without the need for the use of a lengthy simulation program. While the accuracy with which layer thicknesses can be determined will be inferior to that obtained by matching experimental and simulated profiles, the speed of analysis and ease of use (allowing use by semi-skilled operators) will still be of great value in a large scale production context.

### 5.4.2 H.E.M.T. Structures

In the late 1960's it became apparent to device technologists that one way to increase transistor speed was to move away from silicon and choose a different material with more favourable characteristics and band structure parameters. Such a material is gallium arsenide (GaAs) which, like silicon, is a semiconductor. However, the effective mass of electrons in GaAs is about five times smaller than in the case of silicon. Since the electron mobility is inversely proportional to the effective mass, the smaller effective mass of the electrons in GaAs offered an opportunity to increase significantly the transistor switching speed.

The electron flow in GaAs devices is reduced by effects such as lattice vibrations (which are suppressed at low temperatures) and impurity scattering. Since dopants supply carriers which are an integral part of semiconductor device performance their presence in the material is essential. In High Electron Mobility Transistors (HEMT's) modulation doping is used to separate electron current in the active channel from the region where the dopant impurities are located. This leads to suppression of impurity scattering events with the net result of fewer electron collisions and enhanced electron flow. In practice this is achieved by employing heterojunctions that confine carriers on the side of the interface with deeper energy levels. The dopant impurity atoms are located on the other side of the heterojunction.

Large scale production of HEMT structures now comprises a significant fraction of many industrial companies compound semiconductor wafer fabrication output. Device performance is affected by the quality, thickness and composition of the epitaxial layers which comprise the HEMT structure. Methods of characterising HEMT devices which will yield rapidly and non-destructively information upon any of these parameters are thus of obvious benefit. Industrially, stand alone, highly automated double crystal diffractometers are used to characterise these structures. Layer compositions are easily deduced from peak splittings as is crystal perfection from measurement of peak widths. Since these devices also act as Bragg case interferometers, then thickness fringes will appear in the diffraction profile. Providing that the visibility and amplitude of the interference fringes is sufficiently high then Fourier transform analysis will extract the frequency (and hence layer thickness) information from the rocking curve.

For the Fourier transform technique to achieve success a compromise must be found between the two competing factors of length of data collection time and quality of rocking curve data. From his work Miles[12] suggested a set of optimum conditions from which the best Fourier transforms could be obtained.

## 5.5 Optimum Conditions for Fourier Analysis

By applying a Fast Fourier Transform (FFT) algorithm to simulated rocking curve data, Miles[12] reached the following conclusions;

(i) The longer the angular range over which the data is taken, for a given number of steps, the sharper the peaks from the FFT and hence the more precise determination of layer thickness.

(ii) The step size is not an important factor until it becomes larger than about one quarter of the smallest fringe period. Even when it exceeds this , accurate results can still be obtained if a large range is used. Hence the step size should be made as large as possible (within this constraint) in order to maximise counting time.

(iii) The maximum possible range within the limits of the Signal to Noise (S/N) ratio should be used. Table 5.1 shows recommended ranges and step sizes for various S/N ratios.

| S/N | Range(") | Step Size(") |
|---|---|---|
| $\leq 10^3$ | Not adequate for Fourier analysis | |
| $5\times10^3$ | 1000 | 4 |
| $10^4$ | 2000 | 8 |
| $5\times10^4$ | 4000 | 8 |
| $\geq 10^5$ | 4000+ | 8+ |

Table 5.1 (After Miles)[12]

Rocking curves shown in this chapter have a step size of 9 to 10 arc seconds with data being collected over a region of around 4000". The corresponding unit step in the FT is 40Å to 45Å and this represents the accuracy with which layer thicknesses can be determined.

## 5.6 Experimental Requirements

All experimental data from the (001) oriented HEMT structures studied were collected on a prototype Bede 150 Double Crystal Diffractometer in the non-dispersive setting. A thick (001) piece of GaAs was used as the reference crystal and rocking curve data taken from the symmetric (004) sample reflection using $CuK\alpha_1$ radiation. The $CuK\alpha_2$ component was removed with a slit placed between the reference and sample crystals.

Fig. 5.1 shows a typical experimental rocking curve from a HEMT structure (sample 3-0275c) together with a "best fit" simulation (note that the simulated profile has been shifted upwards for clarity). It can be seen that the typical experimental intensity in the region of the thickness fringes is of the order of 20 counts per second, with the amplitude of the fringes considerably smaller than this. The importance of minimising the background countrate is thus obvious. The recorded background can be reduced by minimising two factors:

a) The use of a detector with a small "dark" current and the ability to "window" out pulses of the desired size via the use of discriminating electronics.

b) Using shielding slits to eliminate some of the diffuse scatter from the sample itself. Diffuse scatter will be particularly large if a direct path exists between the slit used to eliminate the $K\alpha_2$ component and the large, open face of the detector.

Fig 5.2 shows the effect of implementing these two methods. Curve (a) shows the data recorded with a "standard" detector (background $\approx$ 5 counts per second) and no shielding slits. The use of a Bede E.D.R. Detector (background $\approx$ 0.15 counts per second) noticeably reduces the background level to around 3 c.p.s.. As this detector has such a low intrinsic background then the background level present can

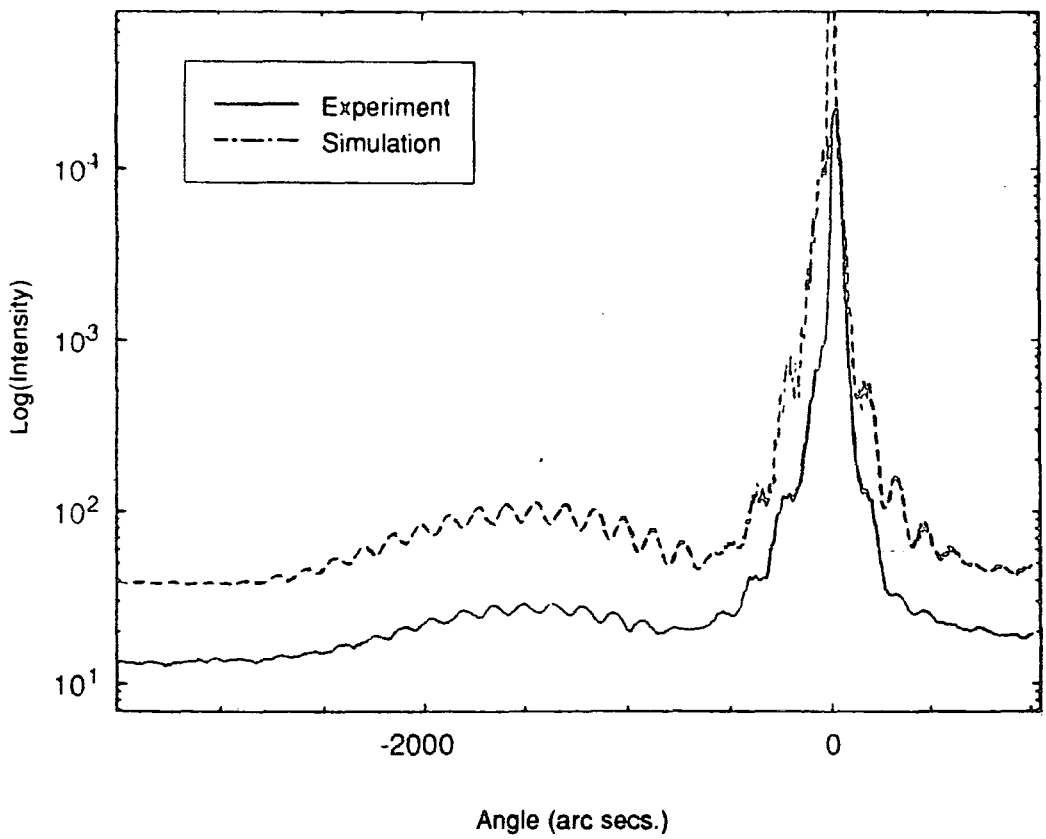


Figure 5.1 : Rocking curve of sample 3-0275c and its best fit simulation (the simulated curve is shifted for clarity). Note the low intensity of the thickness fringes.

Sample structure : GaAs Sub./150Å $In_{0.1}Ga_{0.9}As$/500Å $Al_{0.22}Ga_{0.78}As$/740Å GaAs

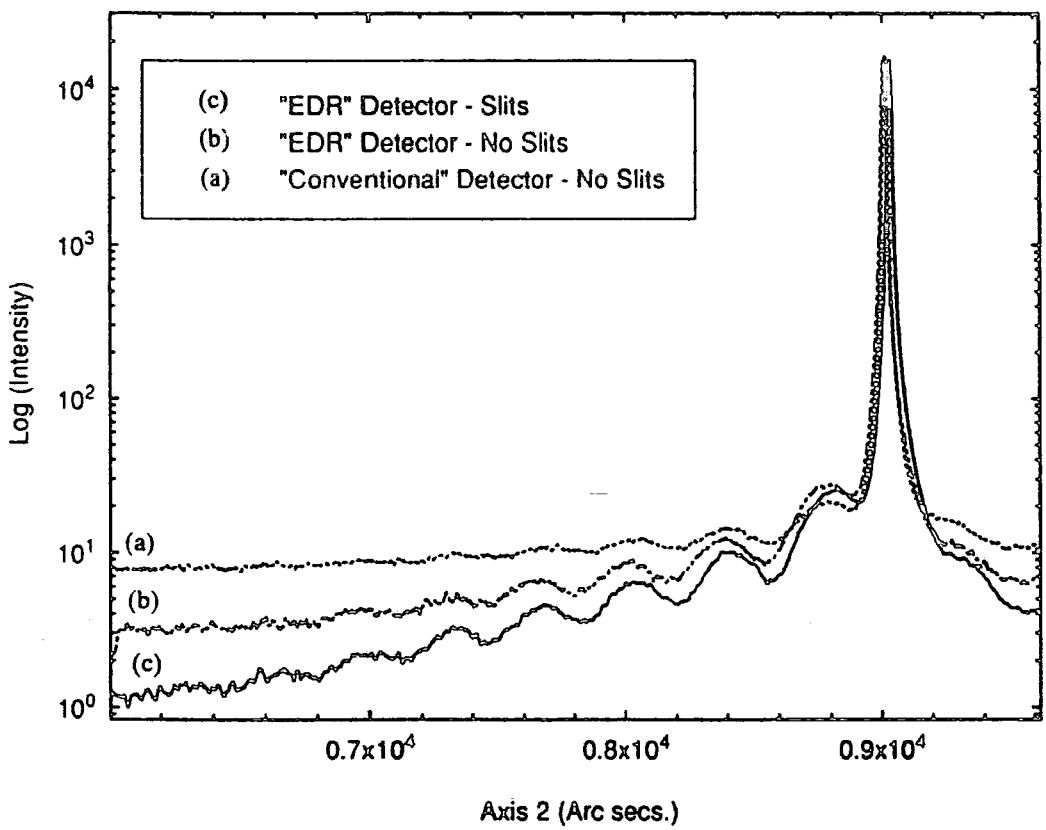


Figure 5.2 : A pHEMT rocking curve recorded with (a) conventional detector, no shielding slits, (b) low background EDR detector, no shielding slits, (c) EDR detector and shielding slits.

be virtually completely attributed to diffuse scatter from the sample. This diffuse scatter can be stopped from reaching the large open face of the detector by the introduction of shielding slits. In practice, slitting out of the scattered radiation is done by placing a set of slits directly onto the detector face. The sample is then rocked until it is on the substrate peak and the slits brought in to the size of the diffracted beam. Since the Bede 150 has no motorised detector axis and a $\theta$-$2\theta$ scan is not possible, then allowance must be left on the low scattering angle side of the slits. This is because the thickness fringes are recorded over a range of over 1° on the low angle side of the substrate peak, and allowance must be made in the slit setting for a change of over 2° in the $2\theta$ angle.

Curve (c) in fig.5.2 shows the effect of introducing shielding slits in conjunction with the Bede E.D.R. Detector. The background level is reduced to just over 1 c.p.s. and the fringe visibility is markedly improved. This experimental configuration has been used for all HEMT rocking curves recorded.

For the samples investigated two different count times were used. Initially long count times of 60 secs. per point (corresponding to scans of around 7 hours) were employed, in order to maximise visibility of the Pendellösung fringes. This length of scan, however, is not appropriate to the industrial situation so a second rocking curve was taken with a count time of 10 secs. per point. This shorter counting interval gives a total scan time of just over one hour which is tolerable by industrial standards.

## 5.7 The FFT Program

The Fourier transformation of the rocking curve data was performed using the Fast Fourier Transform (FFT) algorithm, as first developed by Cooley and Tukey[14], available in the Cambridge Controls PC software package MATLAB. When using this transform it is advantageous to analyse data sets with the number of points equal to a power of two. If this is not the case, then the data set is padded with zeroes until this condition is satisfied and a slight loss in definition of the peaks in the FFT occurs.

A program (see Appendix A) containing routines written in both Pascal and MATLAB formats has been developed which analyses and manipulates the original rocking curve data as follows:

i) The rocking curve (i.e. the raw data as recorded by the Bede Double Crystal Control Software) is loaded into the program. The "header" of the file is stripped away leaving only the raw data in a format recognised by MATLAB.

ii) A Savitsky-Golay smooth is applied in order to enhance the visibility of the thickness fringes.

iii) The user is then given the option to either "window" out a particular part of the data or accept the full angular range.

Once the data has been processed to this stage it is then necessary to address the problem of the small relative size of the interference fringes. As previously stated, the amplitude of peaks in the frequency (or thickness spectrum) depends upon the amplitude of the corresponding oscillation in the initial data. In a typical HEMT rocking curve the interference fringes are some three orders of magnitude less intense than the substrate peak. Some means of increasing the relative size of the fringes must then be employed. Two different techniques have been employed, one of which is simply to take the logarithm of the data before applying the FFT. Another approach is to "normalise" the data by fitting a background envelope and dividing the data by this function. When running the FFT routine, after smoothing and windowing the data, the user must choose whether to simply take the logarithm of the intensity or apply the "normalise" routine. If the log-only method is selected than the routine will take the logarithm of the intensity, subtract any background "d.c." level, FFT the data and then transform from the frequency to a thickness regime using eqn 5.1. If the "normalise" method is employed then the program flow will be (following on from step iii) above;

iv) A "peakfind" routine is applied to identify all peaks present.

v) A cubic spline is fitted to the peak positions, so that a background envelope is obtained.

vi) The rocking curve data is normalised by dividing it by this "spline formed" curve.

vii) The background level is subtracted, an FFT applied and the result scaled to convert to absolute thickness.

The above manipulation and processing of the initial rocking curve data takes around one minute to process on an IBM compatible computer with 486 processor, inclusive of user input time.

## 5.8 Problem Of Incorporation Of The Substrate Peak

One of the most detrimental factors affecting the quality of the final FFT is the presence of the substrate peak. Fig.5.3 shows the effect of Fourier transforming rocking curve 3-0782e.x02 using the log only method with the full data set being transformed (the structure and scan details for this sample are listed in Tables 5.2 and 5.3 respectively). No distinct peak is observed in the FFT. Fig 5.4 shows the result when the region around the InGaAs layer peak only is windowed out and then transformed. In this case a definite peak in the FFT is observed. Clearly the inclusion of the substrate peak in the data analysed wipes out the information content of the final FFT. Note also that, in both fig.5.3 and fig.5.4, a large Fourier ampitude is obtained near the abscissa (i.e., in the very small thickness regime). In cases where no strong periodic component is detected by the transformation, the FFT is dominated by the repeat period corresponding to the entire width of the data set (which is repeated infinitely in the Fourier transformation). This repeat period (which is large in angle) shows up as a low frequency, and hence low thickness, peak in the FFT. For this reason, the measurement of very thin layer thicknesses is difficult using FFT methods, as the "genuine" peak from the thin layer and that produced as an artefact of the FFT process, will be difficult to resolve in the low thickness regime of the FFT plot.

Even when applying the "normalise" routine, incorporation of the region which contained the substrate peak has a disastrous effect upon the FFT (Figs. 5.5 and 5.6). Although the FFT in fig.5.5(iii) does show a peak at around 800Å, the visibilty of this peak is poor. However, the FFT in fig.5.6(iii), where the substrate

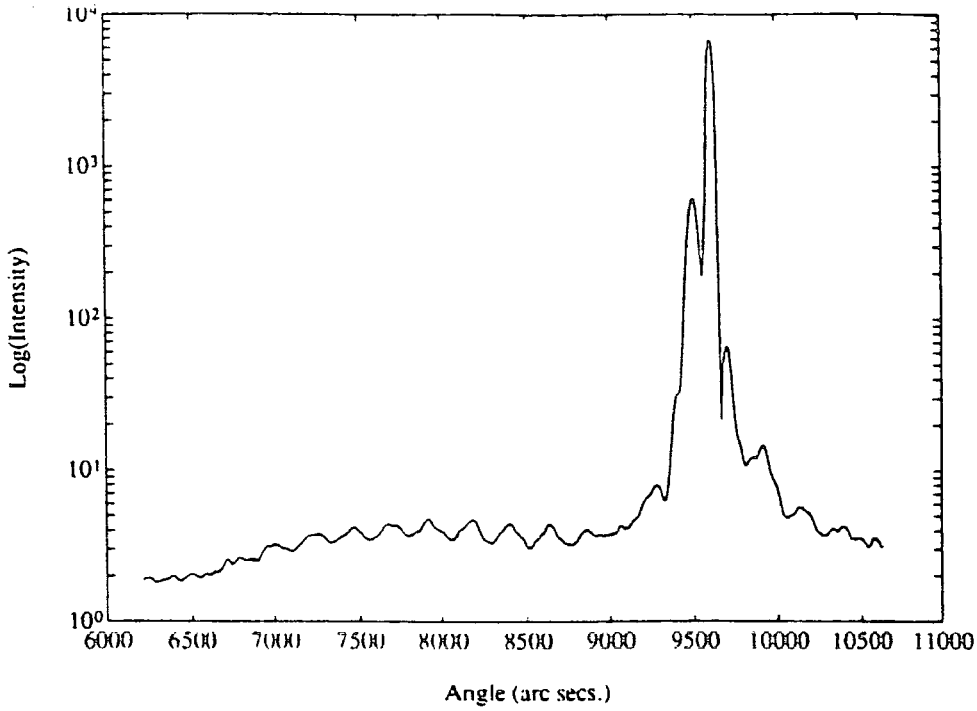


(i) Section of data selected (full data set)

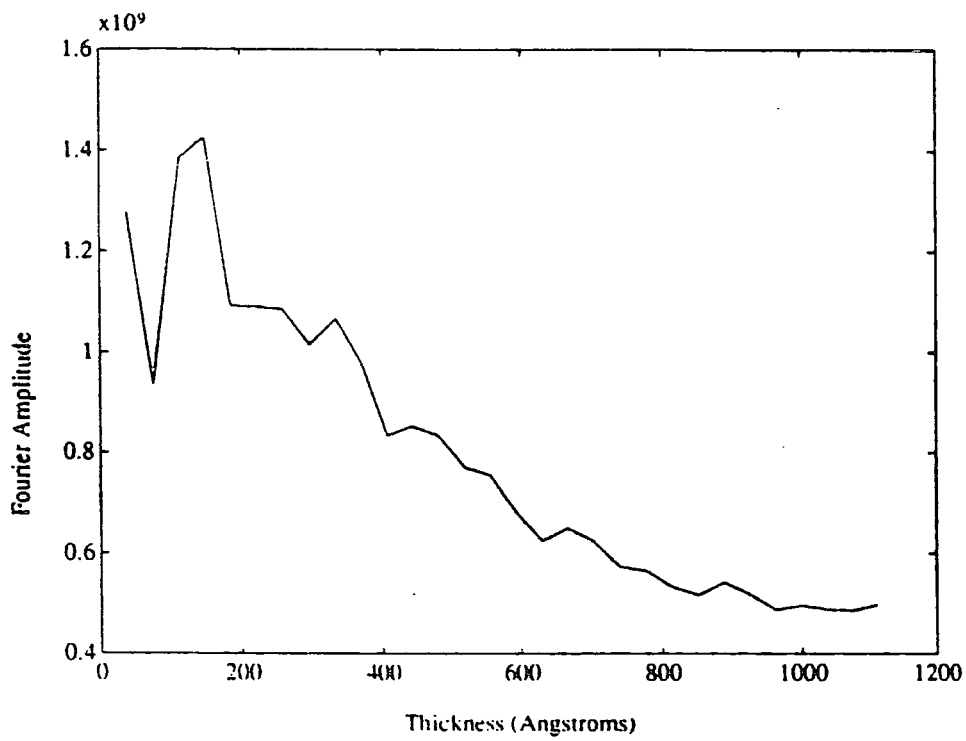


(ii) FFT of data selected

Figure 5.3 : FFT of rocking curve 3-0782e.x02 (Log-only method, full data set)

Sample structure : GaAs Sub./2000Å $Al_{0.2}Ga_{0.8}As$/20Å GaAs/75Å $In_{0.17}Ga_{0.83}As$/470Å $Al_{0.25}Ga_{0.75}As$/305Å GaAs

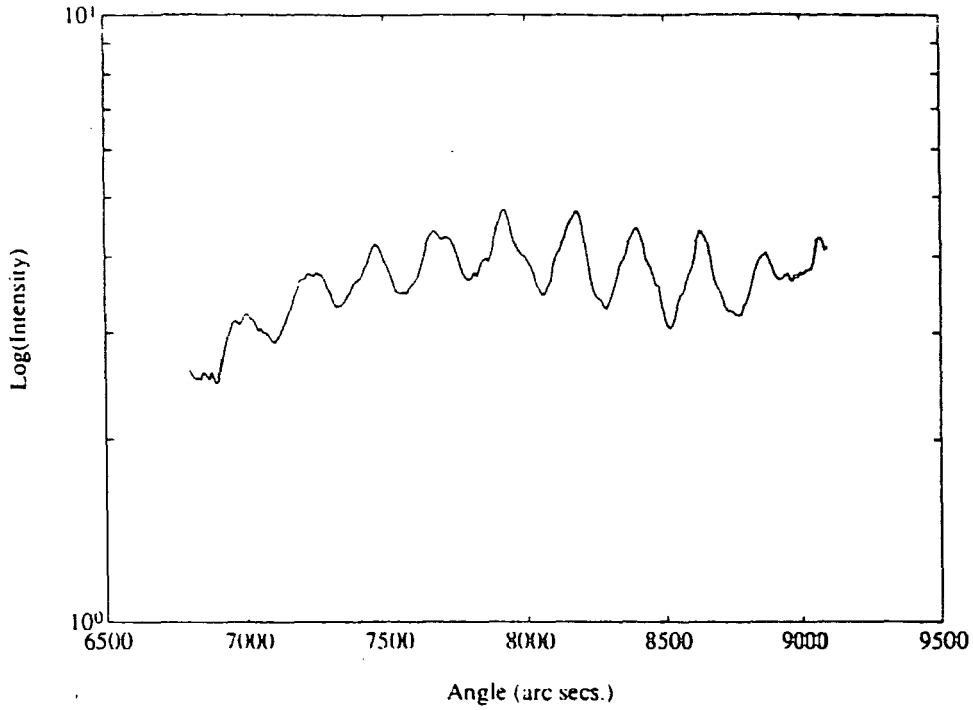


(i) Section of data selected (layer peak only)

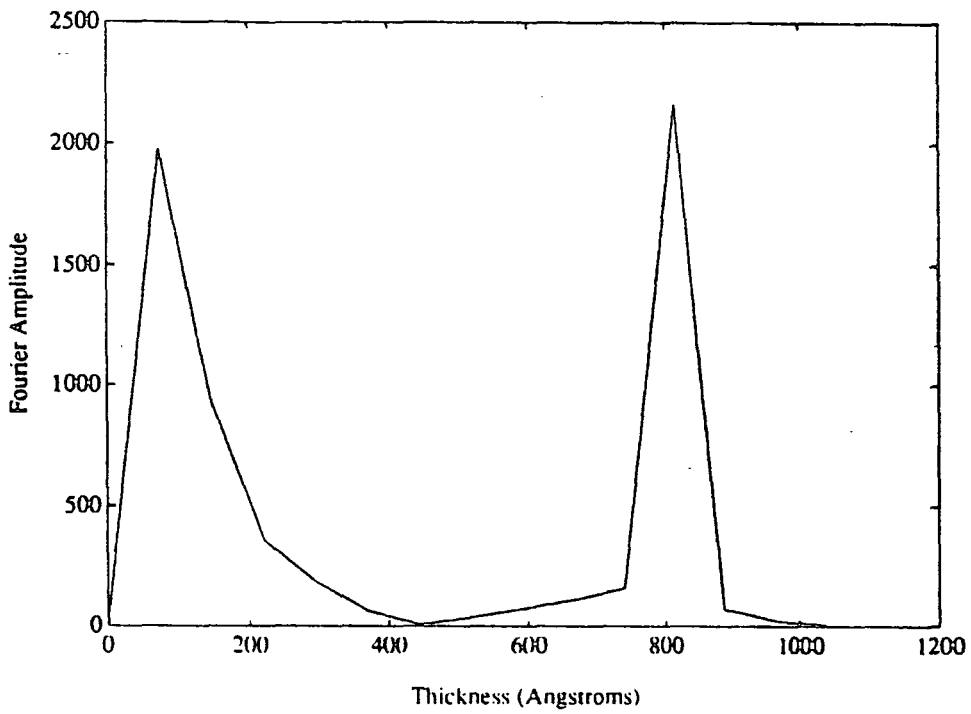


(ii) FFT of data selected

Figure 5.4 : FFT of rocking curve 3-0782e.x02 (Log-only method, windowed data)

Sample structure : GaAs Sub./2000Å $Al_{0.2}Ga_{0.8}As$/20Å GaAs/75Å $In_{0.17}Ga_{0.83}As$/470Å $Al_{0.25}Ga_{0.75}As$/305Å GaAs

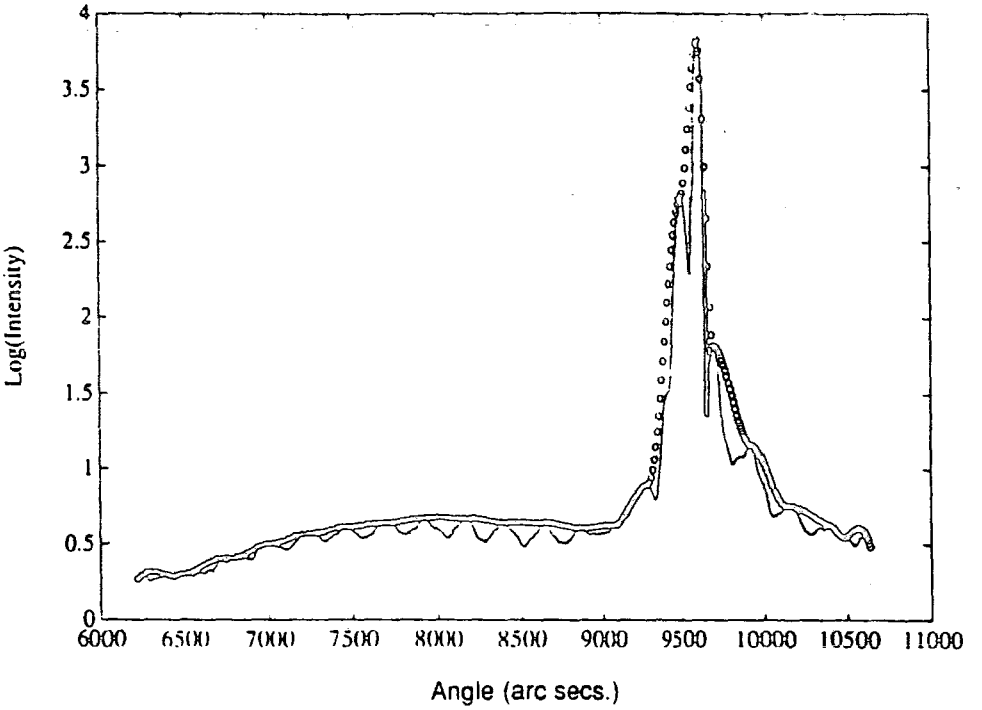


(i) Cubic spline fit to detected peaks

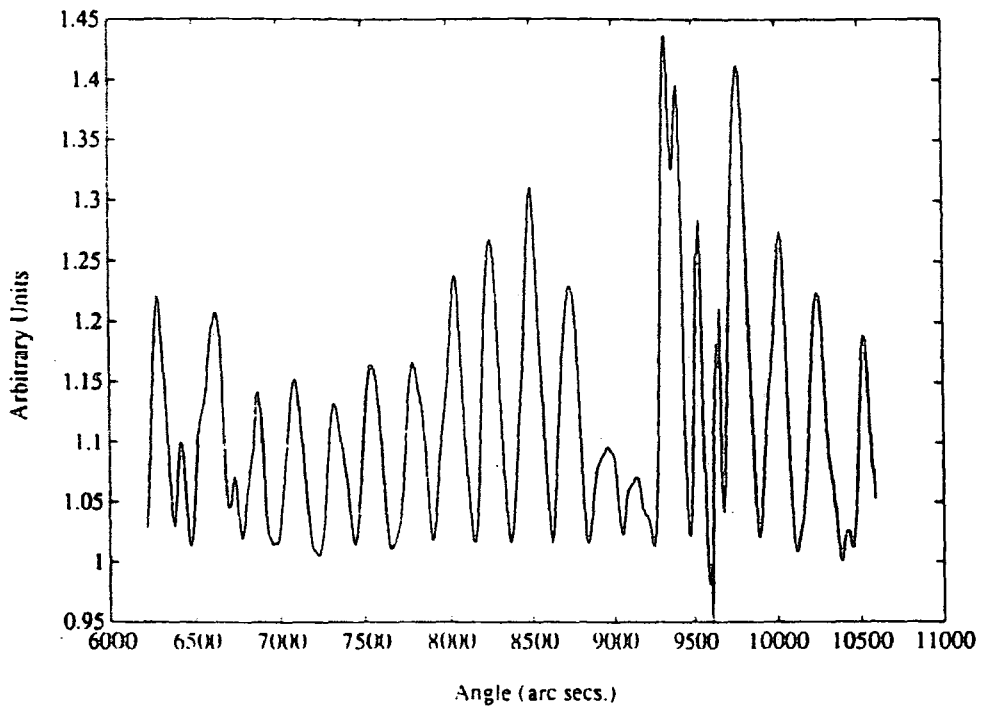


(ii) Normalised data

Figure 5.5 : FFT of rocking curve 3-0782e.x02 (Normalise method, full data set)
Sample structure : GaAs Sub./2000Å $Al_{0.2}Ga_{0.8}As$/20Å GaAs/75Å $In_{0.17}Ga_{0.83}As$/470Å $Al_{0.25}Ga_{0.75}As$/305Å GaAs

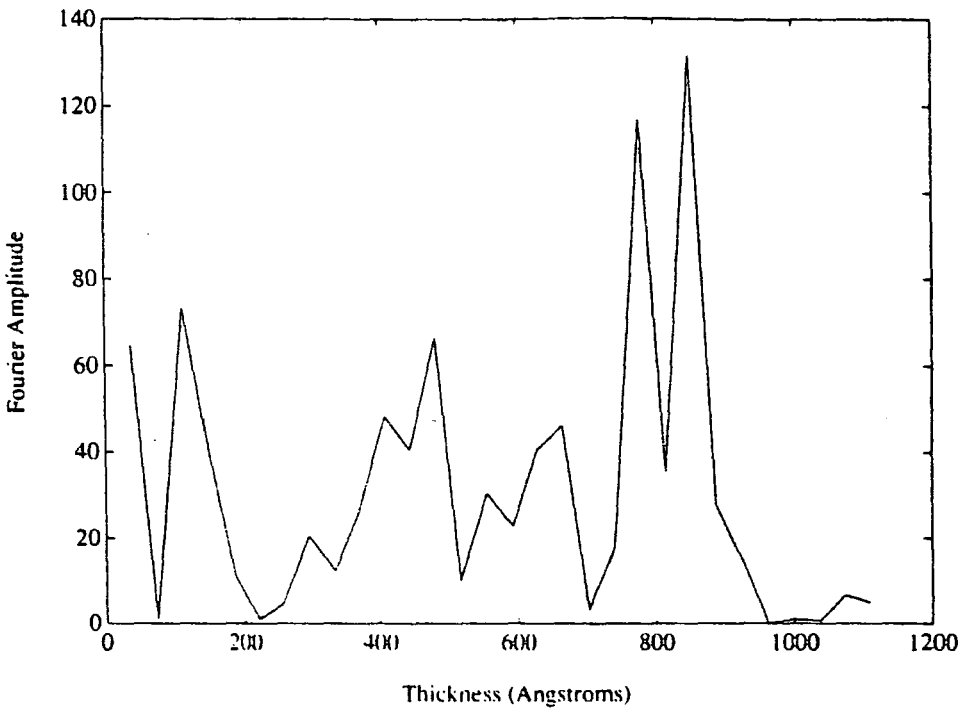


**(iii) FFT of normalised data**

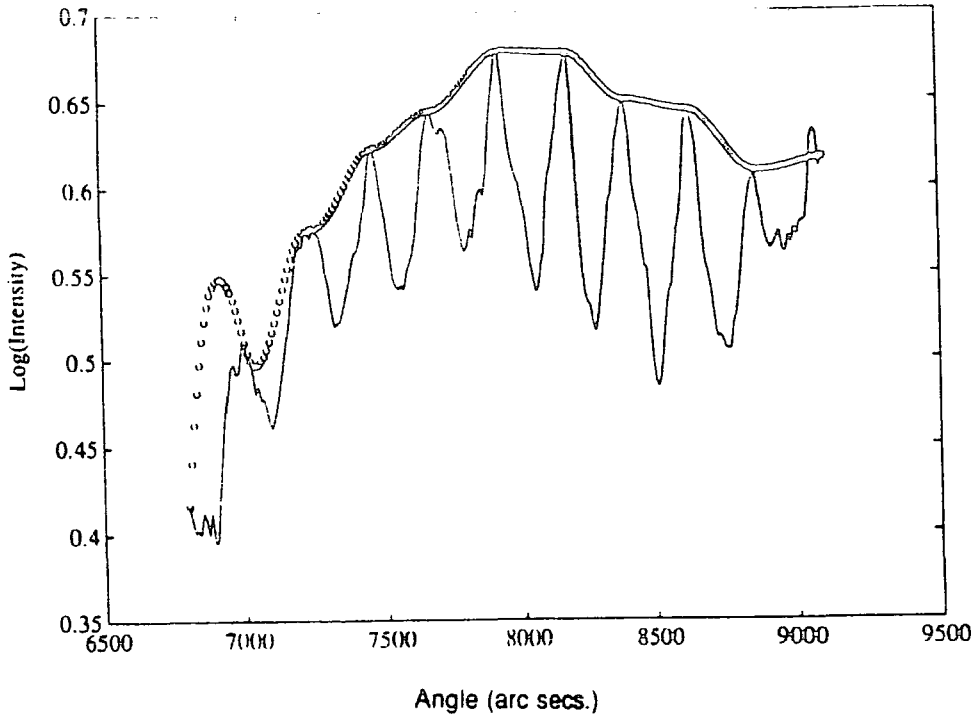


(i) Cubic spline fit to detected peaks

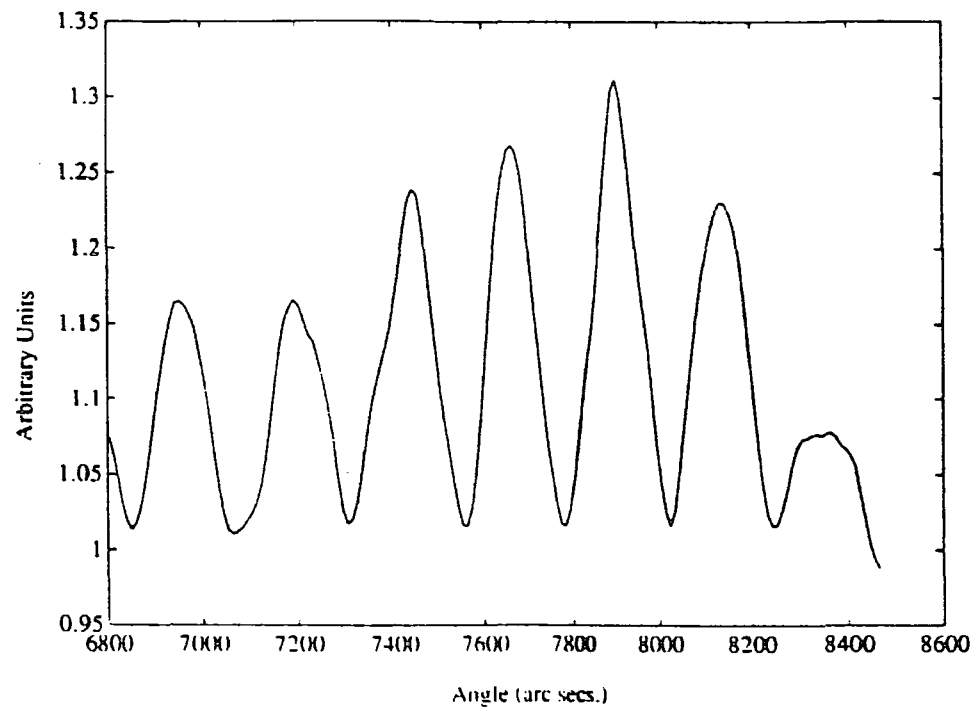


(ii) Windowed, normalised data

Figure 5.6 : FFT of rocking curve 3-0782e.x02 (Normalise method, windowed data)

Sample structure : GaAs Sub./2000Å $Al_{0.2}Ga_{0.8}As$/20Å GaAs/75Å $In_{0.17}Ga_{0.83}As$/470Å $Al_{0.25}Ga_{0.75}As$/305Å GaAs

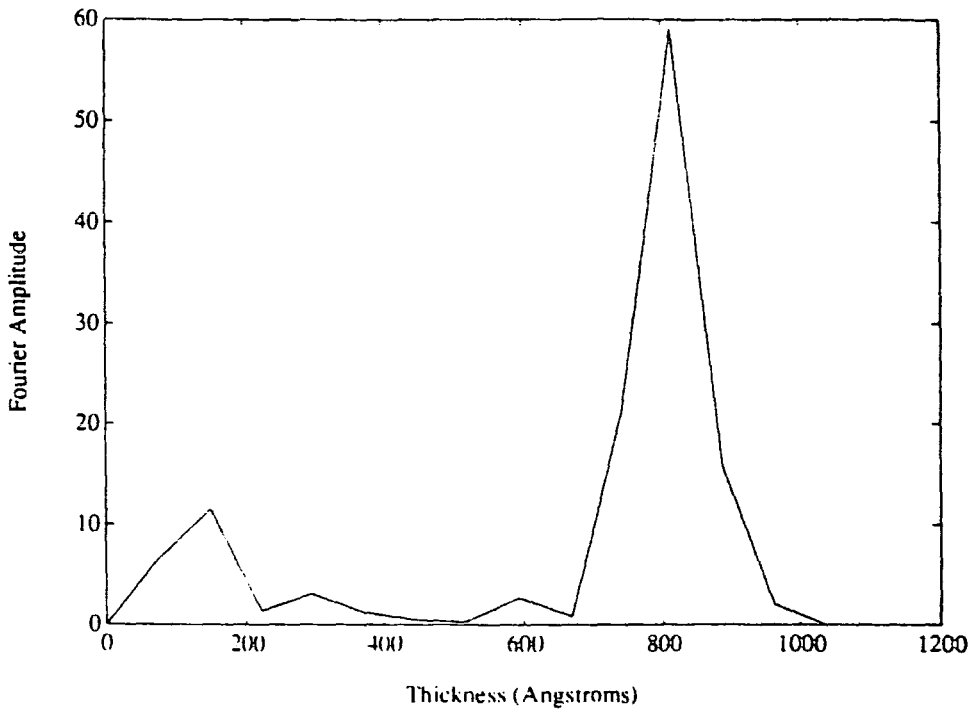


(iii) FFT of windowed, normalised data

has been discarded from the input data set, exhibits a much more pronounced peak.

In principle, the "normalisation" technique should eliminate problems caused by the relatively large size of the substrate peak. However, the presence of small fringes midway up the substrate peak can lead to sharp spikes in the normalised data (these spikes arise from the troughs of these fringes). Also the spline fit does not follow the substrate peak profile closely within this region (this is not surprising as the step size in the spline fit is large compared to the peak width). This leads to a relatively large discrepancy between the intensity values of the initial data and the spline formed "average" curve for a particular angular setting within the region covered by the substrate peak. Thus, division of one curve by the other does not give a normalised amplitude of around 1.0 (as for the rest of the data set) but instead yields a value greater than this. Further, the use of a Savitsky-Golay smooth can often give spikes in the smoothed diffraction profile in the region of the substrate peak, where the intensity drops rapidly down to zero before rising sharply again. These spikes will introduce high frequency components into the FFT further degrading the final quality of the Fourier transform.

To overcome this problem it is necessary to window out the substrate peak from the data to be analysed. This can be achieved either by "windowing" out the region corresponding to the InGaAs layer peak only or by "cutting" out the substrate peak from the data and "stitching" together the two residual pieces. For simplicity the first method is employed in the FFT analysis program with the user being prompted for minimum and maximum values with which to define an angular window. All data points outside of this window are then rejected. This will result in a slight loss of definition in the Fourier transform as the number of data points is now not likely to be to an exact power of two. However, the improvements associated with "windowing" out data from outside of the layer peak are such that this form of manipulation still results in a significantly improved final FFT.

## 5.9 Results Of FFT Analysing HEMT Rocking Curves

A series of MOCVD grown HEMT structures, deposited on (001) oriented GaAs substrates by Epitaxial Products International Ltd. of Cardiff, were examined on the Bede 150 diffractometer at Durham University. The samples consisted of

(working up from the substrate) a thin $In_xGa_{1-x}As$ layer, followed by a thin $Al_xGa_{1-x}As$ layer, capped with GaAs. Two of the samples had $Al_xGa_{1-x}As$ and GaAs layers deposited prior to growth of the $In_xGa_{1-x}As$ layer. Following recording of symmetric (004) rocking curves the sample structures were determined by matching experimental profiles to simulated data using the Bede RADS simulation software. Table 5.2 shows the sample names together with the sample structure (layer thicknesses and composition) used in the best fit simulation.

| Sample | GaAs(Cap) Å | AlGaAs Å (% Al) | InGaAs Å (% In) | GaAs Å | AlGaAs Å (% Al) |
|---|---|---|---|---|---|
| 3-0275c | 740 | 500(22) | 150(10) | | |
| 3-0550e | 415 | 270(22) | 100(13) | | |
| 3-0782e | 305 | 470(25) | 75 (17) | 20 | 2000(20) |
| 3-0960b | 730 | 400 (23) | 103 (29) | 600 | 2000 (23) |
| 3-0964c | 550 | 400 (18) | 180 (13) | | |

Table 5.2 : Structure Of HEMT Samples Analysed

The results of carrying out the FFT analysis on rocking curves of the above specimens and their best fit simulations are shown in Table 5.3. This gives the thicknesses obtained from the FFT routine using the two different normalisation methods. The rocking curve file names, best fit simulations and corresponding scan count times are also listed. Experimental files are distinguished by the extension .x** and simulation files by the extension .g**. The main feature apparent is that both the log-only and normalise techniques give FFT's with detectable peaks at similar positions. As an example, Fig 5.7 shows the rocking curve from sample 3-0964c recorded with a long count time of 60 seconds (file 3-0964c.x03) together with its best fit simulation (file 3-0964c.g13). As well as the highly visible short period present, some long range modulation is also apparent in the diffraction profile. The resulting FFT of the windowed log-only data, shown in Fig 5.8, gives a small but detectable peak at 990Å with a further shoulder at around 1100Å. A similar result is obtained when the FFT analysis is carried out using the normalise method (fig.5.8b(iii)), lthough in this case the visibility of the FFT peaks is slightly greater.

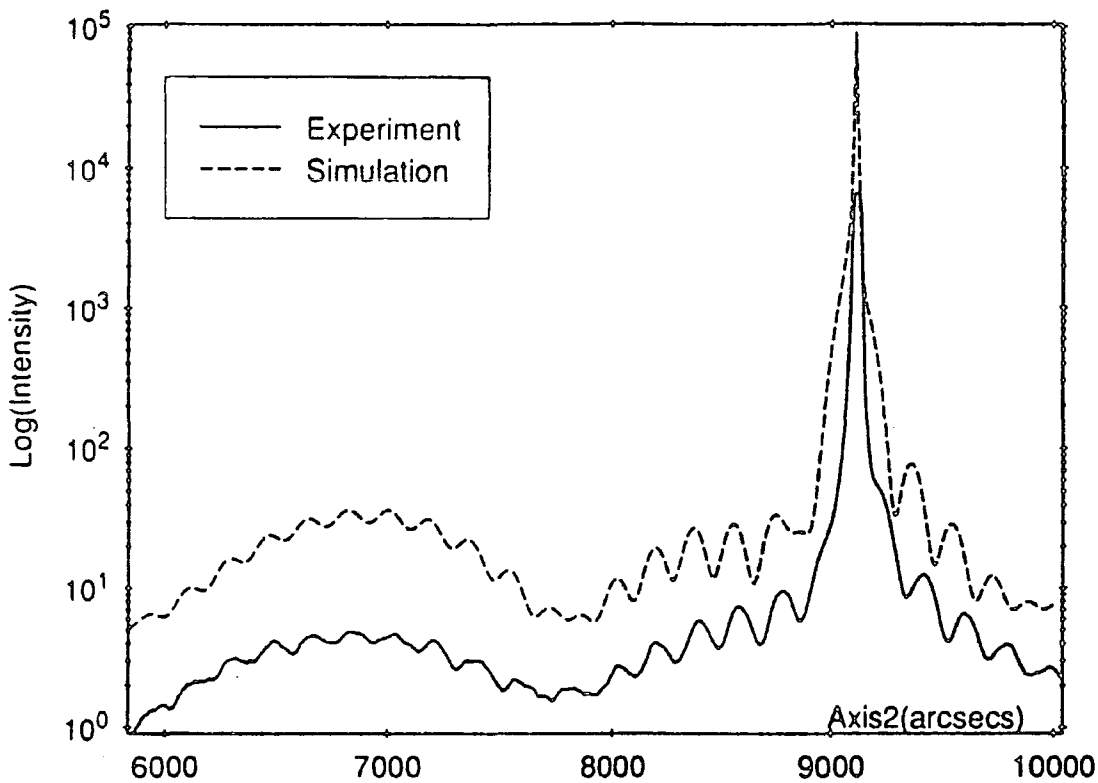


Figure 5.7 : Rocking curve of sample 3-0964c.x03 and its best fit simulation (3-0964c.g13).

Sample structure : GaAs Sub./180Å $In_{0.13}Ga_{0.87}As$/400Å $Al_{0.18}Ga_{0.82}As$/550Å GaAs

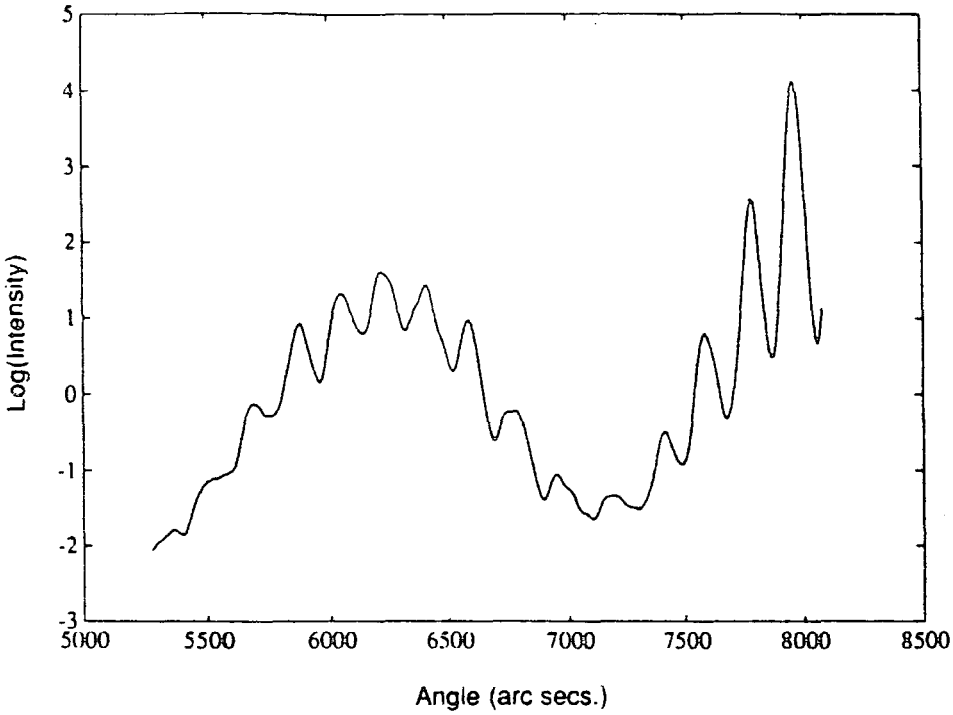


(i) Section of data selected (layer peak only)

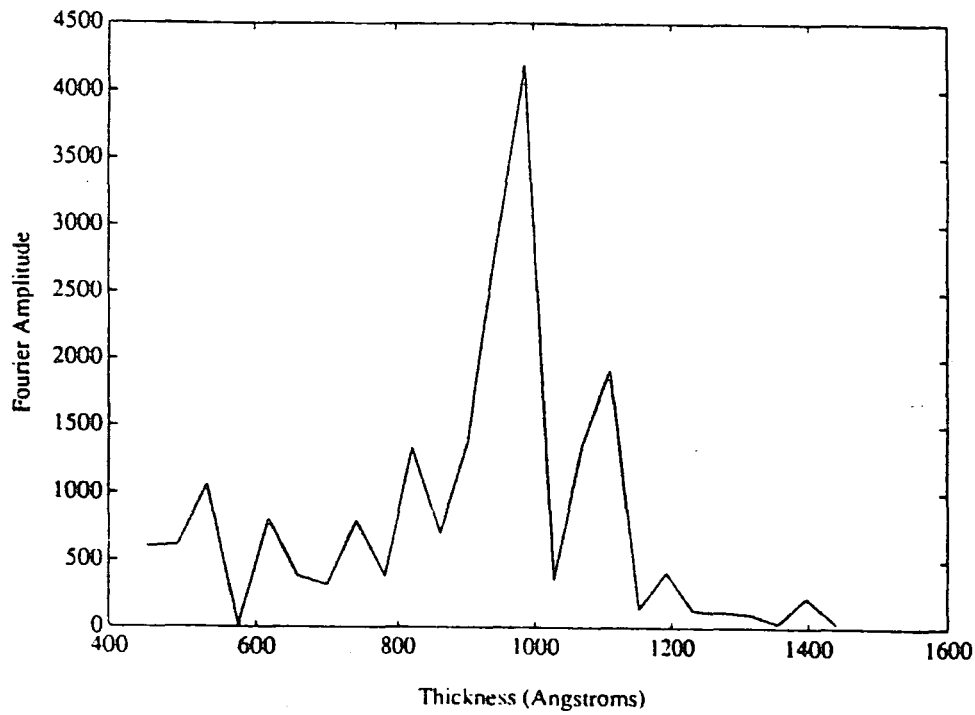


(ii) FFT of data selected

Figure 5.8(a) : FFT of rocking curve 3-0964c.x03 (Log-only method, windowed data)
Sample structure : GaAs Sub./180Å $In_{0.13}Ga_{0.87}As$/400Å $Al_{0.18}Ga_{0.82}As$/550Å GaAs

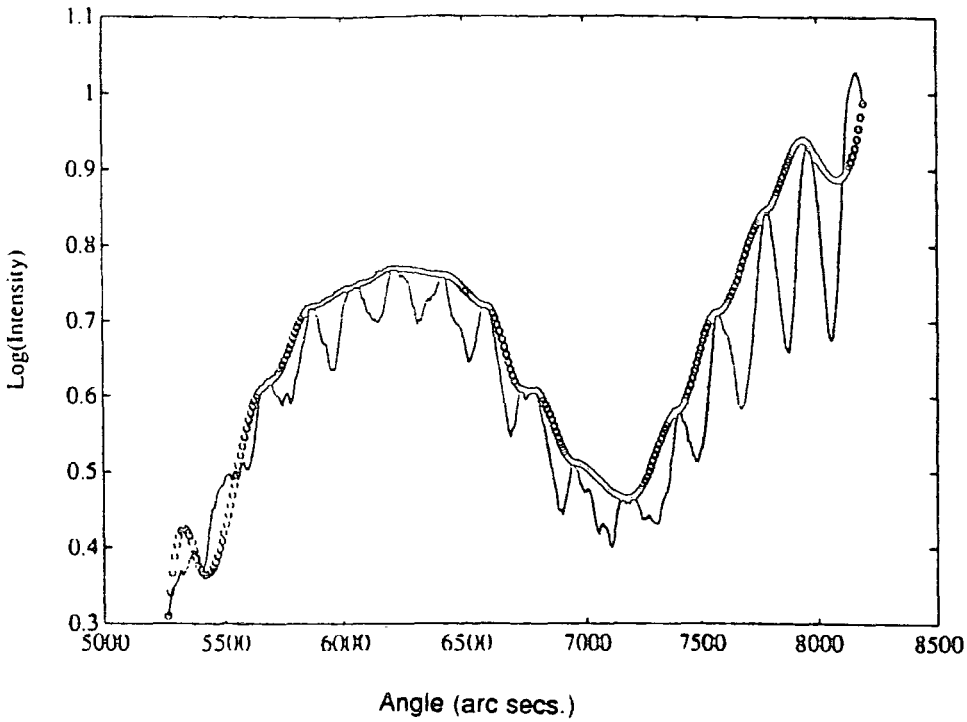


(i) Cubic spline fit to detected peaks

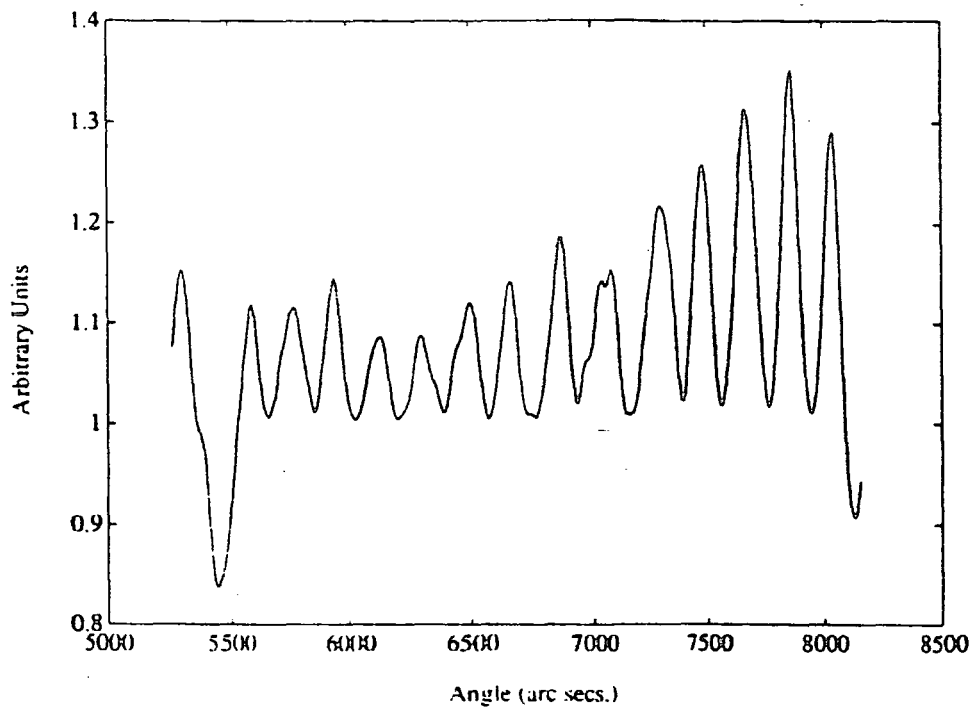


(ii) Windowed, normalised data

Figure 5.8(b) : FFT of rocking curve 3-0964c.x03 (Normalise method, windowed data)
Sample structure : GaAs Sub./180Å $In_{0.13}Ga_{0.87}As$/400Å $Al_{0.18}Ga_{0.82}As$/550Å GaAs

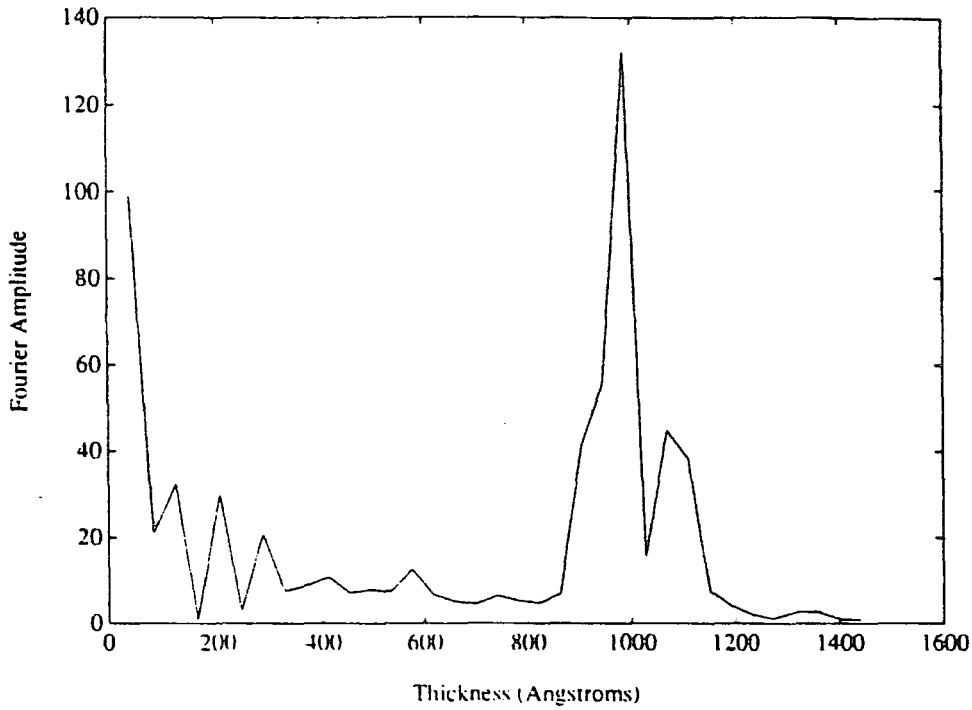


**(iii) FFT of windowed, normalised data**

| File Name | Count (seconds) | Thickness (Measured by FFT) | |
|---|---|---|---|
| | | Log Only (Å) | Normalised (Å) |
| 3-0275c.x17 | 40 | 1250 | 1250 |
| 3-0275c.g01 | N/A | 1340 | 1340 |
| 3-0550e.x01 | 10 | 740 | 740 |
| 3-0550e.x02 | 60 | 740 | 740 |
| 3-0550e.g08 | N/A | 740 | 740 |
| 3-0782e.x01 | 10 | 800 | 810 |
| 3-0782e.x02 | 60 | 810 | 810 |
| 3-0782e.g12 | N/A | 810 | 810 |
| 3-0960b.x04 | 10 | No peak | 1185,1350 |
| 3-0960b.x03 | 60 | 1200,1300 | 1200,1300 |
| 3-0960b.g22 | N/A | 1130,1215 | 1120,1220 |
| 3-0964c.x02 | 4 | 990,1100 | 980,1100 |
| 3-0964c.x01 | 10 | 1000 | 960,1100 |
| 3-0964c.x03 | 60 | 990,1100 | 990,1100 |
| 3-0964c.g13 | N/A | 1000,1100 | 1000,1100 |

Table 5.3 : Rocking Curves of HEMT Samples With Layer Thicknesses As Detected By FFT Routine (Experimental Scans Have File Extensions Of The Form .x** And Simulated Profiles Have File Extensions Of The Form .g**).

However, for the majority of data analysed a particular feature is that, despite having a minimum of three epitaxial layers each with its own thickness fringe frequency, only one peak is present in the FFT. The presence of only one peak in the FFT graph arises because of the beating of the individual fringe frequencies and the limited angular range over which fringes can be recorded experimentally. The main fringe period present corresponds to an "average" thickness with a low frequency modulation envelope superimposed on top. Since interference fringes can be observed to only around one degree below the substrate peak, where their presence is dominated by the diffracted intensity arising from the layer peak, there is insufficient modulation information for the FFT to detect this long period envelope. This results in the appearance of only one peak in the final FFT. How

the measured thickness corresponds to an average of two composite layers is demonstrated below.

## 5.10 Problem Of Beating Of Two Frequencies.

Inspection of a typical HEMT rocking curve (consisting of at least three layers all of differing thickness) shows that only one thickness fringe period is evident. The fringes themselves arise from interference of waves reflected from each interface within the sample. Since the largest phase change will occur as the beam enters and exits the InGaAs layer, then the two main reflected beams will correspond to waves originating from an "effective" layer thickness of the sum of the layers above the InGaAs layer (layer 1 + layer 2) and the thickness of the total stack (layer 1 + layer 2 + layer 3). The observed Pendellösung fringes will thus be due to the interference of these two waves.

## 5.11 Addition Of Waves Of Differing Frequency

For multiple layer heterostructures the thickness fringes observed will arise from the superposition of several waves originating from layers of different thicknesses (and hence different frequencies). The amplitude and frequency of the resultant wave can be easily derived[15].

Consider two waves described by equations (5.2) and (5.3);

$$E_1 = E_{01}\cos(k_1 x - \omega_1 t) \tag{5.2}$$

$$E_2 = E_{01}\cos(k_2 x - \omega_2 t) \tag{5.3}$$

For simplicity assume that both waves have equal amplitude and zero initial phase angles. The net wave is then given by

$$E = 2E_{01}\cos\frac{1}{2}[(k_1 + k_2)x - (\omega_1 + \omega_2)t]\cos\frac{1}{2}[(k_1 - k_2)x - (\omega_1 - \omega_2)t] \tag{5.4}$$

If we now introduce an *average angular frequency* ($\bar{\omega}$) and *average propagation number* ($\bar{k}$) as defined below, together with a *modulation frequency* ($\omega_m$) and *modulation propagation number* ($k_m$)

$$\begin{aligned} \bar{\omega} &= \frac{1}{2}(\omega_1 + \omega_2) \\ \omega_m &= \frac{1}{2}(\omega_1 - \omega_2) \end{aligned} \tag{5.5}$$

$$\begin{aligned} \bar{k} &= \frac{1}{2}(k_1 + k_2) \\ k_m &= \frac{1}{2}(k_1 - k_2) \end{aligned} \tag{5.6}$$

then the composite disturbance arising from the two waves is

$$E = 2E_{01}\cos(k_m x - \omega_m t)\cos(\bar{k}x - \bar{\omega}t) \tag{5.7}$$

We can regard this composite wave as a travelling wave of frequency $\bar{\omega}$ with a modulated amplitude $E_0(x,t)$ such that

$$E(x,t) = E_0(x,t)\cos(\bar{k}x - \bar{\omega}t) \tag{5.8}$$

where

$$E_0(x,t) = 2E_{01}\cos(k_m x - \omega_m t) \tag{5.9}$$

If we have waves of comparable frequency, i.e.,$\omega_1 \approx \omega_2$ , then $\bar{\omega} \gg \omega_m$ and $E_0(x,t)$ will change slowly, whereas $E(x,t)$ will vary rapidly.

In the case of HEMT structures we are interested in the interference of two waves originating from composite layers differing in thickness by the width of the thin InGaAs layer. The above discussion suggests that we will observe fringes with an average frequency $\bar{\omega} = (\omega_1 + \omega_2)/2$ which is modulated by a wave of small frequency given by $\omega_m = (\omega_1 - \omega_2)/2$.

## 5.12 Problem Of Limited Useful Angular Range

The previous discussion has shown one of the chief problems associated with Fourier transforming rocking curve data from HEMT structures. This is that any thickness revealed corresponds to an average of composite layers and does not give the actual thicknesses of individual layers (or even the total stack thickness only). If experimental data could be collected over a much greater angular range then sufficient information on the modulating frequency could be obtained so as to yield two "correct" thickness values as opposed to one "average" value. This is demonstrated in Figs.5.9 and 5.11 which show the simulated rocking curve profiles for sample 3-0550e over two different angular regions. Region 1 corresponds to scanning over the InGaAs layer peak (Fig.5.9), as is typically done when recording a rocking curve. Inspection by eye shows that only one period is observable with the effects of the modulation envelope being washed out by the presence of the layer peak. This is shown also in the FFT with one peak only being visible upon analysis with the log-only and normalise routines (Fig.5.10(a,b)).

The second region covered, shown in Fig 5.11, corresponds to scanning to the low angle side of the layer peak (between -15000" and -4000", where the substrate peak is situated at around 0"). Without the dominating effect of diffraction from the InGaAs layer, the presence of two frequencies and their associated beating can be clearly seen. Analysis of these simulated profiles by the FFT routine, using both the log-only and normalise methods (Fig 5.12), now gives at least two clearly defined peaks in the thickness regime (at 685Å and 785Å). As expected, these correspond exactly to the composite thickness of the first two layers (415Å+270Å) and the total stack (415Å+270Å+100Å). Interestingly the normalise routine has significantly enhanced the amplitude of the modulation prior to transformation to such an extent that a third peak, corresponding to the InGaAs layer thickness of 100Å, is evident in the FFT (Fig 5.12(b)).

Unfortunately the intensity of the rocking curve in the region shown in Fig.5.11 will be so low that the fringes and their associated beating will be undetectable using conventional laboratory equipment. However, this example does serve to show that although, in theory, FFT analysis is capable of resolving the two different frequencies, the limited angular range over which useful data can be collected often means that a single frequency only is picked up by the FFT.

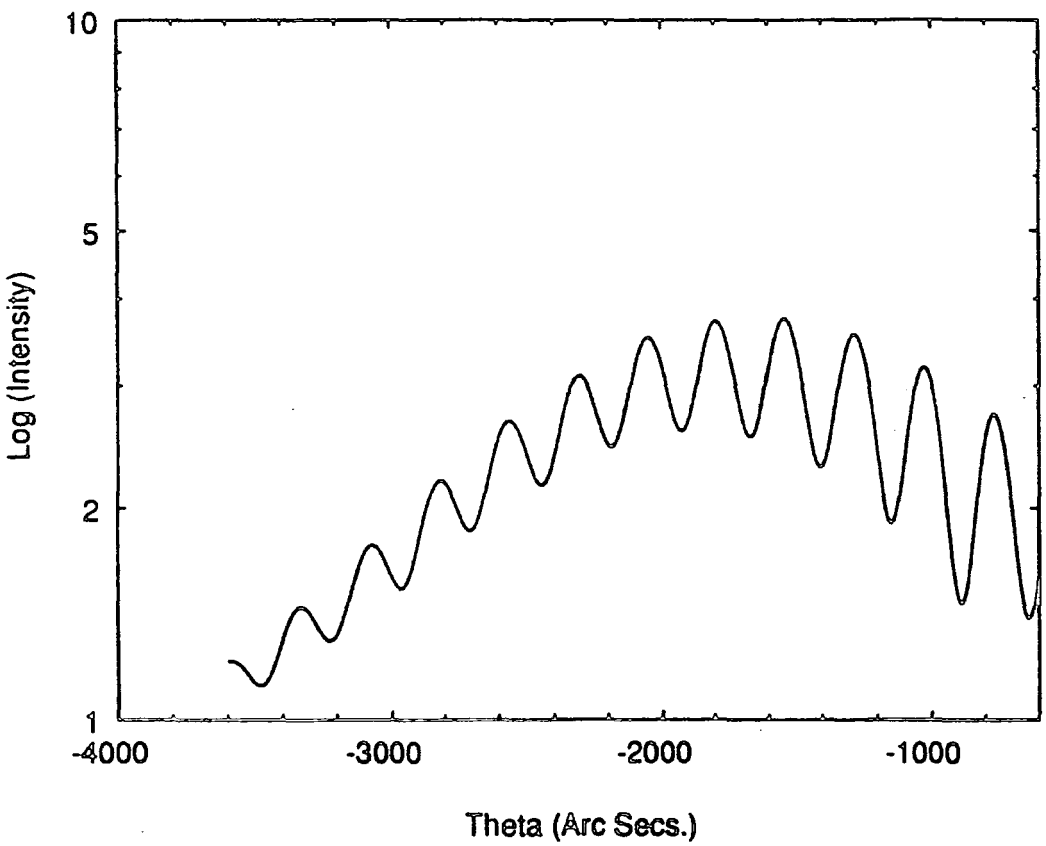


Figure 5.9 : Simulated diffraction profile of sample 3-0550e.
(Region 1 : -4000" to -600")

Sample structure : GaAs Sub./100Å $In_{0.13}Ga_{0.87}As$/270Å $Al_{0.22}Ga_{0.78}As$/415Å GaAs

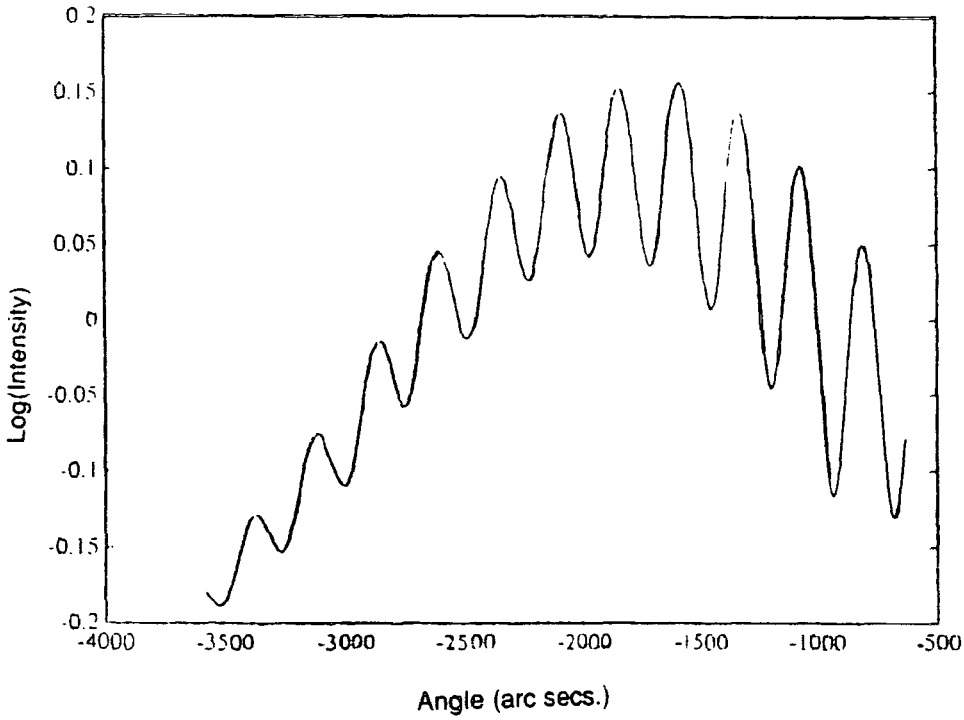


(i) Section of data selected (layer peak only)

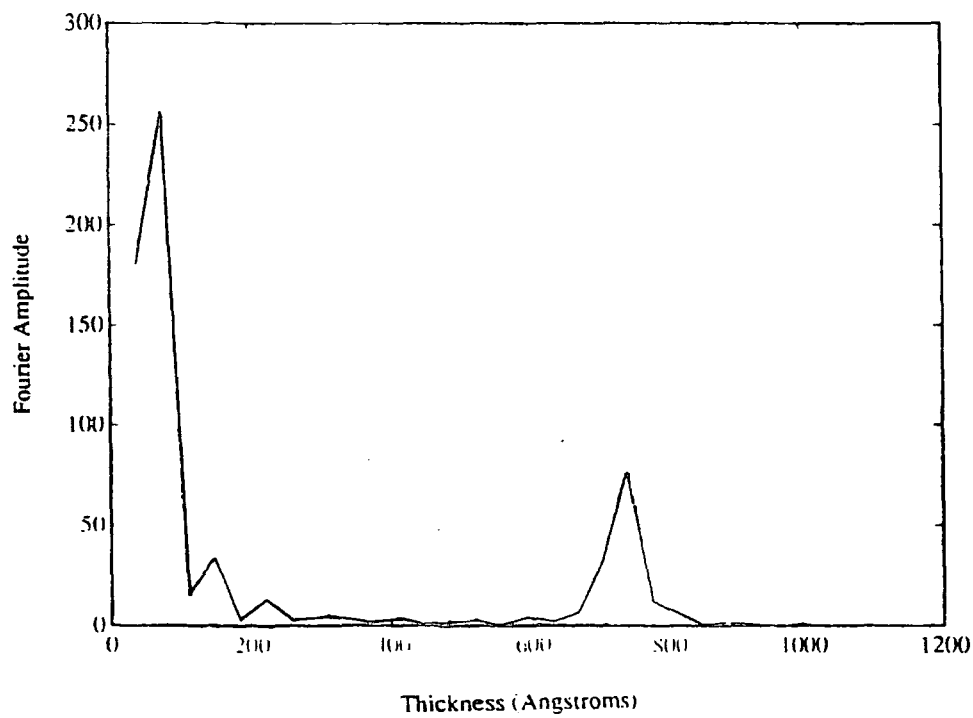


(ii) FFT of data selected

Figure 5.10(a) : FFT analysis of simulated diffraction profile (3-0550e) shown in Figure 5.9 (Log-only method, windowed data).

Sample structure : GaAs Sub./100Å $In_{0.13}Ga_{0.87}As$/270Å $Al_{0.22}Ga_{0.78}As$/415Å GaAs

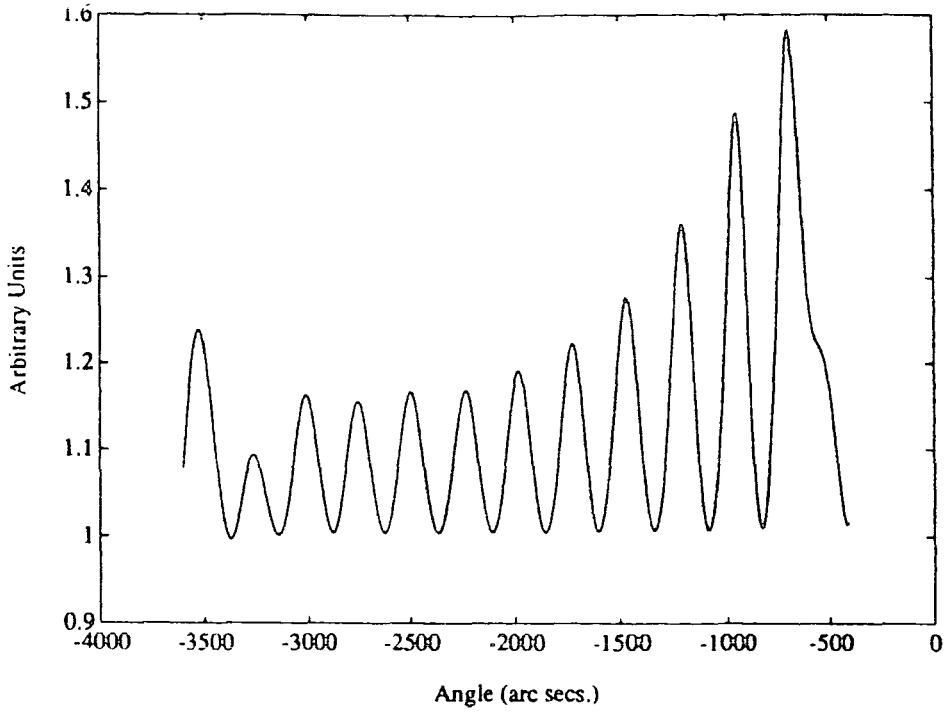


(i) Windowed, normalised data

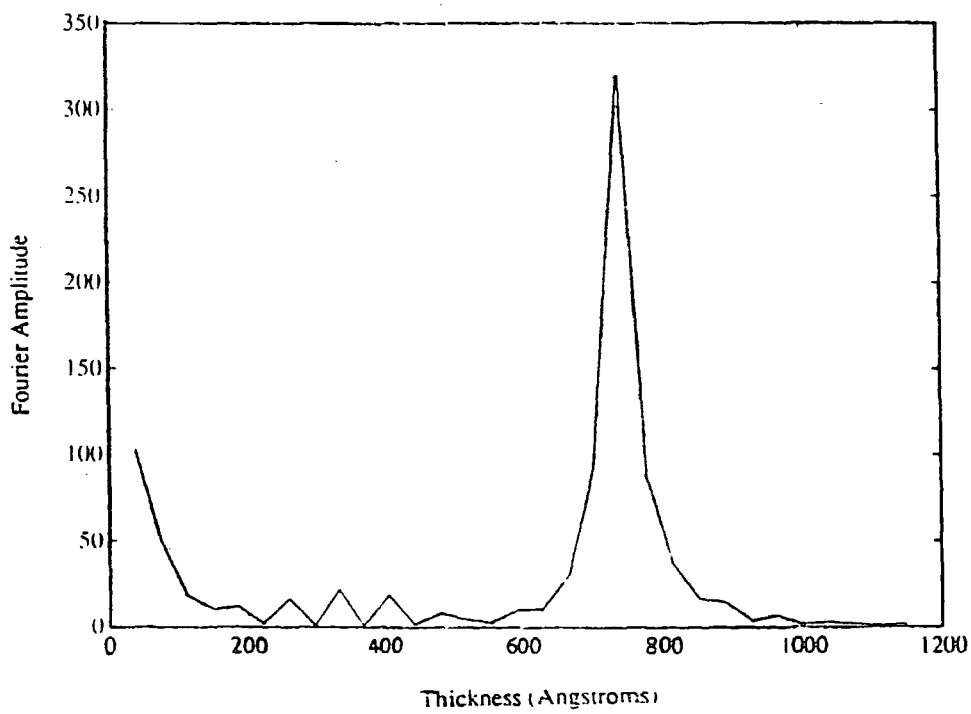


(ii) FFT of windowed, normalised data

Figure 5.10(b) : FFT analysis of simulated diffraction profile (3-0550e) shown in Figure 5.9 (Normalise method, windowed data).

Sample structure : GaAs Sub./100Å $In_{0.13}Ga_{0.87}As$/270Å $Al_{0.22}Ga_{0.78}As$/415Å GaAs

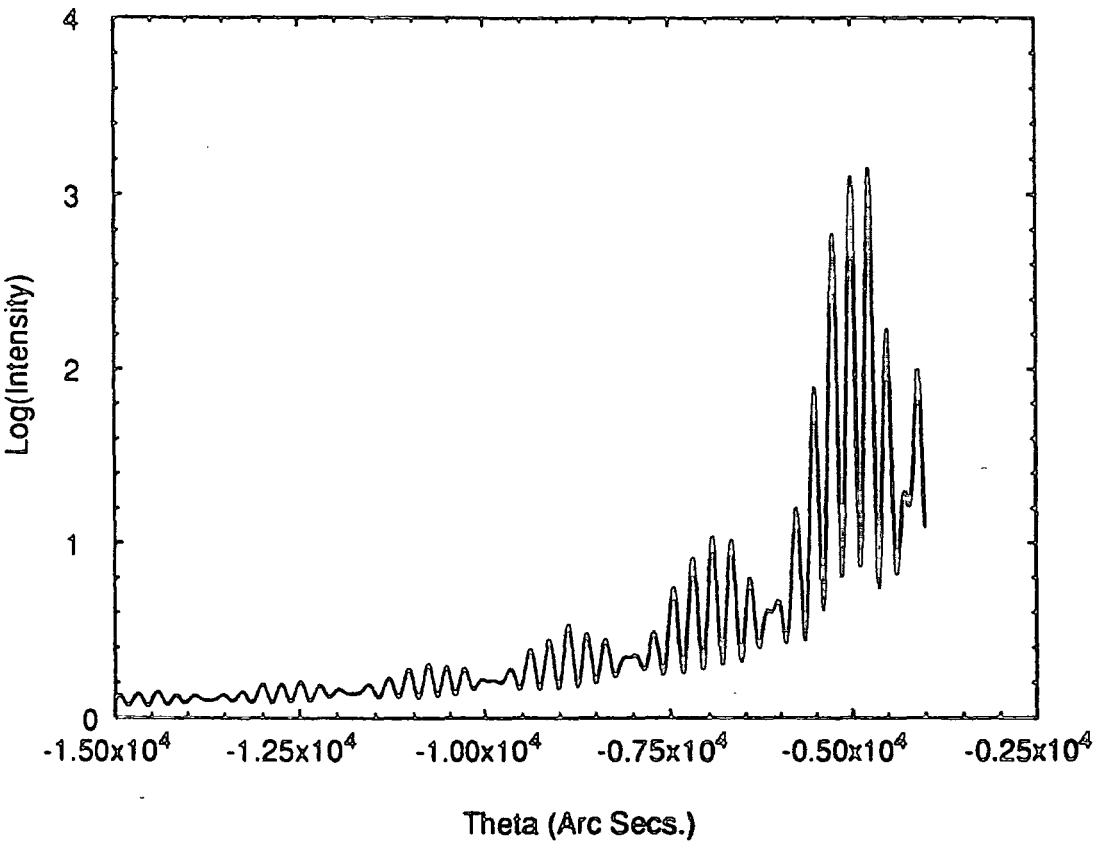


Figure 5.11 : Simulated diffraction profile of sample 3-0550e.
(Region 2 : -15000" to -4000")

Sample structure : GaAs Sub./100Å $In_{0.13}Ga_{0.87}As$/270Å $Al_{0.22}Ga_{0.78}As$/415Å GaAs

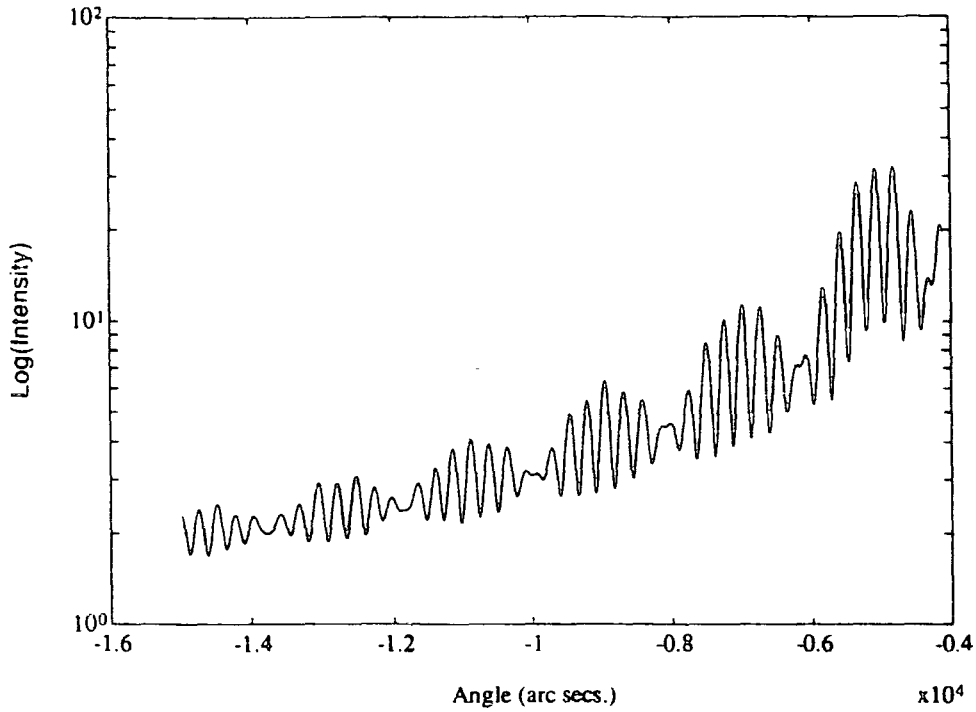


(i) Section of data selected

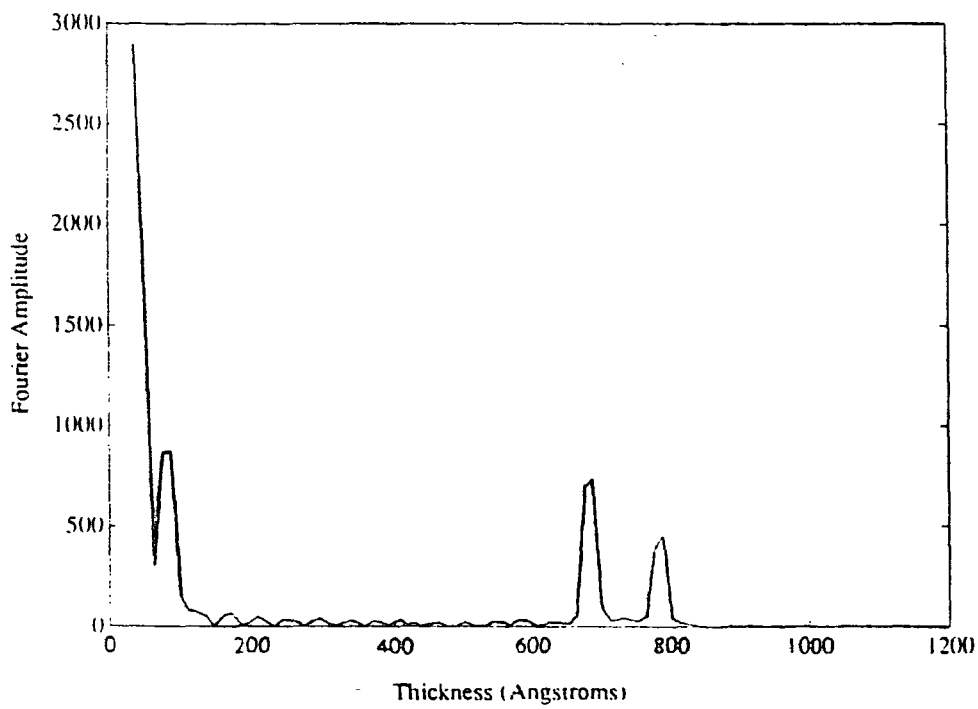


(ii) FFT of data selected

Figure 5.12(a) : FFT analysis of simulated diffraction profile (3-0550e) shown in Figure 5.11 (Log-only method, windowed data).

Sample structure : GaAs Sub./100Å $In_{0.13}Ga_{0.87}As$/270Å $Al_{0.22}Ga_{0.78}As$/415Å GaAs

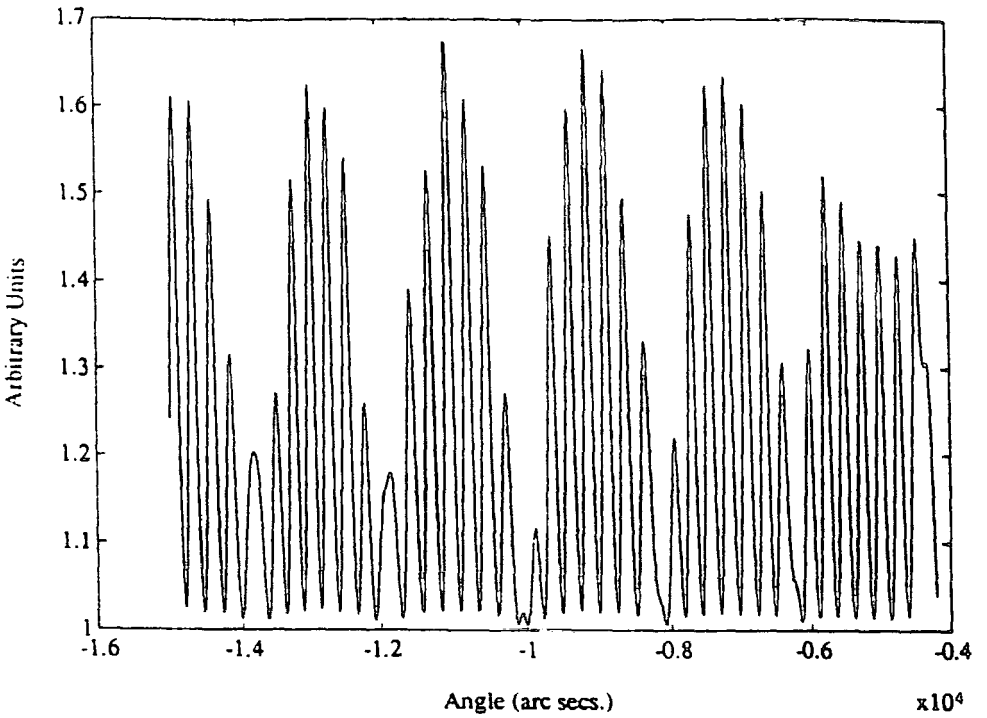


(i) Windowed, normalised data

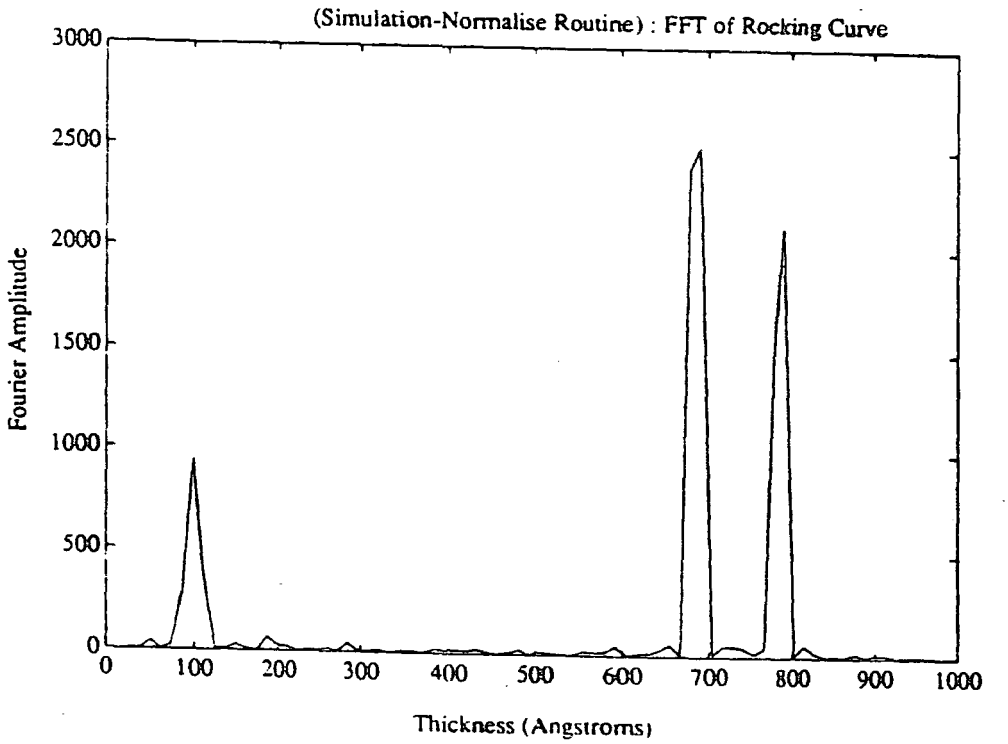


(ii) FFT of windowed, normalised data

Figure 5.12(b) : FFT analysis of simulated diffraction profile (3-0550e) shown in Figure 5.11 (Normalise method, windowed data).

Sample structure : GaAs Sub./100Å $In_{0.13}Ga_{0.87}As$/270Å $Al_{0.22}Ga_{0.78}As$/415Å GaAs

## 5.13 Constraints On Data Collection Time

If FFT analysis of rocking curves is to be used industrially then pressures exerted by equipment availability will probably mean that any data recorded will be done so with a relatively small data collection time. It is therefore essential to know the minimum time necessary over which useful data can be taken. Fig 5.13 shows three rocking curves of sample 3-0964c with count times per point of 4, 10 and 60 seconds. The corresponding total scan times for these curves are 30, 75 and 450 minutes respectively, for data collected over a range of 4500".

Application of the log-only method on all three scans gives a main peak at around 990Å with a smaller "shoulder" at 1100Å. Assuming a lack of sufficient modulation information then the "average" thickness produced from beating would be ~1032Å, which is within the measured accuracy of the main FFT peak (990±45Å). However, this particular sample structure gives good thickness fringe visibility with a much larger degree of modulation information available compared to the other samples examined in this study. If sufficient modulation information is present for the FFT to separate the two frequencies the main peak and "shoulder" could correspond to the material thickness above the InGaAs layer (550Å+400Å) and the total stack thickness (550Å+400Å+180Å) within the accuracy of the FFT method. This would appear to be the case as the shoulder is consistently present in all FFT's and is "real" ,i.e. it does not correspond to noise in the Fourier transform. The Fourier amplitude and visibility of the main peak is similar for all three count times, even in the case of a 4 sec. count time (Fig 5.14(a,b,c)). Although the peaks are certainly visible in the FFT, inspection of the entire thickness axis shows that their size compared to low frequency components is very small.

The results of analysing the same three curves with the normalise method are shown in Fig.5.15. Here, only the windowed, normalised data immediatiely prior to Fourier transformation and the final FFT itself are plotted. Again all three FFT's give peaks at similar positions (~ 990Å and 1100Å) with roughly equivalent Fourier amplitudes. The background noise around the FFT peak for 3-0964c.x02 (4 sec. count) appears to be slightly greater but this small count time is still observed to be sufficient to obtain acceptable results. Fig.5.16 highlights the main advantage of the normalise technique over the log-only method. The graphs show

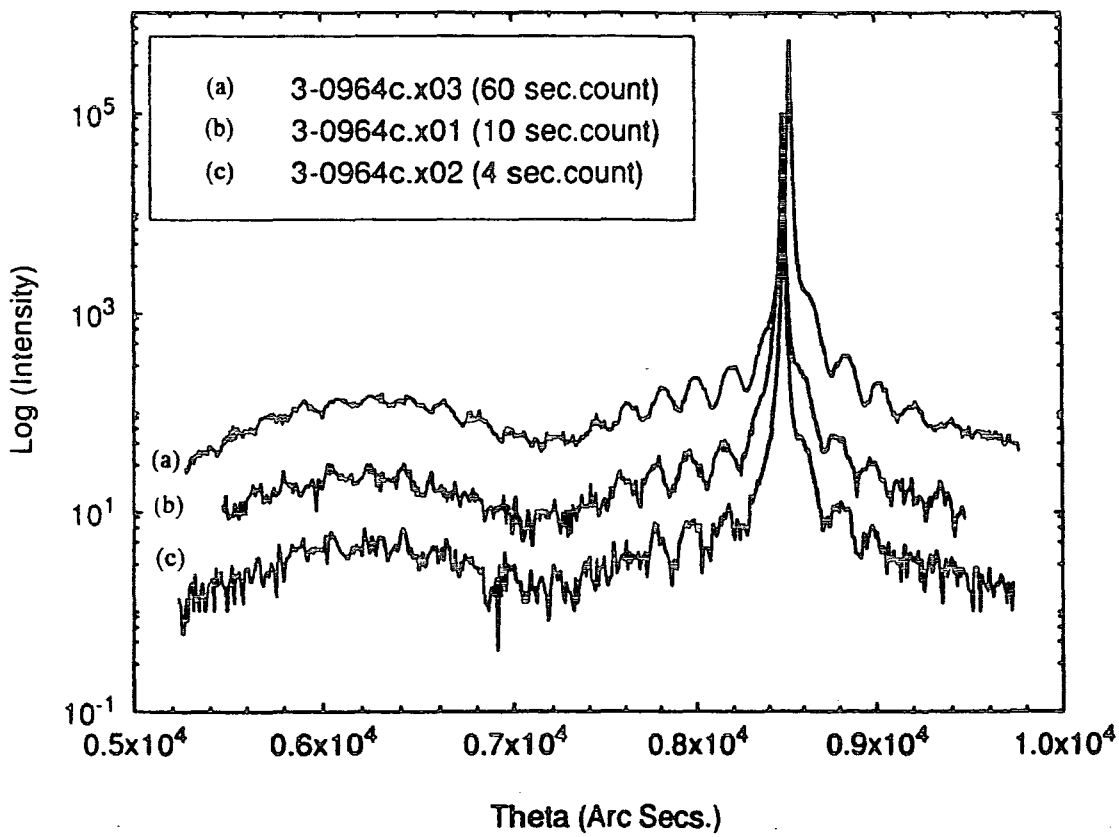


Figure 5.13 : Rocking curves of sample 3-0964c with (a) 60 sec. count, (b) 10 sec. count, (c) 4 sec. count.

Sample structure : GaAs Sub./180Å $In_{0.13}Ga_{0.87}As$/400Å $Al_{0.18}Ga_{0.82}As$/550Å GaAs

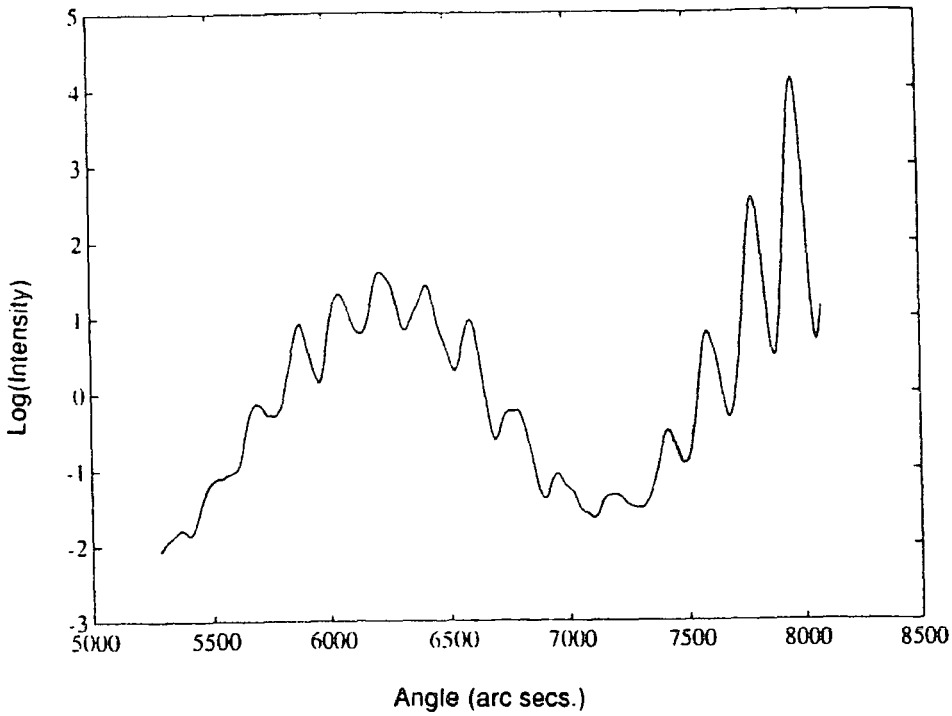


(i) Section of data selected (layer peak only)

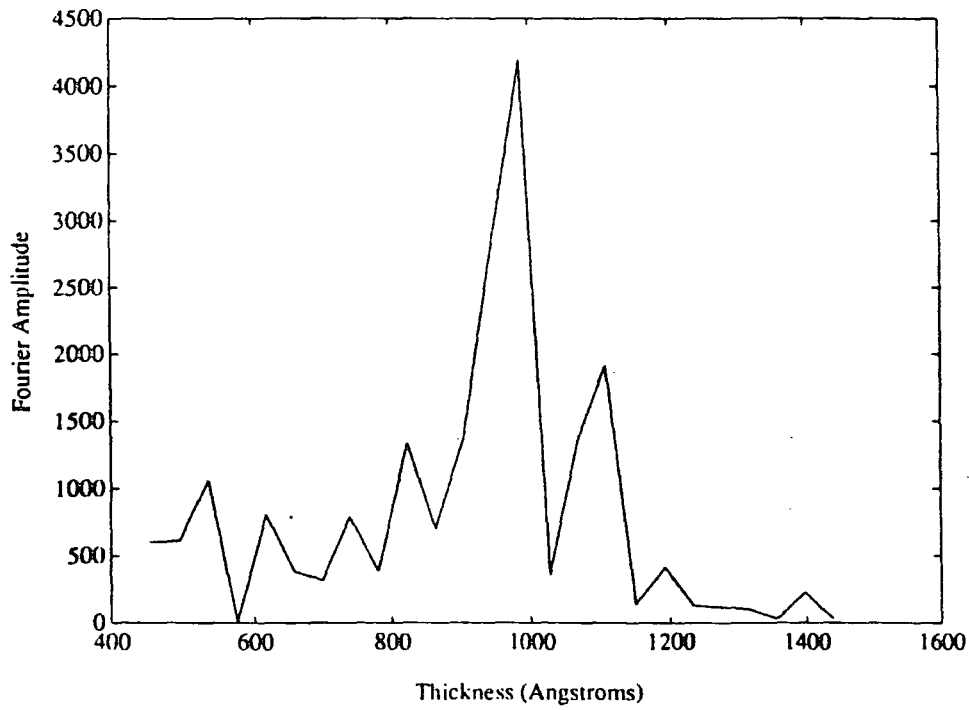


(ii) FFT of data selected

Figure 5.14(a) : FFT of rocking curve 3-0964c.x03 (60 second count time). Log-only method, windowed data.

Sample structure : GaAs Sub./180Å $In_{0.13}Ga_{0.87}As$/400Å $Al_{0.18}Ga_{0.82}As$/550Å GaAs

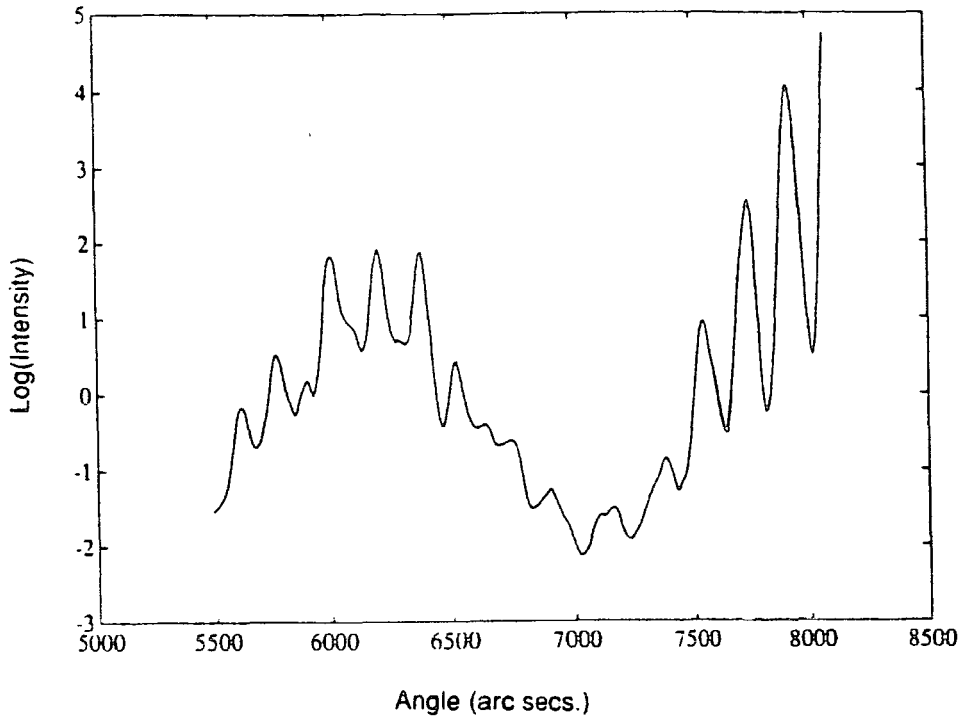


(i) Section of data selected (layer peak only)

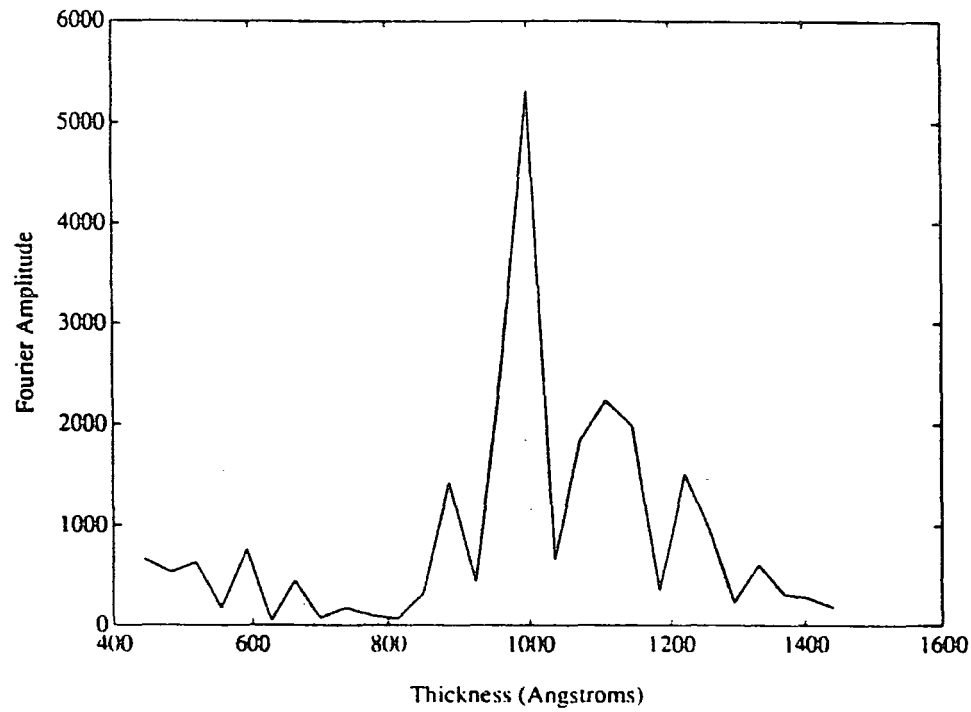


(ii) FFT of data selected

Figure 5.14(b) : FFT of rocking curve 3-0964c.x01 (10 second count time). Log-only method, windowed data.

Sample structure : GaAs Sub./180Å $In_{0.13}Ga_{0.87}As$/400Å $Al_{0.18}Ga_{0.82}As$/550Å GaAs

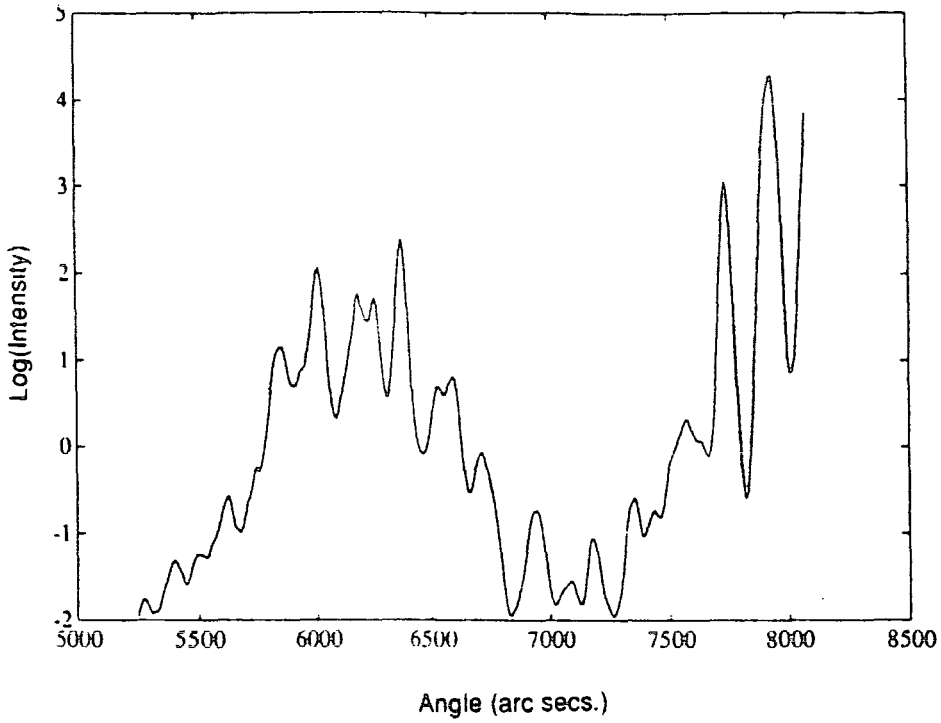


(i) Section of data selected (layer peak only)

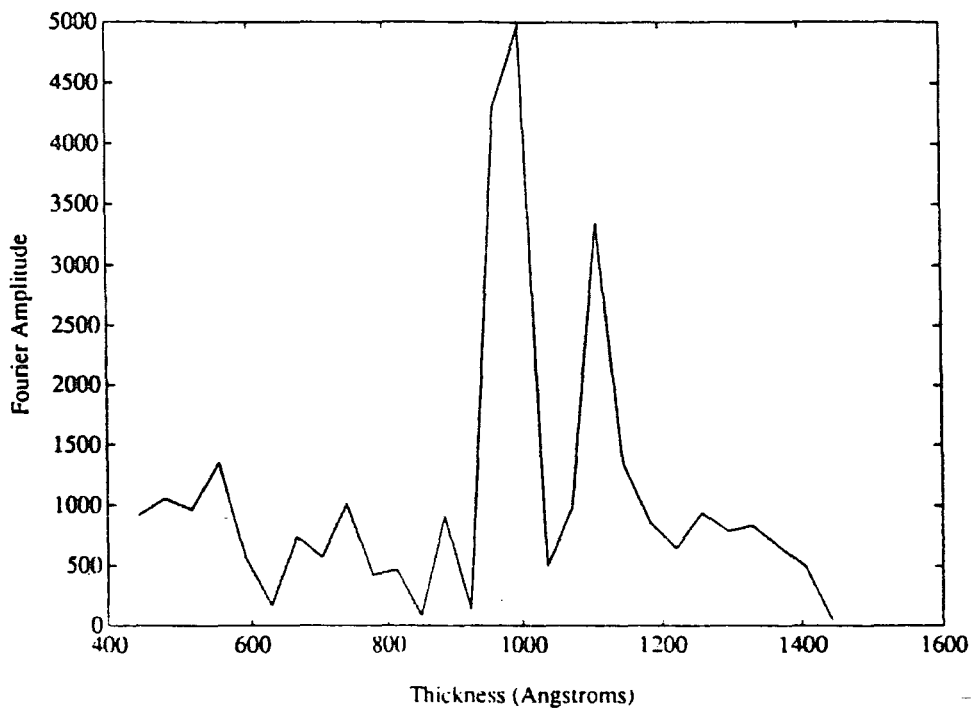


(ii) FFT of data selected

Figure 5.14(c) : FFT of rocking curve 3-0964c.x02 (4 second count time). Log-only method, windowed data.

Sample structure : GaAs Sub./180Å $In_{0.13}Ga_{0.87}As$/400Å $Al_{0.18}Ga_{0.82}As$/550Å GaAs

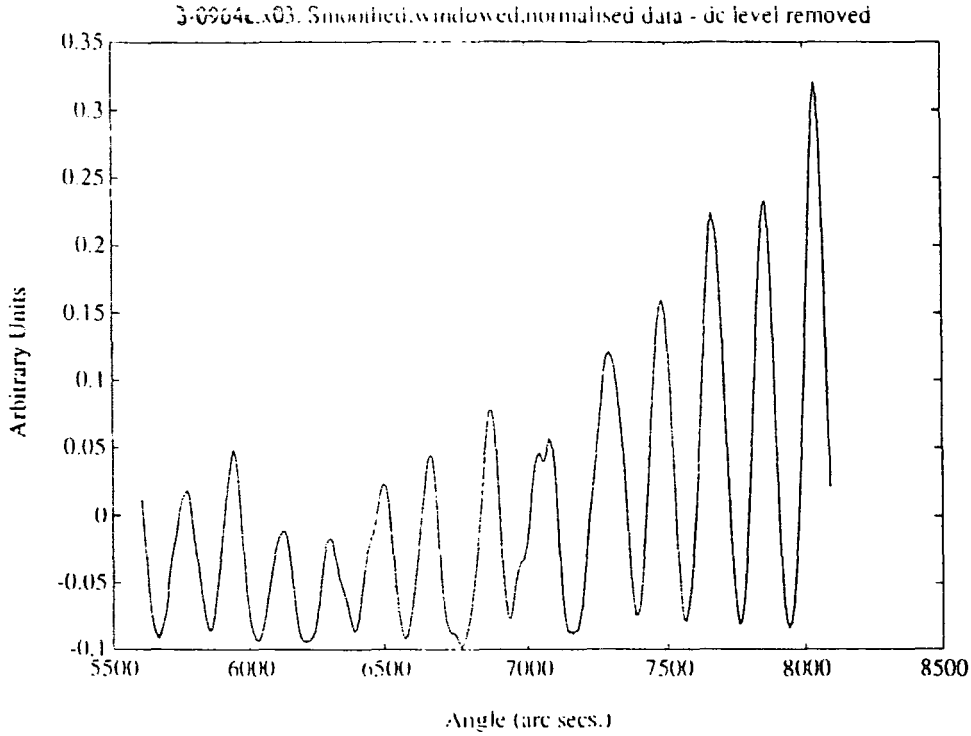


(i) Windowed, normalised data

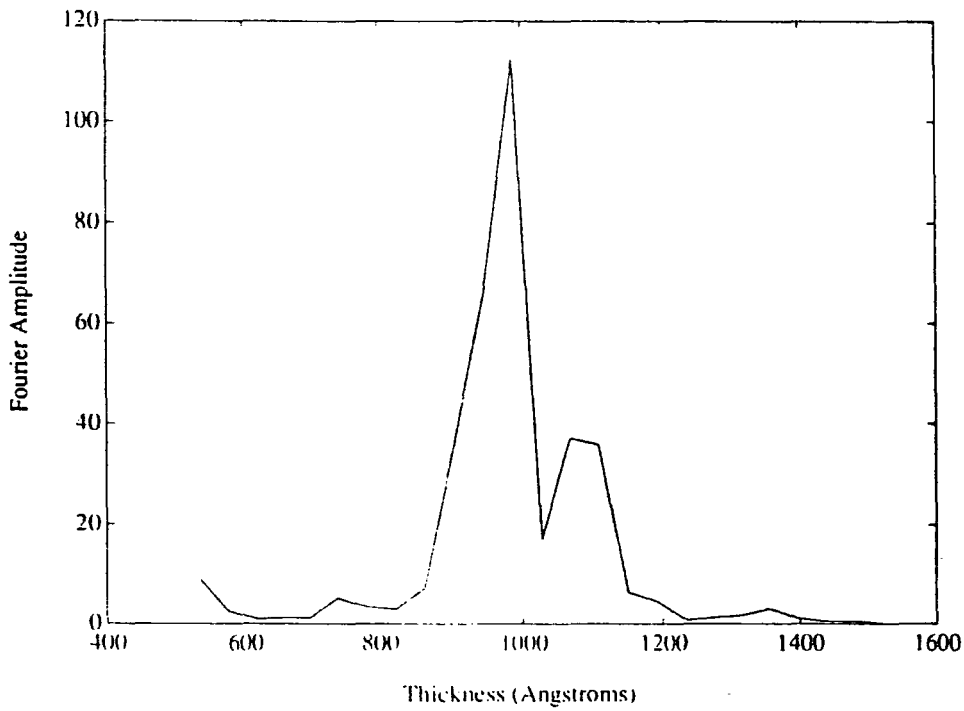


(ii) FFT of windowed, normalised data

Figure 5.15(a) : FFT of rocking curve 3-0964c.x03 (60 second count time). Normalise method, windowed data.

Sample structure : GaAs Sub./180Å $In_{0.13}Ga_{0.87}As$/400Å $Al_{0.18}Ga_{0.82}As$/550Å GaAs

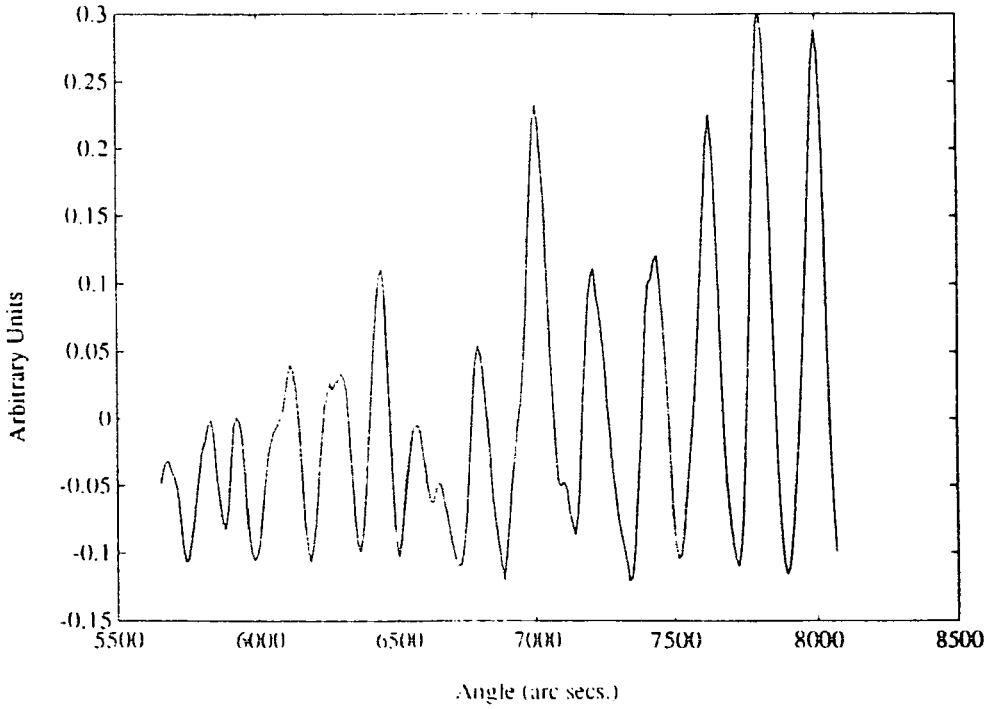


(i) Windowed, normalised data

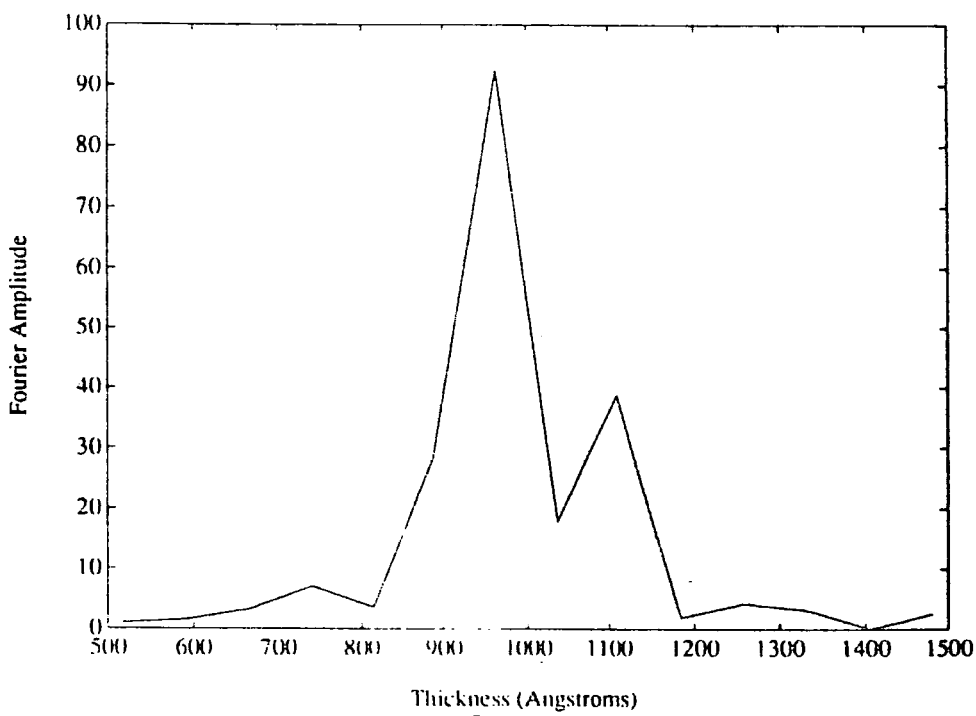


(ii) FFT of windowed, normalised data

Figure 5.15(b) : FFT of rocking curve 3-0964c.x01 (10 second count time). Normalise method, windowed data.

Sample structure : GaAs Sub./180Å $In_{0.13}Ga_{0.87}As$/400Å $Al_{0.18}Ga_{0.82}As$/550Å GaAs

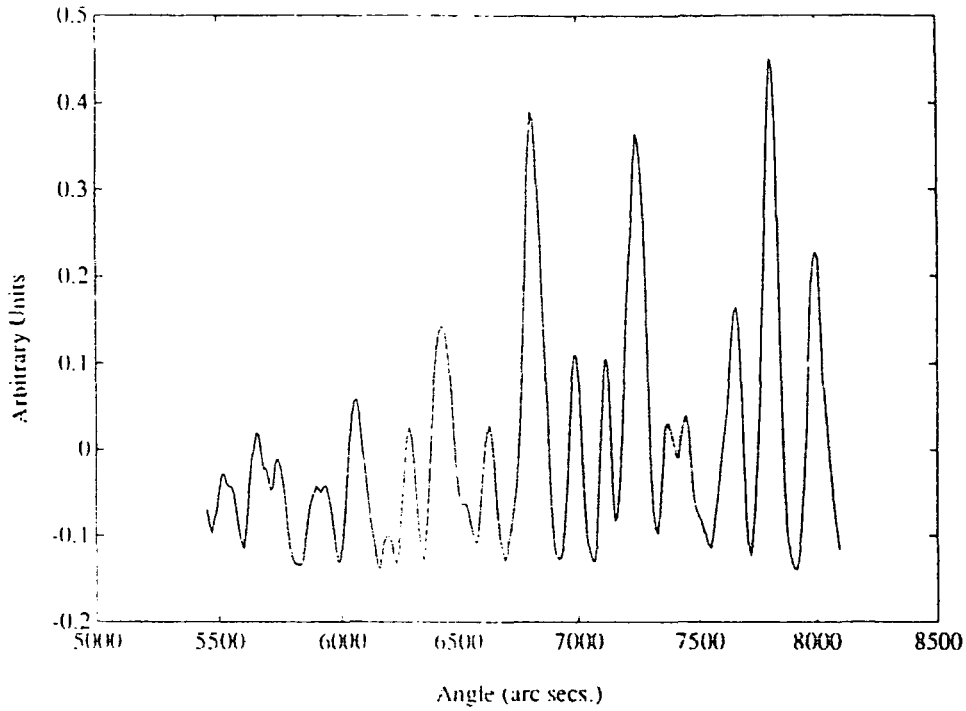


(i) Windowed, normalised data

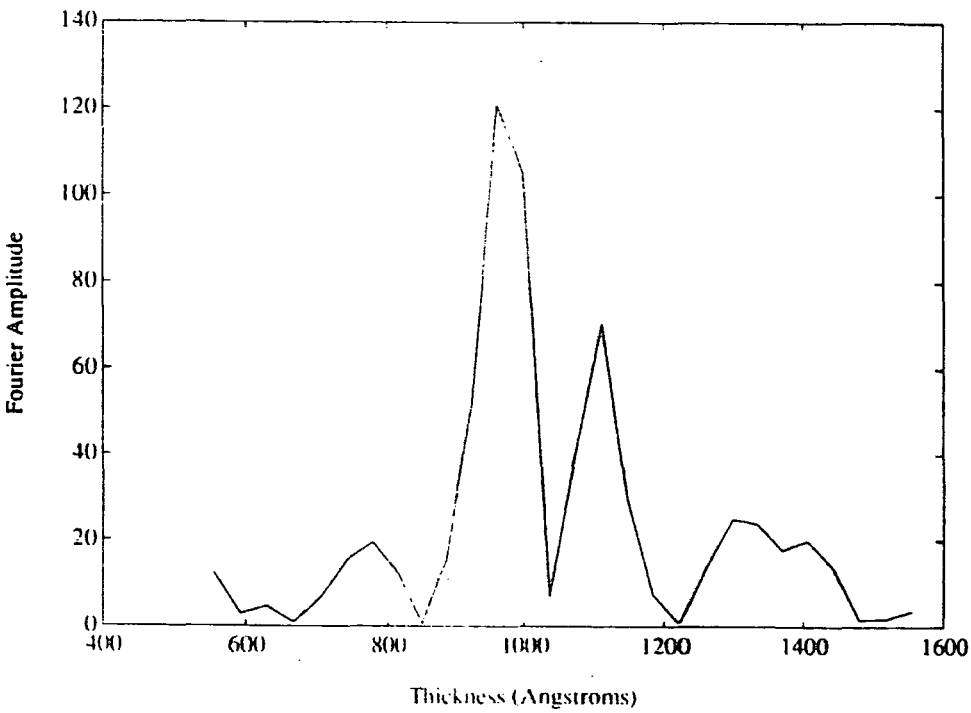


(ii) FFT of windowed, normalised data

Figure 5.15(c) : FFT of rocking curve 3-0964c.x02 (4 second count time). Normalise method, windowed data.

Sample structure : GaAs Sub./180Å $In_{0.13}Ga_{0.87}As$/400Å $Al_{0.18}Ga_{0.82}As$/550Å GaAs

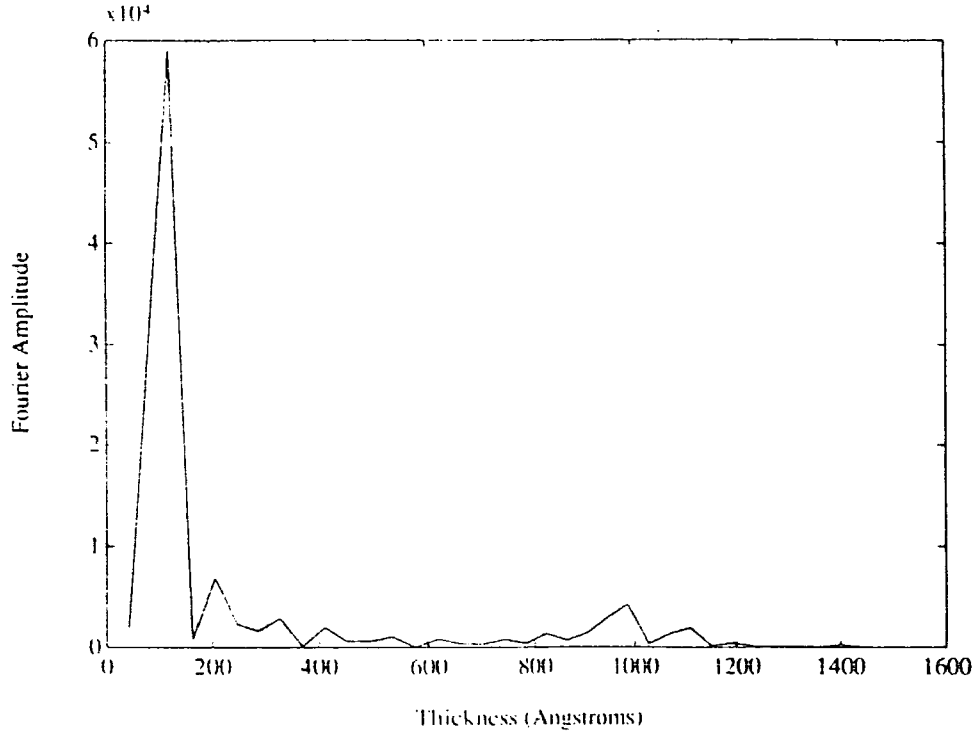


(i) Final FFT of 3-0964c.x03 (Log-only method, windowed data)
Graph plotted from t=0.

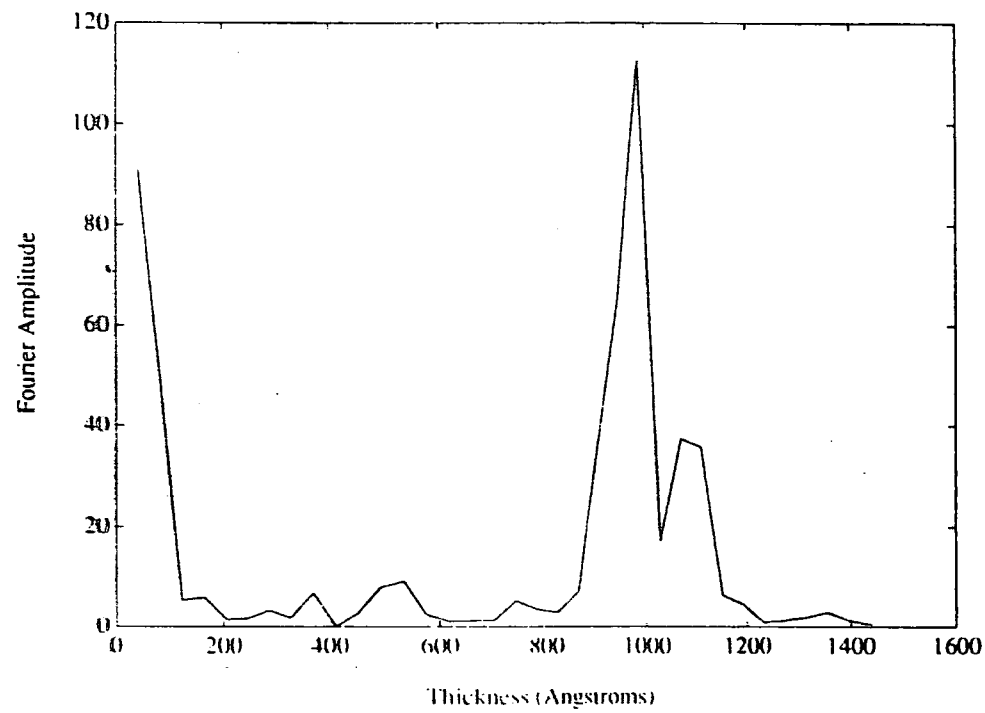


(ii) Final FFT of 3-0964c.x03 (Normalise method, windowed data)
Graph plotted from t=0.

Figure 5.16 : FFT of rocking curve 3-0964c.x03 using the (i) Log-only and (ii) Normalise methods.

Sample structure : GaAs Sub./180Å $In_{0.13}Ga_{0.87}As$/400Å $Al_{0.18}Ga_{0.82}As$/550Å GaAs

the FFT's of file 3-0964c.x03 (60 sec. count) using both the log-only and normalise techniques with the thickness axis from t=0. Although the absolute size of the Fourier amplitude is greater for the log-only method the relative size of the measured FFT peaks is greater when applying the normalise technique..

For comparison the results of analysing the best fit simulation to 3-0964c.x03 are shown in Figs.5.17(a,b). In theory, a perfect fit simulation would give a similar Fourier transform to its experimental counterpart. While their are peaks visible at 1100Å (equivalent to the total stack thickness) and 990Å (equivalent to the sum of the top two layer thicknesses) the size of the peak at 1100Å is greater in this case than that at 990Å. This suggests that the best-fit simulation, while being a very good approximation of the recorded diffraction profile, may still need small further refinement.

For this particular system it would appear that rocking curves recorded in 30 minutes contain adequate fringe structure to gain thickness information. In fact, comparison of the FFT's obtained from using a 4 sec. count time with those obtained from the longest count scans show only a slight improvement when using a much greater counting interval (60 secs.). Although the double crystal diffraction profile of 3-0964c exhibits particularly good thickness fringe structure it should be possible to attain rocking curves of sufficiently high quality for other HEMT structures in much less than one hour. The data collection time for HEMT structures could be further reduced by scanning only over the InGaAs layer peak, as it is only fringes in this region which are selected for FFT analysis. This has the significant drawback, however, that the recorded rocking curve will then be useful for determination of thickness only. Information from peak splittings and fringes with enhanced visibility on the shoulders of the substrate peak will no longer be available to the grower.

Should the quality of data collected in short scans (< 1 hour) still be inadequate then there are other analytic tools available to improve the contrast of periodic components, of which one is discussed below.

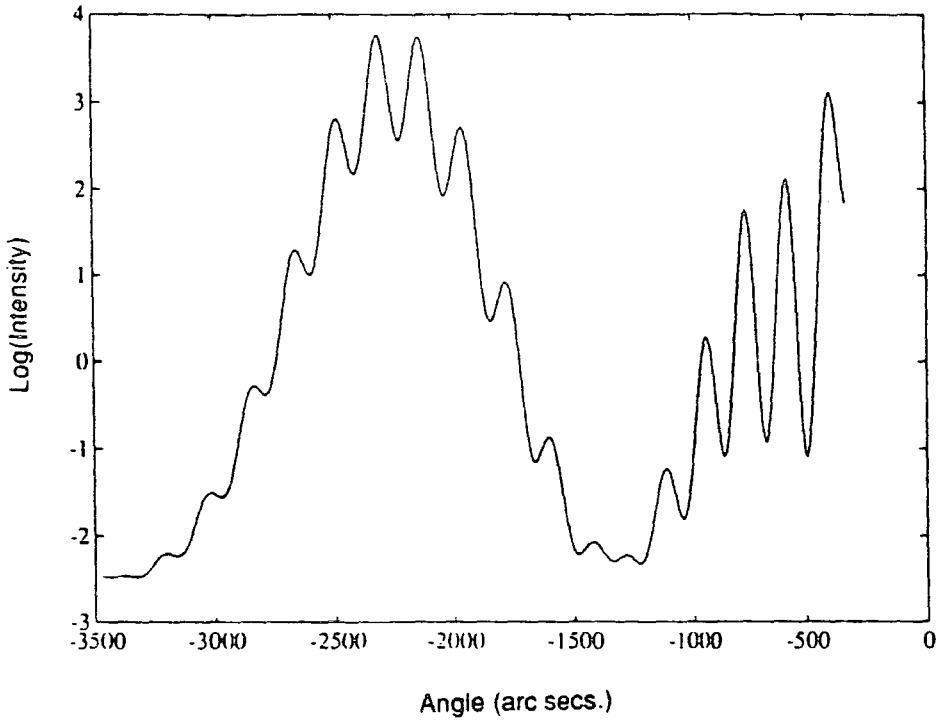


(i) Section of data selected (layer peak only)

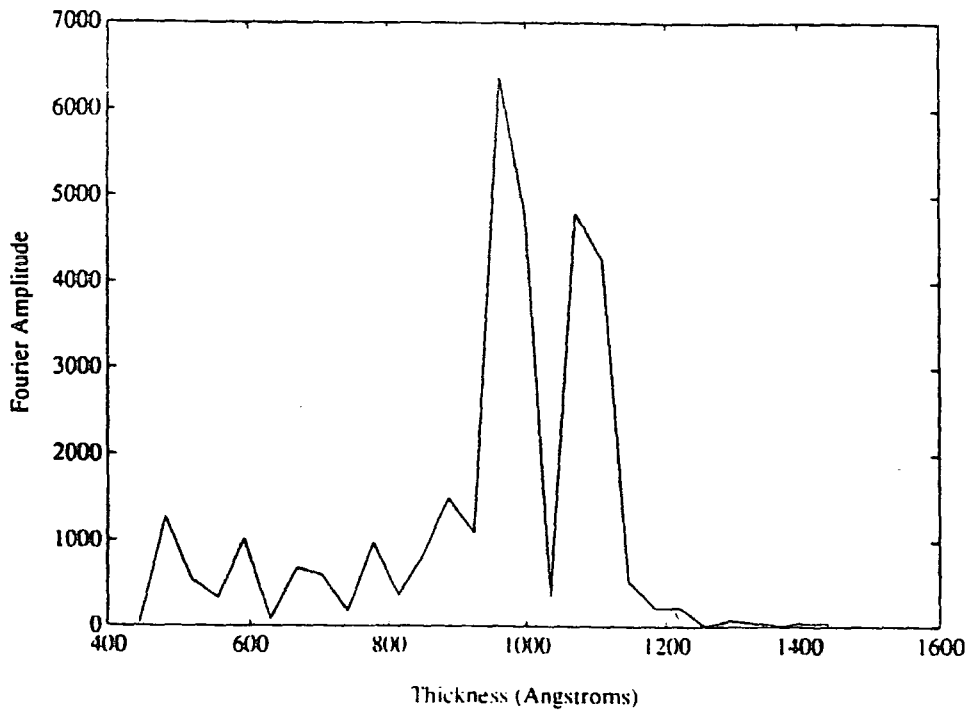


(ii) FFT of data selected

Figure 5.17(a) : FFT of simulated rocking curve 3-0964c.g13 (Log-only method, windowed data)

Sample structure : GaAs Sub./180Å $In_{0.13}Ga_{0.87}As$/400Å $Al_{0.18}Ga_{0.82}As$/550Å GaAs

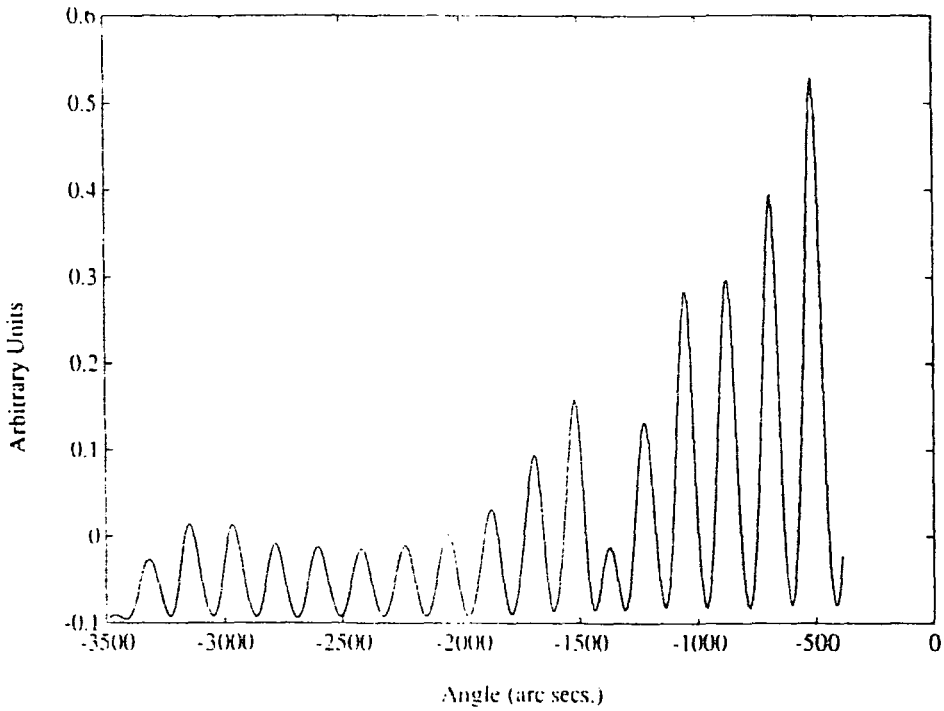


(i) Windowed, normalised data

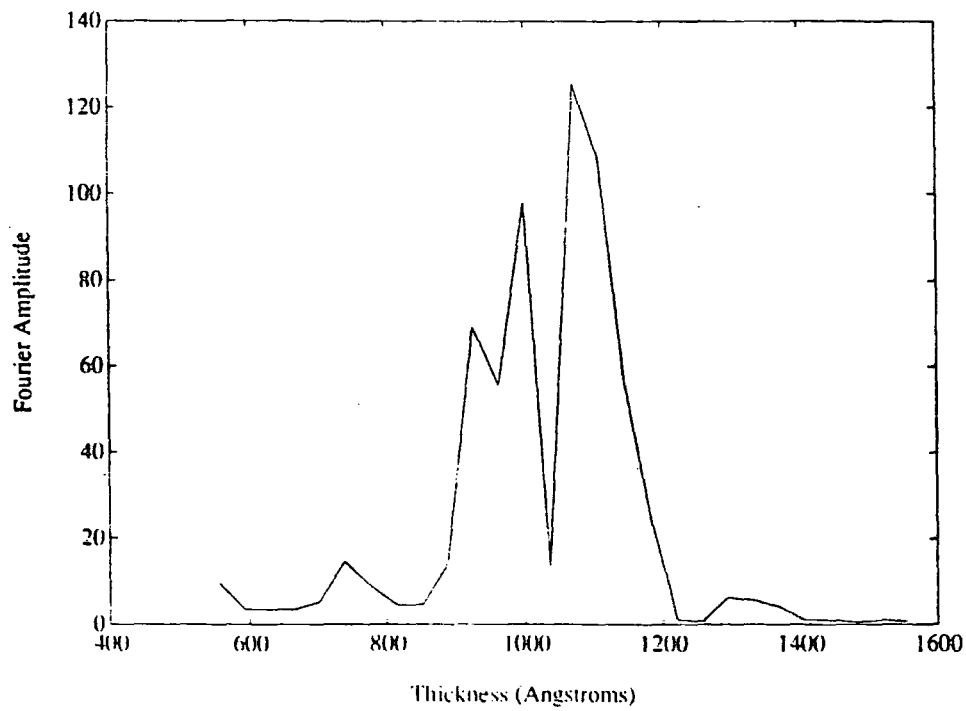


(ii) FFT of windowed, normalised data

Figure 5.17(b) : FFT of simulated rocking curve 3-0964c.g13 (Normalise method, windowed data).

Sample structure : GaAs Sub./180Å $In_{0.13}Ga_{0.87}As$/400Å $Al_{0.18}Ga_{0.82}As$/550Å GaAs

## 5.14 Auto correlation Of Noisy Data Sets

A recognised method for extracting periodic information from a noisy data set, x(t), is by applying an auto correlation to the function[16]. The auto correlation, a(τ), is defined mathematically by,

$$a(\tau) = \lim_{T \to \infty} \frac{1}{2T} \int_{-T}^{T} x(t)x(t+\tau)dt \qquad (5.10)$$

and can be thought of as the matching up of a waveform with a copy of itself. Maximum correlation will occur when the two waveforms lie directly over each other, i.e. when the time lag between the two, τ, is zero. If periodic components are present then as the two waveforms are "moved" over each other, maximum correlation will also occur for all time lags equal to the period of the harmonic component. For other values of time lag, τ, there is little or no overlay and the correlation between the noise in the data sets is small. When applying an auto correlation, extra zeroes are appended to the waveform (to prevent cyclic correlation errors) resulting in the function appearing pulsed rather than continuous. This pulsing or gating of the function produces triangular windowing which diminishes all but the central peak (τ=0) in the auto correlation.

Rocking curve 3-0960b.x04 (with a counting time of 10 secs. per point) shows noisy fringe periods on the layer peak resulting in a very poor result upon application of the log-only method (Fig 5.18). Although the use of the normalise technique when manipulating the data gives a detectable peak in the FFT at 1200Å (Fig 5.19) the magnitude of this peak is small. Unlike the case of 3-0964c there appears to be insufficient modulation information to resolve the two closely matched frequencies which, according to the best fit simulation, would appear at 1130Å and 1233Å. Instead the peak observed corresponds to the "average" thickness of $\{0.5*(1/1130 + 1/1233)\}^{-1} = 1179$Å.

Fig.5.20(a) shows the effect of auto correlating the selected data prior to application of the FFT in the log-only process. Although the data is dominated by the triangular windowing , clean fringes are apparent in the wings of the correlated data. The resulting FFT gives a peak at 1200Å, corresponding to the "average" thickness, showing a significant improvement upon analysis of the uncorrelated

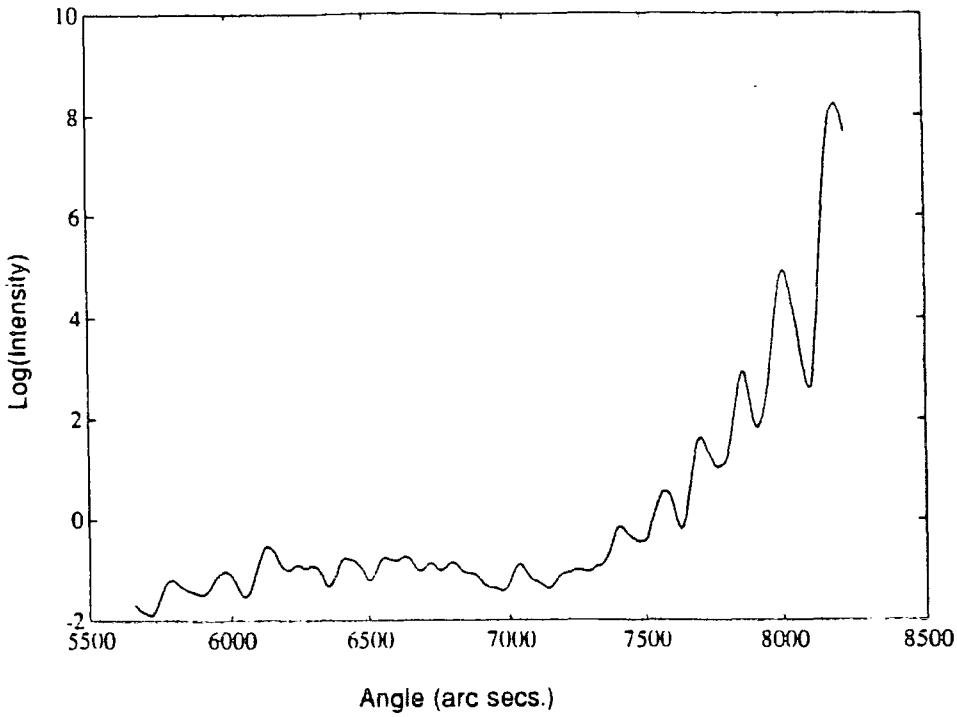


(i) Section of data selected (layer peak only)

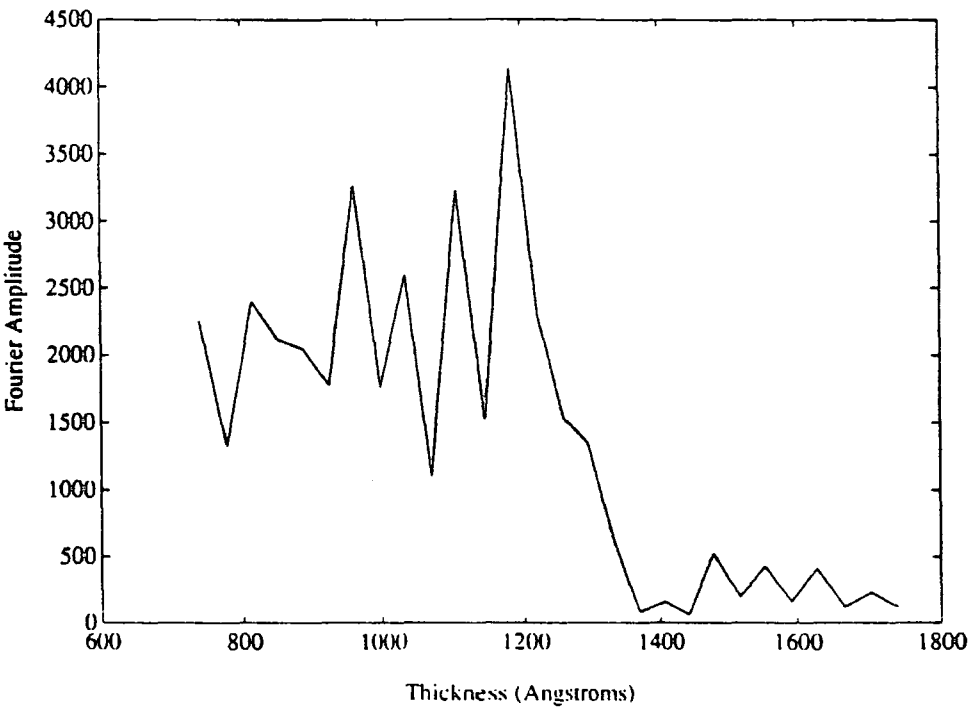


(ii) FFT of data selected

Figure 5.18 : FFT of a "noisy" rocking curve (3-0960b.x04). Log-only method, windowed data.

Sample structure : GaAs Sub./2000Å $Al_{0.23}Ga_{0.77}As$/600Å GaAs/103Å $In_{0.29}Ga_{0.71}As$/400Å $Al_{0.23}Ga_{0.77}As$/730Å GaAs

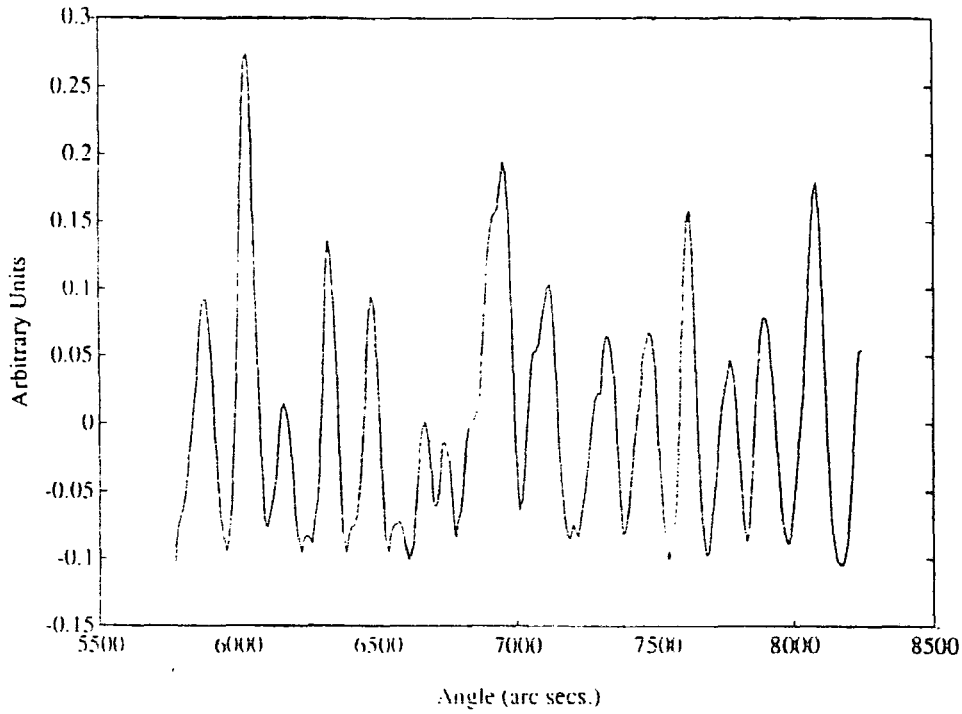


(i) Windowed, normalised data

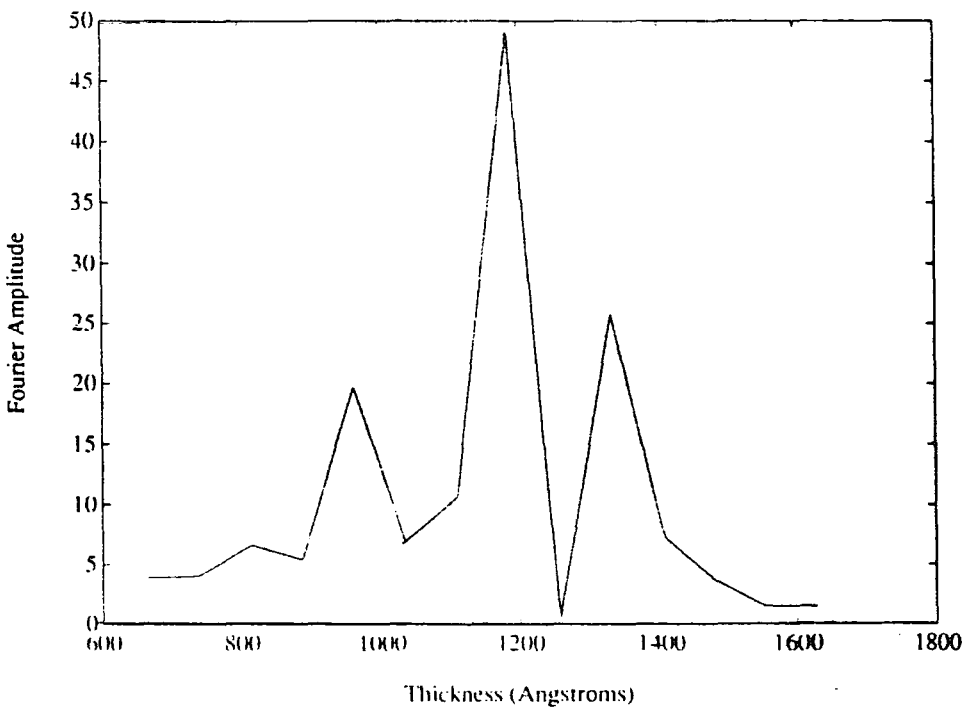


(ii) FFT of windowed, normalised data

Figure 5.19 : FFT of a "noisy" rocking curve (3-0960b.x04). Normalise method, windowed data.

Sample structure : GaAs Sub./2000Å $Al_{0.23}Ga_{0.77}As$/600Å GaAs/103Å $In_{0.29}Ga_{0.71}As$/400Å $Al_{0.23}Ga_{0.77}As$/730Å GaAs

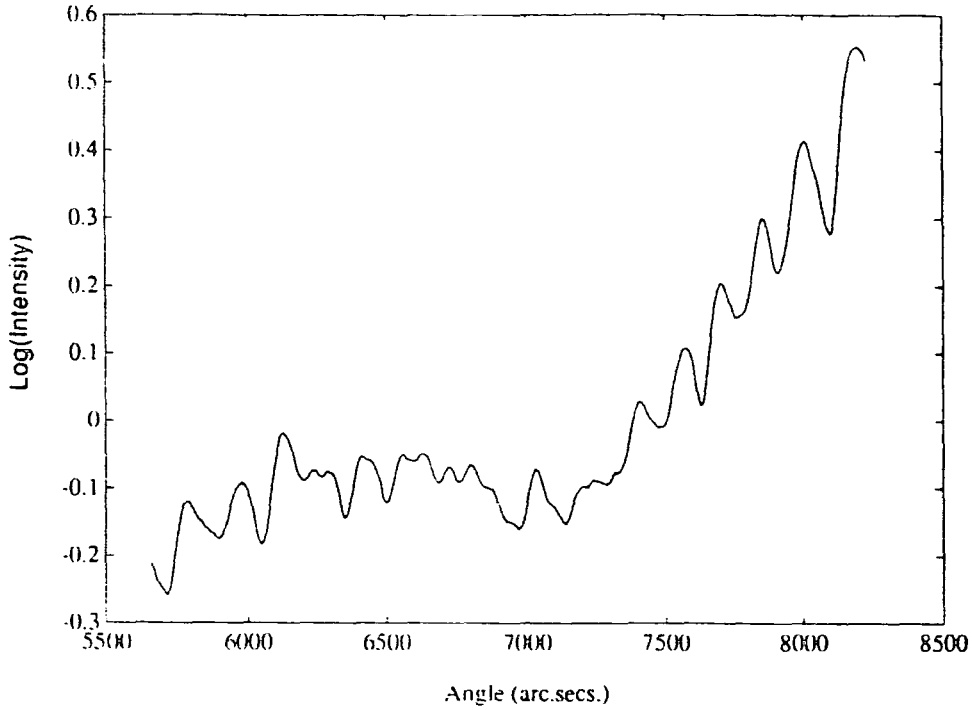


(i) Section of data selected (layer peak only)

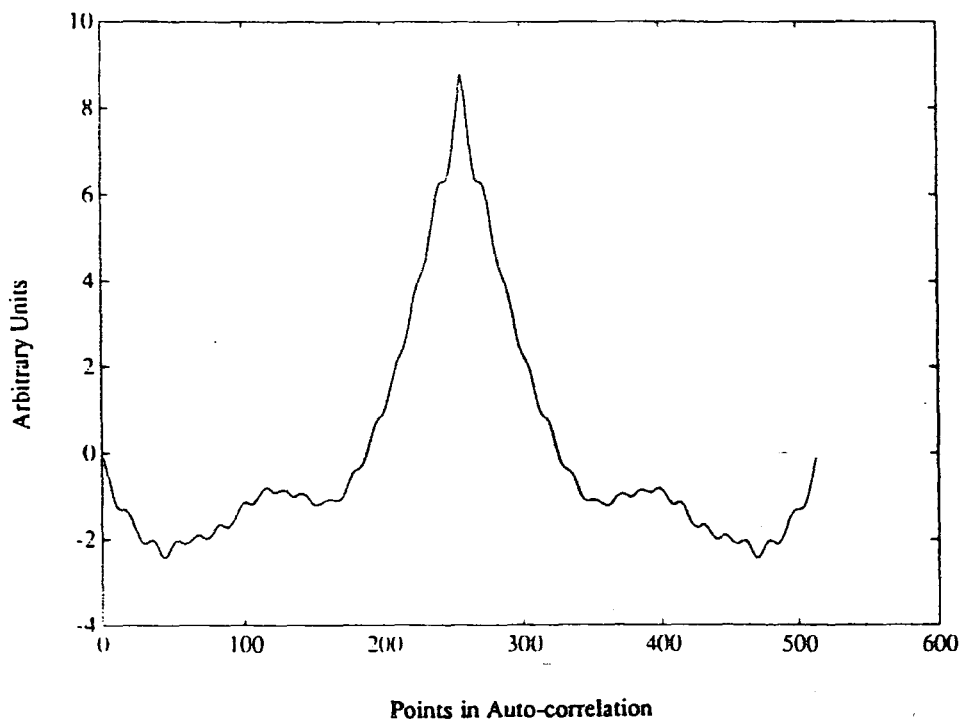


(ii) Autocorrelated data

Figure 5.20(a) : FFT of autocorrelated rocking curve (3-0960b.x04). Log-only method, windowed data.

Sample structure : GaAs Sub./2000Å $Al_{0.23}Ga_{0.77}As$/600Å GaAs/103Å $In_{0.29}Ga_{0.71}As$/400Å $Al_{0.23}Ga_{0.77}As$/730Å GaAs

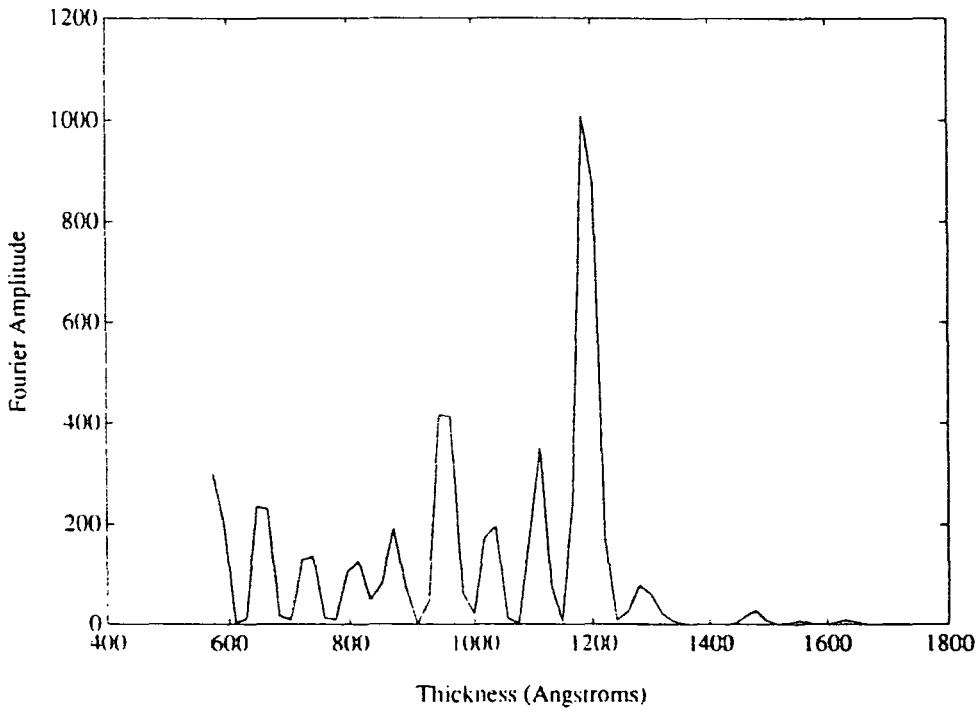


**(iii) FFT of autocorrelated, windowed, normalised data**

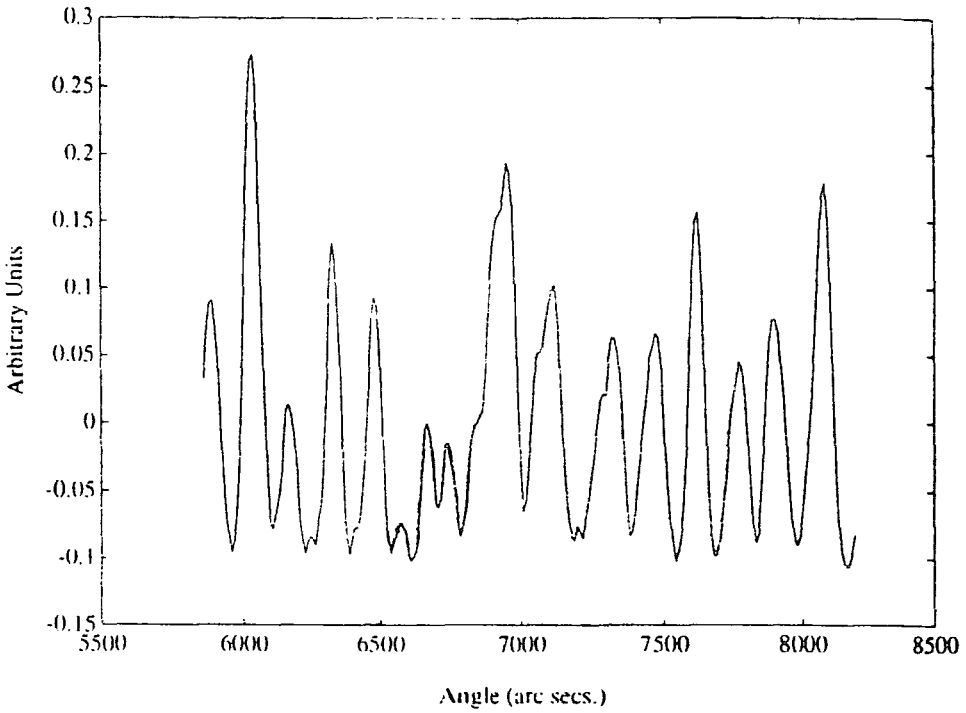


(i) Windowed, normalised data

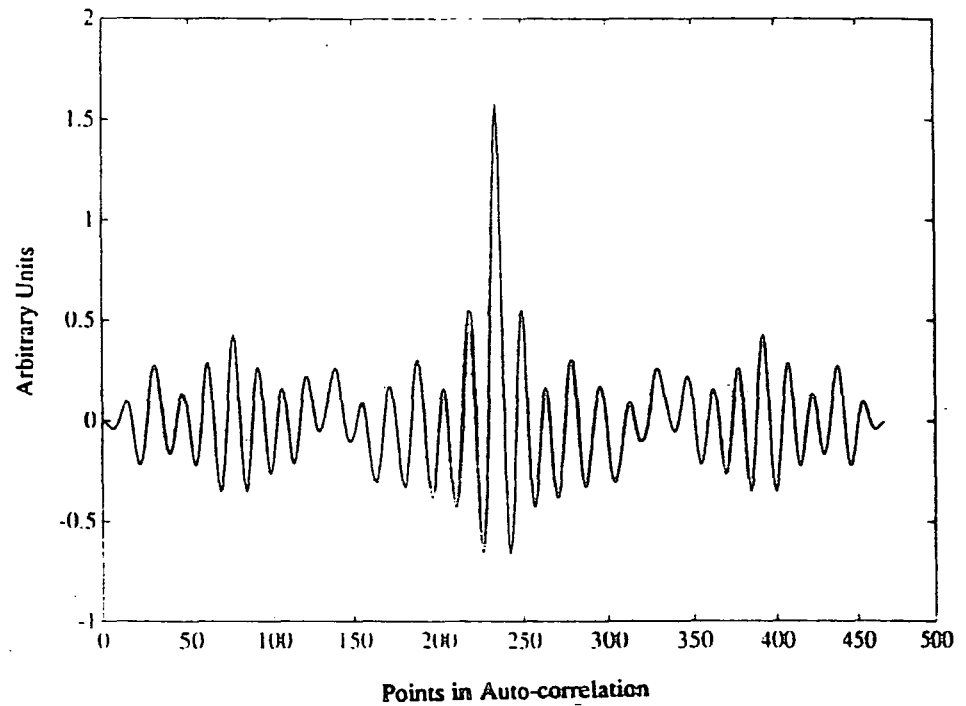


(ii) Autocorrelated data

Figure 5.20(b) : FFT of autocorrelated rocking curve (3-0960b.x04). Normalise method, windowed data.

Sample structure : GaAs Sub./2000Å $Al_{0.23}Ga_{0.77}As$/600Å GaAs/103Å $In_{0.29}Ga_{0.71}As$/400Å $Al_{0.23}Ga_{0.77}As$/730Å GaAs

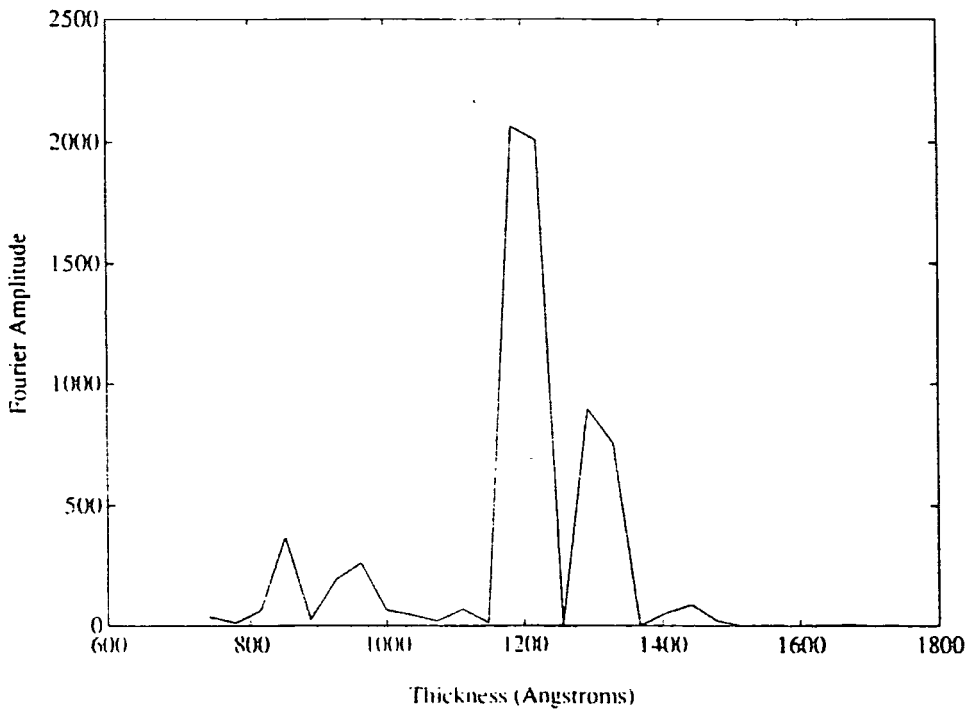


**(iii) FFT of autocorrelated, windowed, normalised data.**

data. The effect of auto correlating the data is even more pronounced when using the normalise routine (Fig.5.20(b)). The autocorrelated data shows excellent fringe clarity and magnitude yielding large peaks in the FFT at 1200Å and 1300Å.

The benefit of manipulating the data in this way is further shown by Figs.5.21(a-d), which show the improvement caused by auto correlating other rocking curves. In all cases the quality of the final FFT is improved.

## 5.15 Conclusions

The problems associated with the Fast Fourier Transformation of HEMT rocking curve data in order to extract layer thicknesses have been discussed. Experimentally, the use of a low background detector and set of shielding slits are imperative if high quality data is to be recorded. To obtain satisfactory Fourier transforms it is essential that,

(a) the substrate peak is not included in the data to be analysed, as its inclusion severely degrades the quality of the resulting FFT.

(b) Before application of the FFT the relative size of the interference fringes must be enhanced, either by using the logarithm of the data (the "log-only" method) or by dividing the data by a background envelope (the "normalise" method).

Both the log-only and normalise methods have been shown to prepare successfully the data for FFT analysis, with the normalise technique in particular significantly increasing the visibility of periodic components.

Rocking curves with sufficiently high fringe visibility can be obtained in around one hour for diffractometers with good Signal to Noise ratios. For scans recorded over shorter time scales or with a poor fringe visibility, application of an autocorrelation to the data can eliminate noisy components, leading to satisfactory results upon FFTing.

A typical HEMT rocking curve does not usually contain sufficient modulation information for the FFT to detect more than a single frequency. This frequency

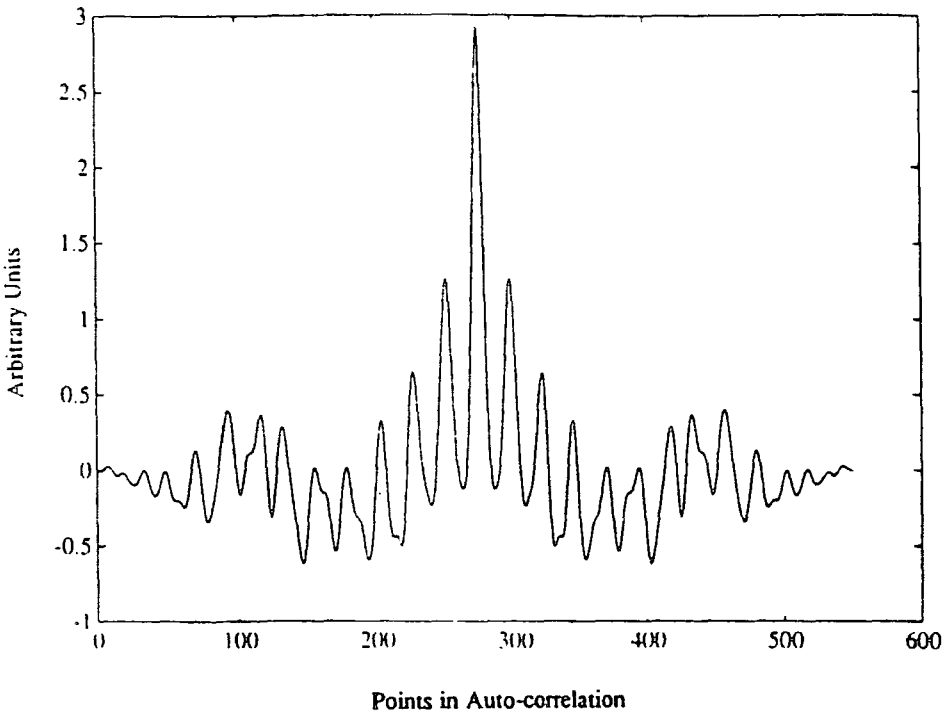


(i) Autocorrelated, windowed, normalised data

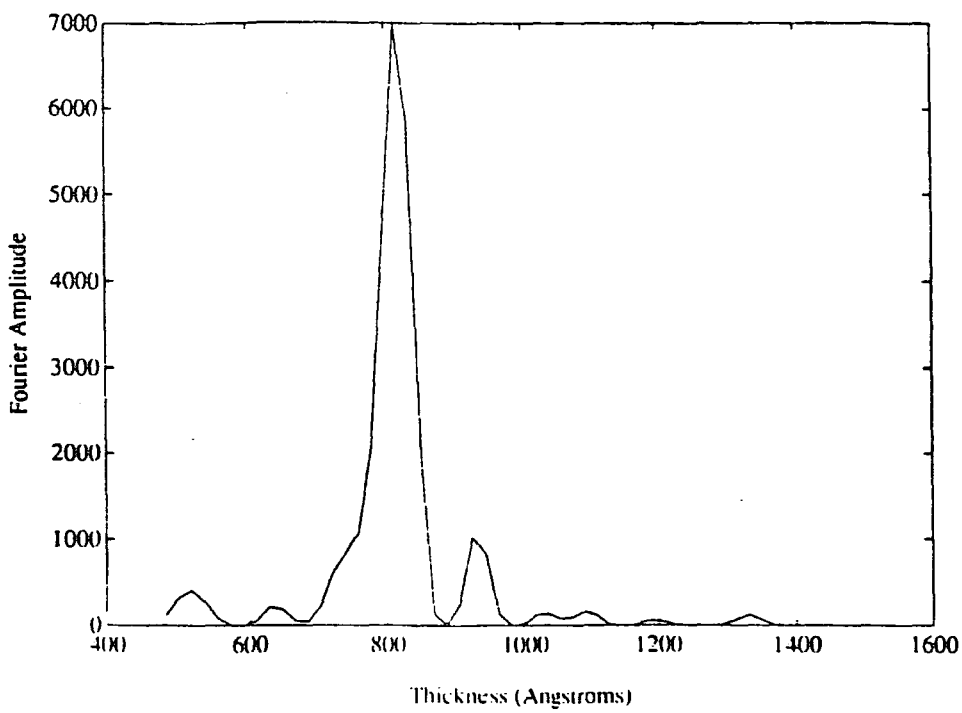


(ii) FFT of autocorrelated, normalised, windowed data

Figure 5.21(a) : FFT of autocorrelated rocking curve (3-0782e.x01). Normalise method, windowed data.

Sample structure : GaAs Sub./2000Å $Al_{0.2}Ga_{0.8}As$/20Å GaAs/75Å $In_{0.17}Ga_{0.83}As$/470Å $Al_{0.25}Ga_{0.75}As$/305Å GaAs

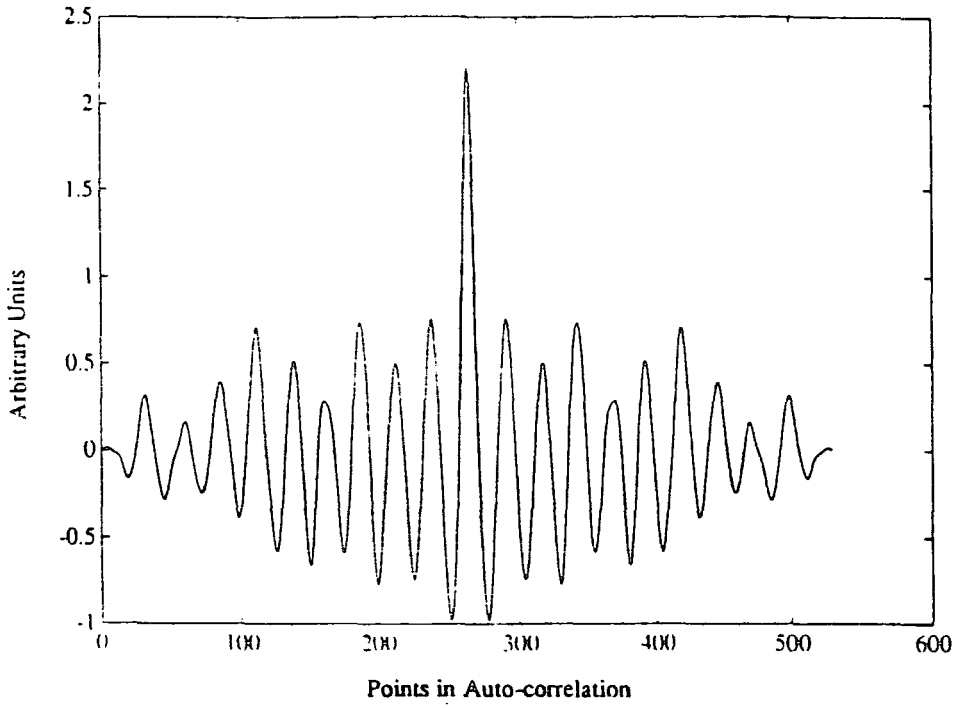


(i) Autocorrelated, windowed, normalised data

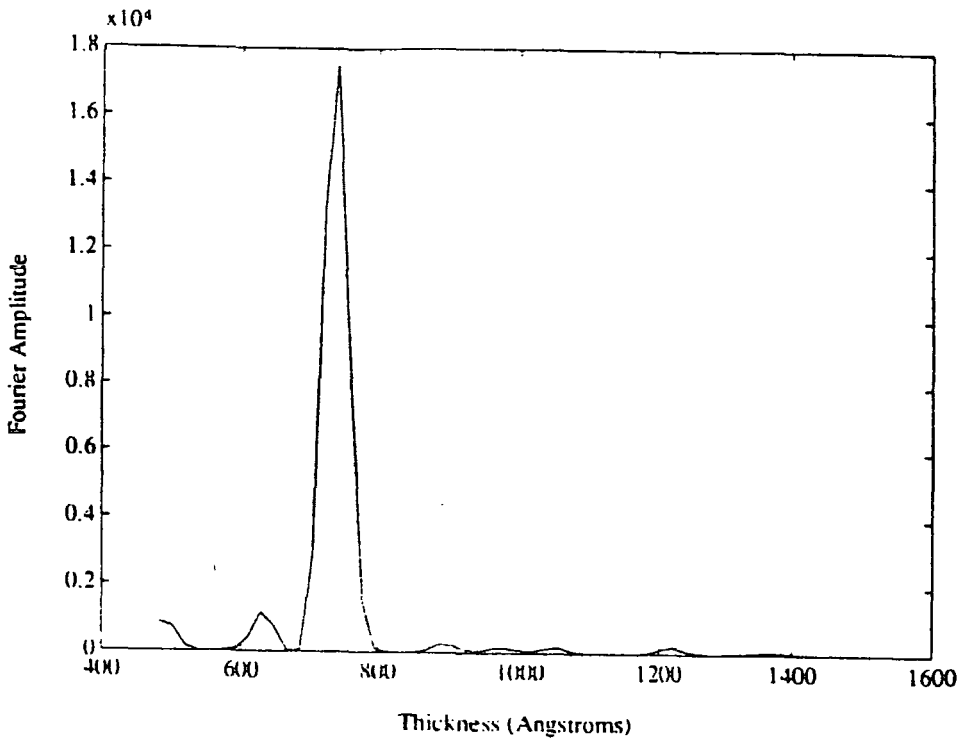


(ii) FFT of autocorrelated, normalised, windowed data

Figure 5.21(b) : FFT of autocorrelated rocking curve (3-0550e.x01). Normalise method, windowed data.

Sample structure : GaAs Sub./100Å $In_{0.13}Ga_{0.87}As$/270Å $Al_{0.22}Ga_{0.78}As$/415Å GaAs

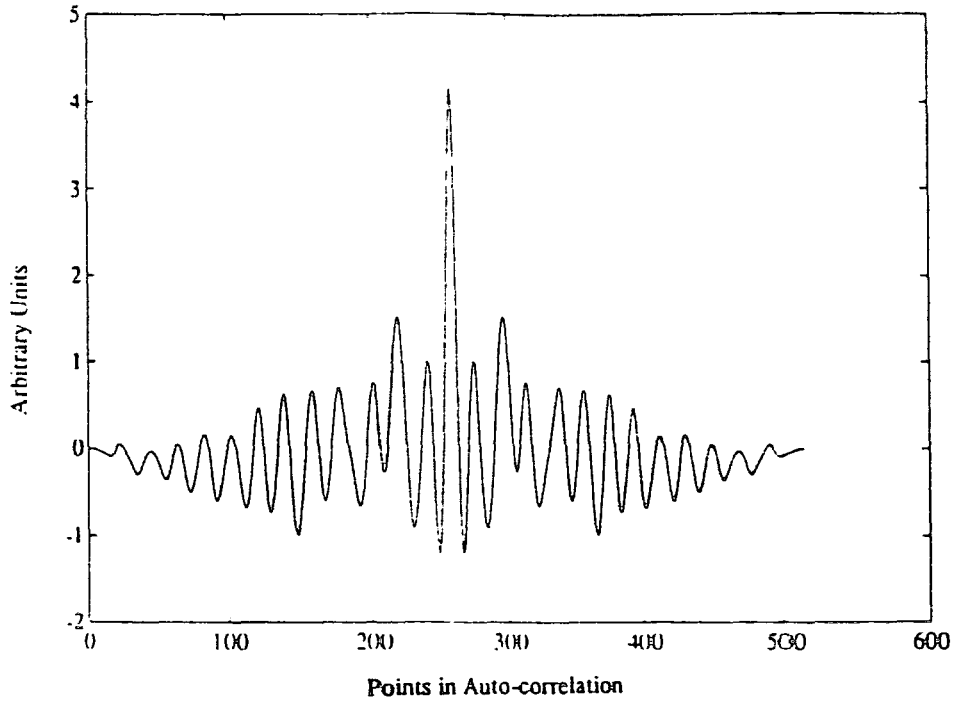


(i) Autocorrelated, windowed, normalised data

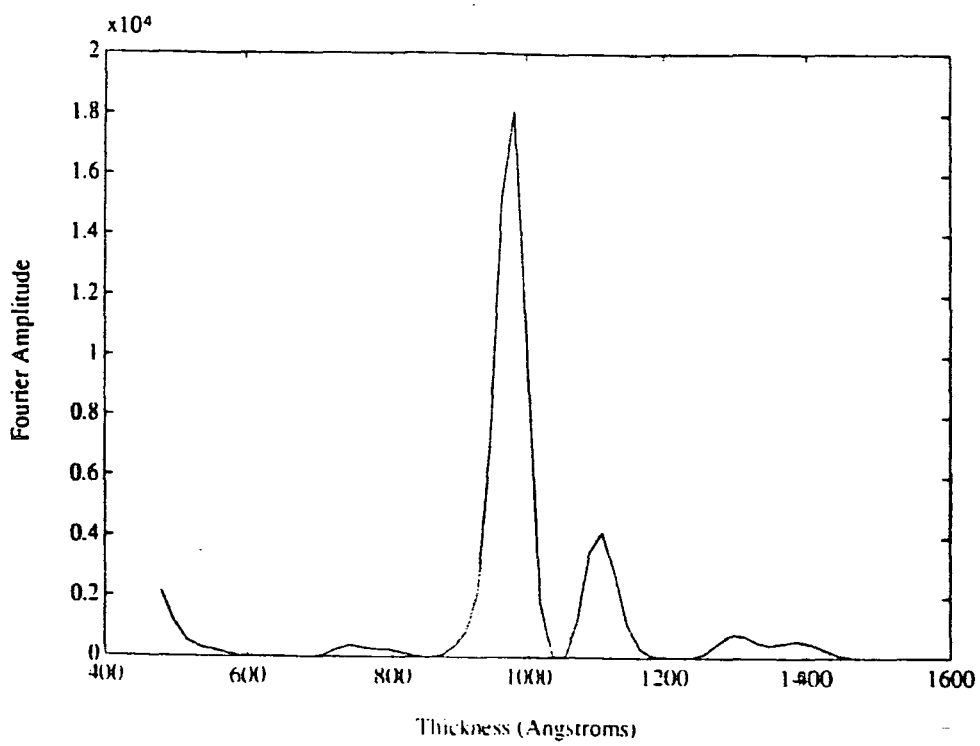


(ii) FFT of autocorrelated, normalised, windowed data

Figure 5.21(c) : FFT of autocorrelated rocking curve (3-0964c.x02). Normalise method, windowed data.

Sample structure : GaAs Sub./180Å $In_{0.13}Ga_{0.87}As$/400Å $Al_{0.18}Ga_{0.82}As$/550Å GaAs

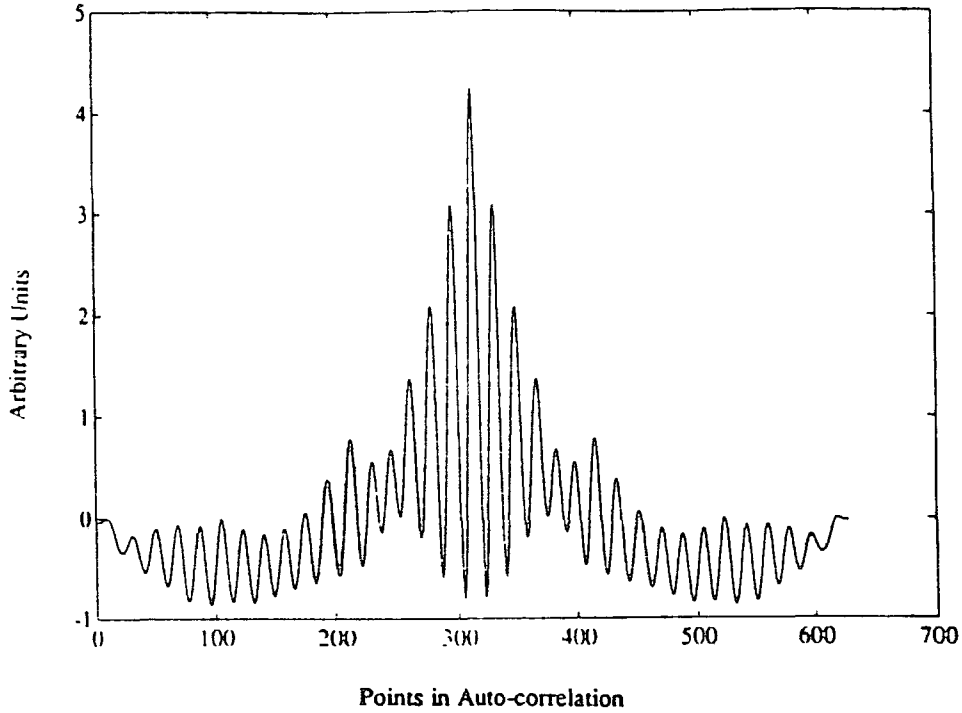


(i) Autocorrelated, windowed, normalised data

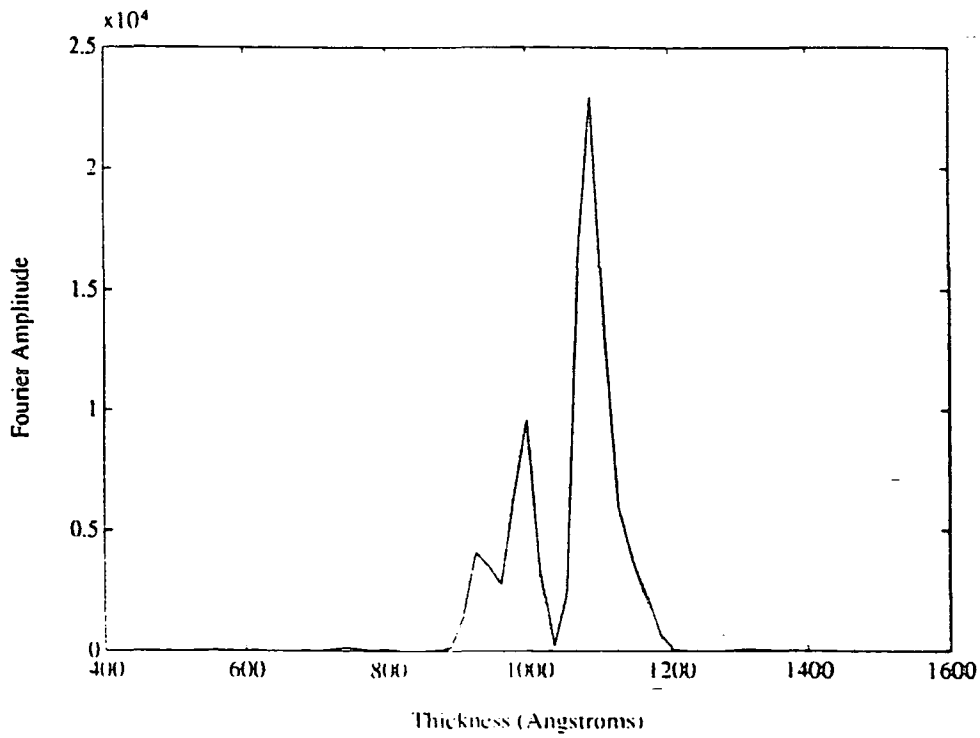


(ii) FFT of autocorrelated, normalised, windowed data

Figure 5.21(d) : FFT of autocorrelated rocking curve (3-0964c.g13). Normalise method, windowed data.

Sample structure : GaAs Sub./180Å $In_{0.13}Ga_{0.87}As$/400Å $Al_{0.18}Ga_{0.82}As$/550Å GaAs

corresponds to an average of the total thickness above the InGaAs layer and the total stack thickness. Whether or not this is of use to the characterisation of the transistor is dependent upon the particular layer which requires characterisation and the availability of other non destructive characterisation techniques for this thickness regime available to the grower. For situations where the same layer system is produced on a large scale, previous calibration of the method could be used as a test of the consistency of layer thicknesses.

# Chapter VI

# Absolute Measurement Of Lattice Parameters Using Triple Axis Diffraction Techniques

## 6.1 Introduction

The use of lattice parameter measurements on semiconducting samples has long been recognised as providing information on sample stoichiometry, alloy composition, dopant and defect concentration. For the case of III-V semiconductors, measurement of the wafer lattice parameter yields information on the dislocations, growth striations and precipitates present within the crystal. Experimental x-ray scattering techniques for accurately determining lattice constants have been available for several decades, an example being the classic single crystal method developed by Bond[1] in 1960. This method (or variations of) has been used by many workers, including Willoughby[2] et al., who undertook a study of sample stoichiometry and homogeneity in a series of GaAs samples fabricated from different growth methods/conditions. This chapter will briefly review some of the more common techniques of lattice parameter measurement before outlining a novel method, using a standard triple crystal diffractometer, of determining lattice constants.

## 6.2 Methods Of Lattice Parameter Measurement

The various experimental methods used to measure lattice constants have been discussed by Hart in a seminal review paper[3], where methods are grouped into either single or double crystal techniques and classified according to their sensitivity. For a complete description of the various methodologies, the reader is referred to the paper of Hart (and references therein) on how the different techniques are conducted (and analysed) in practice. The following section concentrates only on the achievable accuracy of each technique and the instrumentation required to conduct each measurement.

### 6.3.1 Single Crystal Methods

As already stated, one of the most popular single crystal techniques used in lattice parameter determination is the Bond[1] method. The Bond method measures to high accuracy (as well as precision) the absolute Bragg angle of a particular reflection, while ensuring that experimental systematic errors are minimised. By then substituting this measured angle into the Bragg law, a value for the lattice constant is obtained (for a given wavelength value). In common with many single crystal methods the technique utilises the fact that by using high angle Bragg reflections, and measuring angular positions from the sample axis (instead of at the detector position), errors other than the intrinsic error in the location of the Bragg peak (arising from its dispersed width) can be made negligible.

### 6.3.2 The Bond Method

The schematic experimental arrangement for the Bond method is shown in fig.6.1. Here a well collimated incident beam is directed on to the sample, mounted on a standard goniometer, and the difference in the positions of the *hkl* and $\bar{h}kl$ reflections is found. The angular change in going from one reflection to the other is twice the reflection Bragg angle, and this eliminates the uncertainty in the zero setting of the diffractometer. By reference to the differential form of Bragg's law (eqn.6.1), the advantage of working with large Bragg angles can be seen.

$$\frac{\delta d}{d} = \frac{\delta \lambda}{\lambda} - (\cot\theta)\delta\theta \qquad (6.1)$$

For a large Bragg angle the factor cot(θ) is small, giving better overall sensitivity or resolution of lattice parameter determination ($\delta d/d$). Hart[3] points out that, in the laboratory, the use of characteristic lines as the x-ray source means that it is rare to find a combination of x-ray wavelength and interplanar spacing giving Bragg angles of over 80°. By conducting Bond measurements with white radiation sources (i.e. synchrotron radiation) then Bragg angles approaching 90° can be employed, with a corresponding improvement in the resolution of the lattice constant determination. While the Bond technique eliminates zero setting errors, peak asymmetry effects (where the maximum intensity may not necessarily equate to the peak centroid) must be taken into account. Even if a beam conditioner is

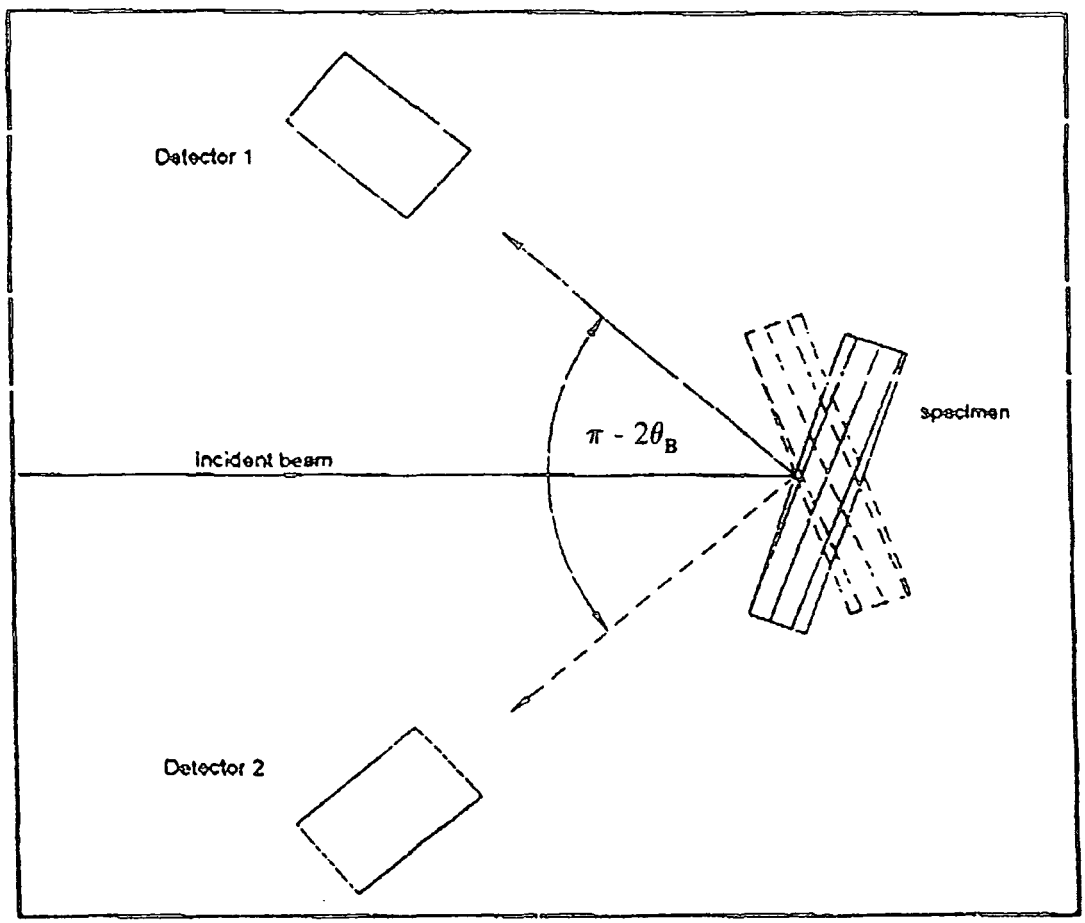


Figure 6.1 : The Bond Method for lattice parameter determination

used, the peak profiles of the *hkl* and $\bar{h}kl$ reflections will be different as only one of the two reflections can be in the non-dispersive geometry. The technique is also sensitive to errors arising from the vertical divergence of the incident beam and the collimator not being normal to the axis of crystal rotation (beam tilt) or the zone axis of the Bragg planes (specimen tilt). Bond has shown that the error in lattice constant determination can be reduced to around 1 part per million (p.p.m.) if the sum of these three errors can be reduced below 5 minutes of arc. The cyclic gear errors inherent in long range goniometer motions must also be taken into consideration, with the use of angular encoders recommended, if a range of around 60° and calibrated accuracy to less than one arc second is required. Finally, it should be noted that the effects of refractive index on the incident beam must also be compensated for if accuracy at the parts per million level is to be achieved. The refractive index of x-rays in materials is slightly less than one, implying that the probing x-ray beam is (slightly) bent towards the sample surface upon entering the crystal bulk. Thus the measured Bragg angle will be slightly larger than that expected kinematically, as the crystal angle must be increased to allow for the refractive index offset. In the Bond method, the refractive index corrections are equal for both reflections and add to the nominal Bragg angles in both measurements. In practice, the Bond method can give repeatable measurements with a precision of better than 1 part in $10^6$. However, comparison between different laboratories using different apparatus and samples gives agreement to only a few parts in $10^6$, and this is probably a more realistic estimate of the absolute accuracy of the Bond technique. It is interesting to note that, when comparing the lattice parameter of different GaAs samples, as deduced from a host of laboratories[4], the overall disagreement between different workers can be as large as 130 p.p.m., even though some individual measurements have quoted errors of only 5 p.p.m. (clearly the lattice parameter of GaAs samples grown by different growth methods/laboratories can vary largely). Often the use of lattice parameter measurements is combined with other techniques, such as x-ray topography, to examine closely defect structure[5]. The use of the Bond method to measure lattice parameters has been combined by Sajovec[6] et al., with high precision density measurements to study the defect structure in GaAs crystals, a method discussed theoretically by Morozov and Bublik[7].

An alternative method of lattice constant measurement, using single crystal techniques, is the Kossel method[3]. All the possible x-ray beam paths of a single

Bragg reflection from a point source lie on the surface of a cone whose semi-vertex angle is $(\pi/2-\theta_B)$ and whose axis is normal to the effective Brag plane. A large number of conic sections can be recorded on a film or photographic plate and their geometry allows a determination of $(a/\lambda)$. A major advantage of the Kossel method is that the technique also allows simultaneous determination of the sample orientation from very small crystal volumes (a few $\mu m^3$). As with the Bond method the error is chiefly dependent upon the x-ray linewidth and lattice parameters can be measured with a precision approaching a few parts per million, although this sensitivity reduces to around 1 part in $10^4$ if photographic plate distances of only a few centimetres are employed[8].

Extremely rapid lattice parameter measurements can be performed by use of synchrotron radiation and an energy dispersive geometry. Here, the incident (white) x-ray beam and the scattered beam are finely collimated so that the angle of Bragg scattering is fixed. Bragg's law can then be written in terms of the incident x-ray energy, E, as shown in equation 6.2.

$$\lambda = 2d\sin\theta = \frac{hc}{E} \tag{6.2}$$

The constants h and c are the Planck constant and the velocity of light, respectively. For fixed Bragg angle and polychromatic incident beam, several different orders of diffraction (from planes of spacing d/n) will be present in the scattered radiation (with energies nE). Measurement of the energies, nE, with a solid state detector permits the interplanar spacings, and hence lattice parameter, of the sample crystal to be determined. With synchrotron radiation collimation of the incident beam to $10^{-4}$ radians allows peak location to $10^{-4}$ of the scattered energy. Hence, lattice parameter determination to one part in $10^4$ is possible in only a few minutes of data collection[9]. While still significantly worse than techniques such as the Bond method, a particular advantage of the energy dispersive technique is that no moving parts are required, and measurements may thus be easily carried out at extreme pressures and temperatures. Application of this technique in the laboratory gives a much poorer resolution of around $10^{-2}$ to $10^{-3}$, mainly due to the inferior collimation of the incident beam, although laboratory based experiments have been usefully applied in the solving of powder and crystalline sample structures by some workers[10,11].

## 6.4 Multiple Crystal Methods

In addition to the several single crystal modes which have been used to determine lattice constants, a variety of multi-crystal methods have been developed by other workers, the most common of which are pseudo non dispersive double crystal techniques. The advantage of non dispersive methods is that they yield diffraction peaks which are, in principle, symmetric. It is now possible to determine precisely the peak location and the error which arises from the dispersed x-ray line shape in single crystal measurements is eliminated. As stated above, the main requirement for lattice parameter determination in single crystal techniques is to measure large angles not only with good precision but also high absolute accuracy. This differs from the use of double crystal methods, which can be thought of as being essentially differential techniques (the Bragg angle is compared with that from a reference crystal of known d-spacing), where precise angular measurements are needed over a much shorter range.

The lattice parameters of Si doped crystals with varying degrees of Boron doping have been measured using a double crystal diffraction technique by Fukumori[12] et al., with the lattice constants measured quoted with an accuracy of 8 parts in $10^6$ (8 p.p.m.). Their method involves using a hand made Ge monochromator which simultaneously diffracts, from different surfaces, the $K\alpha_1$ and $K\alpha_2$ characteristic lines from a standard x-ray tube. This method is typical of many techniques devised, with non-standard monochromating crystals an integral feature of the experimental apparatus. Obviously, those methods which require no specialised crystals or stages to be constructed are potentially of much more interest to the experimentalist who wishes to carry out lattice parameter measurements routinely.

Such a method has recently been proposed by Bowen and Tanner[13] who describe a method of lattice constant determination using a standard high resolution X-ray diffractometer. The Bragg angle of the specimen crystal is compared with that of a Si reference crystal (with known lattice parameter) in order to determine the lattice parameter. The problem when using a reference crystal, which essentially "calibrates" the diffractometer, is that once the instrument zero has been determined it is lost upon replacement of the reference crystal with the specimen. Bowen and Tanner have demonstrated that by using a specimen rotation stage to

record Bragg peaks at rotary stage positions of 0° and 180° (and using the mean value), tilt errors on the specimen setting can be eliminated. Peak location to around 1 arcsecond then permits absolute, traceable lattice parameter determination, in principle, to a few parts in $10^6$. However, lack of precision in the rotation stage is the limiting experimental accuracy and, in practice, the level of reproducibility (at 3 sigma) is set to around 3 parts in $10^5$. The Bowen-Tanner technique has been applied in the determination of the Zn concentration in substrates of $Cd_{1-x}Zn_xTe$, with the Zn fraction being found to an accuracy of 0.1% (this corresponds to a change in lattice parameter, assuming Végards law, of 6 parts in $10^5$)[14]. Fatemi[15] has devised a related technique using a standard double crystal diffractometer, but where the sample and reference crystals are both mounted *simultaneously* on the second axis. The mounting stage (fig.6.2) can be rotated and tilted inwards or outwards to bring the Bragg plane normals parallel to that of the first crystal. By applying his technique to the study of III-V compounds Fatemi could measure lattice parameters to a precision of 8 parts in $10^6$.

Using a triple axis arrangement, incorporating two double leaf Si springs in monolithic crystal assemblies, Häusermann and Hart[16] have measured differences in the lattice spacing of Si crystals from different origins, with an accuracy of 1 part in $10^8$ in experimental periods as short as two minutes. Using methods which simultaneously combine optical and x-ray interferometry, so that measurements of the absolute value of the x-ray wavelength and Bragg angle are not required, the lattice parameter of a Si crystal can be determined with an absolute precision of (± 0.1 p.p.m.)[17]. Buschert[18] et al. have pointed out that, in many cases, the accuracy of some measuring techniques has overtaken the reproducibility of the lattice parameter of Si across a small area (few $mm^2$) of the best hyperpure dislocation free crystal.

In addition to the study of the stoichiometry and defect concentration of Si and III-V single crystals (which are commonly employed as substrates in the semiconductor industry), experimental techniques have been devised to measure the lattice parameter of epitaxial layers grown on thick single crystal substrates. Often the composition of an epitaxial layer can be determined from its lattice constant. For the accurate measurement (i.e. a few parts in $10^6$) of layer lattice constants, single crystal techniques, such as the Bond method, are not appropriate since they involve measurement of peak positions which are broad due to

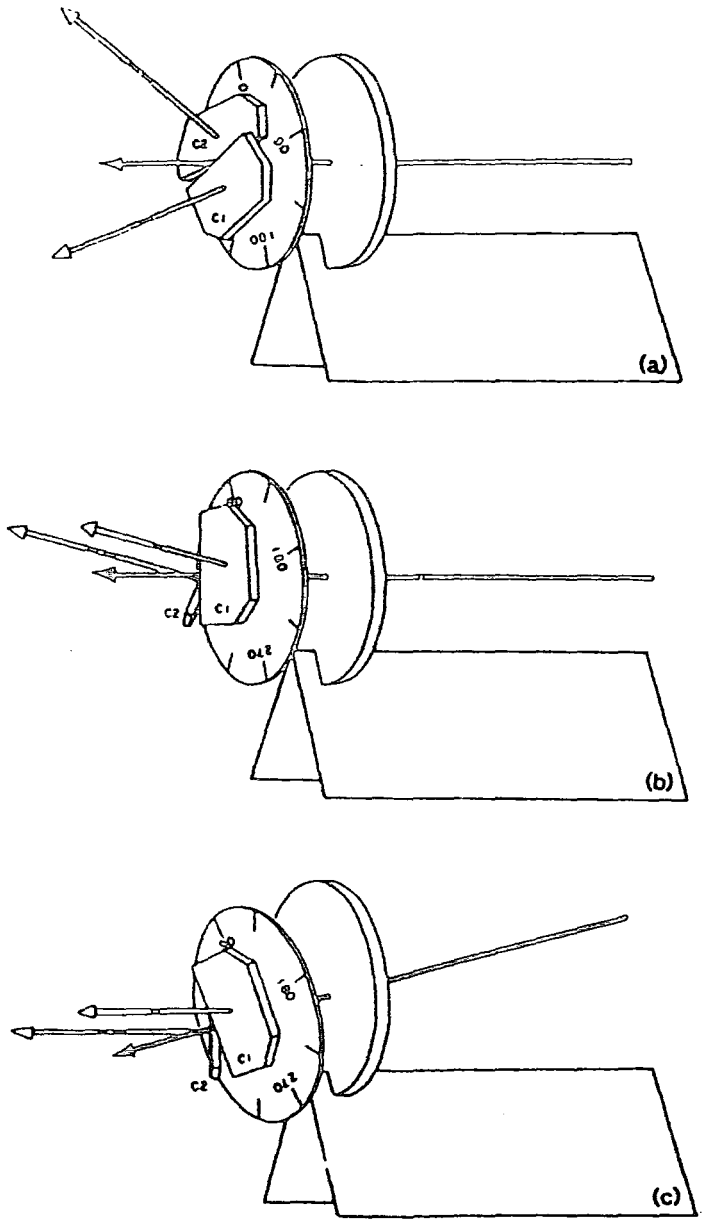


Figure 6.2 : The tilt alignment sequence applied by Fatemi[15] for two crystals.

(a) The plane normals are shown tilted in two arbitrary directions. (b) The two crystal block is rotated to give both normals parallel projections onto a vertical plane. (c) The assembly is tilted inwards (or outwards) to make both tilts parallel to that of the "first" crystal.

dispersion and are the unresolved convolution of the layer and substrate. As outlined above, and in Chapter III, use of a double crystal geometry in the parallel non-dispersive setting, yields diffraction peaks which are both symmetric and narrow. While the separation of the layer and substrate peaks will give the relative difference (i.e. the mismatch) between the lattice parameters of the layer and substrate, the absolute value of the substrate lattice constant is not known (unless previously determined by some other technique) and hence the absolute value of the layer lattice parameter can not be determined. Further, the substrate may also be heavily strained near to the interface region, again leading to a false value for the layer lattice parameter.

One approach to circumvent this problem is to construct a diffractometer capable of recording both double crystal rocking curves and single crystal lattice parameter measurements. This has been done by Fewster[19] who mounted a second motorised axis (for a reference crystal) onto a commercial single axis goniometer (fig.6.3). The sample is mounted on the first axis in the normal way for a standard single crystal lattice parameter determination. The reference crystal is then rotated around the first axis and the double crystal rocking curve recorded. From the single crystal lattice parameter measurements and the measured (double crystal) mismatch the absolute lattice parameter of the layer can be established to a few parts in $10^6$. This idea of combining different techniques has also been used by Estop[5] et al. in the study of epitaxial $Al_xGa_{1-x}As$ layers on GaAs, where double crystal diffraction methods where used to measure the relative mismatch having previously obtained the lattice parameter of GaAs from Debye-Scherrer measurements. The approach of Estop et al. is valid for elastically isotropic structures, and also for anisotropic cubic solids (provided that the growth direction is {001}). For growth directions other than {001}, Hornstra and Bartels[20] have shown how the state of layer strain may be calculated. Pietsch[21] et al. have pointed out that the sensitivity of measurements of the lattice parameter difference between the substrate and heteroepitaxial layer can be enhanced by use of an extremely asymmetric diffraction geometry. For angles of incidence slightly greater than the critical angle for external reflection the Bragg peaks are shifted away from the kinematically predicted positions. For heteroepitaxial structures the layer and substrate peaks are shifted by different amounts. This angular deviation is dependent upon both the angle of incidence and mass density of the material used. Hence, using this technique it is possible to characterise layers of totally

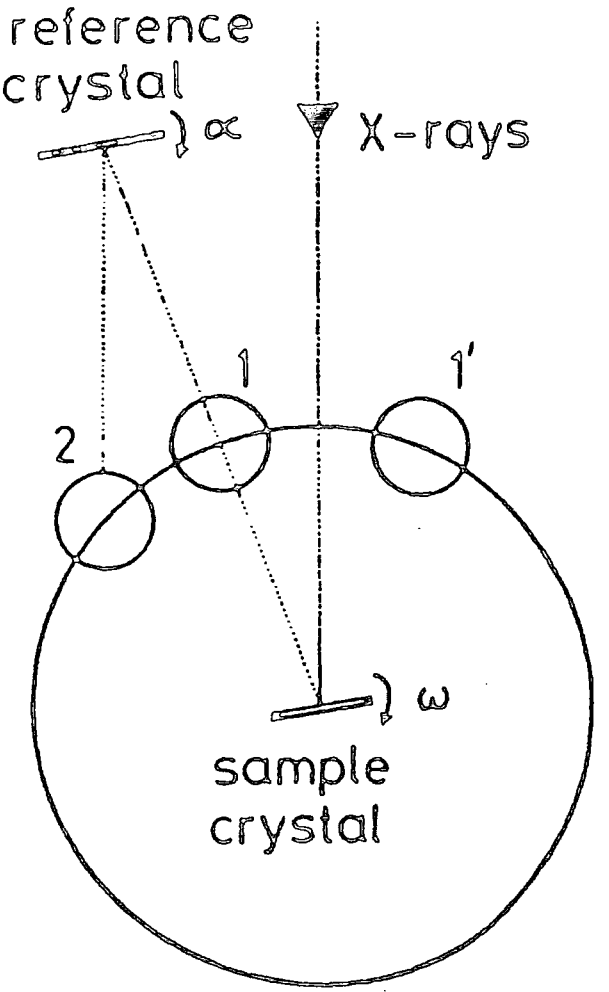


Figure 6.3 : The geometry of Fewsters[19] double crystal method for the lattice parameter measurement of epitaxial layers. For measurement of mismatch the detector is placed at 2. For measurement of lattice parameters the detector is positioned at the points 1 and 1'.

lattice-matched structures (where in the symmetric double crystal geometry only one peak would be recorded).

Finally, it should be noted that the precision of some techniques can be far in excess of the precision with which x-ray wavelengths are known. Hart points out that few x-ray wavelengths are known even to 1 part in $10^6$, with some tabulated values being in error to more than 10 parts in $10^6$. Further, when measuring at the parts per million level the elastic strains induced by variations in temperature, pressure, mechanical stress and electric and magnetic fields must be taken into account. For example, the coefficient of thermal expansion in semiconductor materials ranges from 3 to 30 $x10^{-6}$ $°C^{-1}$ and the bulk compressibility is of the order of $10^{-6}$ $bar^{-1}$. Hence, the variation in the bulk lattice parameter of a semiconductor with temperature and pressure is 3 to 30 parts per million /°C and 0.33 parts per million per bar, respectively. Thus, when quoting lattice parameter values the temperature, pressure and value of x-ray wavelength used should be quoted. Bearden[22] has published a review of x-ray wavelength measurements which has gained wide acceptance in the scientific community, with many workers using the wavelength values reported in this text.

## 6.5 A Triple Crystal Method For Measurement Of Lattice Spacings

Some of the methods used to determine material lattice parameters require the use of specially constructed instruments, dedicated to the measurement of lattice constants. Other methods, such as the Bowen-Tanner technique described in the previous section, utilise standard industrial double crystal diffractometers without the need for additional goniometers or crystal systems (i.e. monochromating elements) to be manufactured, as required in methods employed by other workers[12,16,23]. These techniques are obviously of great practical importance as they can be incorporated into existing x-ray diffraction characterisation with little or even no equipment refinement. In the following section a new technique for lattice parameter measurement is described, using a commercial triple crystal diffractometer. The method requires no additional instrumentation and is no more complicated to perform than a standard triple crystal measurement.

In the triple axis technique a beam conditioning system and analyser crystal are used to define strictly the incident and diffracted wave vectors ($\underline{k}_0$ and $\underline{k}_h$

respectively), thus allowing accurate measurement of the Bragg angle. As for the Bowen-Tanner double axis technique, this angular measurement is compared with that from a silicon crystal, in order to deduce the lattice constant of the specimen relative to that of the (well known) Si reference. The analyser position is set to diffract x-rays of wave vector $\underline{k}_h$ from the reference crystal so that, upon exchanging the specimen for the reference, diffraction from the analyser will only occur when the sample has the "offset" as the reference crystal, thus maintaining the zero setting of the diffractometer. Hence, in this case there is no constraint on the relative sample and reference crystal positions (so long as the analyser setting is left unchanged) and it is therefore straightforward to exchange sample and reference crystals. Care need only be taken that both crystals are correctly tilt optimised after the "double crystal" peak has been found, so that both sets of diffracting planes are in the same relative orientation. The zero position of the diffractometer is found by rotating the analyser, which is set to diffract x-rays of wave vector $\underline{k}_h$, around the detector (2θ) circle until it intercepts the reference diffracted beam, giving a (symmetrical) triply diffracted beam. The measured position of the analyser on the detector circle is compared with that predicted theoretically to determine the instrument zero. The reference is then exchanged with the sample crystal and, with the analyser set to diffract x-rays at the same wave vector value, $\underline{k}_h$, the analyser is moved around the detector circle until the 2θ position of the sample diffracted beam is found (as indicated by a diffracted peak from the analyser). From the Bragg law, $\lambda = 2d \sin\theta$, the lattice constant ($d_s$) of the sample crystal can be deduced (after making offset and refractive index corrections).

## 6.6 Experimental Procedure

Assuming the use of a triple crystal diffractometer (as discussed in Chapter IV, and shown schematically in fig.4.1) which allows the analyser angular setting to be changed either by rotating the analyser crystal around an axis concentric with the sample crystal (i.e. the 2θ or "detector" axis), or by rocking the analyser about an axis co-planar with the sample rotation, centred about the analyser crystal itself ("Axis 3"), then the measurement procedure is as follows.

1. The analyser is moved around the motorised 2θ axis until it is brought into the path of the monochromator beam (i.e. at zero on the 2θ circle) and the Bragg

peak found (by rocking Axis 3). Having established the position of the analyser Bragg peak at this point on the third axis, subsequent peak location procedures using the analyser crystal should involve only small angular motions.

2. The analyser is then rotated or translated away.

3. The reference crystal is placed on the second axis and the double crystal peak found (Axis 2). A tilt optimisation procedure is then performed to bring the Bragg diffracting planes of the reference crystal parallel to the diffracting planes of the monochromator and channel cut collimator.

4. With the reference crystal set for maximum diffraction, the analyser crystal is moved into the path of the diffracted beam ("detector" axis) and the triply diffracted peak maximum found precisely (Axis 3).

5. The detector circle position of the analyser peak maximum is recorded.

6. Using either the detector drive circle or a precise linear translation (the "Xscan" motion), the analyser is moved back out of the sample diffracted beam.

7. The specimen is then substituted for the reference crystal on the second axis, the doubly diffracted beam found and tilt optimised.

8. Moving only the detector circle drive, the analyser is rotated to locate the triply diffracted beam maximum.

9. Finally, the detector circle position is recorded at this peak maximum.

It is important to stress that once the peak from the analyser crystal is found for the first time, the setting of the fine (third) axis used to adjust the analyser angular position is left unchanged. This setting defines the value of $\underline{k}_h$ passed through the diffractometer and all subsequent motions must be on the detector circle. Extreme care should also be taken that all motor movements are carried out in a consistent manner, avoiding the incorporation of gear "backlash" errors.

In stage 6 above, two methods were given by how the analyser could be moved away from the reference diffracted beam, in order to find the "double crystal" peak from the specimen crystal. The analyser can either be rotated back around the detector circle ("detector" motor) or translated linearly out of the diffracted beam ("Xscan" motor). The particular technique used depends to some extent on the experimental resources available. The third crystal stage supplied for the Bede model 200 diffractometer incorporates a specially built housing, sited directly behind the analyser crystal, in which the scintillation detector is held. As this is a fixed part of the third crystal stage, then as the analyser stage is rotated back around the (2θ) circle, the detector is also moved away from the reference diffracted beam. It is therefore useful, when swapping over to the sample crystal, to use a second free standing detector in order to find the sample "double crystal" diffraction peak. Thus in finding the analyser position on the detector circle for the sample triply diffracted beam, the only motion of the analyser crystal has been around the detector circle. The alternative method, translating the detector away using the "Xscan" motor, has the advantage that only one x-ray detector is necessary as the Xscan motion moves only the analyser crystal and no other part of the third crystal stage (which incorporates the detector housing). Experimentally, this would then mean that two separate motions of the analyser have been carried out (a linear translation followed by a rotation around the detector circle) which, potentially, provide two separate sources of error. In particular, if the analyser is to be moved away with a linear translation, then it should be ensured that the quality of the translation stage construction is high so that the analyser does not significantly "wobble" slightly as the analyser stage travels up and down the lead screw thread. The effect of this "wobble" would be to change slightly the (set) angular position of the analyser (Axis 3) so that x-rays of wave vector $\underline{k}_{H'}$ are diffracted into the detector. The quality of the linear translation stage on the Bede 200 is such that, if the analyser is set to its Bragg peak (typical width 4"), then if the analyser is repeatedly translated in and out of the diffracted beam then the analyser Bragg peak position can be reproduced with an accuracy of 1-2".

## 6.7 Analysis Of Results

The role of the reference crystal in the above procedure is to determine the instrument zero. The theoretical 2θ position of the Si crystal peak can be accurately determined, using the Bragg law, so long as the wavelength of the

incident radiation and lattice parameter of Si are accurately known. The measured $2\theta$ position of the reference beam (i.e. the detector circle position of the analyser crystal, when set to diffract x-rays of wave vector $\underline{k}$), is compared with that predicted theoretically in order to determine the diffractometer offset angle. This offset is then subtracted from the measured position of the sample diffracted beam (on the $2\theta$ circle) to get the apparent Bragg angle of the sample reflection. To obtain the *actual* Bragg angle, $\theta_s$, from this apparent value, a small refractive index correction must then be applied, to take account of the peak shift from the predicted kinematical position. This adjustment is, in fact, the difference between the refraction corrections of the specimen and reference crystals and is usually of the order of a few arc seconds. The exact size of the refractive index shifts can be calculated from the Bede RADS simulation program. Now that the "true" specimen Bragg angle has been determined the lattice parameter of the sample can be determined by equating the Bragg conditions of the sample and reference crystals, i.e.

$$\lambda = 2d_r \sin\theta_r = 2d_s \sin\theta_s \tag{6.3}$$

$$\therefore \quad d_s = d_r \frac{\sin\theta_r}{\sin\theta_s} = d_r \frac{\sin\theta_r}{\sin(\theta_r + \delta\theta)} \tag{6.4}$$

Here the subscripts r and s refer to the sample and reference crystals respectively, and the factor $\delta\theta$ is the difference between the two sample's Bragg angles.

## 6.8 Accuracy Of The Triple Axis Technique

The accuracy of the lattice parameter determination is dictated by how accurately measurement of the Bragg angles can be accomplished. The Bragg angle measurement will be affected by two factors, namely how precisely the instrument zero can be calculated and by how well the actual Bragg peak positions can be physically located and measured. To minimise the error in determining the instrument zero, accurate values for the x-ray wavelength and Si lattice parameter presumed, must be used. This latter requirement presents no difficulty as the lattice constant of commercially available Si is reliable to around 1 part in $10^6$ (in fact, the lattice parameter of highly pure Si is known accurately to 8 part in $10^8$ and is actually a length standard in the nanometre region). The error associated with the wavelength used is not of paramount importance because, as pointed out

by Bowen and Tanner[13], the wavelength error enters only as a second order correction. Hence the precision of the lattice parameter determination depends mainly on the (experimental) measurement of the angles. The Bede 200 diffractometer uses a spur gear and gearbox drive to achieve a step resolution of 1". Hence, the dominating factors on the lattice parameter determination will arise from the precision of the gear cutting and the accuracy with which the peak position can be resolved.

## 6.9 Effect Of Sample Tilt

One other factor which will affect the Bragg peak position (and hence the entire lattice parameter calculation) is the presence of a sample tilt. The effect of a sample tilt will be to record a smaller Bragg angle than that predicted theoretically.

The effect of sample tilt has been investigated empirically by noting the change in analyser peak position when a small movement away from the tilt optimised position is introduced. Using a crystal of InAs, a deviation of 0.2° from tilt optimisation gave a change in the measured 2θ position of the analyser crystal corresponding to less than 2". A deviation of 0.4° from the optimised position resulted in a reduction in the InAs (004) 2θ value of 6". Since the sample tilt could be optimised to within ± 0.1°, the error from incorrect tilt setting is estimated to be at around 1".

## 6.10 Example Measurements From The Triple Axis Technique

A set of exemplary data, illustrating the use of triple crystal methods to determine lattice constants, is presented below. The results were collected on a commercial Bede 200 diffractometer fitted with a third crystal stage. Incident beam angular divergence was restricted to 5" using a Si (022) Channel Cut Collimator crystal. The wavelength dispersion was limited to 1.4 $x10^{-4}$ by a Si monochromator crystal and a four bounce Si (111) channel cut crystal was used as the analyser. All measurements were carried out at room temperature (22°C) and normal atmospheric conditions.

Initially, the lattice constant of a GaAs crystal (obtained from Bede Scientific Instruments Ltd., Durham and grown by the Horizontal Bridgman method) was

determined using the (004) reflection from an (001) oriented Si reference. The experiment was then repeated for the same GaAs crystal but with the reference reflection changed to the (333) peak from a (111) oriented Si crystal.

Tables 6.1 and 6.2 record the average of repeated measurements of the analyser peak position on the (2θ) circle. At first, the peak position was recorded 20 times but it was found that repeated measurement of this position gave values which at worst were 1" in disagreement. Hence, this number of scans was taken to be excessive and the total number of measurements used to record an average detector position was kept much smaller than this (5).

GaAs Sample (With Si(004) Reference)

| Measured 2θ (Si(004)) | Measured 2θ (GaAs) | Zero Error | "Corrected" θ (GaAs) | Lattice Parameter (Å) |
|---|---|---|---|---|
| 69.14203° | 66.05472° | 0.00749° | 33.01923° | 5.65426 |
| 69.14250° | 66.05528° | 0.00773° | 33.01927° | 5.65426 |
| 69.14222° | 66.05528° | 0.00759° | 33.01941° | 5.65424 |
| 69.14250° | 66.05583° | 0.00773° | 33.01955° | 5.65424 |

$\bar{d} = (5.65424 \pm 0.00006)$Å

Table 6.1 : Measured and corrected 2θ values for a GaAs crystal. The instrument zero has been determined with an (004) reflection from an (001) Si crystal.

The "measured" 2θ values in the above table (and in all subsequent tables) correspond to the actual analyser position on the detector circle, at the point that the triply diffracted beam was found. Each value is the average of five separate measurements of the analyser position. In no case did any of the recorded values differ from the other members of its set by more than 1". Hence, by also taking into account the error associated with incorrect sample tilt positioning (±1"), the maximum total error in the measured 2θ position is estimated to be ±2", placing a limit on the (theoretical) resolution of the technique of just under 2 parts in $10^5$. The parameters used to calculate the theoretical Bragg angle of the Si crystal reflection are 1.540562 Å for the CuK$\alpha_1$ wavelength[22] and 5.43102 Å for the Si lattice parameter[24], giving $\theta_B$ (004) =34.563523° and $\theta_B$ (333) =47.47392°. The

column with the "corrected" sample Bragg angle is the value of $\theta_B$ obtained after subtracting the instrument zero error and refractive index correction. The refractive index corrections for the GaAs(004) and Si(004) reflections are (+6.4") and (+4.1"), respectively. Hence, 2.3" has been subtracted from the measured GaAs Bragg angle.

Using the data in Table 6.1, an average value for the GaAs lattice parameter of (5.65424 ± 0.00006) Å, is obtained (to the 3 sigma confidence level). While these results are internally consistent to 1 part in $10^5$ (i.e. a small random error) the systematic/instrumental errors are expected to be greater than this.

GaAs Sample (With Si(333) Reference)

| Measured 2θ (Si(333)) | Measured 2θ (GaAs) | Zero Error | "Corrected" θ (GaAs) | Lattice Parameter (Å) |
|---|---|---|---|---|
| 94.96028° | 66.05639° | 0.00622° | 33.02137° | 5.65394 |
| 94.96083° | 66.05750° | 0.00649° | 33.02165° | 5.65390 |
| 94.96000° | 66.05806° | 0.00608° | 33.02234° | 5.65379 |

$\bar{d}$=(5.65388 ± 0.00018)Å

Table 6.2 : Measured and corrected 2θ values for a GaAs crystal. The instrument zero has been determined with a (333) reflection from a (111) Si crystal.

Table 6.2 shows the data collected from the same GaAs crystal but using the (333) reflection from a (111) oriented Si crystal. Again, the zero offset adjustment and refractive index corrections have been applied before calculation of the final lattice parameter values in the above table (thus the "corrected" $\theta_B$ is the "true" value). From RADS the refractive index shifts are (+4.2") for the Si(333) reflection and (+6.4") for the (004) GaAs peak. Hence, 2.2" has been subtracted from the measured GaAs Bragg angle.

Taking an overall average for the GaAs lattice parameter using the results in Table 6.2 yields a value of (5.65388 ± 0.00018) Å (the error quoted is, again, to the 3 sigma level). The precision of this result corresponds to 3 parts in $10^5$. Comparing the results from Tables 6.1 and 6.2 the two GaAs lattice parameter

values are in agreement to 6 parts in $10^5$. This latter figure is probably a much more realistic measure of the true accuracy of the Bede model 200 diffractometer.

Measurements of the lattice parameter of GaAs have been made by several other workers and Fig. 6.4 shows the spread of GaAs lattice parameter values reported. Taking one of the most widely accepted values for the GaAs lattice parameter of 5.65375 Å (reported by Usuda[25] et al. from synchrotron radiation Bond measurements) it can be seen that the values reported here are in agreement to 8.6 parts in $10^5$ and 2.3 parts in $10^5$, for the data in Tables 6.1 and 6.2, respectively.

Having demonstrated the triple axis technique with a GaAs sample, a further demonstration experiment was also performed on an LEC grown InAs crystal, using the same experimental geometry and measurement procedure.

InAs (With Si(004) Reference)

| Measured 2θ (Si(004)) | Measured 2θ (InAs) | Zero Error | "Corrected" θ (InAs) | Lattice Parameter (Å) |
|---|---|---|---|---|
| 69.14000° | 61.14889° | 0.00648° | 30.56725° | 6.05865 |
| 69.14000° | 61.14944° | 0.00648° | 30.56752° | 6.05860 |
| 69.14028° | 61.14917° | 0.00662° | 30.56725° | 6.05865 |
| 69.14028° | 61.14917° | 0.00662° | 30.56725° | 6.05865 |
| 69.14000° | 61.14890° | 0.00648° | 30.56725° | 6.05865 |

$\bar{d} = (6.05864 \pm 0.00006)$Å

Table 6.3 : Measured and corrected 2θ values for an InAs crystal. The instrument zero has been determined with an (004) reflection from an (001) Si crystal.

Refractive index corrections made were (+4.1") for the Si(004) reference and (+6.7") for the InAs(004) reflection. Thus, a further 2.6" has been subtracted from the measured InAs Bragg angle.

Taking an average of the lattice parameters deduced in Table 6.3, the value for the InAs lattice parameter so obtained is (6.05864 ± 0.00006) Å, again with the associated error taken at the 3 sigma level. While the internal consistency here is 1



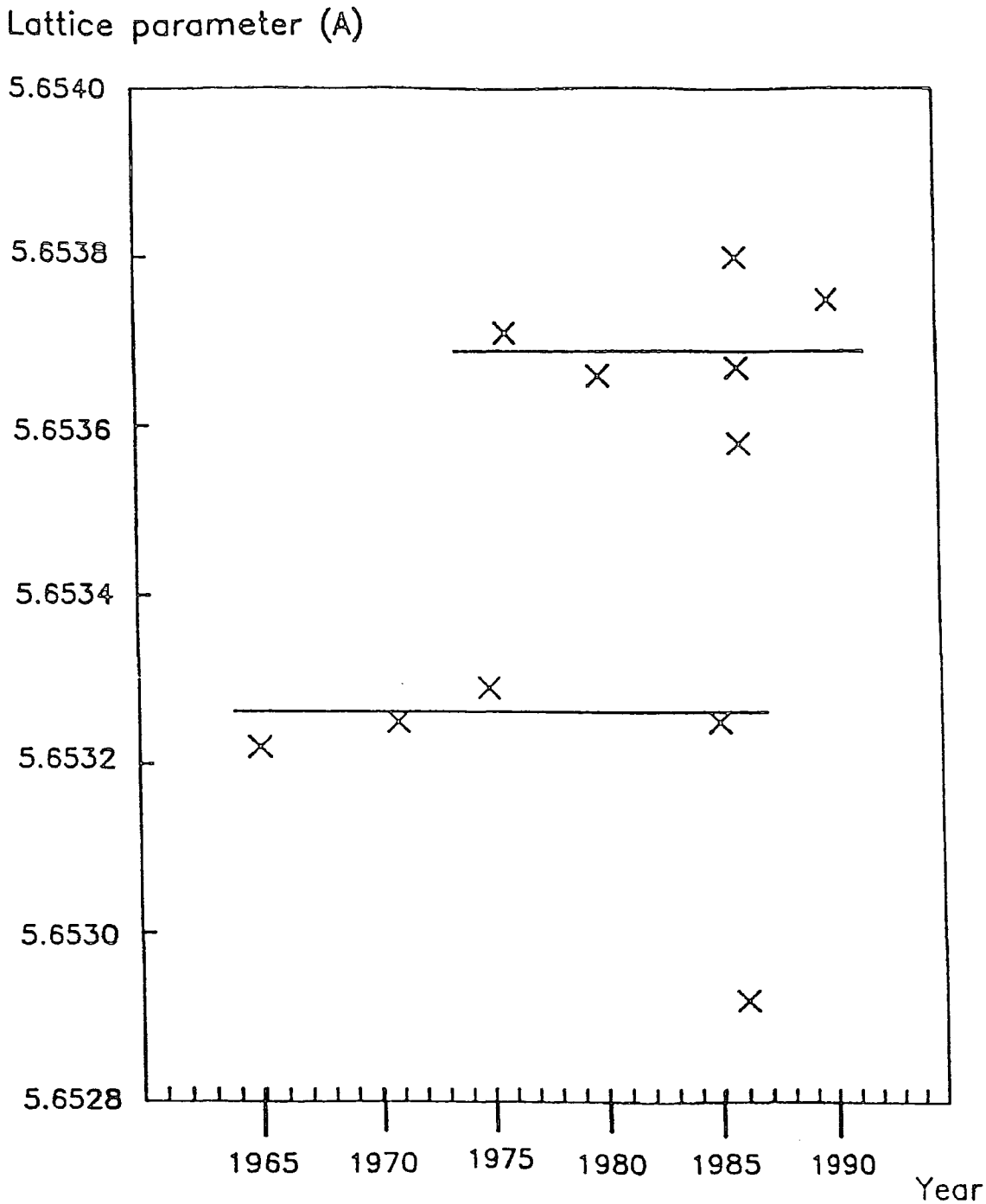


Figure 6.4 : Values of GaAs lattice parameter determined by x-ray methods between 1965 and 1990. After Turnbull[4].

part in $10^5$, comparison with values previously reported in the literature[26,27] of (6.05850 Å) indicate a discrepancy of just over 2 parts in $10^5$.

## 6.11 Conclusions

A method of lattice parameter determination is described which is capable of measuring lattice constants with a precision (i.e. "repeatability" of results) of around 1 part in $10^5$ and an absolute accuracy traceable (theoretically) to 2 parts in $10^5$. The diffractometer offset error is determined by use of a reference crystal for which the lattice parameter is accurately known. The Bragg angle of a sample reflection is then measured, taking into account the offset error and refractive index corrections, in order to determine the lattice parameter from the Bragg law. The technique requires only the use of a conventional triple crystal diffractometer with motorised $2\theta$ circle movement and the provision for a fine, precise rocking motion of the analyser crystal. Exemplary data from GaAs and InAs crystals is presented. Two values for the GaAs lattice parameter are determined, 5.65424 Å and 5.65388 Å, which differ from a currently accepted value of 5.65375 Å by 8.6 and 2.3 parts in $10^5$, respectively. The lattice parameter of the InAs crystal was determined to be 6.05864 Å, which compares with a published value of 6.05850 Å (i.e. a difference of 2 parts in $10^5$). While not as precise as some methods the technique could prove of great use in the measurement of semiconductor alloy composition in, for example, II-VI materials, where mismatch values between substrate and layer can be large (in these cases, the non-linearity of standard double crystal diffractometers over large angular ranges introduces significant error in the DCD measured mismatch). In particular, the technique can be performed on a standard triple crystal diffractometer with no additional equipment requirements. The actual experimental procedure involved is very similar to the normal alignment routine in triple axis diffractometry (Chapter IV), and could easily be carried out routinely, prior to the recording of a triple crystal scan.

# Chapter VII

# Triple Crystal Diffraction And X-Ray Topographic Studies Of Semiconductor Materials

## 7.1 Introduction

The work discussed in Chapters V and VI describes techniques which record the coherently scattered radiation, in order to determine (relatively quickly) structural parameters. Of great interest also is the information content of the diffuse radiation scattered from the sample. The study of this diffuse component requires the use of techniques other than double crystal diffraction, which does not separate the coherent and non-coherent elements of the total sample scatter. The use of double axis diffraction techniques to study defect structure is severely limited by the use of an open faced radiation detector. In the conventional double crystal geometry the scattering from all regions of the sample, both perfect and imperfect, is integrated to form the total diffracted signal. By using a third crystal to "analyse" the scattered radiation as a function of its wave vector (i.e. a triple crystal diffraction geometry), or, by replacing the detector in a double crystal diffraction experiment with a medium which is sensitive to both the intensity and position of the scattered radiation (i.e. a photographic plate or film), the strength and angular distribution of the diffuse scatter can be obtained. Since this diffuse scatter arises from misorientations or imperfections of the crystal lattice, it can be used to identify the defect structure of a sample crystal. The uses of triple crystal diffractometry and double crystal topography (and the information content of each) were reviewed in Chapter IV.

As the diffuse scatter from crystalline structures is normally weak, long experimental data collection times are required if the diffuse signal is to be readily extracted from the background noise. Hence, diffuse scatter studies in x-ray diffraction experiments do not lend themselves easily to routine analysis, where time constraints and high throughput of samples dictate that the characterisation methods employed should be rapid. However, since the collection of the diffuse scatter can reveal structural information which is of use to the crystal grower on a much more fundamental level, the use of such techniques plays an important role in the study of material systems. This is of particular importance for studies of systems whose structural properties

are not well understood, as triple crystal diffraction can help to identify the type and extent of defect structure within a crystalline material, yielding information which may help to correlate structural properties with observed physical/electrical phenomena. In this chapter, triple crystal analysis is applied to the study of three different systems of current technological interest, the $Hg_{1-x}Mn_xTe$ on GaAs, the $Cd_{1-x}Hg_xTe$ on $CdTe/Cd_{1-x}Zn_xTe$ and the low temperature grown GaAs systems. In each case the material system has extensive potential applications for the fabrication of optical and electronic devices. In the study of the $Hg_{1-x}Mn_xTe$ on GaAs system, supporting evidence upon the sample structure is provided by the use of double crystal topographic techniques to study the lattice strain.

### 7.2.1 X-Ray Characterisation Of $Hg_{1-x}Mn_xTe$ (MMT) Epitaxial Films

Semiconductor compounds based on elements from Group II and Group VI of the periodic table display a rich array of potentially exploitable properties, with high carrier mobilities (approaching $10^6$ $cm^2V^{-1}s^{-1}$) and direct energy band gaps ranging from a fraction of an electron volt in mercury containing compounds, to over 3 eV in ZnSe. For very large band gap materials, potential applications exist in the design of injection lasers and LED's operating in the blue portion of the visible spectrum. If the Group II element is substituted for a magnetic transition ion (such as Mn), a new class of materials known as semi-magnetic semiconductors or dilute magnetic semiconductors is formed. These compounds retain the semiconducting properties of the original II-VI compound, but the presence of the unfilled 3d electron shell in the transition element gives rise to localised magnetic moments. Large magneto-optical effects have been observed in these materials (i.e., Faraday rotation, Zeeman splitting in magnetic fields) and this behaviour has been exploited in, for example, optical isolator devices.

$Hg_{1-x}Mn_xTe$ (MMT) is such a dilute magnetic semiconductor having both semiconducting and magnetic properties. The band gap of MMT at room temperature varies continuously from -0.15eV for HgTe to 2.9eV for cubic MnTe[1], with the magnetic and optical properties of MMT making it a likely candidate for the design of magnetically sensitive infra-red devices[2].

The first bulk crystals of MMT were grown by Delves and Lewis[3], who used elemental Hg as the source. The advantage of employing an elemental source lies in

the facts that elemental Hg is available in high purity at reasonable cost, has sufficient vapour pressure for growth and the toxicity of elemental Hg when absorbed into the body is several times less than that of metalorganic sources of Hg (e.g., dimethyl mercury). The MMT layered samples examined in this chapter were grown by MOVPE at the University of Durham by M. Funaki. The growth of MMT on the Durham University MOVPE reactor, using a direct alloy growth procedure (DAG) has previously been reported by Clifton[4] et al. and more recently by Funaki[5] et al.. The DAG technique refers to the growth of epitaxial layers using compounds containing the required elements (Hg, Mn and Te) which are brought together at the susceptor, reacting to produce directly an alloy of the required composition. The work of Funaki et al. describes the influence of growth conditions on the quality of DAG grown MMT epitaxial layers, concluding that the Mn concentration depends strongly upon the growth temperature and the position of the substrate on the susceptor, a dependence attributed to the large difference in pyrolysis characteristics between the Mn and Te carrying precursors, tri-carbonyl methylcyclopentadienyl manganese (TCMn) and di-isopropyl telluride (DIPTe), respectively[5].

Before MMT infra-red devices can become a commercial possibility (in addition to fulfilling other integrated optics potentials), the high quality growth of epitaxial MMT is essential. The following sections utilise x-ray scattering techniques to assess the crystalline quality of MOVPE grown epitaxial films on GaAs substrates. The characterisation techniques described collect both the specular and diffuse components of the diffracted x-ray beam, enabling the distribution of the scattered radiation, in addition to its intensity, to be determined.

### 7.2.2 Double Crystal Topography Analysis

The MMT samples analysed in this study were grown by M.Funaki on the University of Durham MOVPE reactor. Other MMT samples, grown using the same method and reactor, have been analysed by Hallam et al.[6] using the double crystal diffraction (DCD) technique, where the FWHM of the diffraction peak is used as an indication of the crystalline quality of the MMT samples. By illuminating various different regions of the sample surface, it is possible to obtain some spatial information using the DCD technique. However, in this case the signal recorded by the detector corresponds to the sample diffracted signal integrated over the cross sectional area of the illuminating x-ray beam. For an appreciable diffracted signal to be recorded,

an incident beam of (at least) $0.5mm^2$ is typically used in DCD analysis. Hence, spatial resolution below this size is not possible using the standard DCD technique. Much greater spatial resolution can be achieved by replacement of the detector with an x-ray sensitive photographic medium, in which case the spatial resolution of the x-ray analysis is limited only by the grain size of the photographic film. Media commonly used for the recording of diffracted images range from high resolution nuclear emulsion plates (undeveloped grain size of 0.25μm) to low resolution, but high speed, dental film (grain size around 10μm). Since many sub-grain/crystallite features are of micron dimensions, double crystal topography is thus a highly appropriate technique for the study of the spatial distribution of crystalline defects.

Laboratory based double crystal topography experiments were performed on a specially adapted Bede 150 double crystal diffractometer. The incident x-ray beam was obtained from the spot source of a 1.5kW Cu x-ray tube (beam dimensions 0.8mm by 0.4mm) with a vertical slit of dimensions 30mm by 1mm replacing the pinhole on the end of the collimator. Beam expansion in the horizontal direction can be achieved by use of an asymmetric, grazing incidence (113) reflection from a (111) oriented Si crystal. However, this has the disadvantage of not allowing separation of the $K\alpha_1$ and $K\alpha_2$ components with a slit placed between the first and second axes. An alternative method is to utilise the (004) reflection from an (001) oriented Si crystal at the first axis and employ an asymmetric, grazing incidence reflection at the sample axis, in order to achieve significant sample coverage. This geometry allows the slit separation of the two Kα lines and, compared to the first method, results in a more intense sample diffracted beam reaching the detector/photographic plate, allowing corresponding shorter topograph exposure times to be employed. This last point is particularly important when it is realised that exposure times in laboratory based double crystal topography experiments of II-VI compounds can be of the order of a week (using high resolution nuclear emulsion plates) or, at the minimum, 24 hours (using high speed, low resolution x-ray dental film).

Fig.7.1(a) shows the double crystal topograph from a 10μm thick (001) oriented MMT layer grown on an (001) GaAs substrate above a 1μm thick CdTe buffer layer, using the direct alloy growth (DAG) technique. For the reasons discussed above, the (004) reflection from the Si reference crystal was chosen and an asymmetric sample reflection employed. The lattice parameter of the MMT layer (a=6.481Å) is such that alignment of the sample for the (224) reflection gives an

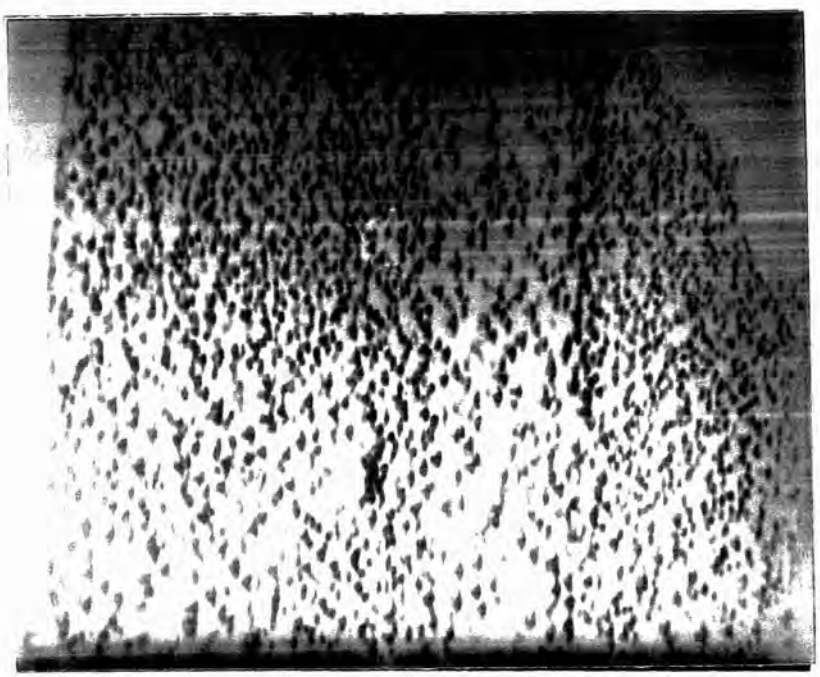

Figure 7.1 (a): The (224) double crystal topograph of 10μm thick (DAG grown) MMT layer grown on (001) GaAs. Image recorded on dental film at diffraction peak maximum (magnification = x12).

incidence angle of around only 0.5°. This results in excellent coverage of the sample surface by the incident, ribbon x-ray beam.

The structure apparent in the topograph is typical of that obtained from other DAG grown MMT layers. A very clear sub-grain structure is visible, with a mean diameter of the individual sub-grains of 130μm (± 5μm standard error on 30 random measurements). Only a fraction of the grains satisfy the Bragg reflection condition for a particular angular setting with respect to the incident beam, but this fraction is distributed widely across the wafer area. While there are some regions where grains of a particular orientation are concentrated, the distribution is fairly uniform across the wafer surface. The effect of epitaxial (i.e. coherent) growth of a mismatched layer on a substrate, is to strain the layer leading to a bowing or curvature of the sample. For significantly curved specimens, the Bragg condition is satisfied over only a narrow band of the sample surface. The fact that the MMT sub-grain images are distributed uniformly across the wafer surface implies that bowing of the specimen has not occurred and hence that the substrate and layer are not coherently strained, i.e., the layer is virtually fully relaxed. Such a high degree of relaxation may be expected when the large mismatch between the substrate lattice parameter (5.65375Å) and epitaxial layer lattice parameter (~ 6.481Å) is taken into account.

Figs.7.1(b,c) shows the topographic images, also recorded on dental film, obtained when the specimen is rocked in the dispersion plane to sit successively at around half height on the negative flank of the rocking curve (fig.7.1(b)), a shift of -100" from the peak maximum, and at half height on the positive flank (fig.7.1(c)), a shift of +100" from the rocking curve peak maximum. If these two topographs are compared with that obtained from sitting on the diffraction peak maximum (fig.7.1(a)), it can be seen that some grains remain in contrast as the sample is rocked, while the diffracted intensity from others is seen to change dramatically. This implies that some sub-grains have a very low level of internal strain, being simply tilted with respect to adjacent grains. Other grains, which remain in contrast for all three sample settings, possess a much larger amount of internal strain.

The internal contrast of sub-grain images can be investigated using high resolution nuclear emulsion plates to record the topographic image. A typical topograph, recorded with such a plate, is shown in fig.7.2, where the contrast associated with intragranular strains can be seen. The contrast is observed to vary within the grain

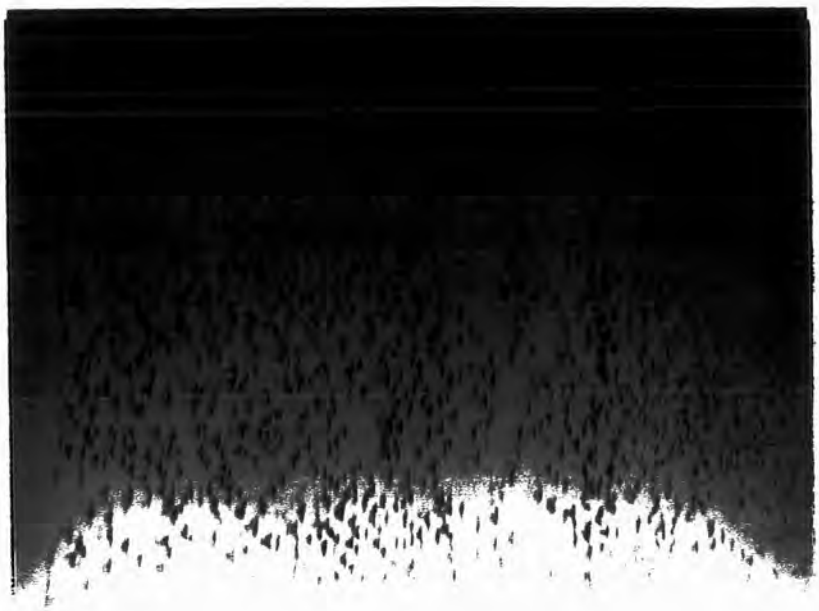

Figure 7.1 (b): The (224) double crystal topograph of 10μm thick (DAG grown) MMT layer grown on (001) GaAs. Image recorded on dental film at -100" from diffraction peak maximum (magnification = x12).

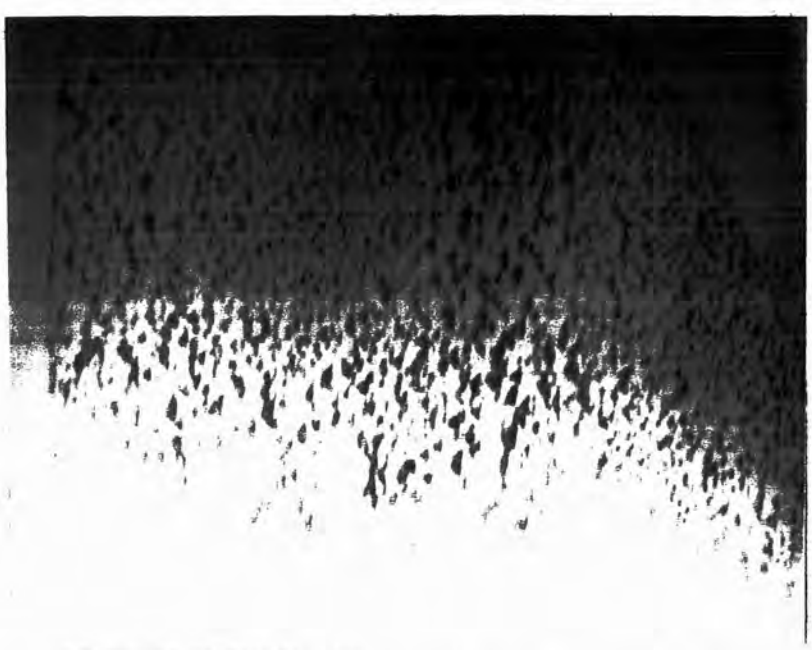

Figure 7.1 (c): The (224) double crystal topograph of 10μm thick (DAG grown) MMT layer grown on (001) GaAs. Image recorded on dental film at +100" diffraction peak maximum (magnification = x12).

Figure 7.2 : The (224) double crystal topograph of 10μm thick (DAG grown) MMT layer grown on (001) GaAs. Image recorded on nuclear emulsion plates at diffraction peak maximum (magnification = x30).

image, although the dislocation density is too high for individual dislocations to be resolved. It is also noted that, while the grain edges appear to be straight at low magnification, this is not borne out by high resolution (and high magnification) topographs

Even with three topographs taken at widely spaced points across the rocking curves, there are many regions of the crystal which show no diffracted intensity. This suggests that there are many grains with very large misorientations or that the lattice strain within the majority of crystals is small. The former explanation is rejected as it would result in a very wide rocking curve. In the latter case, as the intrinsic rocking curve of the (perfect) sample crystal has a FWHM of the order of 12", the sampling range of each topograph is small and we would expect to have to superimpose at least 10 topographs to obtain complete image coverage. Hence, the topographic evidence suggests a predominant structure for the DAG grown layer of misoriented grains with little internal strain.

### 7.2.3 Triple Crystal Diffraction Analysis Of (DAG) MMT Films

The contribution to the rocking curve widths from the sub-grain tilts and lattice dilations can be separated by use of triple axis diffraction (as discussed in Chapter IV). The triple axis diffractometer can be used in its highest mode of resolution by inclusion of a multi bounce channel cut collimator (CCC) in the scattering geometry. The CCC drastically reduces the angular divergence of the x-ray beam, allowing the first crystal to act as a "true" monochromator (the separation of the $CuK\alpha_1$ and $K\alpha_2$ components is sufficiently large, 300", for the first crystal to "sit" on one of these components only). It also reduces the size of the "beam conditioner streak" in reciprocal space so that when a reciprocal space map of the total sample scattering is recorded, the scattering seen is due to that from the sample itself and is not obscured by experimental artefacts. The use of the triple crystal diffractometer in its highest mode of resolution is appropriate to the study of relatively perfect samples (i.e. III-V semiconductors), where the scatter is over only a small region of reciprocal space and hence a high resolution is required to probe defect structure. The drawback in these circumstances is that the x-ray beam experiences up to 10 Bragg reflections before reaching the detector, and the attenuation of the beam can be severe. This is particularly true for experiments using conventional x-ray tube sources (which may have a power rating of only 1.5kW). The narrow widths of III-V rocking curves

mean that the intensity of the Bragg peak is high and the large attenuation of the x-ray diffracted beam, as it passes through the diffractometer, can be tolerated. This is no longer true for the (relatively imperfect) II-VI compounds with the resulting Bragg peaks being both broad and much weaker. In this case the eventual intensity of the diffracted beam reaching the x-ray detector is often insufficient to conduct a meaningful experiment. The intensity of scatter away from the reciprocal lattice point will be less than the detector background and long range diffuse scatter will be undetectable. In effect, the sample scatter in reciprocal space can be thought of as a kind of "iceberg" - should the total intensity be poor, then only the peak will be visible above the constant detector background, with the diffuse scatter (which contains the information of interest) hidden beneath the "surface". Thus, it is strongly recommended that if a conventional laboratory x-ray tube and generator are to be used as the x-ray source in the study of relatively imperfect samples, the total intensity should be boosted by removal of the CCC, with a conventional pinhole collimator being used in its place. The resolution of the diffractometer will be worsened by this action, with the introduction of a beam conditioner "streak" in reciprocal space. However, as will be seen, for some II-VI compounds the sample scatter can extend some way from the exact Bragg position (i.e. at the reciprocal lattice point) so that the "streak" is dominated by the sample scatter and its presence can be ignored.

The use of a pinhole collimator means that the first crystal will simultaneously diffract the CuK$\alpha_1$ and K$\alpha_2$ components, so that it is then necessary to remove the K$\alpha_2$ line by placing a slit between the first and sample crystal axes.

Triple axis measurements have been performed on an 8μm thick MMT layer (5.8% Mn), grown (by the DAG process) on an (001) oriented GaAs substrate. The sample scatter, recorded around the 004 reciprocal lattice point, is shown in fig.7.3. Note that the contours on this, and all subsequent reciprocal space plots, represent the logarithm of the diffracted intensity. The diffuse scattered intensity remains high some distance away from the exact Bragg condition and thus there is no evidence of the weak beam conditioner and analyser streaks, which are visible in equivalent data (i.e., using the same diffractometer configuration) taken from a relatively perfect GaAs crystal (fig.4.5). The tilt distribution is symmetric with respect to the origin in $\Delta Q_y$ and is greatly extended over that seen from a nearly perfect crystal. A transverse scan in reciprocal space through the maximum intensity position,

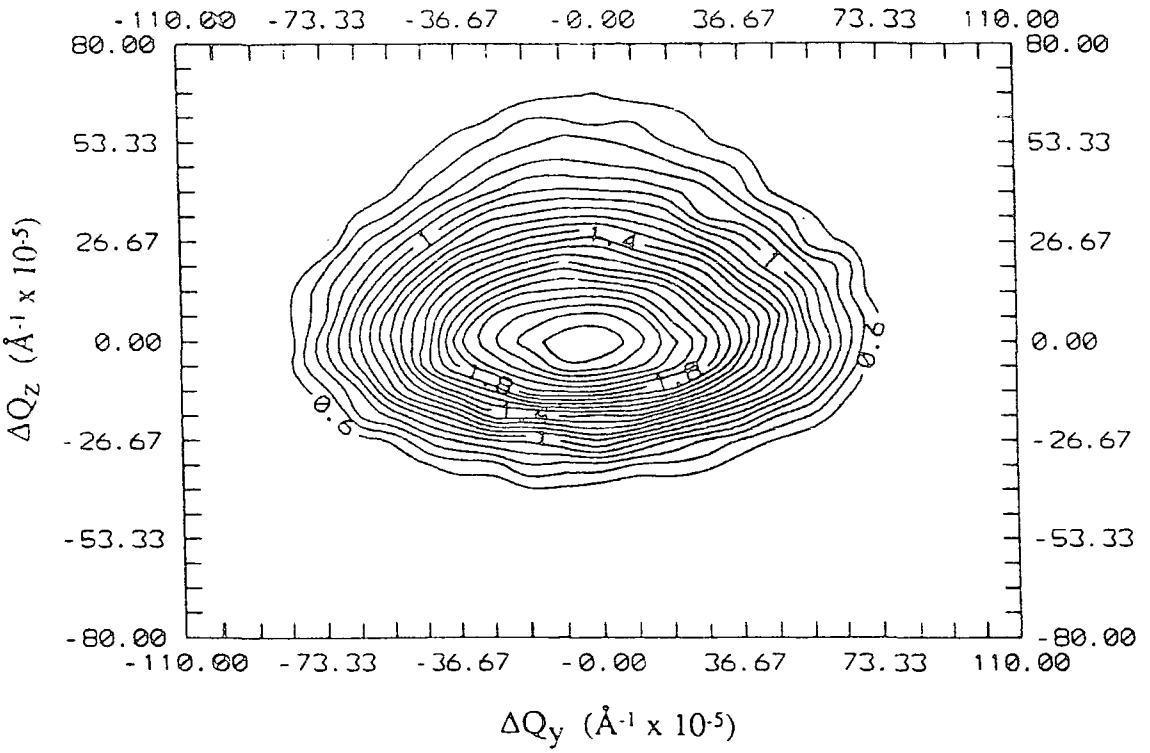


Figure 7.3 : Reciprocal space plot of the scatter around the (004) reciprocal lattice point of an 8μm layer of $Hg_{.942}Mn_{.058}Te$ on (001) GaAs.

recorded by scanning only the specimen for a fixed analyser position, has a FWHM of 168". This measures the range of the tilt distribution independently of the lattice dilations, which influence the scattering only in the $\Delta Q_z$ direction. Very significant asymmetry is seen in the intensity distribution about the reciprocal lattice point in the $\Delta Q_z$ direction. The FWHM of the longitudinal scan, measuring the lattice dilation distribution, is 44". Note that the absolute intensity of this "asymmetric" $\Delta Q_z$ scattering is weak, with the asymmetry visible only when the scatter is plotted on the logarithmic scale of (fig.7.3). When plotting the transverse and longitudinal scans on a linear scale (fig.7.4), the asymmetry of the (narrow) $\theta/2\theta$ scan is much less visible. Fig.7.4 further displays graphically how the spread of sub-grain tilts within the crystal is much larger than the lattice dilation distribution. A double axis diffraction experiment, where the detector is open, corresponds to a scan in the $\Delta Q_y$ direction integrated along a line inclined at the Bragg angle to the $\Delta Q_y$ axis. Thus the triple axis plots reveal quantitatively that the major contribution to the rocking curve width is from the tilt distribution, a conclusion supported by the topographic evidence presented in Section 7.2.2 above. These results show a similar pattern to triple axis measurements obtained by Keir[7] et al. for two CdTe on GaAs samples. Although they did not make full reciprocal space maps, they found FWHM values of 40" and 44" in coupled $\theta/2\theta$ scans, compared to widths of 277" and 580" recorded in transverse scans (i.e. rocking of the specimen for a fixed detector position)

Fig.7.5 shows an equivalent set of iso-intensity contours for a 7μm thick MMT layer grown on the (001) surface of a $Cd_{0.96}Zn_{0.04}Te$ (CZT) substrate. The FWHM of the transverse and longitudinal scans are 207" and 68", respectively. The scattering distribution is remarkably similar, despite the fact that the lattice mismatch between MMT and CMT is small (very much lower than that between MMT and GaAs), with the tilt distribution significantly greater than the (asymmetric) lattice dilation spread.

The asymmetry in the $\theta$-$2\theta$ scan arises because of excess scattering being recorded with scattering vectors, $\underline{q}$, larger than that observed at the exact Bragg peak. These larger scattering vectors correspond to diffraction from lattice planes smaller than those which would be observed in the perfect crystal. The x-ray beam will penetrate to a depth of 2-3 μm beneath the sample surface, and the information gathered refers to the sample structure within this near surface region. The nature of the Bragg peak asymmetry can be used to deduce the nature of the microdefects present within the sample. If the diffracted intensity is greater on the high angle side of the Bragg

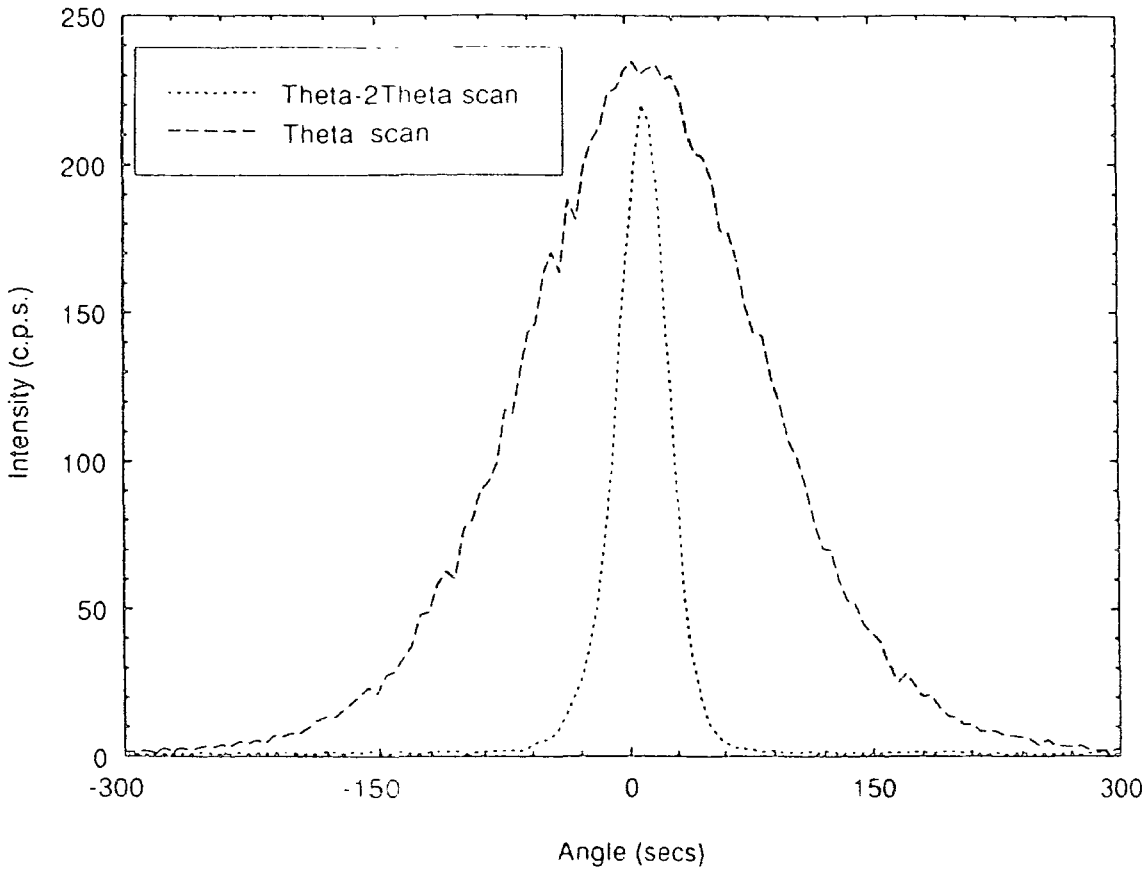


Figure 7.4 : Longitudinal (θ-2θ) and transverse (θ) scans from 8μm thick layer of $Hg_{.942}Mn_{.058}Te$ on (001) GaAs.

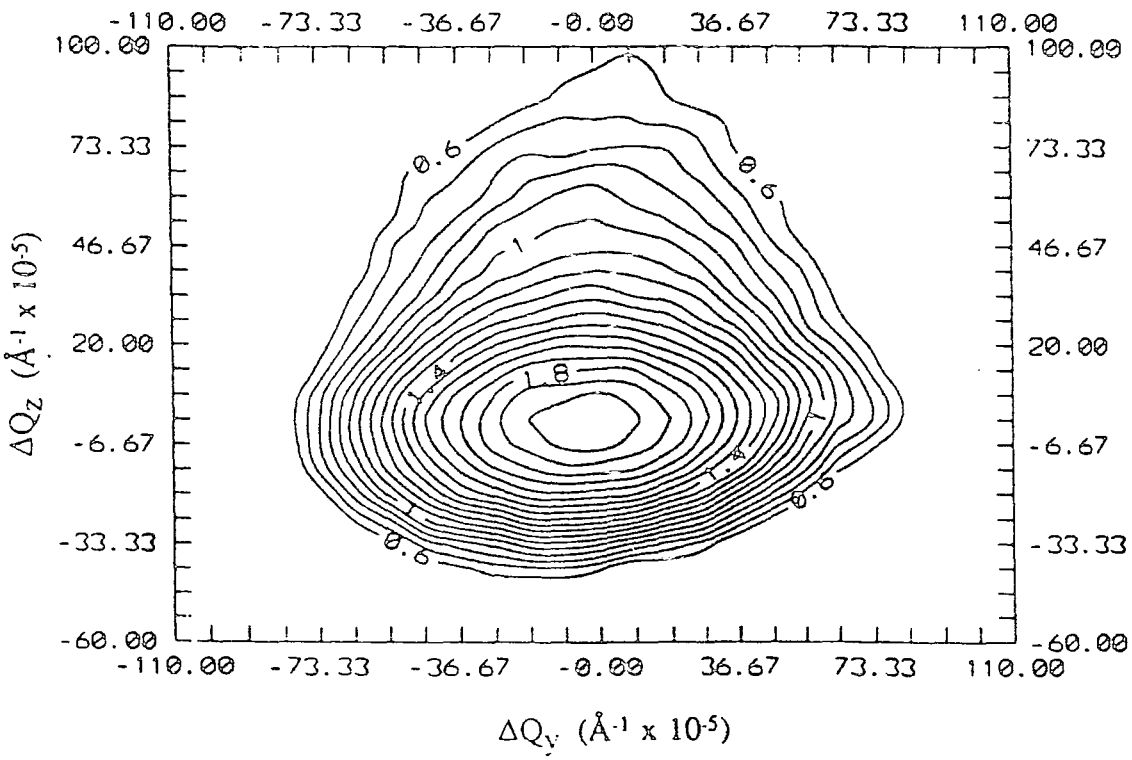


Figure 7.5 : Reciprocal space plot of the scatter around the (004) reciprocal lattice point of a 7μm layer of HgMnTe on (001) $Cd_{.96}Zn_{.04}Te$.

peak (i.e., corresponding to larger scattering vectors) then the microdefects are of an interstitial nature. For Bragg peaks exhibiting excess intensity on the low angle side of the Bragg peak (corresponding to scattering with a smaller scattering vector) then the microdefects are of vacancy character.

The asymmetry in the longitudinal direction for the MMT sample may be caused by either a high concentration of lattice interstitials (resulting in an effectively smaller lattice spacing) or an increase near the surface in the concentration of the binary alloy (HgTe) whose lattice parameter is smaller than its binary partner (MnTe) in the ternary alloy (MMT). The information content of the triple crystal diffraction data is formed by integrating the diffracted signal from the entire volume of the crystal sampled by the x-ray beam. The triple crystal technique is not able to yield compositional information as a function of depth and use of a technique such as SIMS (Secondary Ion Mass Spectroscopy) would be required to test the hypothesis that an excess of HgTe is found near the surface, compared to within the bulk of the crystal.

The difficulty experienced in growing a spatially uniform layer of MMT has been attributed to the difference in the pyrolysis temperatures of the Mn and Te precursors, TCMn and DIPTe, respectively. Funaki[5] et al. propose that the pyrolysis rate of the DIPTe precursor decreases dramatically along the gas flow direction, while that of the TCMn precursor decreases only slightly. At a substrate temperature of 380°C, the TCMn/DIPTe pyrolysis ratio was found to increase by a factor of five along the susceptor, resulting in an increasing Mn concentration in the epitaxial layer, along the direction of the gas flow, which contradicts the supposition above that an increase in the Hg(Te) concentration near the surface leads to the asymmetry in the $\theta$-$2\theta$ scan. However, the asymmetry may be explained by evaporation of Hg from the surface, which is possible due to the relatively high vapour pressure of Hg. This process could generate a significant amount of mercury vacancies, which would then help to explain the excess of high $\underline{q}$ scattering observed in the $\Delta Q_z$ direction. The large reduction in the pyrolysis rate of the DIPTe is also thought to account for the non-uniform thickness of the MMT layers grown by Funaki et al.. As the pyrolysis rate of the DIPTe decreases along the flow direction a corresponding reduction in the growth rate will occur, leading to a decrease in epitaxial layer thickness in the direction of gas flow. Double axis diffraction area maps show these effects dramatically[8].

### 7.2.4 Double Crystal Topography Of IMP Grown MMT

The problem of non-uniform layer composition and thickness has previously been reported by researchers working on the growth of Cadmium Mercury Telluride (CMT) and was solved, in that instance, by use of the interdiffused multilayer process (IMP)[9,10]. The IMP process involves the growth of very thin alternate layers of the constituent binary compounds (e.g., CdTe and HgTe, or, MnTe and HgTe) under the optimum deposition conditions for each compound. By holding the MOVPE reactor for a short period (~ 10 minutes) at the growth temperature at the end of each growth run, complete interdiffusion of the alternate binary alloys results in the production of a (hopefully) homogenous, ternary alloy. The composition of the ternary alloy is then determined by the thickness ratio of the individual constituent binary layers.

MMT samples have been grown by M.Funaki on the University of Durham MOVPE kit, using the IMP process[11]. Thin, alternate layers of MnTe and HgTe were deposited onto a (001) GaAs substrate with a 1μm thick CdTe buffer layer. The growth cycle was repeated up to 100 times in order to grow a layer of total thickness around 3μm.

The double crystal topographic image obtained from a 5μm IMP grown MMT (15% Mn) layer on GaAs is shown in fig.7.6. The experimental configuration for this topograph was similar to that used in the case of the DAG grown MMT, i.e., a Si reference (symmetric) reflection with the sample (224) reflection imaged (giving an incidence angle of 0.5°). Note that in this case no mosaic structure is observed and a large portion of the IMP grown sample is imaged onto the photographic medium (dental film). This wide area imaging of the sample surface implies a reasonably high degree of uniformity in the crystalline quality across the surface of the IMP grown sample. While dislocation structure is visible in the topograph, no subgrain boundaries are visible, indicating a great reduction in the amount of lattice tilting for the IMP sample. It should be realised that the IMP grown layer analysed here is thinner than the DAG grown samples characterised in sections 7.2.2 and 7.2.3. Bearing in mind that the crystalline quality of the DAG grown structures has been found to deteriorate with sample thickness (with thin DAG samples having very wide DCD rocking curves), this serves to further emphasise the improvement in

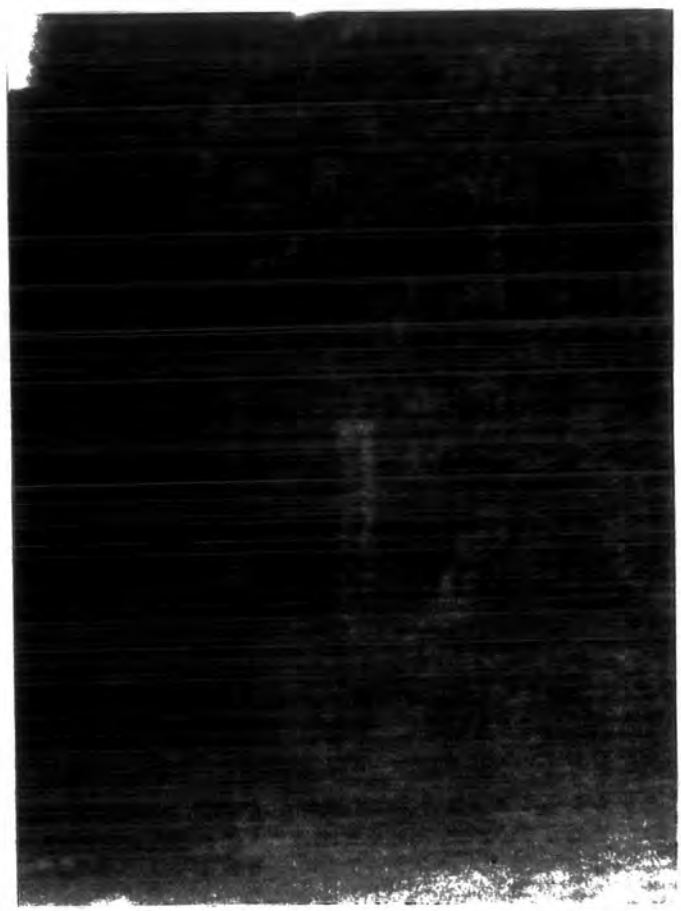

Figure 7.6 : **The (224) double crystal topograph of a 5μm thick (IMP grown) HgMnTe layer grown on (001) GaAs. Image recorded on dental film at diffraction peak maximum (magnification = x19).**

crystalline quality of IMP grown MMT over that grown by the DAG technique. These findings are in agreement with those of Hallam[12], who found that the DCD diffraction FWHM were significantly less in the case of IMP grown MMT, compared to samples fabricated using the DAG method. A possible explanation for the improvement in crystalline could lie in the large number of thin layers grown. As a small mismatch exists between the HgTe and MnTe layers, it may be reasoned that the lattice strain is relieved by the presence of threading dislocations, which are bent over at the interface between the two binary compounds. Since the total structure consists of around 100 HgTe/MnTe interfaces, the probability that threading dislocations, bent over at the interfaces, will interact and annihilate each other, will greatly increase, leading to a significant reduction in the layer dislocation density with the formation of subgrain boundaries inhibited.

While the double crystal topographic (DCT) data is useful in determining the spatial distribution of crystal defects, the triple crystal technique gives information on the *type* of defect, although this is averaged over the incident area of the x-ray beam. Historically, the double crystal topography method has been extensively employed for materials characterisation, with the triple crystal technique being less popular with material scientists. Work presented in the remainder of this chapter involves using triple crystal methods to obtain information which would be complementary to that gained from topography.

### 7.3.1 Triple Axis Characterisation Of $Cd_xHg_{1-x}Te$ (CMT) Epitaxial Films

$Cd_{1-x}Hg_xTe$ (CMT) is a semiconductor alloy with a narrow band gap energy. For mercury fractions of around 0.8, the material is used in infra-red detectors operating at 77K (in the second atmospheric window)[13]. In order to achieve high detector performance, it is important that high quality crystalline material is used as the presence of grain and sub-grain boundaries has been found to have an adverse effect on the electrical properties of detectors[14,15,16]. As well as finding applications in the fabrication of infra-red detectors, CMT has also been proposed as a suitable candidate for solar cells, optical waveguides[17], amplifiers and mixers[18], high frequency devices (such as microwave oscillators), electrically controlled optical switches, heterojunction bipolar transistors for ultrahigh speed VLSI circuits[19], optically bistable devices[20], light emitting devices[21] (in the 2 - 4 μm range), and double heterostructure lasers[22]. The possibility of the development of ultra low loss

fluoride glass fibres has stimulated interest in the use of CMT optoelectronic devices in the 2 - 5 μm band[23]. CMT has also been recognised as potentially offering several advantages over conventional III-V and IV compounds for the 1.33 μm[24] and 1.55 - 1.6 μm[25] silica fibre systems.

CMT has been deposited using various thin film growth techniques including MBE[26], sputtering[27], MOCVD[28] and LPE[29,30]. For sample purity, control of composition and compositional uniformity, liquid phase epitaxy (LPE) is considered to have the highest potential for future practical applications[28].

### 7.3.2 Analysis Of Substrate Quality

For the growth of high quality epitaxial CMT the choice of substrate is critical. Dislocations may occur in the CMT layer as a result of a difference between the lattice parameters of the substrate and the CMT layer (misfit dislocations). Although misfit dislocations are the most efficient means by which misfit strain is relieved, they are not the only form of dislocation found in epitaxial layers. In the Matthew-Blakeslee model for lattice relaxation of epitaxial films, dislocations which extend through from the substrate into the layer itself (threading dislocations) also eliminate some of the layer strain. Driven by the lattice strain, the vertical segments of the threading dislocation in the substrate and layer move in opposite directions, leaving a segment of misfit dislocation lying in the plane of the substrate/layer interface. In an epitaxial layer, provided their are sufficient threading dislocations to relieve completely the strain, the threading dislocation density of the substrate should correlate with the final density of misfit dislocations in the layer. To ensure low layer dislocation density the quality of the substrate itself must therefore be high (to minimise the threading dislocation density) and the lattice mismatch between the substrate and layer sufficiently low so that a dense network of misfit dislocations is not nucleated at the interface.

Substrates commonly used for the epitaxial growth of CMT are CdTe and $Cd_{1-x}Zn_xTe$. CMT layers grown on these two types of substrate have previously been studied using destructive TEM[31] and etch-pitting[32] techniques. The work presented in this and following sections examines the crystalline quality of CdTe/$Cd_{1-x}Zn_xTe$ substrates and CMT layers using non-destructive, triple crystal x-ray diffraction. The CdTe substrates were sourced from GEC Marconi Infra-red, Southampton and

were grown using conventional vertical Bridgman techniques. The CdZnTe substrates were also obtained from GEC Marconi Infra-red but these were originally grown (under a Cd overpressure) using conventional Bridgman techniques by the Nippon Mining Co., Japan.

For the triple crystal analysis the diffractometer was configured in the high resolution, non-dispersive setting, with a four bounce Si (022) CCC used to pre-condition the beam, and a symmetric (111) Si reflection employed at the monochromating stage. The sample and monochromating crystals were in the parallel position with the sample diffracted beam then undergoing a four bounce reflection from a Si (111) analyser. The complete experimental configuration is similar to that depicted in fig 4.1, with the final configuration being (+,-,+,-,+,-,+,-,+,-). The use of the diffractometer in such a high resolution setting, with 10 Bragg reflections in all, results in a relatively low diffracted intensity from the CdTe/CdZnTe substrates. However, unlike the case of the MMT layered samples, the final diffracted intensity recorded by the scintillation counter was sufficient to provide meaningful statistics, although long scanning times were required (around 12 hours for a full reciprocal space map). This fact in itself implies a relatively high degree of crystal perfection (certainly when compared to the DAG grown MMT material studied by triple crystal diffraction in the previous section). In addition to full reciprocal space maps of the substrate scatter being collected, individual $\theta$ and $\theta/2\theta$ scans were carried out to measure diffraction peak widths in the transverse and longitudinal directions, respectively. The 2-D reciprocal space maps, obtained from around the (333) reciprocal lattice points of the (111) oriented CdTe and $Cd_{0.96}Zn_{0.04}Te$ (CZT) substrates, are shown in Fig. 7.7(a,b). The transverse and longitudinal scans' FWHM are given in Table 7.1.

| Substrate Type | Rocking Curve FWHM | Transverse FWHM (tilts) | Longitudinal FWHM (dilations) |
|---|---|---|---|
| CdTe | 31" | 25" | 11" |
| $Cd_{0.96}Zn_{0.04}Te$ | 17" | 8" | 9" |

Table 7.1 : FWHM data for the two different types of substrate.

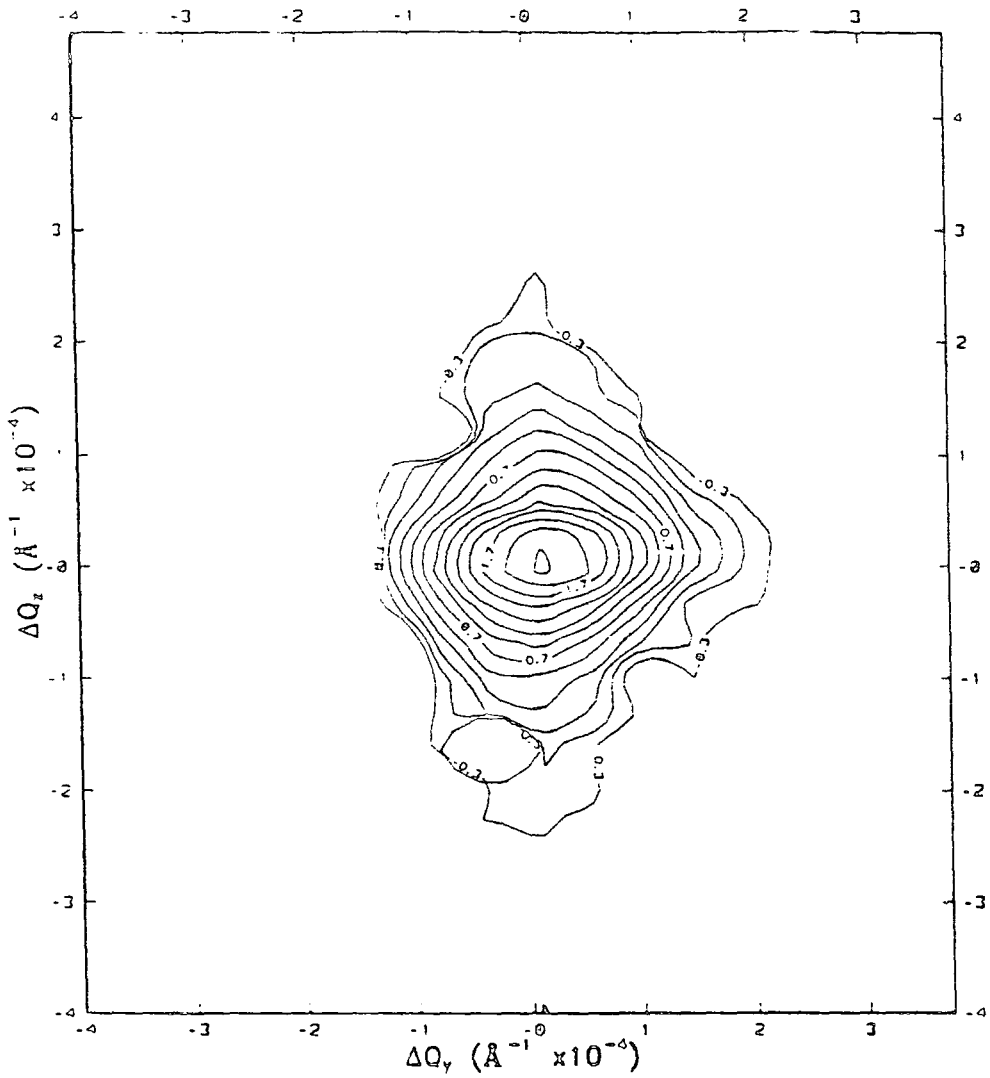


Figure 7.7 (a): Reciprocal space plot of the scatter around the (333) reciprocal lattice point of a (111) oriented CdTe substrate.

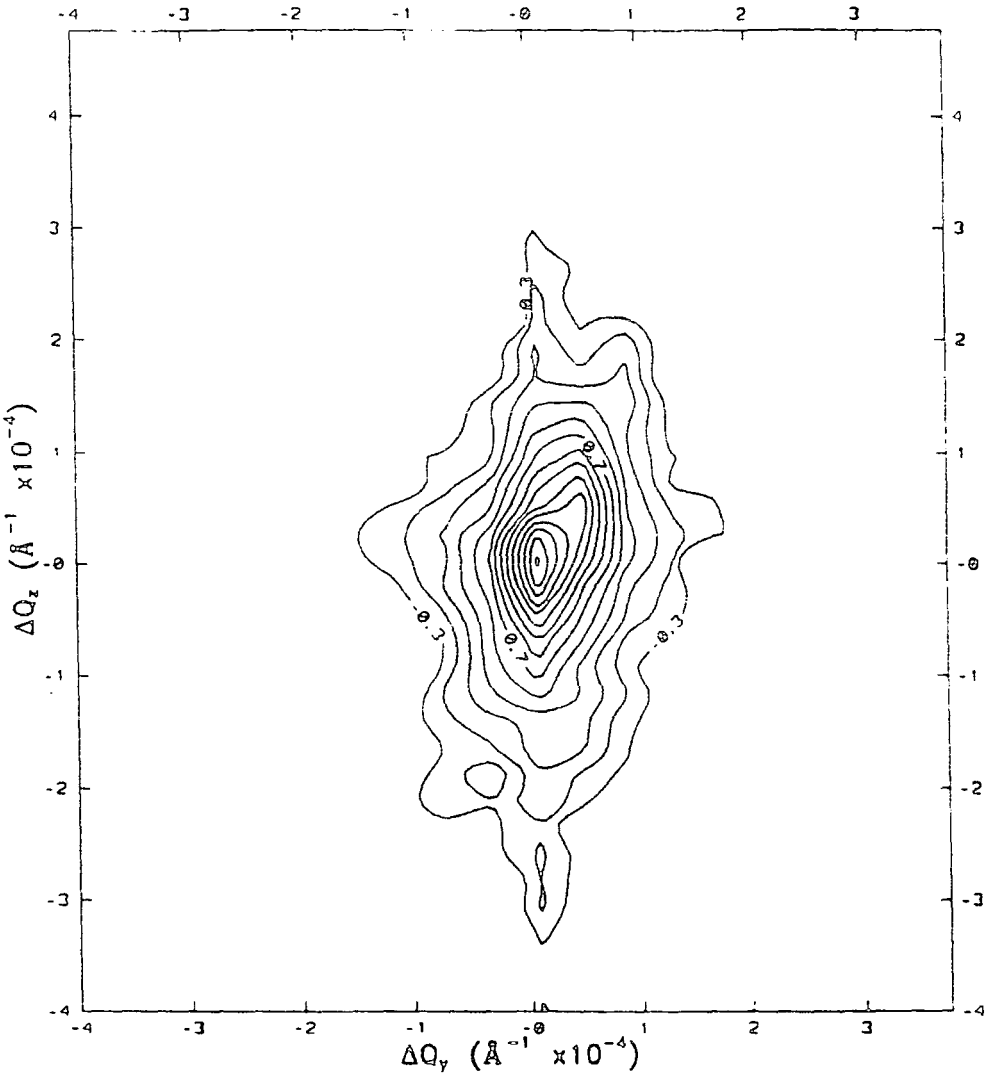


Figure 7.7 (b): Reciprocal space plot of the scatter around the (333) reciprocal lattice point of a (111) oriented $Cd_{.96}Zn_{.04}Te$ substrate.

In order to ease comparison, the reciprocal space maps of the CdTe and $Cd_{0.96}Zn_{0.04}Te$ substrates are plotted to the same scale.

Inspection of figs.7.7(a,b) shows that the scatter from both substrate types extends over a roughly equivalent region of reciprocal space. However, the sharpness of the diffracted peak is greater in the case of the $Cd_{0.96}Zn_{0.04}Te$ substrate, particularly along the (horizontal) $\Delta Q_z=0$ direction.

For comparison, the FWHM's of a "good" piece of GaAs, known to produce high quality, epitaxial layers (whose reciprocal space map is shown in Fig. 4.5) are 11" (rocking curve), 7" (transverse) and 8" (longitudinal). The FWHM for the longitudinal (lattice dilation) directions are roughly the same as that for the "good" GaAs crystal, indicating a very narrow lattice parameter distribution for both the CdTe and $Cd_{0.96}Zn_{0.04}Te$ substrates.

The main difference between the CdTe and $Cd_{0.96}Zn_{0.04}Te$ substrates arises in the amount of lattice tilt within the two samples. The transverse width of the CdTe is three times larger than for the $Cd_{0.96}Zn_{0.04}Te$ substrate, indicating a more mosaic structure within the CdTe crystal. These findings are contrary to those reported by Dean et al.[33] who used topographic synchrotron radiation techniques to analyse CdTe and $Cd_{0.955}Zn_{0.045}Te$ substrates, concluding that more severe lattice distortion was apparent in the $Cd_{0.955}Zn_{0.045}Te$ substrate. Although the values for the transverse widths of the CdTe based layers are significantly greater than in the case of the $Cd_{0.96}Zn_{0.04}Te$ based CMT layers, the *absolute* value of the widths are still small when compared to the large values observed in other II-VI systems (i.e., the MMT layers studied in section 7.2). Comparison of the substrate TCD data in this section also shows a significant difference in the value of the lattice distortion compared to that reported by Dean et al., who had to step their substrate through an angle of some 250" in order to obtain "corner to corner" topographic sample imaging using synchrotron radiation, implying that the crystallinity of the CdZnTe substrates employed in their experiments was significantly worse than the CdZnTe substrate analysed here.

### 7.3.3 Analysis Of Layered Samples

Having investigated the crystalline quality of the two substrate types, layers of CMT were grown by LPE and analysed using the same diffractometer setting employed in the analysis of the substrates. The orientations of the layers grown were similar to those of the substrates, i.e., (111) and the scatter around the (333) reciprocal lattice point recorded. Diffraction measurements were first performed on thick (~10μm) layers of CMT, grown on CdTe and $Cd_{0.96}Zn_{0.04}Te$ substrates similar to those analysed in the preceding section. The layers were then etched back using a 0.5% bromine in methanol solution, and their crystalline quality re-assessed using triple crystal diffraction methods. The layer growth, etching and layer composition measurements (using optical transmission techniques) were conducted by C.C.R.Watson[34] of Durham University.

The CMT layer thicknesses (both initial and post-etching) are recorded in Table 7.2, together with the peak widths of the sample rocking curves, transverse and longitudinal scans. The reciprocal space maps representing the x-ray scatter recorded from each sample are displayed in figs. 7.8(a-d).

| Sample | Layer Thickness (± 0.1μm) | Rocking Curve FWHM (± 2") | Transverse FWHM (tilts) (± 2") | Longitudinal FWHM (dilations) (± 2") |
|---|---|---|---|---|
| CMT/CdTe | 10 | 50 | 39 | 12 |
| CMT/CdTe | 2 | 52 | 46 | 13 |
| CMT/CZT | 12 | 35 | 29 | 12 |
| CMT/CZT | 5 | 46 | 36 | 14 |

Table 7.2 : FWHM for CMT layers.

Again, the plots shown in fig. 7.8(a-d) are all drawn to the same scale (a similar one to that employed in the plotting of the substrate scatter) so that direct visual comparison can be made of the scatter from both substrate-only and layered samples.

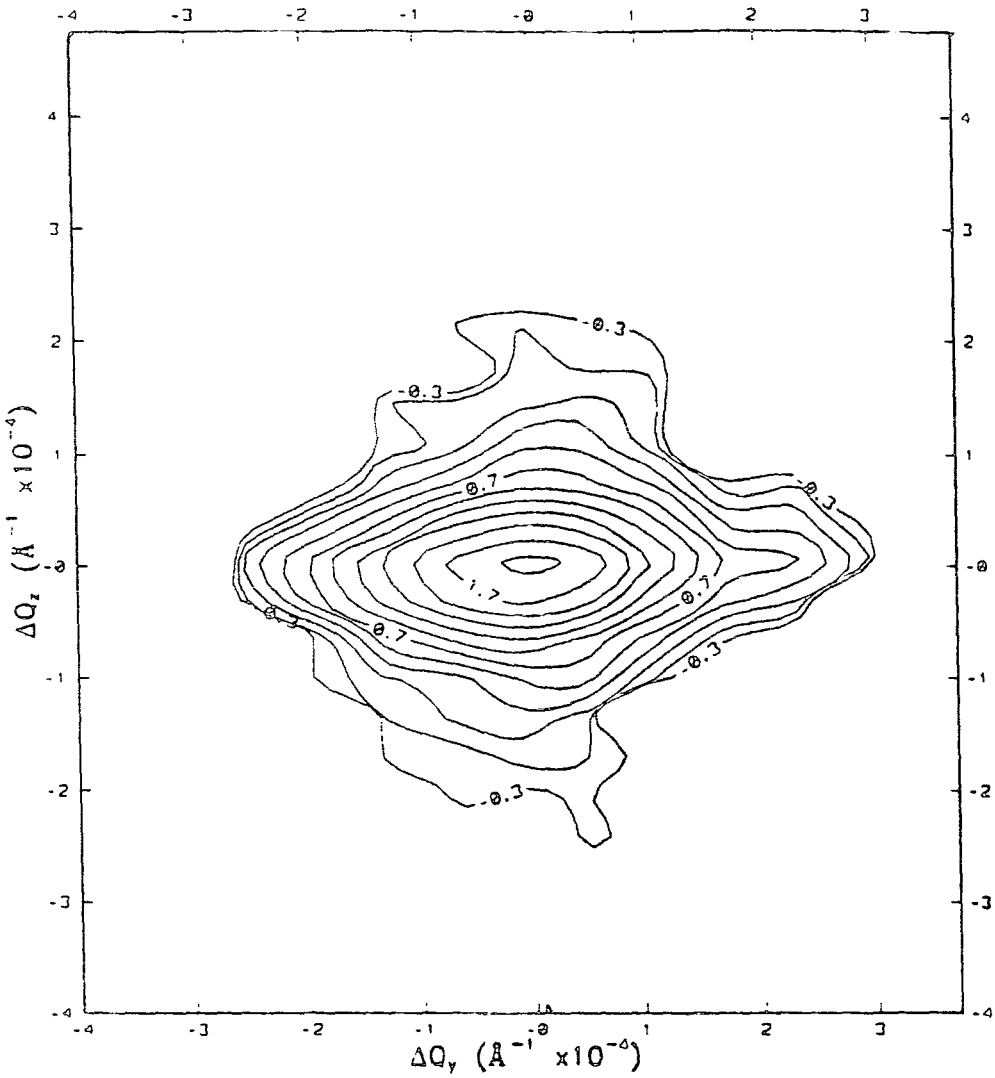


Figure 7.8 (a): Reciprocal space plot of the scatter around the (333) reciprocal lattice point of a 10μm thick $Cd_{.24}Hg_{.76}Te$ layer on (111) CdTe.

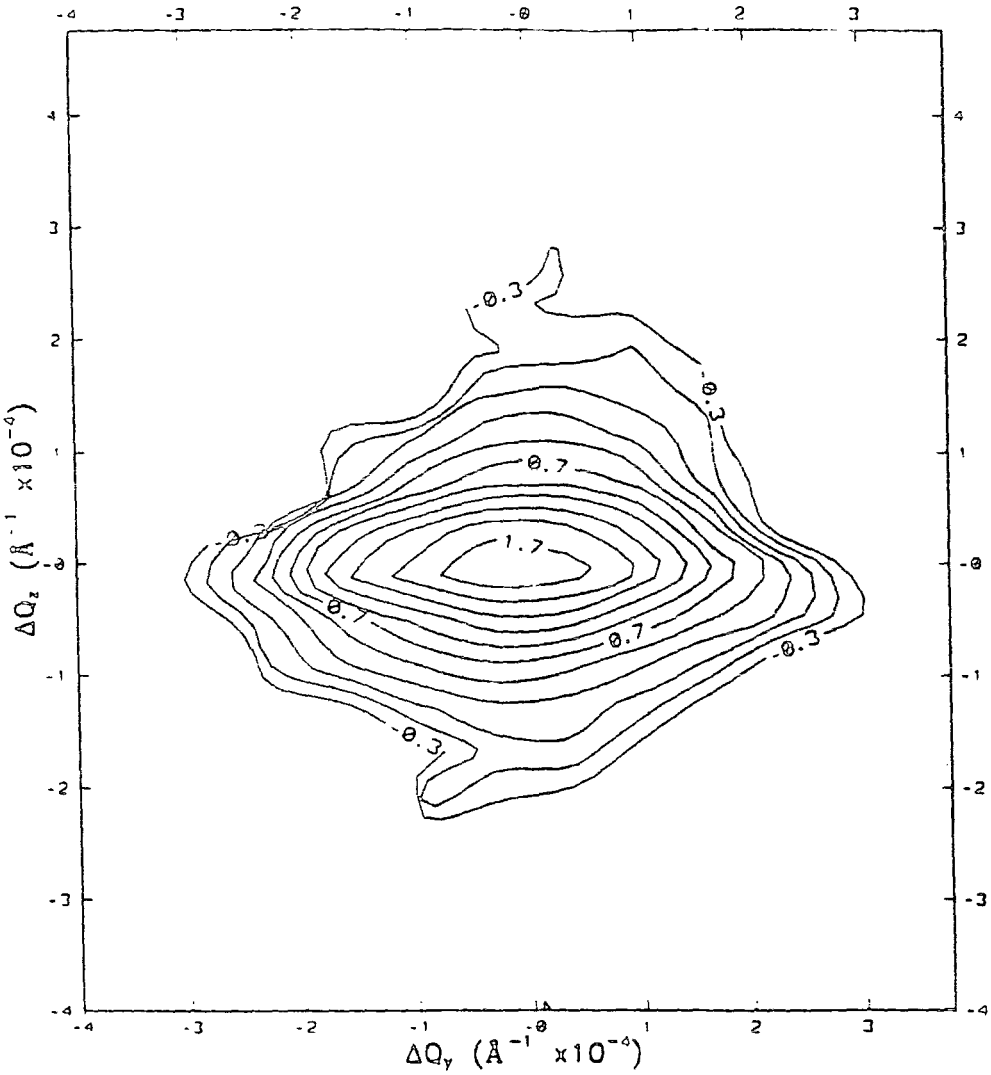


Figure 7.8 (b): Reciprocal space plot of the scatter around the (333) reciprocal lattice point of a $Cd_{.24}Hg_{.76}Te$ layer on (111) CdTe (layer thickness etched down to 2μm).

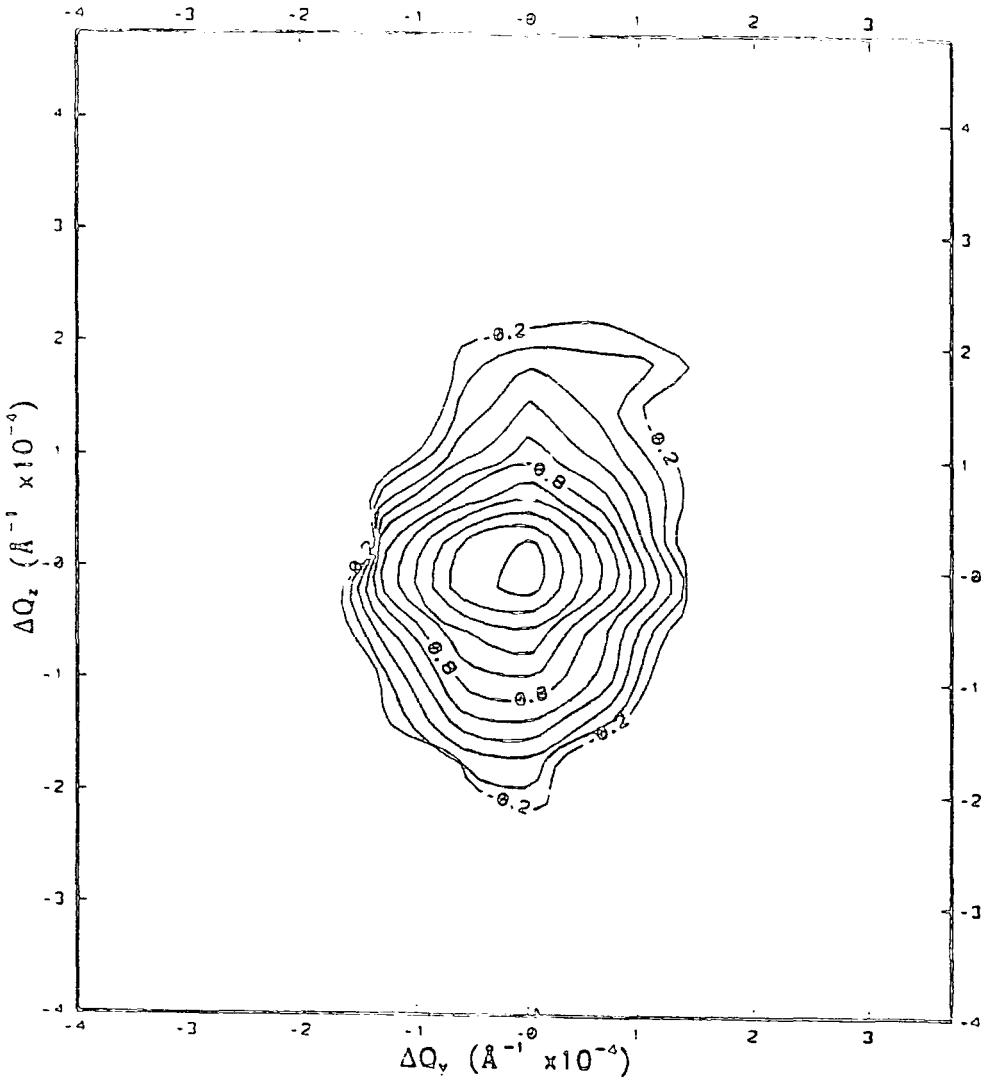


Figure 7.8 (c): Reciprocal space plot of the scatter around the (333) reciprocal lattice point of a 12μm thick $Cd_{.24}Hg_{.76}Te$ layer on (111) $Cd_{.96}Zn_{.04}Te$.

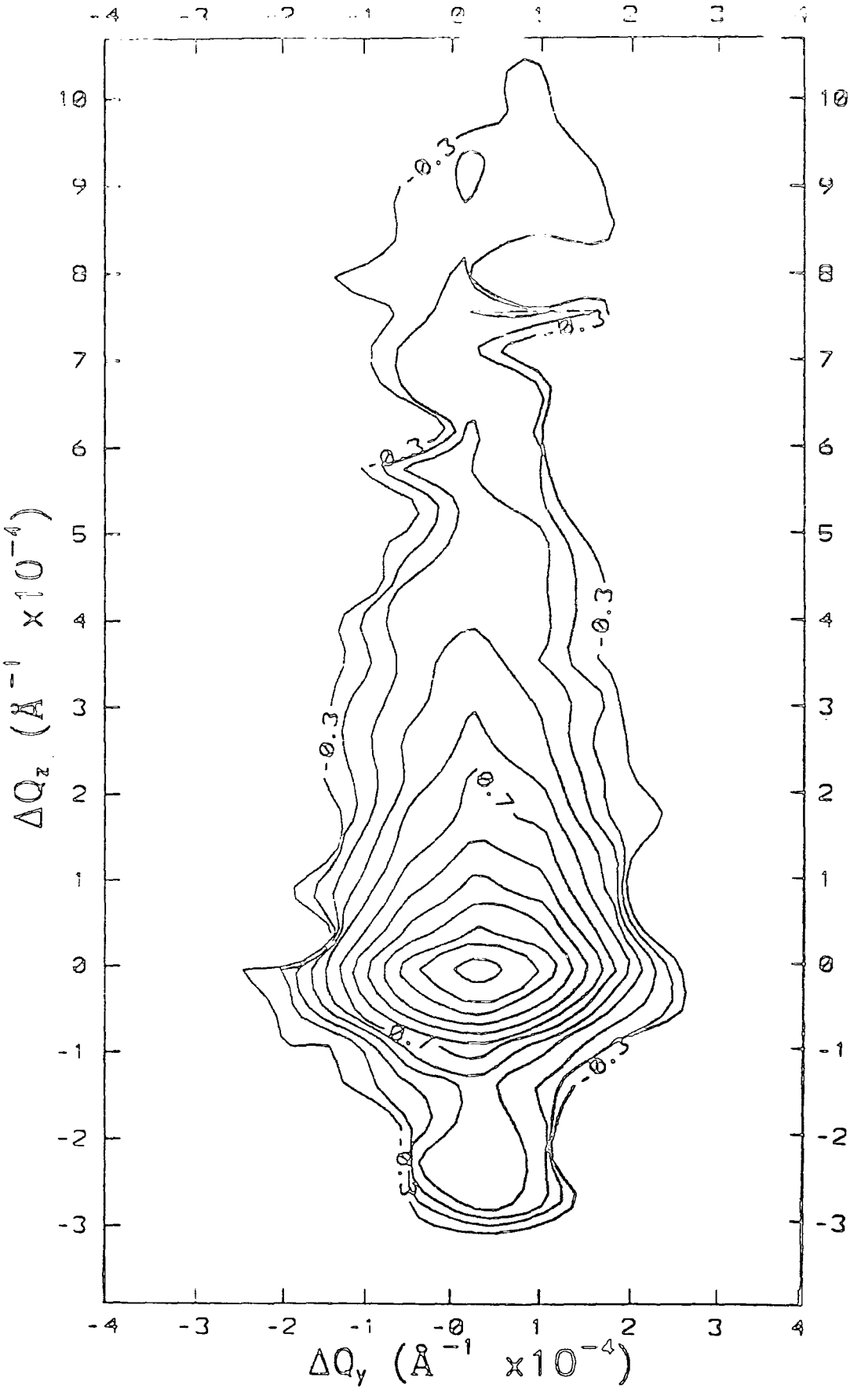


Figure 7.8 (d): Reciprocal space plot of the scatter around the (333) reciprocal lattice point of a $Cd_{.24}Hg_{.76}Te$ layer on (111) $Cd_{.96}Zn_{.04}Te$ (layer thickness etched down to 5μm).

The scatter from the CMT on CdTe samples (figs.7.8 a,b) extends over a roughly similar range in the $\Delta Q_z$ direction to that observed for the CdTe substrate only (fig.7.7 a). The main difference between the layered and substrate only samples exists in the distribution of the scatter in the (horizontal) $\Delta Q_y$ direction, with scatter being observed over a much greater range for the layered samples. The distribution of scatter for the 10μm and 2μm layers is, however, similar although the contours on fig (7.8 a) indicate a much sharper diffracted peak. This finding is supported by the data in table 7.2, which show that the lattice tilts FWHM increase as the layer is etched back. It should be mentioned that a comparison of the "sharpness" of diffracted peaks should be made by analysis of the spacing of the contour lines only, and not the absolute value of the maximum contour. While the measurement of the peak widths in Table 7.2 is accurate to around 1" (obtained from individual small step size scans), peak widths are not well represented by the logarithmic scale of the reciprocal space plots. Further, the grid used in the construction of the contour maps is coarse in comparison to the width of the diffracted peaks (so that the exact maximum of the peak can be "missed" by the contour mapping software), but appropriate to the plotting of the diffuse scatter which extends over a much further angular range.

Data for the samples grown on CZT show similar trends to those reported for the CdTe based layers. The FWHM of the CMT layers are broader than those measured for the substrate due mainly to an increase in the lattice tilts (and hence dislocation densities). Inspection of Table 7.2 reveals that peak FWHM increase as the layer thickness decreases with a very significant "tail" of scatter appearing for the 5μm layer (fig.7.8 d)

For all samples, the values for the longitudinal width are only very slightly greater than those for the corresponding substrate only system. From this, it can be inferred that the compositional homogeneity of the CMT layers, grown on CdTe and $Cd_{0.96}Zn_{0.04}Te$, is good. For layers grown on both types of substrate, an increase in the overall rocking curve width is seen to occur as the layer is etched back to a smaller thickness. This increase is represented almost solely by an increase in the transverse width of the diffraction peaks, indicating larger tilt distributions (and dislocation densities) in thin layers of CMT when compared to thicker layers.

The data in Table 7.2 also shows that the quality of the layer material grown on $Cd_{0.96}Zn_{0.04}Te$ substrates is, in general, superior to that grown on CdTe. This could be attributed to the superior quality of the initial $Cd_{0.96}Zn_{0.04}Te$ substrate and the lower mismatch of the $Cd_{0.96}Zn_{0.04}Te$/CMT system, with the density of misfit dislocations nucleated being less than in the case of the CdTe/CMT system.

### 7.3.4 Correlation With Defect Selective Etching Studies

Defect selective etching studies have been performed by Watson[34] on the CMT layered samples, using saturated aqueous ferric chloride and Hähnert etches, to investigate the dislocation density as a function of the distance from the substrate/layer interface.

Fig.7.9(a) shows the variation of etch pit density of a thick $Cd_{0.24}Hg_{0.76}Te$ layer grown on a CdTe substrate. Fig.7.9(b) shows the equivalent plot for a layer of similar composition grown on a $Cd_{0.96}Zn_{0.04}Te$ substrate. These results reveal that the dislocation density decreases with increasing layer thickness, for film thicknesses up to ~6μm. Beyond this value the dislocation density settles out to a "constant" background level of $9 \times 10^4$ $cm^{-2}$ for the CMT/CZT system and $3 \times 10^5$ $cm^{-2}$ for the CMT/CdTe system. Both of these values are significantly greater than the dislocation density found in the substrates only, which were measured to be $3 \times 10^4$ $cm^{-2}$ for each substrate type.

Although the FWHM in Table 7.2 indicate that the crystalline quality of the CZT substrate is superior to that of the CdTe substrate, the defect etching results report a similar defect density for both substrate types ($3 \times 10^4$ $cm^{-2}$). The major difference between the two systems lies in the greater lattice tilt distribution observed on the CdTe. The incorporation of 4% of Zn into the lattice appears to result in a less dense dislocation network, although increased diffuse scatter (at low intensity levels) is observed in the (vertical) $\Delta Q_z$ direction (fig.7.7 b). This extra scatter could be linked to possible point defect structure arising from imperfect incorporation of the Zn into the crystal lattice, in the form of Zn vacancies and interstitials. The presence of these additional point defects in the CZT substrate, may explain why the defect density revealed by the etching studies is then similar for both the CdTe and CZT, whereas analysis of the FWHM data in Table 7.2 would suggest that a lower dislocation density would be expected in the CZT system.

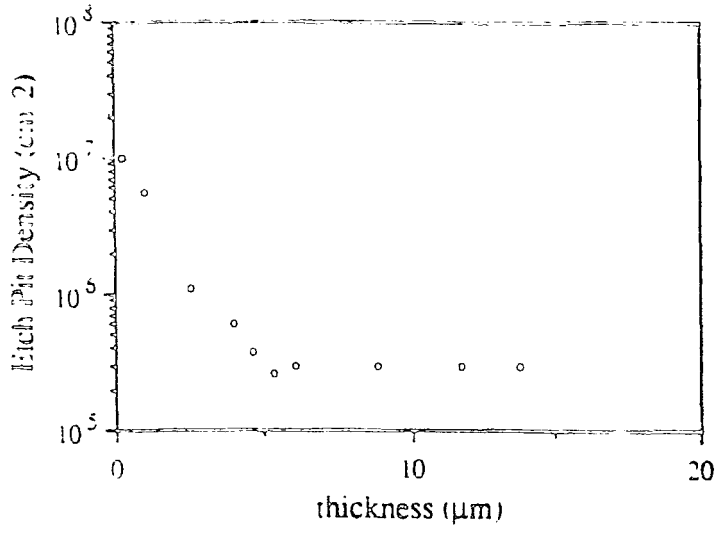


Figure 7.9 (a): Variation in etch pit density with layer thickness in the $Cd_{.24}Hg_{.76}Te$ on CdTe system. After Watson[32].

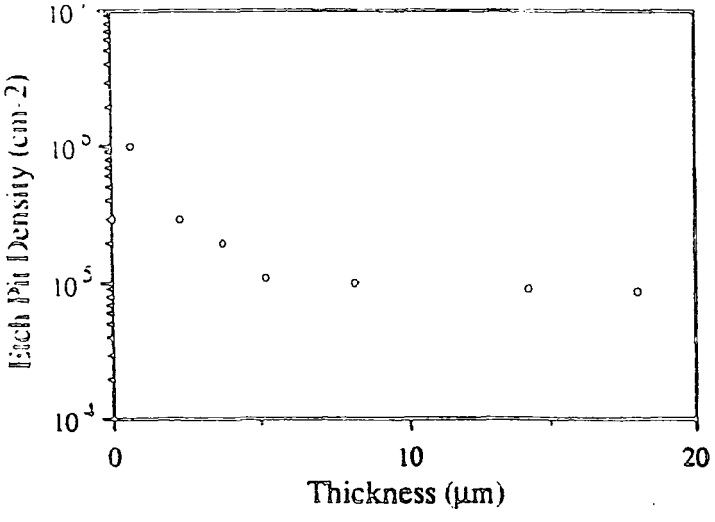


Figure 7.9 (b): Variation in etch pit density with layer thickness in the $Cd_{.24}Hg_{.76}Te$ on $Cd_{.96}Zn_{.04}Te$ system. After Watson[32].

Both the triple crystal and etching data show that the dislocation density (and hence degree of lattice tilt) of the CMT layered samples is higher than in the case of the substrate only systems. Hence, it may be concluded that the dislocation density of the CMT layers does not shadow that of the substrates, a finding which is contrary to that reported by Yoshikawa[35], who states that the CdTe and CZT substrate dislocation density is preserved in LPE grown CMT layers.

In section 7.3.1. the Matthew-Blakeslee model[36] for lattice relaxation of epitaxial films was briefly discussed, with lattice strain being relieved by threading dislocations so that the dislocation density observed in the substrate correlated with that in the layer. The fact that the CMT layer dislocation density is greater than that in the substrates implies that lattice relaxation is occurring by mechanisms other than relief by threading dislocations. Such a possible process is the half loop mechanism[37], which considers the nucleation of a dislocation loop at the layer surface. This loop glides to the substrate/layer interface, giving two threading dislocations linked by a misfit segment. Hence, two threading dislocations are introduced for each segment of misfit dislocation, and the dislocation density in the layer will be greater than that in the substrate.

However, it should be recognised that the samples investigated by Yoshikawa were grown on substrates whose initial dislocation density ($3 \times 10^5$ $cm^{-2}$) was an order of magnitude greater than those examined in this study. If the substrates used by Yoshikawa had sufficient density of threading dislocations to relieve fully the lattice strain, without the need for formation of dislocation half loops, then the layer dislocation density should indeed shadow that of the substrate. Hence, it may be concluded that a critical threshold exists for the dislocation density, above which a sufficient density of threading dislocations exists to relieve layer strain, resulting in matching of the dislocation densities in the layer and substrate.

Assuming that the substrates used in this study have a dislocation density below this threshold value, so that relief of lattice strain occurs by some other mechanism (such as the half loop mechanism mentioned above), then the larger (transverse) tilt FWHM recorded for the CdTe based samples suggests that more dislocations are formed in layers grown on this substrate type compared to CZT based samples. This conclusion is supported by Watson's measurement of the dislocation densities

as a function of thickness[34], which quantitatively show a more dense dislocation network exists in CdTe based layers with respect to a layer of equivalent composition and thickness grown on CZT. This difference in dislocation density can be attributed to the difference in mismatch of the two substrate/layer systems. The mismatch between CdTe and $Cd_{.24}Hg_{.76}Te$ is 0.3% compared to 0.01% between the CdZnTe and $Cd_{.24}Hg_{.76}Te$ system. Hence, nucleation of more misfit dislocations (by the half loop method) is required to relieve lattice strain in the CdTe samples, resulting in a larger dislocation density (and hence lattice tilt FWHM) being recorded for CdTe based samples. Again, this finding is contrary to that of Yoshikawa who reports that the dislocation density is independent of the substrate/layer mismatch but proportional to the substrate dislocation density.

## 7.4 Triple Axis Characterisation Of Low Temperature Grown GaAs Epitaxial Films

MBE grown epitaxial layers of GaAs are usually grown with substrate temperatures in the range 550°C to 600°C, in order to optimise their optical and electrical properties. Layers grown using substrate temperatures below 300°C exhibit high electrical resistivity and degraded optical properties, which would seem to limit their usefulness in semiconductor devices. However, recently GaAs layers grown at low temperature (commonly referred to as LT-GaAs) have attracted great attention for their possible application as an insulating buffer layer in field effect transistor devices[38]. Such low temperature buffer layers have been shown to improve the performance of GaAs electronic devices/integrated circuits and are a suitable material for the fabrication of ultrafast photoconductive switches[39,40,41]. There has also been evidence of superconductivity at low temperatures in layers of LT-GaAs[42].

A series of epitaxial GaAs layers have been grown on GaAs substrates, at the University of Crete. Different substrate temperature were employed during each growth run, with some of the samples being grown by MBE (molecular beam epitaxy) and the rest by ALE (atomic layer epitaxy) in the same MBE reactor. The sample identifiers, together with their corresponding growth technique and substrate temperature (during growth) are detailed in Table 7.3

| Sample I/D | Growth Temperature | Growth Method | Thickness | Annealed |
|---|---|---|---|---|
| 701 | 600 | MBE | 2μm | No |
| 709 | 300 | MBE | 2μm | No |
| 710 | 200 | MBE | 2μm | No |
| 711 | 200 | MBE | 2μm | Yes |
| 712 | 300 | MBE | 2μm | Yes |
| 730 | 450 | ALE | 2.5μm | No |
| 732 | 300 | ALE | 2.5μm | No |
| 734 | 200 | ALE | 2.5μm | No |
| 736 | 600 | ALE | 2.5μm | No |

Table 7.3 : Growth parameters for the low temperature GaAs layers.

The thermal treatment for the two annealed samples (711 and 712) was heating at 600°C for 15 mins., under excess As pressure. Triple crystal analysis of the LT-GaAs samples was performed using the diffractometer in the high resolution, non-dispersive setting (as described above in the study of the CMT on CdTe/CZT system). Full reciprocal space maps were recorded (total data collection time of around 12 hours), with individual transverse and longitudinal triple crystal scans also performed. Table 7.4 lists the FWHM of the longitudinal and transverse scans for each sample investigated.

| Sample | Transverse FWHM (tilts) | Longitudinal FWHM (dilations) |
|---|---|---|
| 701 (MBE) | 15 (15) | 16 (12) |
| 709 (MBE) | 28 | 14 |
| 710 (MBE) | 16 (15) | 15 (13) |
| 711 (MBE) | 24 | 20 |
| 712 (MBE) | 9 | 15 |
| 730 (ALE) | 8 | 11 |
| 732 (ALE) | 8 | 11 |
| 734 (ALE) | 13 (9) | 14 (11) |
| 736 (ALE) | 8 | 9 |

Table 7.4 : FWHM values for the low temperature GaAs samples.

Following the convention adopted in previous sections, the reciprocal space maps for the LT-GaAs samples are plotted to the same scale.

Inspection of the reciprocal space maps (Fig.7.10(a-h)) shows that two separate diffraction peaks are recorded from the samples (710 and 734), whose layers were grown at the lowest temperature (200°C). In these cases, the first figure in Table 7.4 refers to the width of the LT-GaAs layer peak, while that in brackets corresponds to the observed width of the substrate peak. A previous study on MBE grown LT-GaAs[43] found that, although crystalline layers are formed, the final stoichiometry of the layer could include up to 1% excess of As, which is incorporated as antisite defects. This non-stoichiometric ratio will lead to a slight change in the lattice parameter of the deposited layer, leading to a splitting of the layer and substrate peaks, and this is indeed observed in fig. 7.10(b,g), for the samples grown at low temperature by both MBE and ALE. For layers grown above 200°C, only one diffraction peak is recorded.

In Fig. 7.10(b), (g) the "substrate" peak corresponds to the upper of the two peaks visible, i.e., the peak with the largest scattering vector (more positive value of $\Delta Q_y$). The (rocking curve) peak splittings for samples 710 and 734 were measured as 194" and 124", respectively. These peak splittings can be converted into a mismatch by use of the differential form of Bragg's law (Eqn. 7.1),

$$\frac{\delta a}{a} = -\cot\theta_B \delta\theta_B \qquad (7.1)$$

where a is the GaAs lattice parameter, $\theta_B$ the Bragg angle, $\delta\theta_B$ the peak splitting (in radians) and $\delta a$ the difference between substrate and layer lattice parameter. Substitution of the above peak splittings into eqn. (7.1) yields effective lattice mismatch values, m*, of 1447 ppm (sample 710) and 925 ppm (sample 734). Using equation (1.4), real mismatch values, m, of 761 ppm (sample 710)and 486 ppm (sample 734) are obtained.

Growth of GaAs layers at high temperatures (600°C) results in layers of excellent quality with narrow peak widths (sample 736, fig. 7.10 h). This is not altogether surprising as GaAs is usually deposited at temperatures of between 550°C to 600°C, where it exhibits excellent optical and electrical properties in addition to high

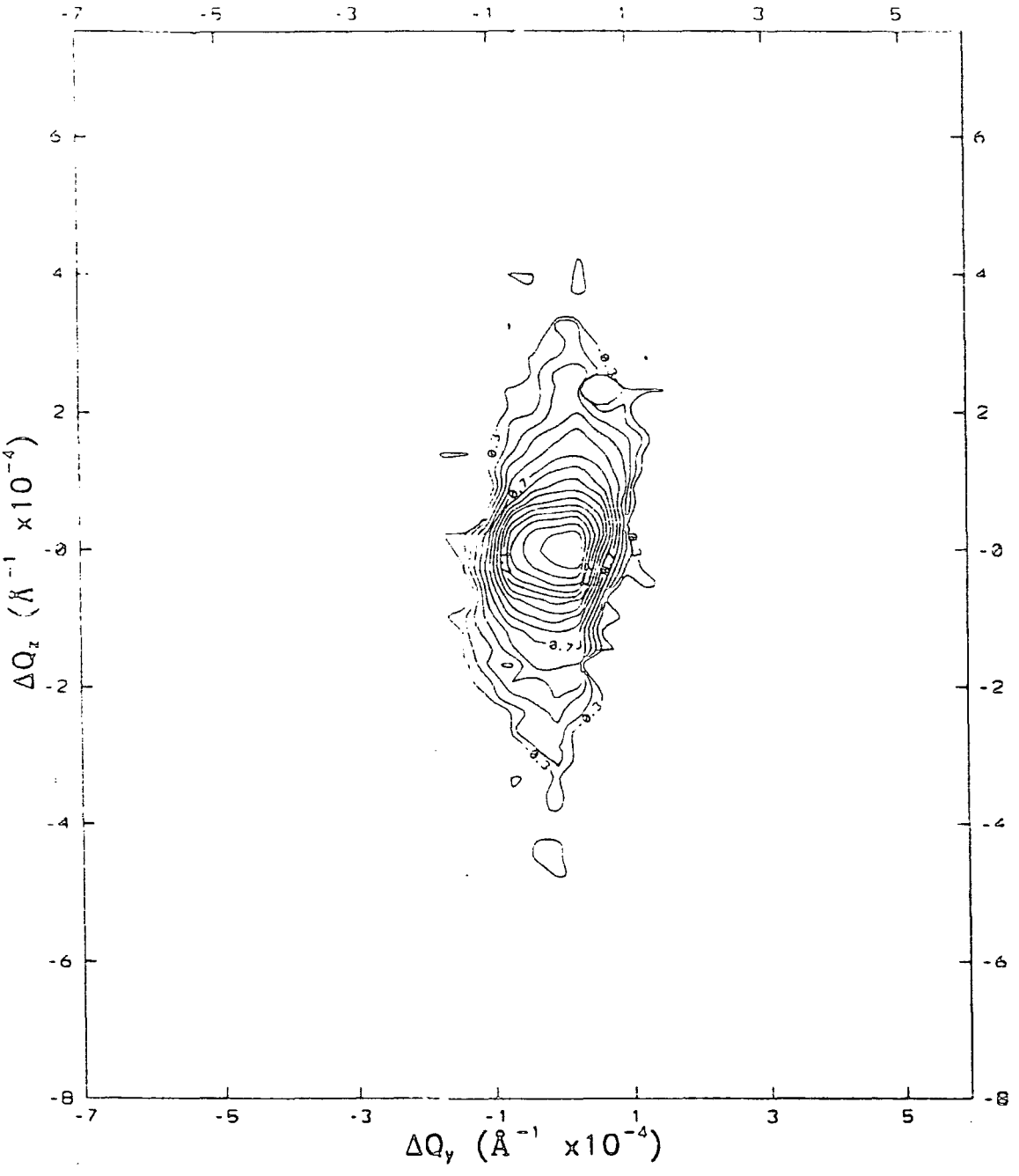


Figure 7.10(a): Reciprocal space plot of the scatter around the (004) reciprocal lattice point of a 2μm layer of GaAs grown on GaAs (sample 709).
Growth temperature = 300°C
Growth method = MBE

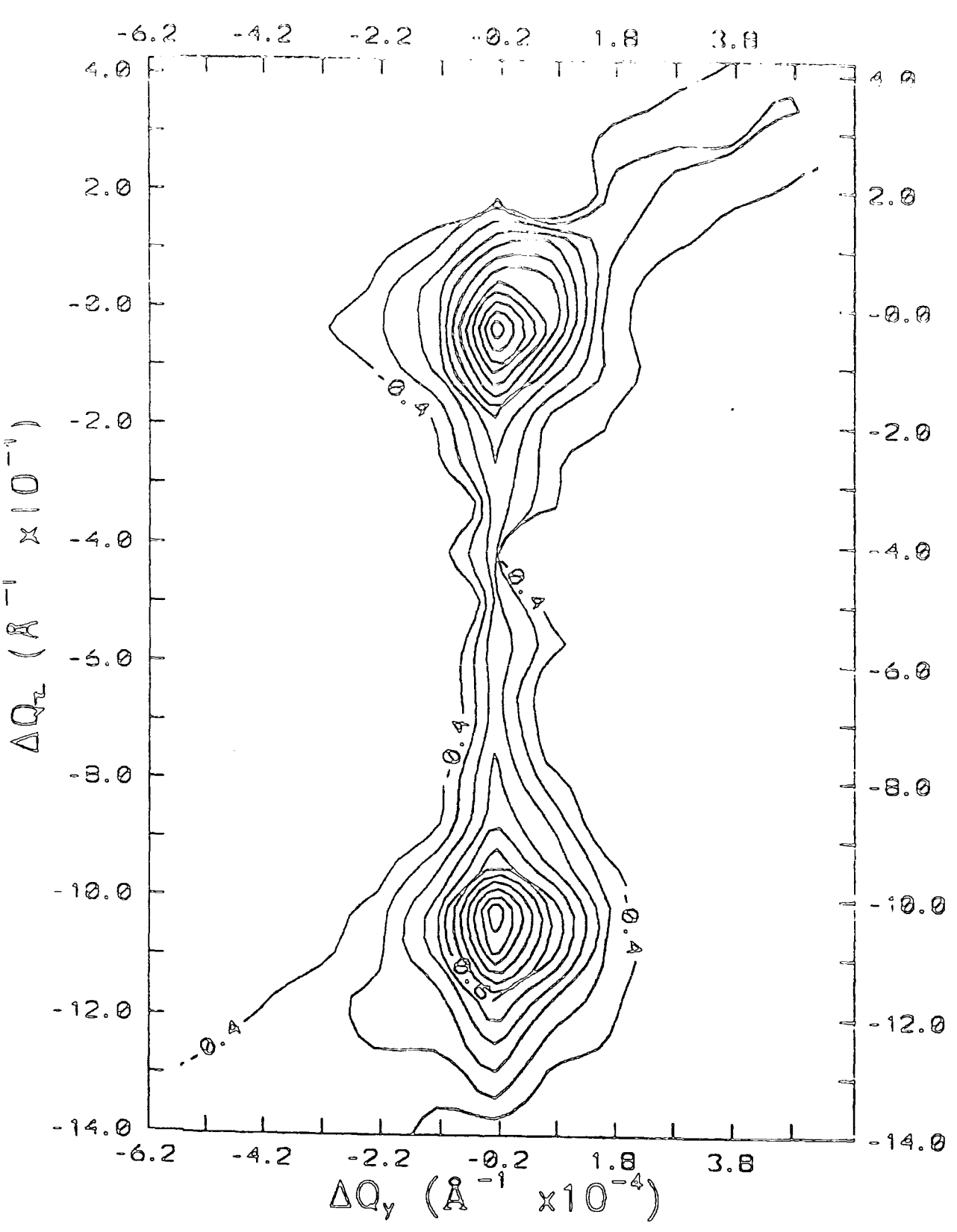


Figure 7.10(b): Reciprocal space plot of the scatter around the (004) reciprocal lattice point of a 2μm layer of GaAs grown on GaAs (sample 710).
Growth temperature = 200°C
Growth method = MBE

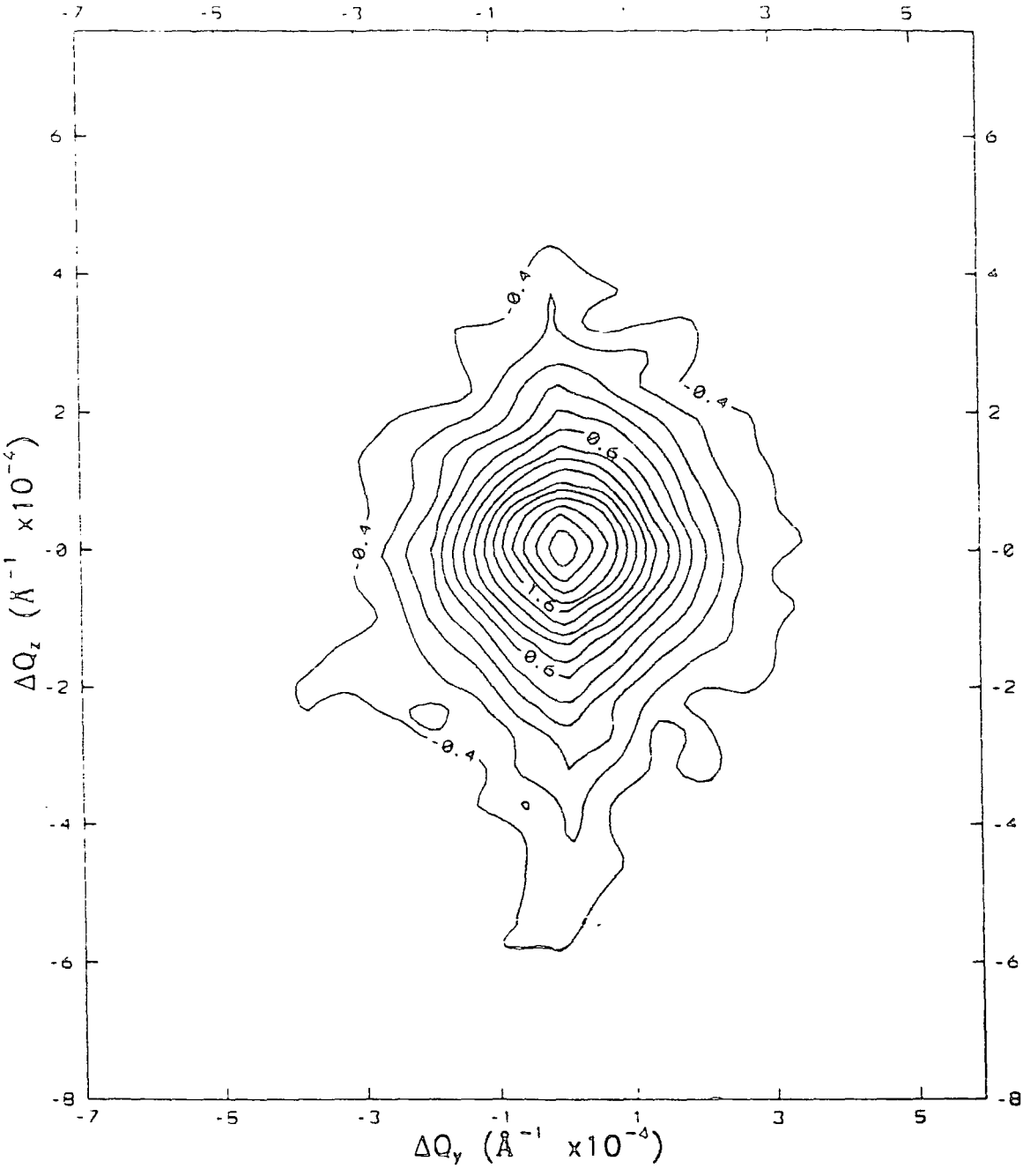


Figure 7.10(c): Reciprocal space plot of the scatter around the (004) reciprocal lattice point of a 2μm layer of GaAs grown on GaAs (sample 711).
Growth temperature = 200°C (Annealed at 600°C for 15 mins.)
Growth method = MBE

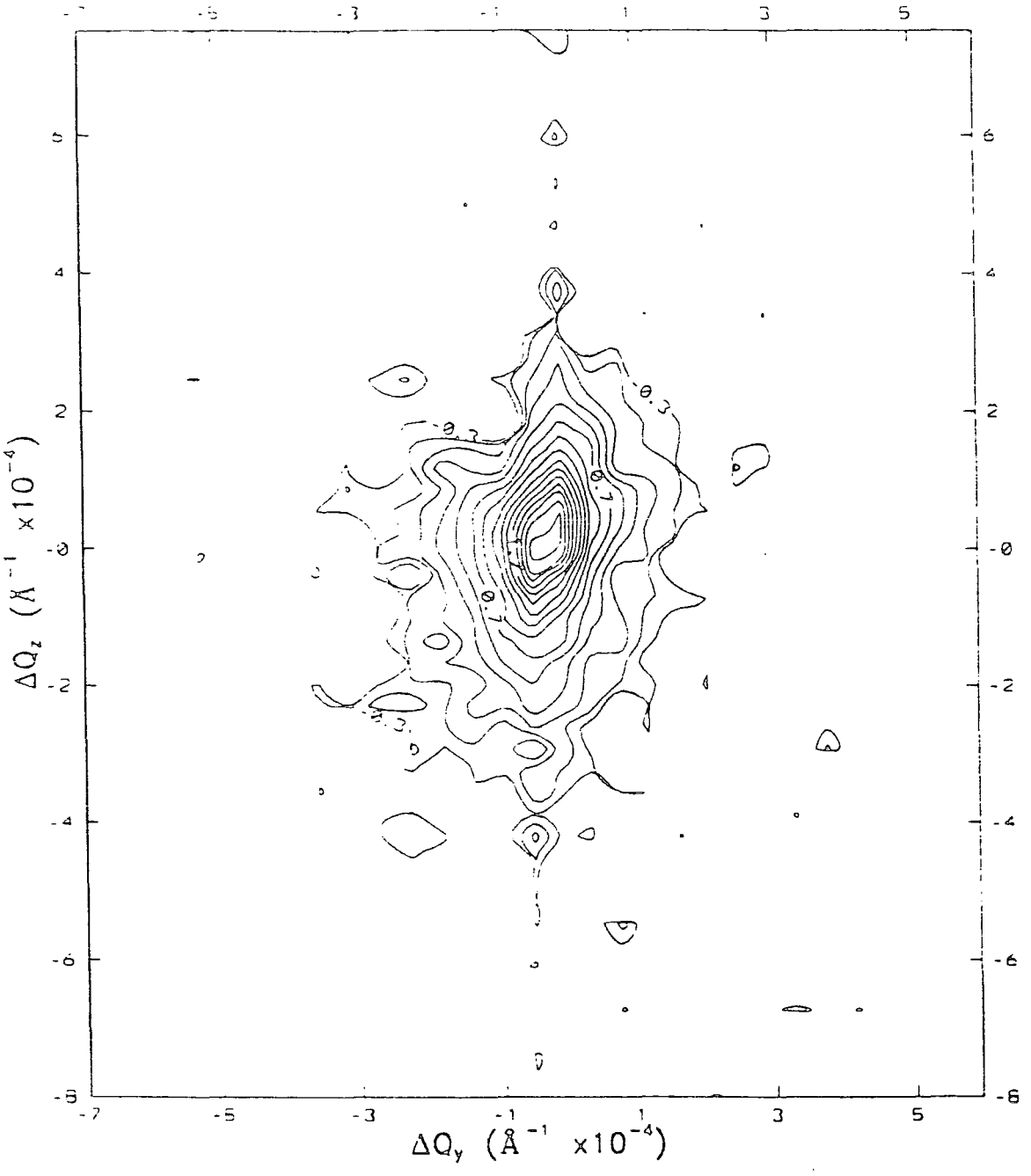


Figure 7.10(d): Reciprocal space plot of the scatter around the (004) reciprocal lattice point of a 2μm layer of GaAs grown on GaAs (sample 712).
Growth temperature = 300°C (Annealed at 600°C for 15 mins.)
Growth method = MBE

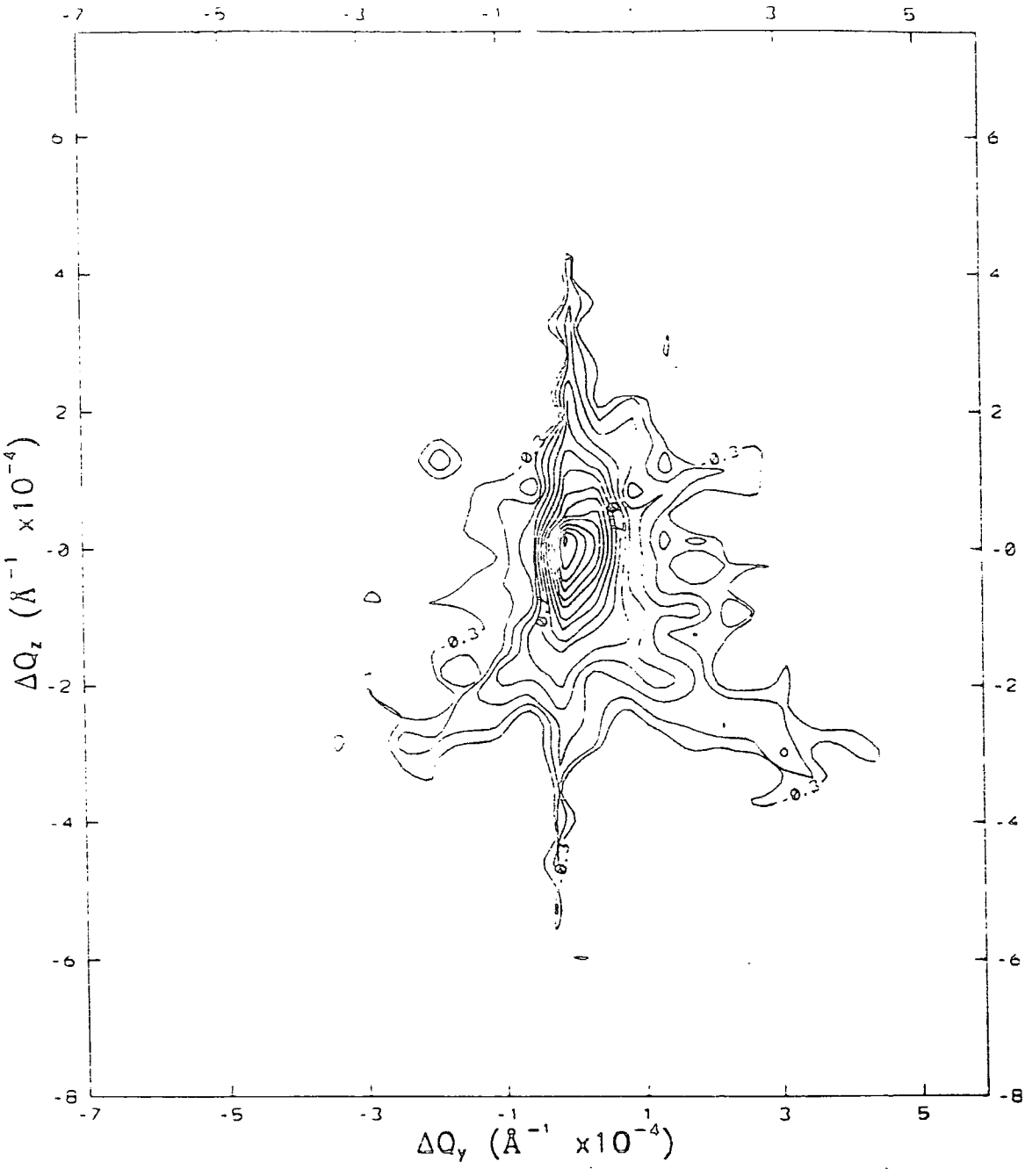


Figure 7.10(e): Reciprocal space plot of the scatter around the (004) reciprocal lattice point of a 2.5μm layer of GaAs grown on GaAs (sample 730).
Growth temperature = 450°C
Growth method = ALE

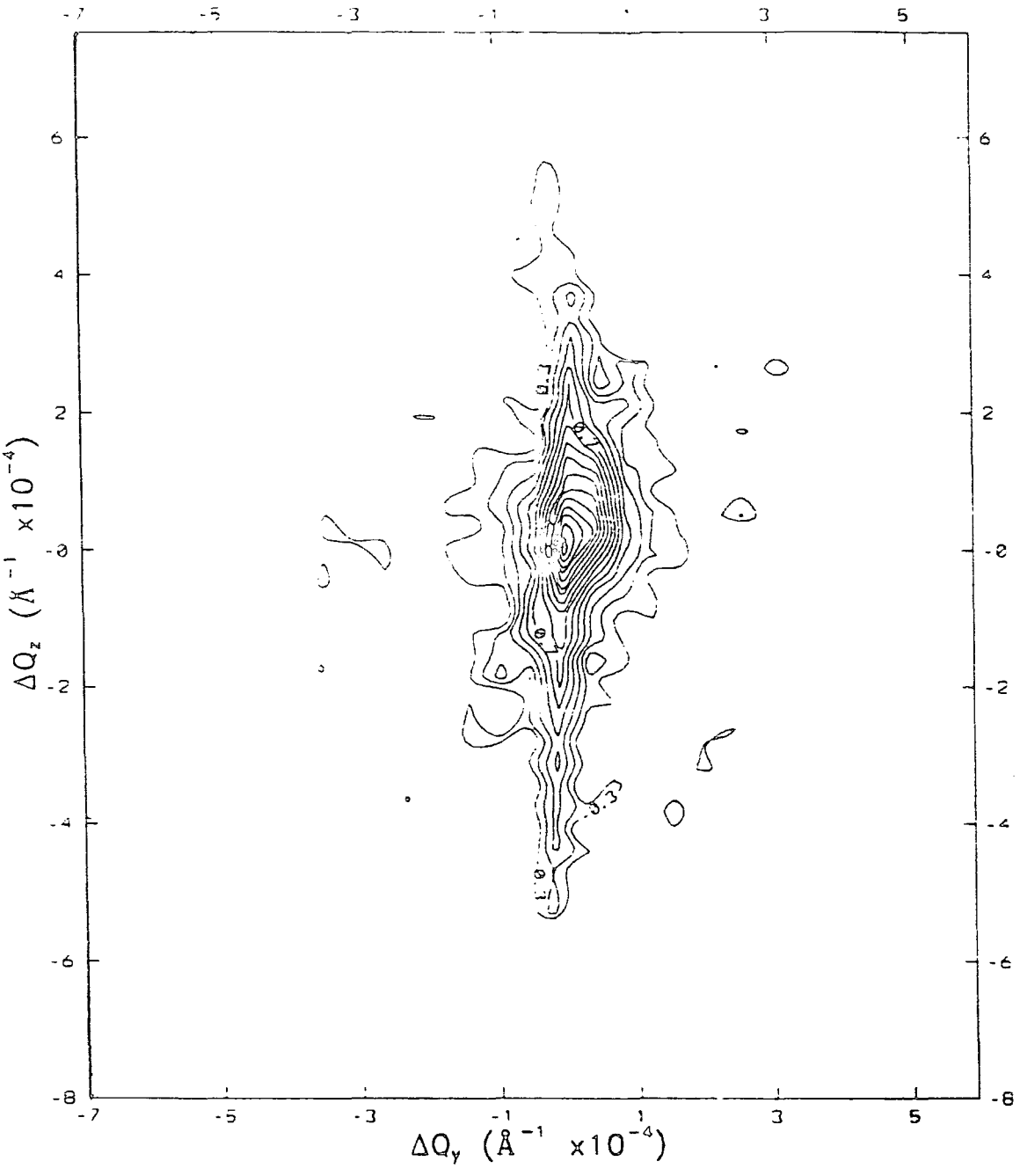


Figure 7.10(f): Reciprocal space plot of the scatter around the (004) reciprocal lattice point of a 2.5μm layer of GaAs grown on GaAs (sample 732).
Growth temperature = 300°C
Growth method = ALE

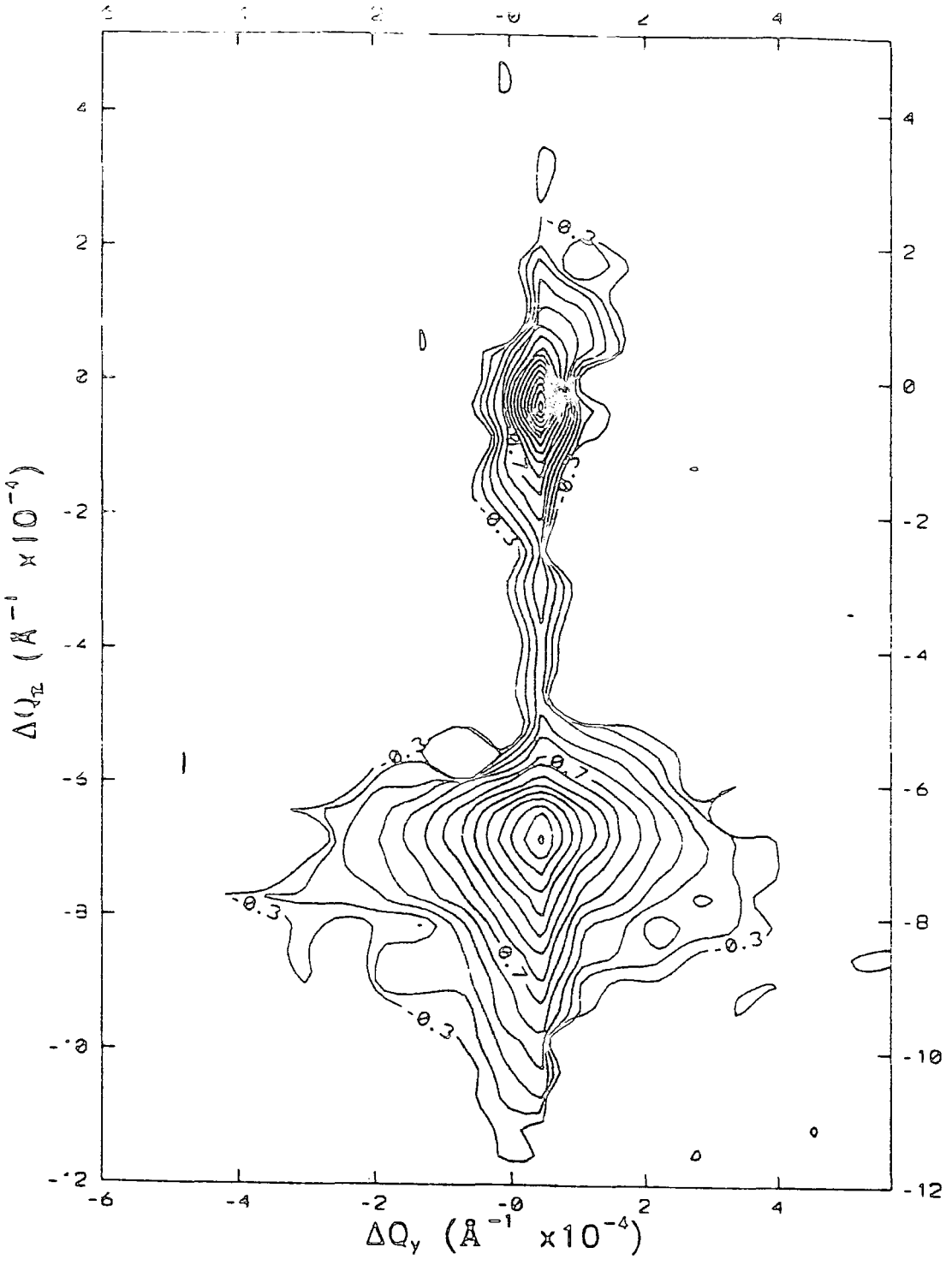


Figure 7.10(g): Reciprocal space plot of the scatter around the (004) reciprocal lattice point of a 2.5μm layer of GaAs grown on GaAs (sample 734).
Growth temperature = 200°C
Growth method = ALE

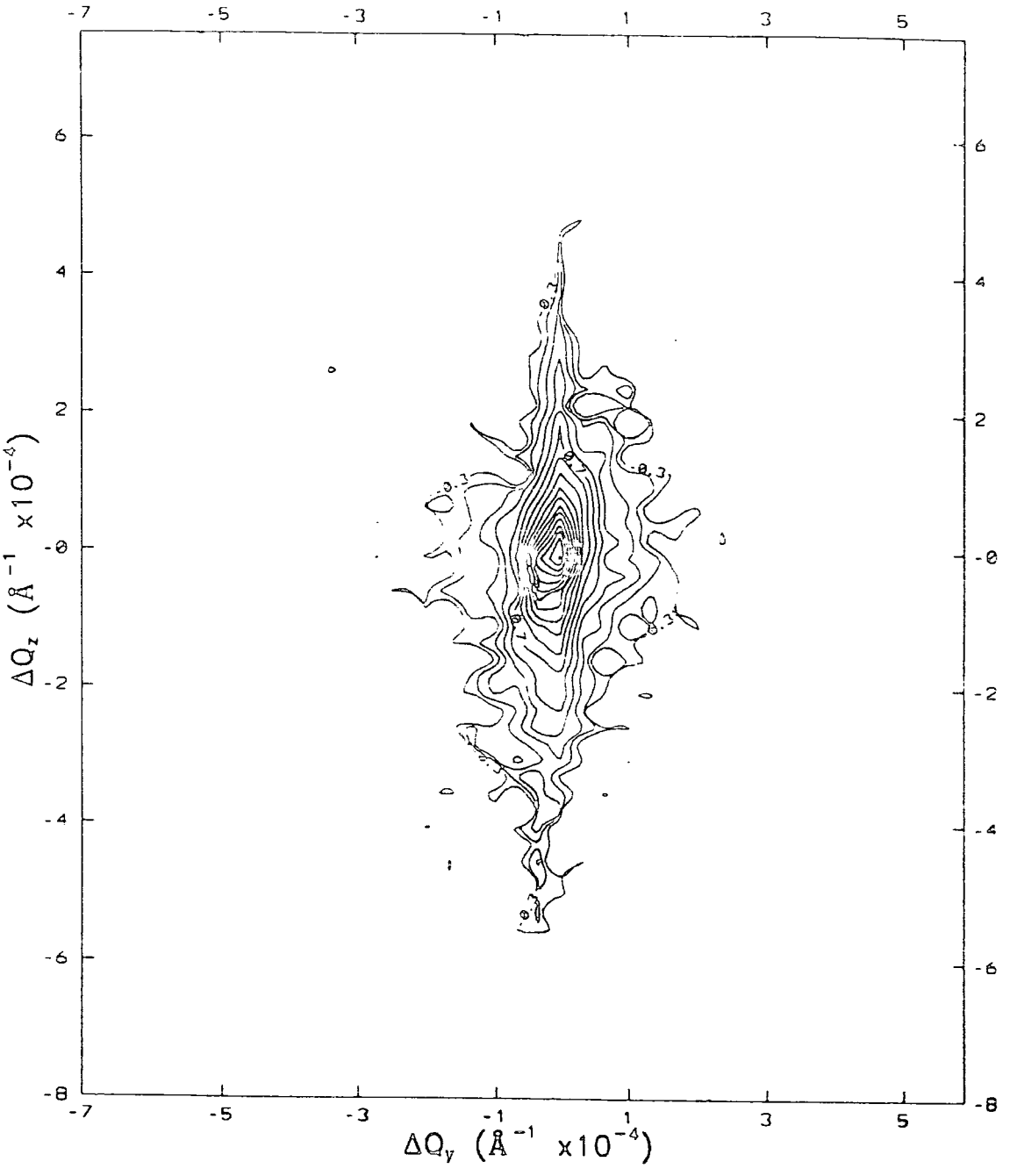


Figure 7.10(h): Reciprocal space plot of the scatter around the (004) reciprocal lattice point of a 2.5μm layer of GaAs grown on GaAs (sample 736).
Growth temperature = 600°C
Growth method = ALE

crystalline quality. The aim in the growth of LT-GaAs layers is to deposit material with a similar high degree of lattice perfection, while tailoring specific, desired insulating electrical properties.

The data gathered for the LT-GaAs samples shows, in general, that the crystalline quality increases as the growth temperature is raised. A guide on the relative perfection of the various LT-GaAs samples can be obtained by comparing their diffraction peak widths with those expected from a "good" (i.e., high quality) conventional GaAs specimen. By defining the "good" GaAs sample to have widths of approximately 7" (transverse) and 8" (longitudinal), Table 7.4 shows that ALE samples grown at temperature as low as 300°C have very narrow peak widths (sample 732, fig.7.10 f), indicating high crystalline perfection. In the case of MBE, growth at an equivalent temperature (sample 709, fig.7.10 b), gives peak widths significantly larger, although the diffuse scatter at very low intensity levels extends slightly further in reciprocal space for the 300°C, ALE grown sample. This suggests that although the dislocation density (and hence extent of sub grain tilt) is less for the ALE sample, a significant level of point defects still exists within sample 709.

As the growth temperature for the ALE samples is increased above 300°C, the diffraction peaks become very narrow, approaching the width of an "ideal" piece of GaAs. Interestingly, an appreciable amount of diffuse scatter, away from the main Bragg peak, is still observed, with the diffuse scatter from sample 730 (growth temp. 450°C) exhibiting asymmetry, corresponding to point defects of an interstitial nature.

The samples grown by MBE (709 and 710) have much broader diffraction peaks although they display slightly less diffuse scatter away from the main peak. Specimens 711 and 712 correspond to annealed samples of 710 and 709, respectively. Taking the samples grown at 200°C first (710 and 711), it can be seen that the effect of annealing is to relax the layer material, with one broad diffraction peak being recorded. The diffuse scatter from the annealed sample (711) extends over a large region of reciprocal space, indicating a high point defect concentration. For the layer deposited by MBE at 300°C (sample 709), the effect of annealing is to again introduce considerable point defect scattering, although, in this case, the extent of lattice tilting (as represented by the transverse FWHM) reduces considerably to only 9". This small transverse width indicates a large reduction in

the mosaicity of the LT GaAs layer, which may be attributed to the interaction, and subsequent annihilation, of dislocations, which are highly mobile at elevated temperatures. The influence of annealing has previously been reported as causing the excess As to form small precipitates, which may explain the wide distribution of diffuse scatter in reciprocal space[44].

The data in Table 7.4 also shows that the layers grown by ALE have narrower tilt and lattice dilation distributions, and are generally of a higher crystalline quality than layers grown at corresponding temperatures by MBE. In particular, all specimens grown by MBE display some variation of lattice parameter, in excess of that which would be expected from a "good" quality sample. This contrasts with the samples grown by ALE which exhibit excellent compositional uniformity (i.e., a narrow lattice dilation distribution).

## 7.5 Conclusions

Double crystal topography studies of direct alloy growth (DAG) MMT layers show that the layers are highly mosaic, with a typical grain size of (130 ± 5) μm, with little internal strain within each sub-grain. This conclusion is supported by triple crystal diffraction analysis of the MMT layers which shows that the principal contribution to the layer rocking curve width arises from the tilt (i.e., mosaicity) of the layer sub-grains. Topographic studies of MMT grown by the interdiffused multilayer process (IMP) show that this sample does not exhibit a mosaic structure, and although heavily dislocated, the IMP sample is essentially single crystal, with the complete sample surface being imaged in the topograph.

Triple crystal diffraction studies of CdTe and $Cd_{0.96}Zn_{0.04}Te$ substrates show the $Cd_{0.96}Zn_{0.04}Te$ substrate to be of higher quality with larger tilt distributions observed in the CdTe sample. Subsequent layers of CMT grown on these two types of substrate reveal that:

i.) The dislocation density (and tilt distribution) of the CMT layer increases as the layer thickness decreases.

ii.) The main contribution to the rocking curve width arises from the lattice tilts within the sample. The values for the longitudinal scan width for all of

the CMT samples examined are small, indicating a high degree of compositional homogeneity (narrow lattice dilation distribution).

iii.) The layers grown on $Cd_{0.96}Zn_{0.04}Te$ substrates are generally of a higher quality, as attested by the triple crystal diffraction peak widths, than those grown on CdTe substrates. This is due to the higher initial quality of the $Cd_{0.96}Zn_{0.04}Te$ substrates and the smaller mismatch ($\approx$ 0.3 %) of the $Cd_{0.96}Zn_{0.04}Te$/CMT system, compared to the CdTe/CMT system (mismatch $\approx$3 %).

These findings are contrary to those reported in the literature which claim that the substrate dislocation density is shadowed by the layer, although studies by other groups relate to substrates with higher initial threading dislocation densities. These conflicting findings can be explained if it is assumed that a threshold dislocation exists above which the residual lattice strain is entirely relieved by threading dislocations. Below this critical value, dislocations are nucleated by some other multiplying process (i.e., the half loop mechanism), resulting in a larger dislocation density being observed in the layer compared to the substrate.

Triple crystal XRD has also been used to assess the crystalline quality of low temperature grown, epitaxial GaAs layers (LT-GaAs). Diffraction measurements of a series of layers, fabricated with different growth temperatures, show that the tilt and lattice dilation distributions increase as the layer growth temperature is decreased. For layers grown at temperatures of 200°C, separate diffraction peaks are obtained from the layer and substrate material. These separate peaks are believed to arise from the non-stoichiometric deposition of GaAs at low temperatures, with an excess As concentration being incorporated into such layers. The excess As leads to a slightly higher lattice parameter for the LT-GaAs layer, resulting in a diffraction peak with a correspondingly lower Bragg angle (and hence smaller scattering vector). Mismatch values for layers grown at this low temperature were calculated to be 761 ppm (MBE) and 486 ppm (ALE). As the growth temperatures is increased, the layer diffraction peak "moves" closer to that of the relatively perfect substrate until, eventually, a single, narrow diffraction peak is obtained, indicating good epitaxial growth (and low defect concentration) at high growth temperatures.

Annealing of the 200°C MBE grown GaAs layers for 15 minutes at 600°C (with an As overpressure) leads to an improvement of the crystalline quality as indicated by the transverse and longitudinal FWHM. The triple crystal diffraction data from the annealed sample 711 (2μm thick, MBE grown at 200°C) shows that only one diffraction peak is obtained, although a significant defect concentration is still apparent as indicated by the relatively large spread of diffuse scatter in reciprocal space. For MBE grown samples deposited at a slighter higher temperature of 300° C, annealing under the same conditions results in a significant reduction in the diffuse scatter, mainly due to a large decrease in the diffraction peak transverse width (the longitudinal width remains essentially unchanged). This may be due to the annihilation of misfit dislocations, nucleated during low temperature growth of mismatched material, upon thermal treatment, leading to a lower dislocation density (and hence less mosaic tilting) with a large reduction in the measured lattice tilt distribution.

Comparison of the data obtained from samples grown by two different deposition techniques indicates that slightly higher quality samples were deposited by the Atomic Layer Epitaxy technique as opposed to those deposited from MBE. In particular, LT-GaAs layers fabricated using ALE, with growth temperatures of as small as 300°C, exhibit narrow lattice dilation and tilt distributions, with small amounts of diffuse scatter. At equivalent growth temperatures a larger lattice parameter distribution is observed in MBE grown samples. The ALE technique appears to be an extremely attractive method for the deposition of high crystalline quality LT-GaAs, and represents a promising route for the fabrication of high crystalline quality layers which will exhibit the required insulating electrical properties.

# Chapter VIII

# Grazing Incidence X-Ray Reflectivity Studies Of Thin Films And Interfaces

## 8.1 Introduction

The previous chapters have demonstrated that the coherent and diffuse scatter from high resolution diffraction experiments contains, in principle, extensive structural information. However, application of diffraction techniques is dependent upon a relatively perfect crystal structure in order to obtain an intense Bragg diffracted beam. When the sample is of poor crystalline quality, or even amorphous, alternative characterisation methods must be employed. As stated in Chapter IV, one technique which is not reliant on some degree of structural order within the sample is Grazing Incidence X-Ray Reflectometry (GIXR). The GIXR technique is particularly suited to the analysis of thin films and can be used to probe the abruptness of layer surfaces and interfaces. The method has recently gained increased popularity due not only to the increasing number of synchrotron radiation sources but also the availability of a dedicated commercial instrument for routine use within the laboratory[1]. Characterisation by GIXR displays many parallels to analysis using diffraction in that the maximum information is extracted by matching simulated to experimental profiles and, while collection of the specular radiation is the common mode of operation, the information present in the diffuse scatter is currently attracting increasing interest.

The small penetration depth associated with the GIXR technique is particularly suited to the study of samples for which near surface information is required. Rabedeau[2] et al. have used GIXR to study thin native oxide films of thickness less than 1 nm on Si (001) surfaces while Krol[3] et al have analysed the growth of $In_xGa_{1-x}As$ epitaxial layers on GaAs and InP substrates, concluding that the main factors which control the interfacial roughness are the quality of substrate and/or growth conditions rather than strain or lattice mismatch. GIXR has also been applied to multilayer systems, an example being the work of Akhsakhalyan[4] et al who have investigated the diffusion of carbon atoms upon annealing of metal-carbon multilayers. The application of the reflectivity technique has not been limited to examination of solids only. Sanyal[5] et al. have examined the liquid-

vapour interface of ethanol at room temperature to measure the root mean square fluctuation of the liquid surface and Braslau[6] et al have studied the liquid-vapour interface for water, carbon tetrachloride and methanol, linking the observed surface roughness to the effects of thermally induced capillary waves and the dimensions of the constituent molecules. Other applications for the GIXR technique have been found in the study of adsorbed monolayers, surfactants, wetting films, Langmuir Blodgett films, film growth morphology, adhesion and surface phase transitions amongst many others.

## 8.2 Layer Thickness Measurements

One of the principle features of the GIXR technique is its ability to measure accurately the thickness of very thin, near surface layers. The presence of thin layers in a sample structure leads to interference or Kiessig[7] fringes at angles just greater than the critical angle in the reflected profile. In a similar way to the use of thickness fringe spacing in diffraction profiles, these measured periods can be used to deduce directly the layer thickness. The relation connecting the observed fringe period, $\Delta\phi$, with associated layer thickness, $t_L$, is given by equation (8.1), and is deduced by considering the conditions necessary for constructive interference of x-rays from different interfaces. Essentially it is equivalent to Braggs law with the interplanar spacing replaced by the layer thickness.

$$\Delta\phi = \frac{\lambda}{2t_L \cos\psi} \cong \frac{\lambda}{2t_L} \tag{8.1}$$

Here, $\lambda$ is the x-ray wavelength and $\psi$ the incidence angle. Since the x-rays are incident at grazing angles the value of $(\cos\psi)$ is approximated to unity.

The visibility of Kiessig fringes is determined by the difference in electron density in going across an interface from one material to another. For single layers of high density grown on substrates with significantly lower densities, highly visible Kiessig fringes are obtained. This is demonstrated in fig.8.1, which shows the specular GIXR profile from a thin layer of $Si_3N_4$ grown on a Si substrate. Substitution of the fringe period, as measured by hand, into equation (8.1) yields a film thickness of (565 ± 20) nm. The reverse situation is demonstrated in fig.8.2, which shows the GIXR profile from an InP based HEMT structure comprising of

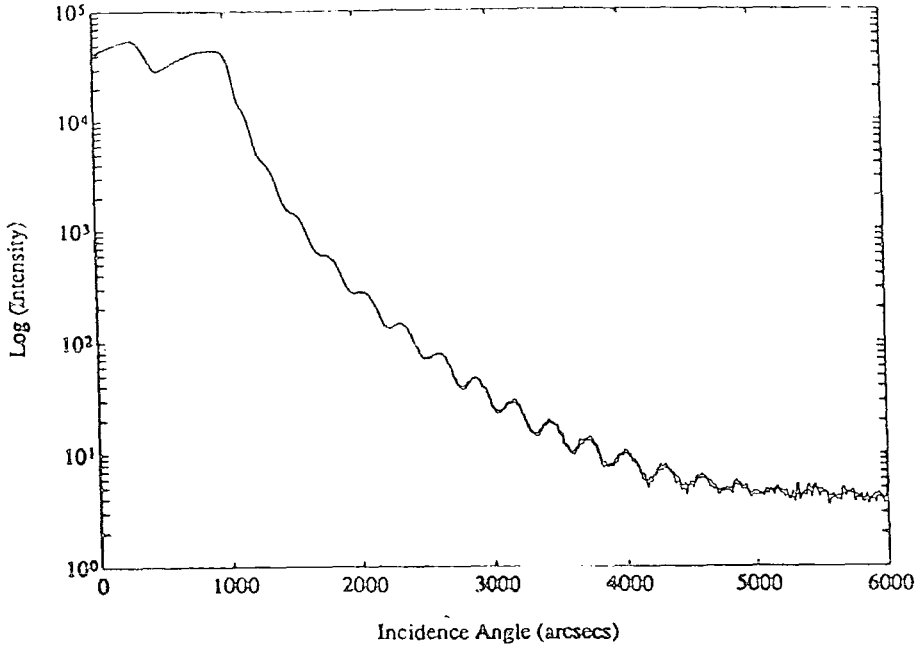


Figure 8.1 : Specular GIXR profile from thin layer of $Si_3N_4$ grown on a Si substrate. Note the high contrast of the interference fringes.

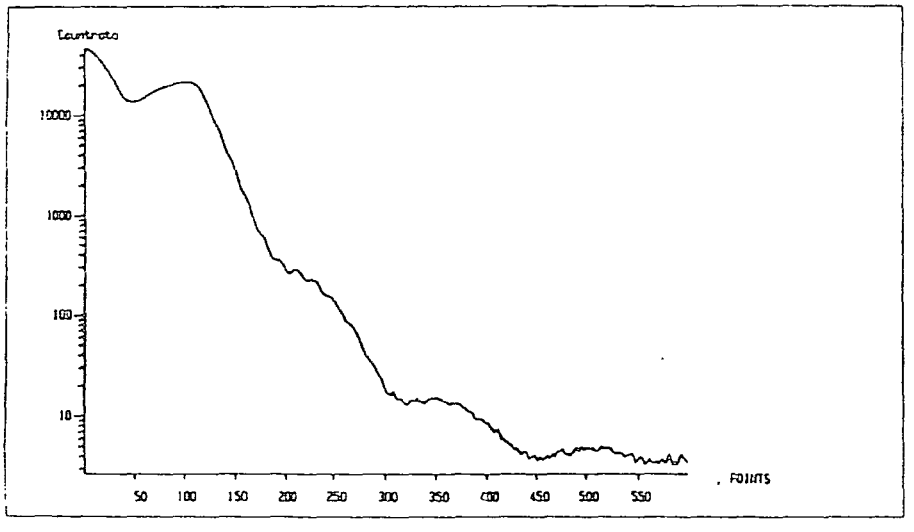

Figure 8.2 : Specular GIXR profile of a GaAs HEMT structure (1 point ≡ 10"). Note the low contrast of the interference fringes.

two layers ($In_xGa_{1-x}As$ and $Al_xIn_{1-x}As$) with a thin $In_xGa_{1-x}As$ cap. While a long range oscillation is observed in the GIXR data (which derives from the thin capping layer thickness), the Kiessig fringes from the total stack thickness, superimposed upon the long range modulation, have low contrast and are only visible at around 2000" (i.e. 200 points). This is due to the difference in electron density between each of these separate layers being small and hence the magnitude of interfering waves from internal interfaces being weak (in the limiting case of the layers having exactly the same electron density, then no interference of reflected waves would occur, as the x-ray beam would effectively not "see" the interface). Thus Kiessig fringes of much smaller amplitude are obtained from this system. While these are still useful for the measurement of layer thicknesses, greater experimental care and longer scan times are needed if the fringes are to be clearly observed in systems with near matched electron densities.

If high precision measurements of layer thickness are not required then measurement of the fringe period by hand is adequate. Layer thicknesses may then be determined with an accuracy dependent upon how precisely fringe spacing can be measured. It should be noted, however, that the period of Kiessig fringes is not constant over the entire reflectivity profile, a contraction in the fringe period occurring at low angles. This is a refractive index effect and arises from the deviation of the x-ray wavefront on crossing an interface. If Fourier transform techniques are to be applied, then account of this variation of period with angle must be taken or erroneous results may be obtained[8]. Only beyond twice the critical angle does the observed fringe spacing become (relatively) constant, and manual measurement of the fringe period beyond this point leads to an approximate layer thickness value. For multiple layer systems, or cases where accurate thickness determination is needed, a simulation program is used to model the reflected intensity. By comparing experimental and simulated profiles, the thickness of single layers can often be measured to the monolayer level, though the quality of data in individual circumstances is obviously critical. For the simulation work carried out in this thesis the Bede Scientific REFS program is used, whose performance has been discussed elsewhere[9]. This program employs the Parratt formalism of the Fresnel equations, as discussed in Chapter II, to calculate the theoretical reflected intensity. The package also includes the effects of surface roughness on the reflected profile. Thus in addition to accurate determination of layer thicknesses the abruptness of layer interfaces may also be obtained.

## 8.3 Interface Roughness Measurements

Real surfaces are not ideally flat and the scattering of x-rays from rough interfaces has been developed by several authors[10,11,12,13]. Taking the z-axis as perpendicular to the interface (i.e. in the growth direction), then the rough interface is represented by an ensemble of flat surfaces whose positions are characterised by a distribution $\omega(z)$ about an average value $z_0$, as shown in fig.8.3(a). If we assume this distribution to be Gaussian, with standard deviation $\sigma$ then it can be shown[14] that the specular reflectivity is reduced by an exponential damping factor (equation 8.2).

$$R = R_F \exp\left[-\left(\frac{4\pi}{\lambda}\psi\sigma\right)^2\right] \tag{8.2}$$

Here, $R_F$ is the Fresnel reflectivity and $\psi$ the incidence angle. For this model, it can be seen that the more grazing the incidence angle then the smaller the effect of roughness on the specular profile. However, it should be noted that this treatment does not consider diffuse scattering as the set of flat surfaces representing the rough interface all reflect the beam in the same direction. The model leading to the derivation of equation(8.2) may be visualised in another manner. The rough surface can be replaced by an interface in which the density, $\rho$, increases gradually, from an initial value, to the bulk density in such a way that the change in density (i.e. $\delta\rho/\delta z$) has a Gaussian form (fig.8.3(b)).

Since roughness has a damping effect upon the specular reflectivity, then by measuring the deviation from the "ideal" GIXR reflection profile the roughness may be measured quantitatively. Further, it has been demonstrated that the effects of roughness at buried interfaces and top surfaces have distinctive effects upon the reflectivity profile, which may, in principle, be distinguished[15]. Top surface roughness results in an increase in the fall off of the reflected signal with angle, whereas buried interface roughness leads only to a damping of the amplitude of the Kiessig fringes. Hence, in order to fit a simulation to an experimental data set, a typical strategy is to first determine layer thicknesses from Kiessig fringe periods and then, by matching to the overall intensity fall off and magnitude of fringe peaks/troughs, top surface and interface roughnesses may be determined.

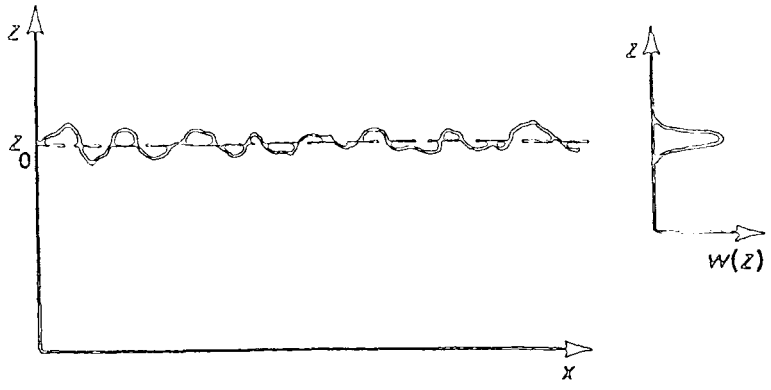


Figure 8.3(a) : Model for the roughness of an interface. The rough surface is represented by a set of flat surfaces with a (Gaussian) distribution, $\omega(z)$ about an average position, $z_0$.

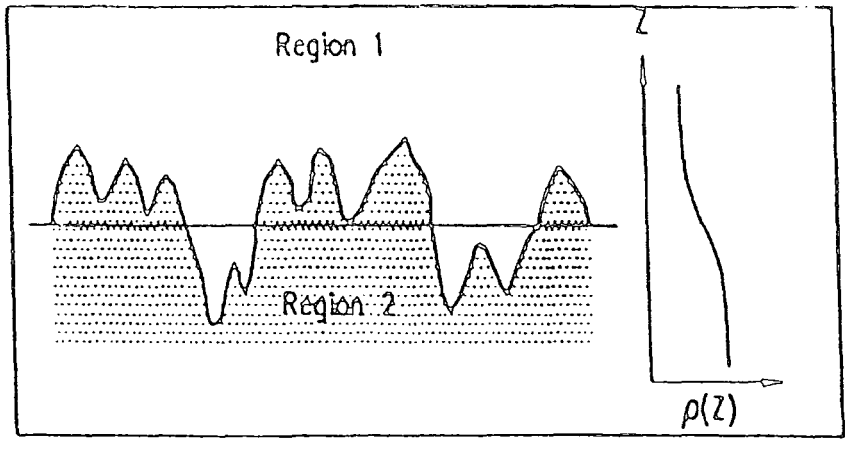


Figure 8.3(b) : A rough surface and its longitudinal density distribution.

This is demonstrated in fig.8.4 which shows the GIXR profile of a single layer of the alloy Ni-Fe (permalloy) grown on Si by MBE at York University by Dr.S.Thompson. Shown as a dashed line on fig.8.4 is the best fit simulation, with model parameters of 17.2 nm for the layer thickness and 0.8 nm of roughness at the top and buried interface. In this case, the data is of a very high quality and the layer thicknesses and interface roughnesses may be determined with an accuracy of ± 0.2 nm. The precision with which structural parameters may be determined depends upon the small changes in the reflectivity profile which can be detected by eye. The quoted errors are those outside of which a detectable worsening of the overall fit to the experimental data occurs. Spirkl [16] has made the process of fitting simulated curves to real data less subjective by devising a computational method for automatic parameter fitting to GIXR data. Based on a least squares approach to minimise the difference between the two curves, the initial starting parameters are constantly changed until the global minimum in the least squares deviation is obtained. In this way (depending upon the layer thickness and data quality) length parameters such as thickness and roughness can be determined automatically to a precision of ± 0.1nm, though only in special cases is it possible to determine material constants such as compositional fractions or densities.

## 8.4 Specular GIXR Studies Of Multilayer Structures

The above examples demonstrate the power of the GIXR technique, in conjunction with a simulation program, of accurately characterising relatively complicated structures. Parameters such as layer thicknesses and interface roughnesses can be obtained with high accuracy. Since many of the new generation of electronic devices require the growth of epitaxial layers in the nanometre regime it is thus of obvious benefit to have a characterisation technique sensitive to such small length scales. By combining GIXR with a method of accurately measuring material composition, such as double crystal diffractometry (or grazing incidence fluorescence[17]), then complete characterisation of complicated sample structures can be achieved. This combination of x-ray characterisation techniques is particularly useful in circumstances where the sample material is initially of high crystalline quality but is then severely degraded by subsequent sample processing. Such a situation exists in the superlattice system of Si \ $Si_xGe_{1-x}$. The $Si_xGe_{1-x}$ alloy is finding increasing use in electronic devices because of its excellent

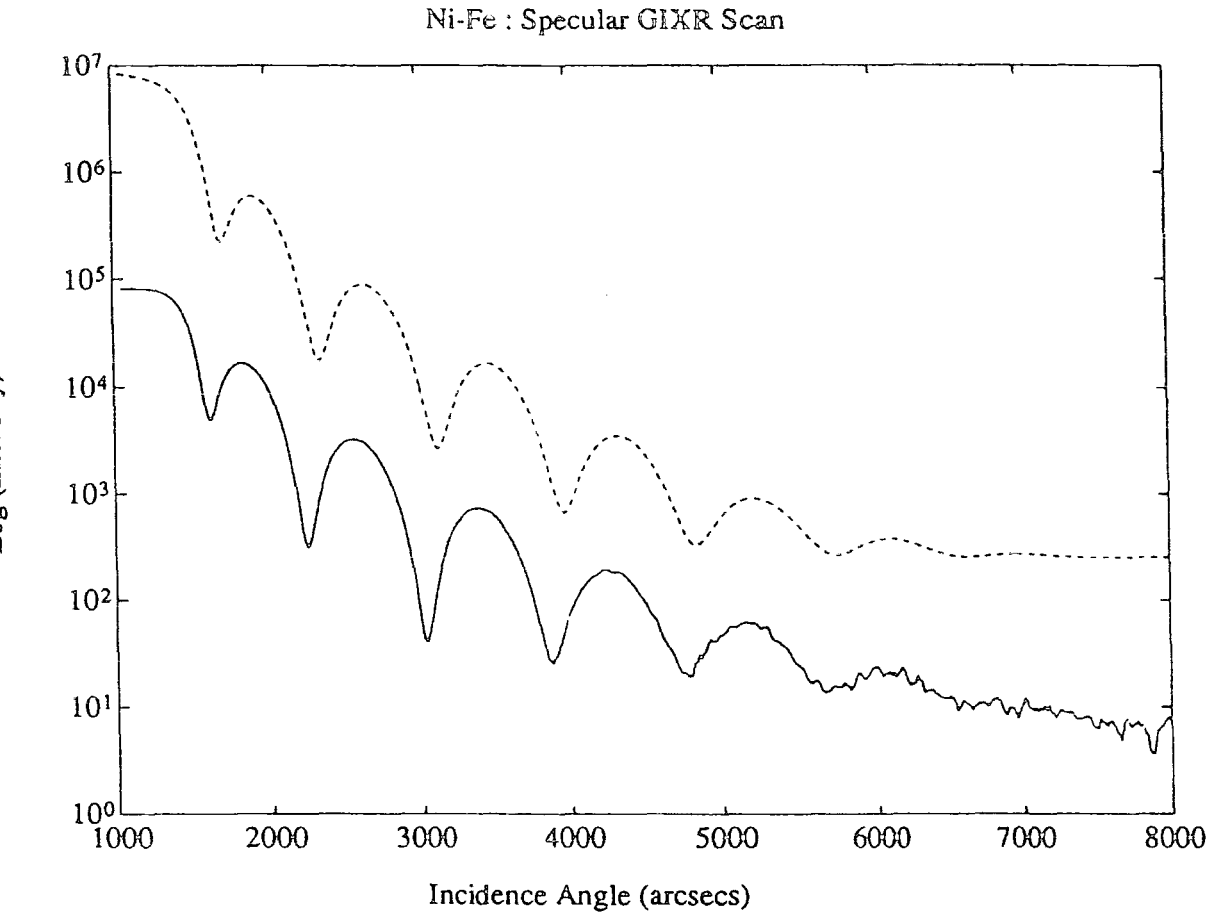


Figure 8.4 : Specular GIXR profile from a thin layer of MBE grown Ni-Fe (permalloy) on a Si substrate. The simulated fit is shown as a dashed line.

electrical properties[18,19]. A great flexibility in the design and fabrication of many types of high performance electronic devices is obtained by using heterostructure or superlattice materials. Properties that cannot be achieved in bulk materials are provided by quantum size effects or by the artificial modulation of superlattice structures[20]. However, prior to its integration into existing silicon technologies the properties of the Si \ $Si_xGe_{1-x}$ system, before and after thermal annealing need to be understood. One of the features of the $Si_xGe_{1-x}$ alloy, especially where the Ge content is high, is that the lattice mismatch results in the production of misfit dislocations. As the dislocation density increases with Ge content, double crystal diffraction curves suffer severe degradation for large mismatched systems. As the GIXR technique is sensitive only to changes in electron density this method maintains its sensitivity as the crystalline quality of the alloy decreases. In the work presented in the following section, conducted in collaboration with workers at Warwick University, the GIXR technique is used to measure changes in the Si \ $Si_xGe_{1-x}$ multilayer structure induced by thermal processing, after the initial structural parameters have been determined from a combination of GIXR and double crystal diffraction techniques.

## 8.5 Characterisation Of Si \ $Si_{1-x}Ge_x$ Superlattice Structures

### 8.5.1 The pre-annealed Si \ $Si_{1-x}Ge_x$ samples

The $Si_{1-x}Ge_x$ samples studied were grown on Si substrates by MBE in a VG Semicon chamber at Warwick University by A. Powell. The substrate temperature during deposition was 550°C and the matrix flux deposition rate around 0.1 nm $s^{-1}$. The structures consisted of a five period superlattice with (nominally) 24 nm of Si and 8 nm of $Si_{1-x}Ge_x$, capped with 10 nm of Si, as shown in Table 8.1. Five similar structures were grown with (nominal) $Si_{1-x}Ge_x$ layer compositions of x=0.1, 0.2, 0.3, 0.4 and 0.5.

Composition values and layer thicknesses were determined using double crystal diffraction (DCD) techniques on a Bede 150 diffractometer with $CuK\alpha_1$ radiation. The angular dispersive x-ray reflectivity measurements were carried out using a Bede GXR1 reflectometer with, again, $CuK\alpha_1$ radiation. Results from these two types of experiments were modelled with the Bede RADS and REFS simulation programs.

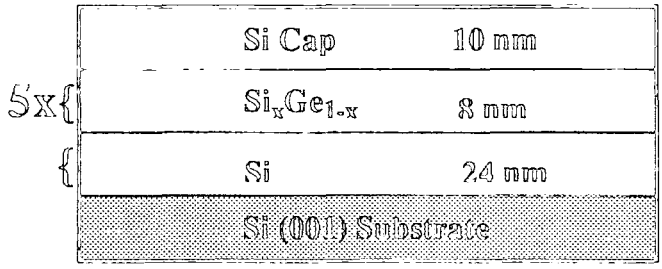


Table 8.1 : Nominal sample structure of pre-annealed $Si \setminus Si_xGe_{1-x}$ superlattices.

Table 8.2 shows the Ge composition as deduced by DCD and the superlattice period, as obtained from both techniques, for the five samples. The main period observable in the diffraction and GIXR profiles arises from the superlattice period, i.e., the thickness of the repeat unit consisting of one Si layer and one $Si_xGe_{1-x}$ layer.

| | Double Crystal Diffraction | | GIXR |
|---|---|---|---|
| Sample | $Si_{1-x}Ge_x$ Composition (±0.005) | Superlattice Period (± 0.3 nm) | Superlattice Period (± 0.3 nm) |
| ap1312 | 0.100 | 30.8 | 30.8 |
| ap1316 | 0.206 | 33.1 | 32.8 |
| ap1314 | 0.325 | 32.2 | 31.9 |
| ap1315 | 0.432 | 33.3 | 33.4 |
| ap1313 | 0.57 ± 0.05 | - | 32.3 |

Table 8.2 : Measured composition and superlattice period of pre-annealed samples.

DCD Data :

The first thing to note from Table 8.1 is the excellent agreement obtained for the superlattice period as measured by both techniques. Double crystal rocking curves for the samples ap1314 (32.5% Ge) and ap1313 (57% Ge) are shown in fig. 8.5(a,b). Here, the rocking curve for ap1314 exhibits excellent peak and fringe structure, from which the superlattice period may be determined. However, in the case of ap1313 the high lattice mismatch has resulted in the relaxation of the

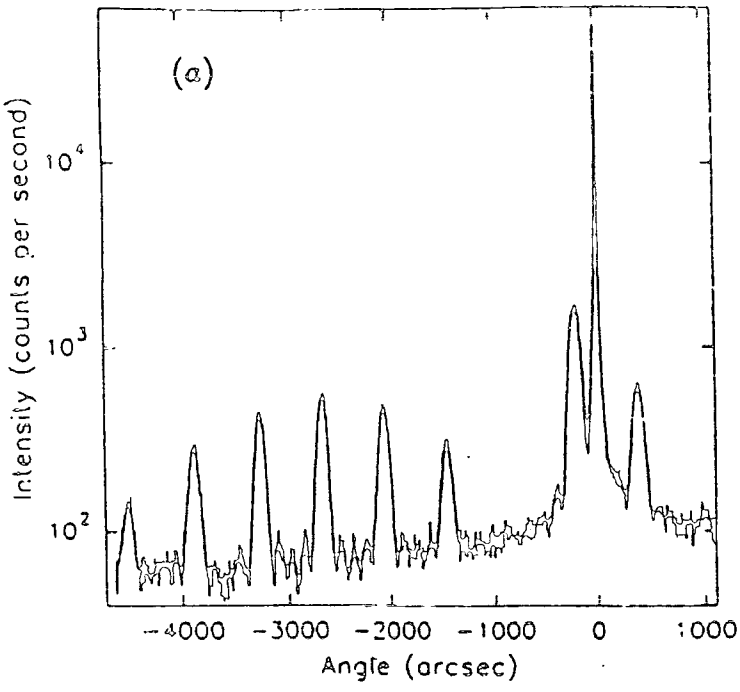


Figure 8.5(a) : DCD rocking curve of sample ap1314 (before annealing).
Ge content = (32.5±0.5)%.

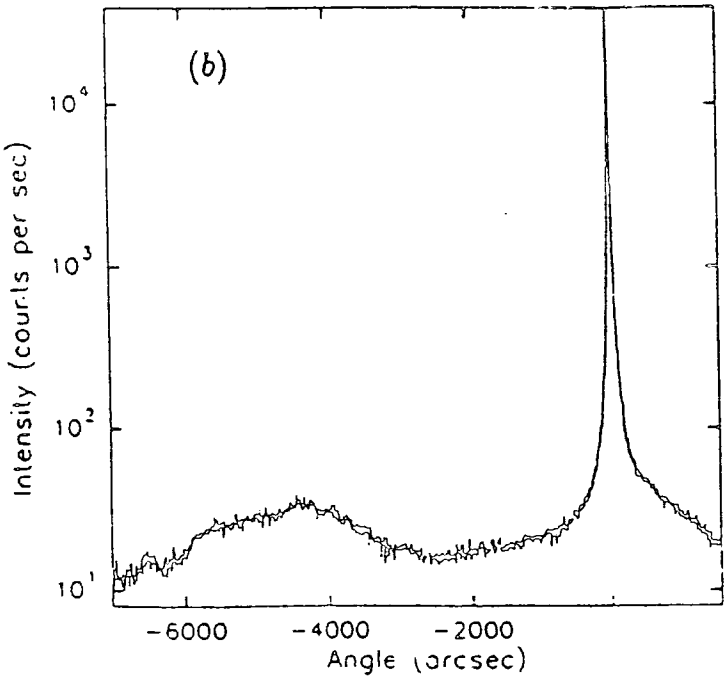


Figure 8.5(b): DCD rocking curve of sample ap1313 (before annealing).
Ge content = (57±5)%.

superlattice structure via the nucleation of misfit dislocations. No fringe structure is visible and it is not possible from this data to determine the superlattice period. Even though the individual superlattice peaks have broadened beyond recognition, recording of a second, asymmetric reflection, allows the composition to be deduced from their average position.

GIXR Data :

The recorded GIXR data for each sample is shown in fig.8.6(a-e) together with its best fit simulation. Included in the simulation models is a 2.5 nm silicon oxide layer, present in order to model the effects of the thermal oxide growing on top of the sample since it was removed from the high vacuum growth chamber[21]. The large low order Bragg peaks arise from the superlattice period whereas the small interference (Kiessig) fringes, visible between the Bragg peaks, are related to the thickness of the total layer stack. For incidence angles above the critical angle, $\psi_c$, the reflected specular intensity falls off as the inverse fourth power of the scattering vector. Hence, by subtracting the constant detector background and multiplying the reflected intensity by a factor of $\psi^4$, the top surface roughness can be determined from consideration of the gradient. This form of data manipulation is illustrated in fig.8.7, which shows the transformed data for samples ap1314 and ap1313. Having measured the superlattice period, the effects of the modulating envelope are examined in order to pull out the individual layer thicknesses. The relative ratio of the Si and $Si_xGe_{1-x}$ thicknesses affects markedly the mark/space ratio of the Bragg peaks. The two thicknesses are adjusted to give broad agreement to the observed relative peak heights. Consideration is then given to fine tuning the shape of the modulation envelope by introducing surface and interface roughening into the model. Interface roughness can be assigned to either of the two types of interface within the sample, the Si interface on which is grown $Si_xGe_{1-x}$ (labelled as $Si \rightarrow Si_xGe_{1-x}$) or the $Si_xGe_{1-x}$ interface onto which Si is deposited (denoted hereafter by $Si_xGe_{1-x} \rightarrow Si$). It should be noted that roughness at both the $Si \rightarrow Si_xGe_{1-x}$ and $Si_xGe_{1-x} \rightarrow Si$ interfaces is required to reduce the fringe amplitude as only one of the interface types needs to be sharp in order to define the superlattice period. A larger roughness at one of the two types of interface ($Si \rightarrow Si_xGe_{1-x}$ or $Si_xGe_{1-x} \rightarrow Si$) alters the effect of the modulation envelope and a detectable change in the relative peak intensities occurs. Careful modelling is thus able to determine two separate values for interface roughness.

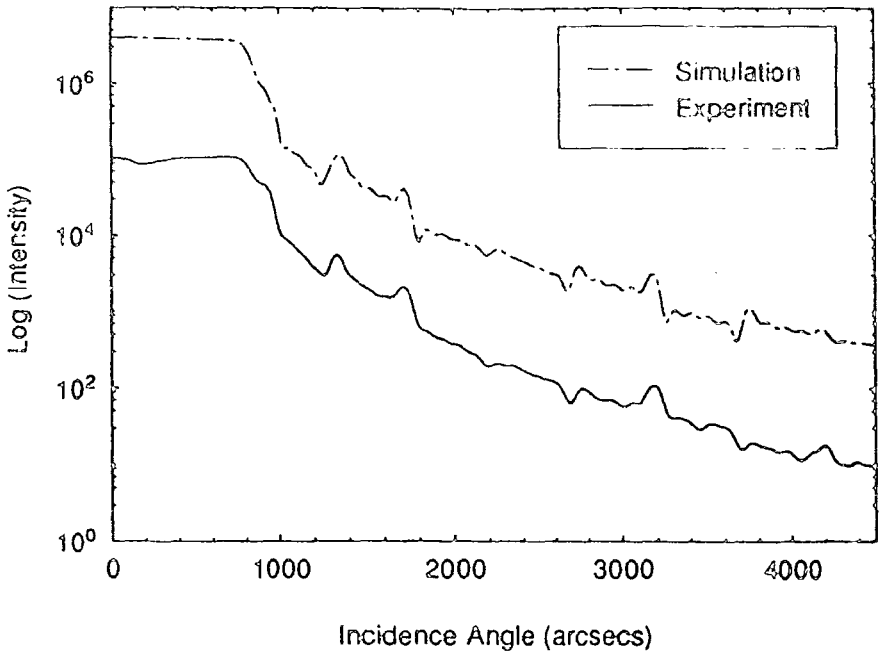


Figure 8.6(a) : GIXR profile of pre-annealed ap1312 sample (%Ge=10).

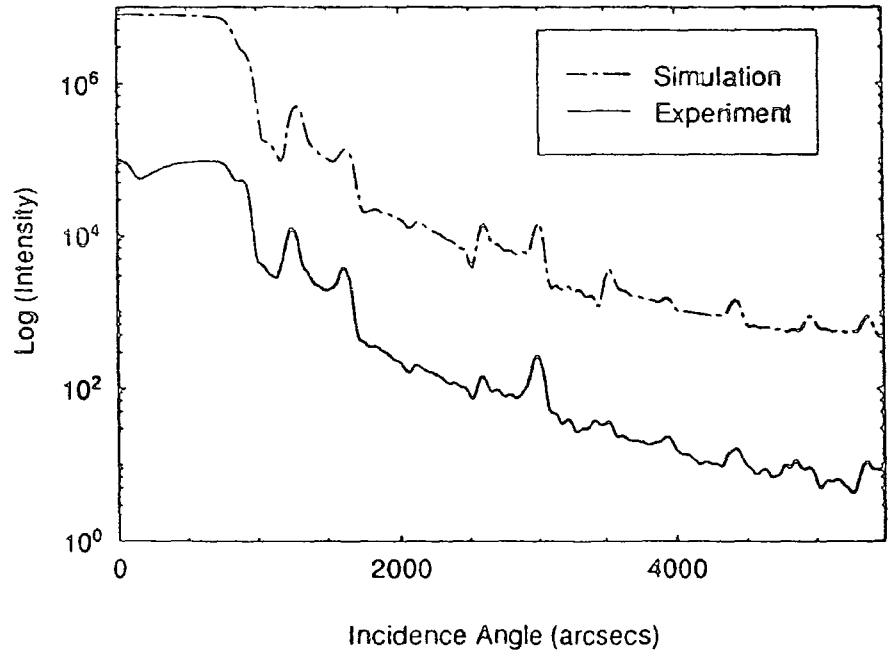


Figure 8.6(b) : GIXR profile of pre-annealed ap1316 sample (%Ge=20.6).

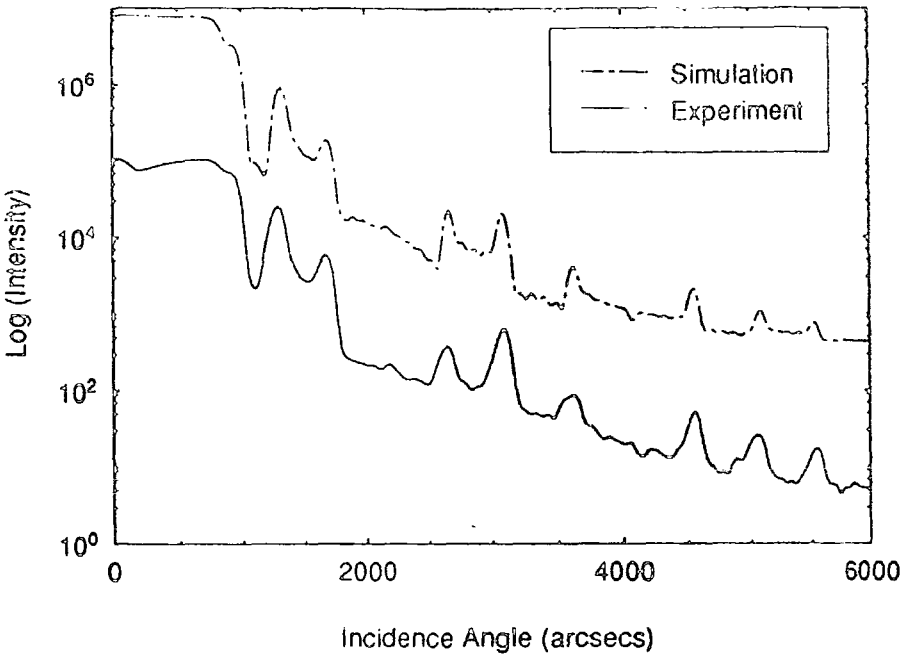


Figure 8.6(c) : GIXR profile of pre-annealed ap1314 sample (%Ge=32.5).

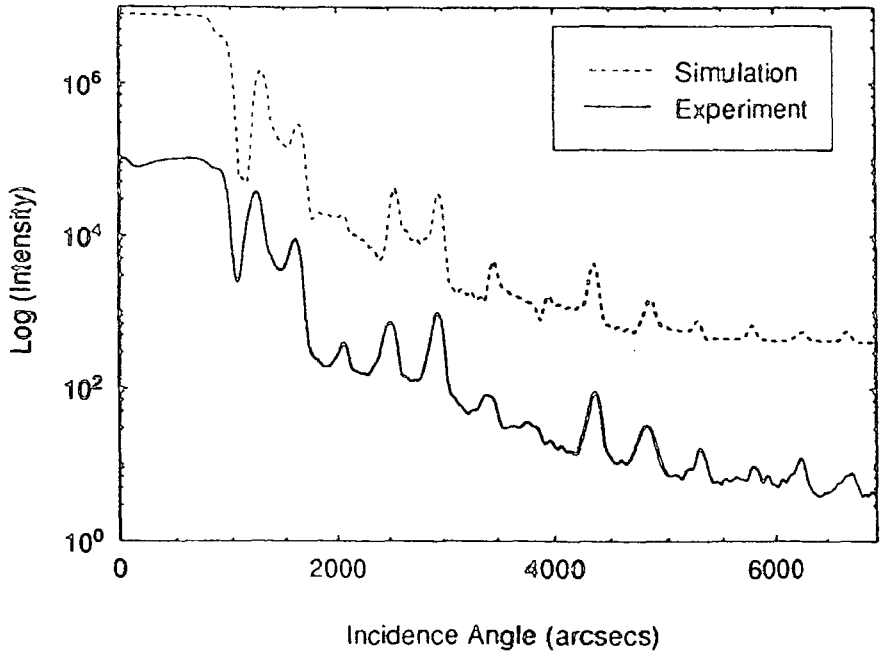


Figure 8.6(d) : GIXR profile of pre-annealed ap1315 sample (%Ge=43.2).

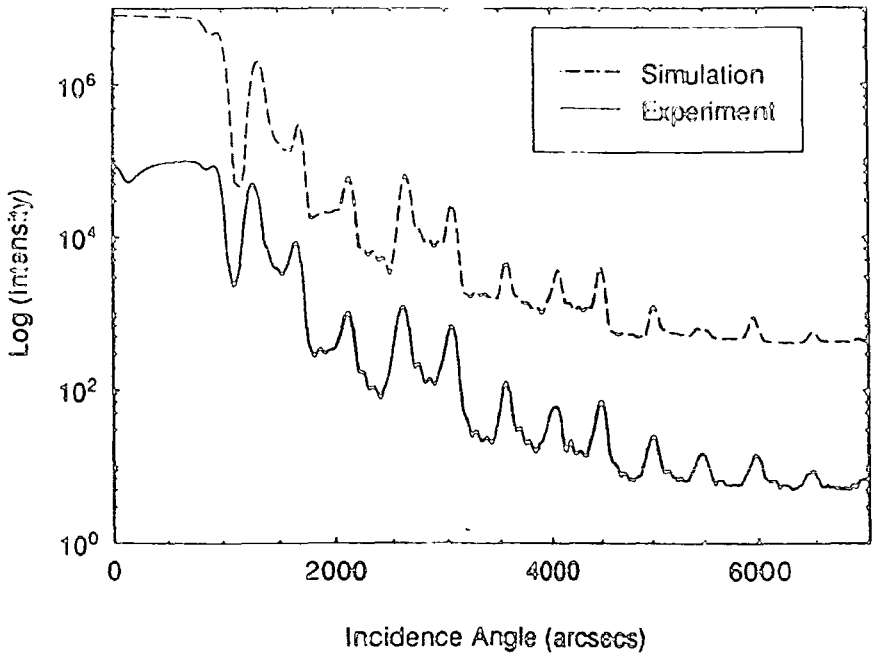


Figure 8.6(e) : GIXR profile of pre-annealed ap1313 sample (%Ge=57).

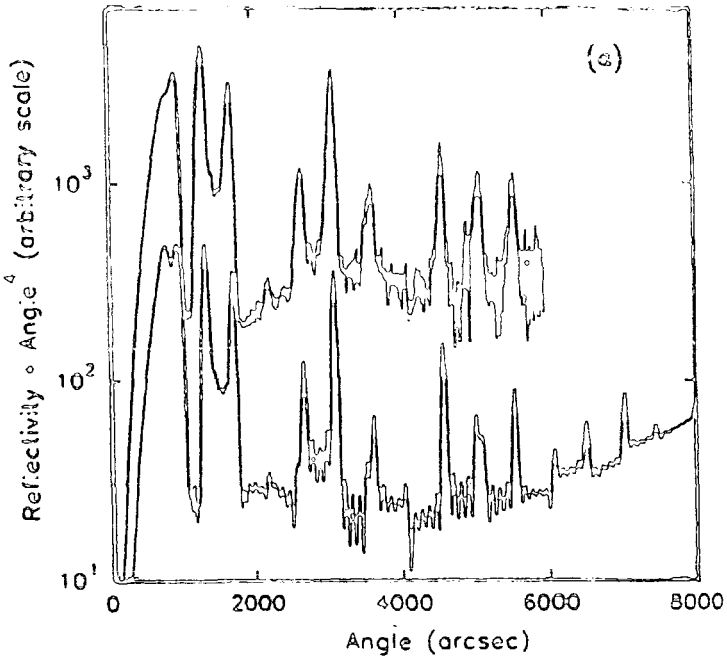


Figure 8.7(a) : Specular GIXR data for sample ap1314. The reflected intensity has been multiplied by a factor of $\psi^4$ (after subtraction of the constant detector background). The upper trace is the experimental data and the lower trace is the best fit simulation.

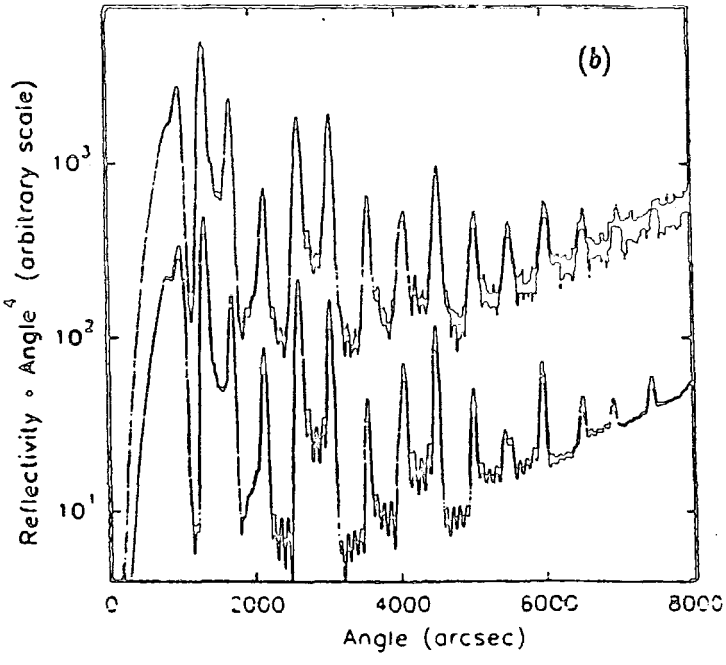


Figure 8.7(b) : Specular GIXR data for sample ap1313. The reflected intensity has been multiplied by a factor of $\psi^4$ (after subtraction of the constant detector background). The upper trace is the experimental data and the lower trace is the best fit simulation.

The individual layer thicknesses and interface roughnesses used to obtain the best fit simulations are shown in Table 8.3.

| Sample | Si Layer Thickness (nm) | $Si_xGe_{1-x}$ Layer Thickness (nm) | $Si \rightarrow Si_xGe_{1-x}$ Roughness (nm) | $Si_xGe_{1-x} \rightarrow Si$ Roughness (nm) |
|---|---|---|---|---|
| ap1312 | 23.5 ± 0.3 | 7.3 ± 0.3 | 0.5 ± 0.3 | 0.5 ± 0.3 |
| ap1316 | 24.8 ± 0.3 | 8.0 ± 0.3 | 0.5 ± 0.3 | 0.5 ± 0.3 |
| ap1314 | 23.8 ± 0.2 | 8.1 ± 0.2 | 0.5 ± 0.2 | 0.7 ± 0.3 |
| ap1315 | 24.6 ± 0.2 | 8.8 ± 0.2 | 0.5 ± 0.2 | 1.0 ± 0.3 |
| ap1313 | 22.9 ± 0.2 | 9.4 ± 0.2 | 0.5 ±0.2 | 1.0 ± 0.3 |

Table 8.3 : Sample parameters of pre-annealed Si / $Si_xGe_{1-x}$ samples, as determined from GIXR.

Not included in the above table is the value for top surface roughness, which was found to be (0.5 ± 0.2) nm for each sample. Table 8.3 shows that as the Ge concentration in the $Si_xGe_{1-x}$ layer is increased there is a corresponding increase in the roughness of one of the two types of interface. It is not possible using the x-ray reflectivity technique to say which of the two interfaces is the rougher but the quality of the top surface suggests that the Si provides the smoother interface. This conclusion has been confirmed by TEM analysis, carried out by P.D Augustus of GEC-Marconi Materials Technology Ltd., which shows the $Si_xGe_{1-x} \rightarrow Si$ interface to possess a regular long range thickness variation. This type of sinusoidal thickness variation has been reported in other superlattice systems[22]. TEM micrographs demonstrating this effect are shown in fig.8.8(a,b). The $Si_xGe_{1-x} \rightarrow Si$ interface, at the top of the darker $Si_xGe_{1-x}$ layers, has a long range r.m.s roughness of (1.0 ± 0.3) nm with period around 70 nm. The $Si \rightarrow Si_xGe_{1-x}$ interfaces in the micrograph appear to be smooth as compared to a roughness value of (0.5 ± 0.2) nm from the reflectivity results. This may be accounted for by assuming either a short range roughness too small to be observable by TEM or a slight grading of the $Si \rightarrow Si_xGe_{1-x}$ interface (some compositional intermixing of Si and Ge has been reported for temperatures as low as 450°C)[23]. The specular GIXR technique cannot distinguish between genuine random roughness and

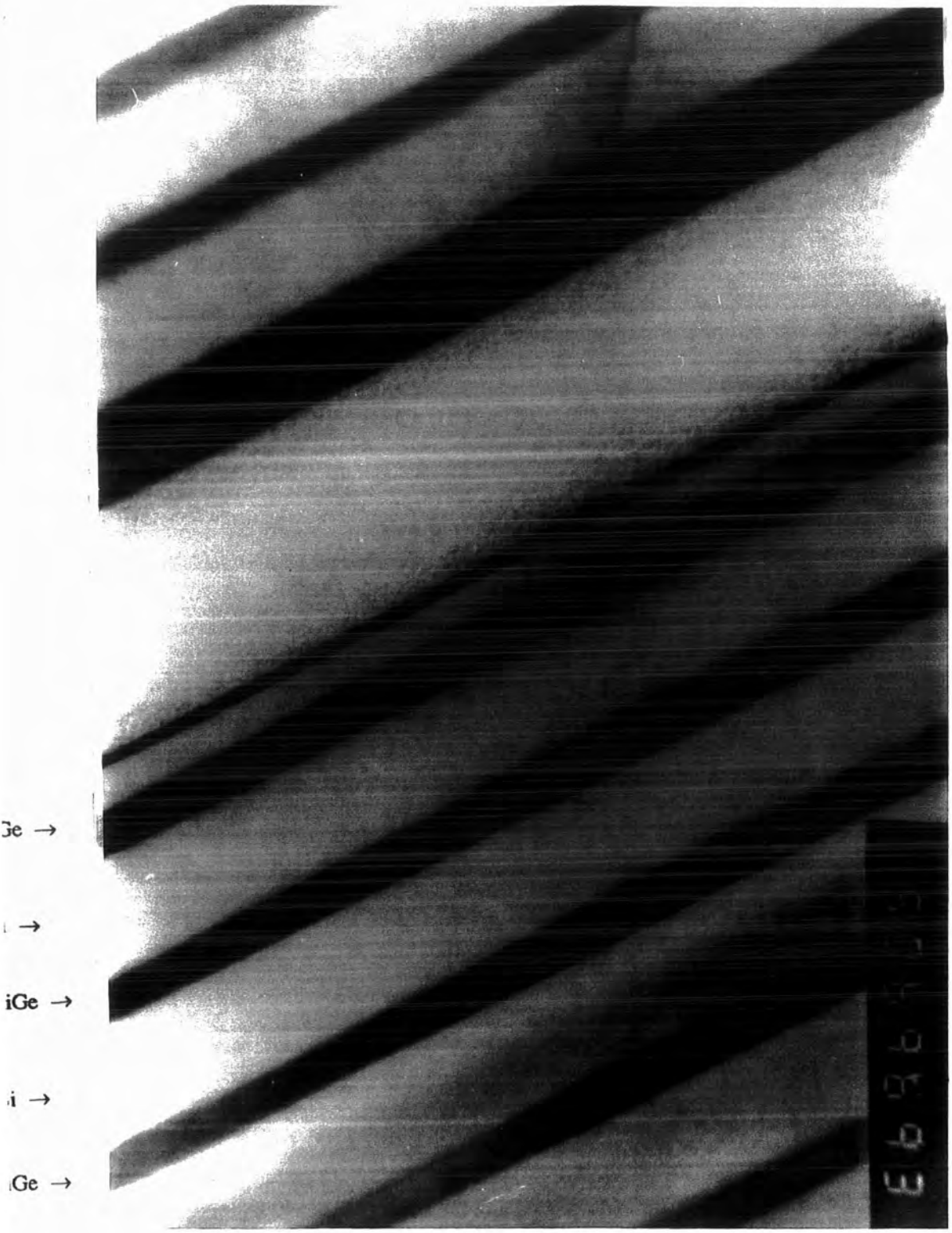


Figure 8.8(a) : TEM of preannealed ap1315 sample. Courtesy of P.D.Augustus.

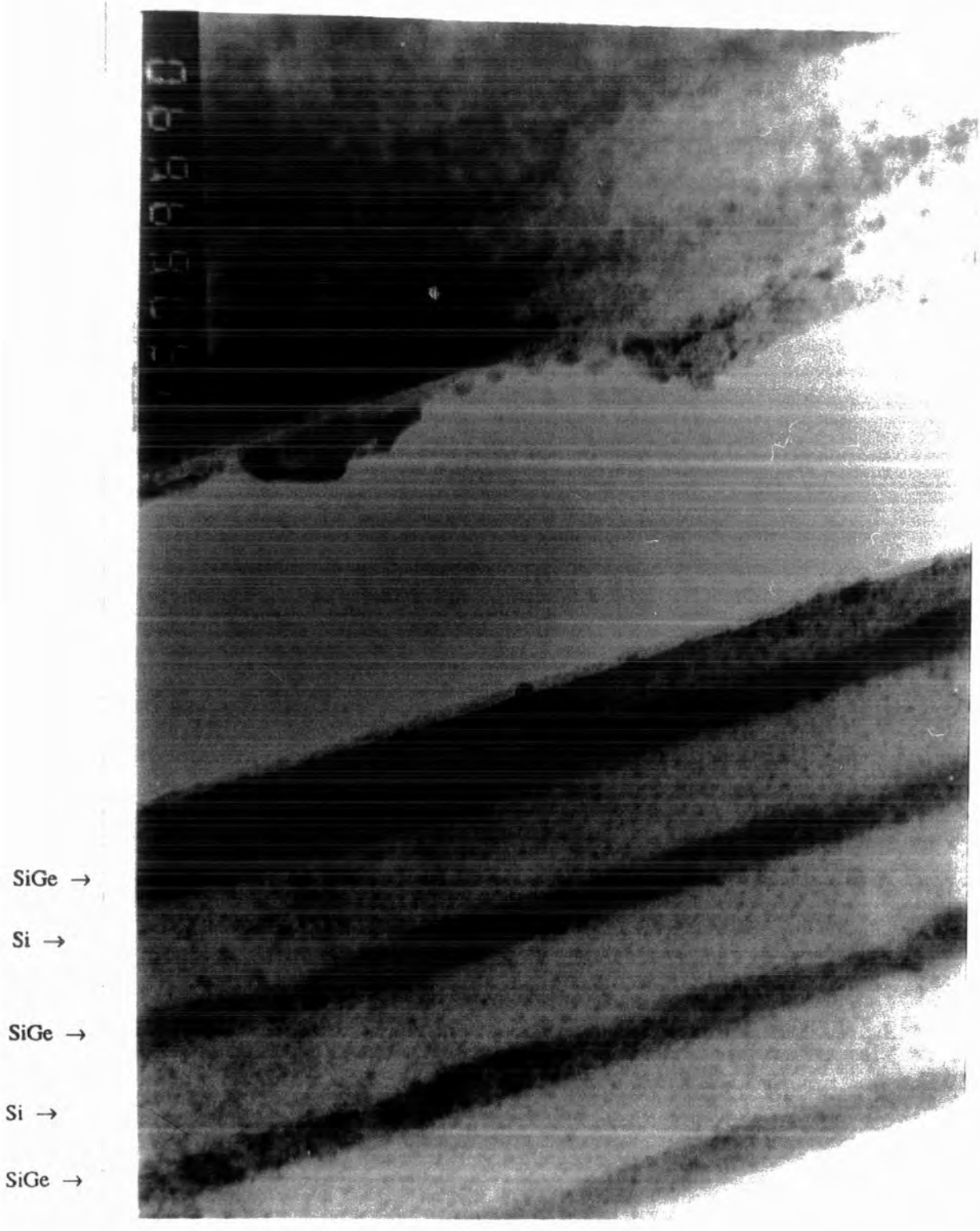


Figure 8.8(b) : TEM of preannealed ap1313 sample. Courtesy of P.D.Augustus.

interdiffusion. It seems reasonable to assume this short term roughness or grading must also be present at the $Si_xGe_{1-x}$→Si interface, superimposed upon the long range thickness variation. Reflectivity measures the total roughness which can be considered as the root mean square of both the long and short term roughnesses present[6]. This suggests that for ap1313 (Ge content of 57%), the $Si_xGe_{1-x}$→Si interface has a short range roughness of (0.5 ± 0.2) nm and a long range roughness of (0.9 ± 0.3) nm. The long range roughness will continue to affect the peak intensities until the wavelength of the roughness exceeds the coherence area of the x-ray probe (typically 1μm)[24].

### 8.5.2 The annealed Si \ $Si_{1-x}Ge_x$ samples

After carrying out the diffraction and reflectivity experiments a piece of each superlattice wafer was annealed under nitrogen at 850°C for one hour. These samples were then studied again to determine the effects of thermal processing. The increase in defect density, induced by annealing, is demonstrated by the symmetric (004) DCD rocking curves of samples ap1316, ap1314 and ap1315, shown in fig.8.9(a,b,c). For sample ap1315, where the Ge content in the pre-annealed sample was over 43%, heat treatment has resulted in severe degradation of the superlattice peaks, indicative of the onset of sample relaxation.

The reflectivity curves obtained after annealing, fig.8.10(a-e), show a marked change from the pre-annealed data, which is attributed to the onset of diffusion of Si and Ge atoms into and out of the $Si_xGe_{1-x}$ layer. Note, however, that no loss in sensitivity is suffered by the reflectivity technique even when the structures are highly dislocated, as is often the case when Si\$Si_xGe_{1-x}$ superlattices are annealed[25]. The GIXR profiles still contain a wealth of structural information. The main fringe period gives a superlattice period identical to the pre-annealed data. This is not surprising, as since the total stack thickness and number of constituent layers will not have changed, then there can be no change in superlattice period. However, the relative positions of the lowest intensity Bragg peaks has changed and a different mark/space ratio (i.e. the ratio of the Si layer thickness to the $Si_{1-x}Ge_x$ layer thickness) will be needed to fit the experimental profile. The effect of interdiffusion can be modelled in the simulation profile by inclusion of thin linearly graded layers either side of the $Si_{1-x}Ge_x$ layer. Linear grading is a reasonable approximation at this annealing temperature as the amount

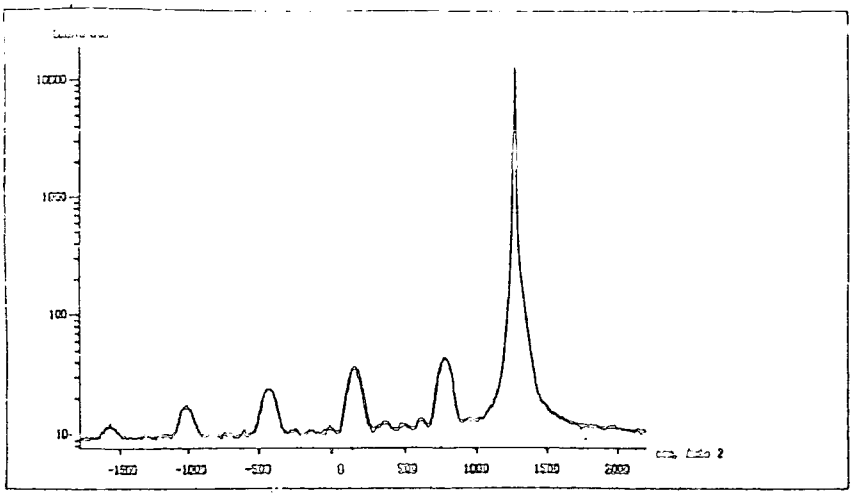

(a) ap1316

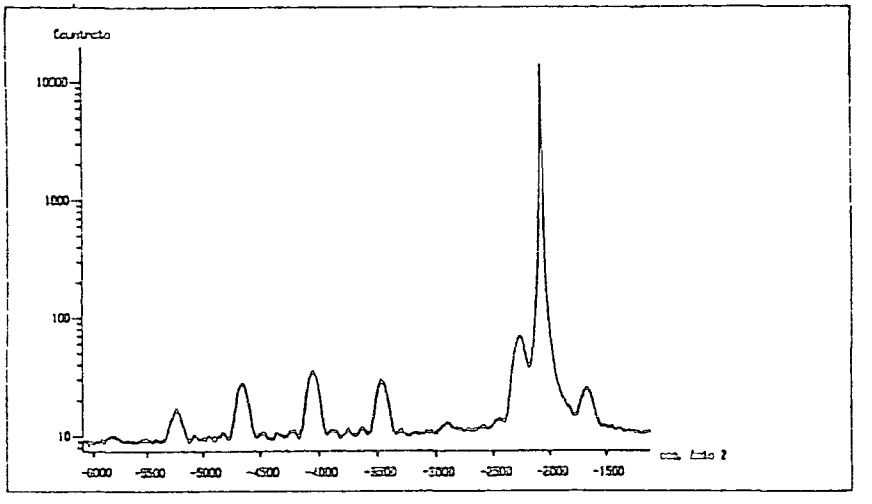

(b) ap1314

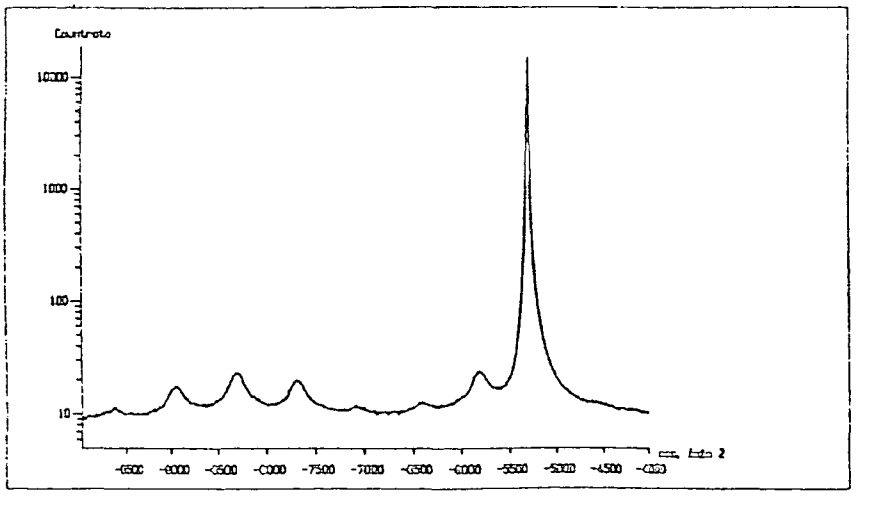

(c) ap1315

Figure 8.9 : (004) DCD Rocking Curves of the annealed $Si_{1-x}Ge_x$ samples.

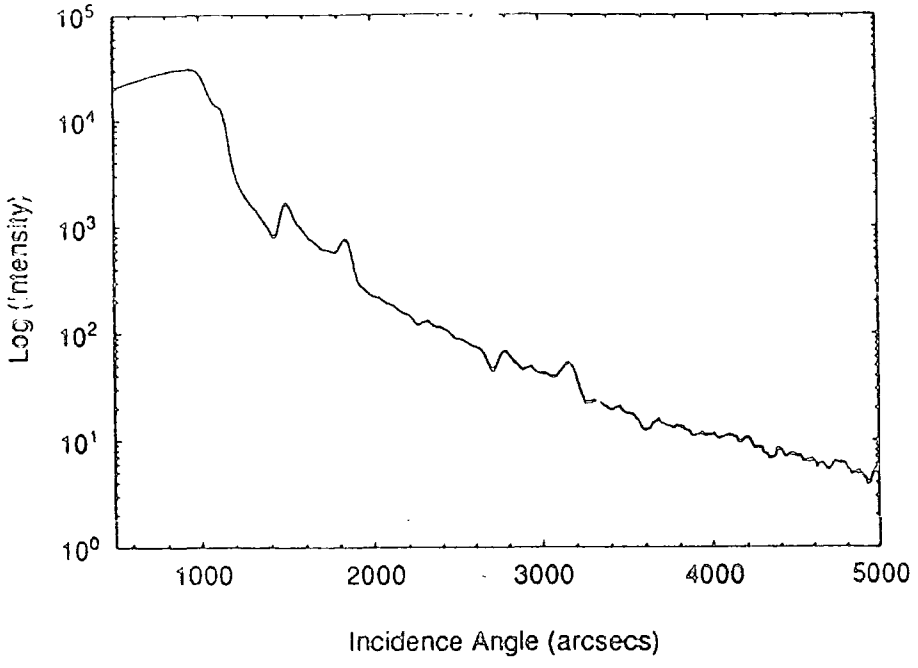


Figure 8.10(a) : GIXR profile of annealed ap1312 sample.

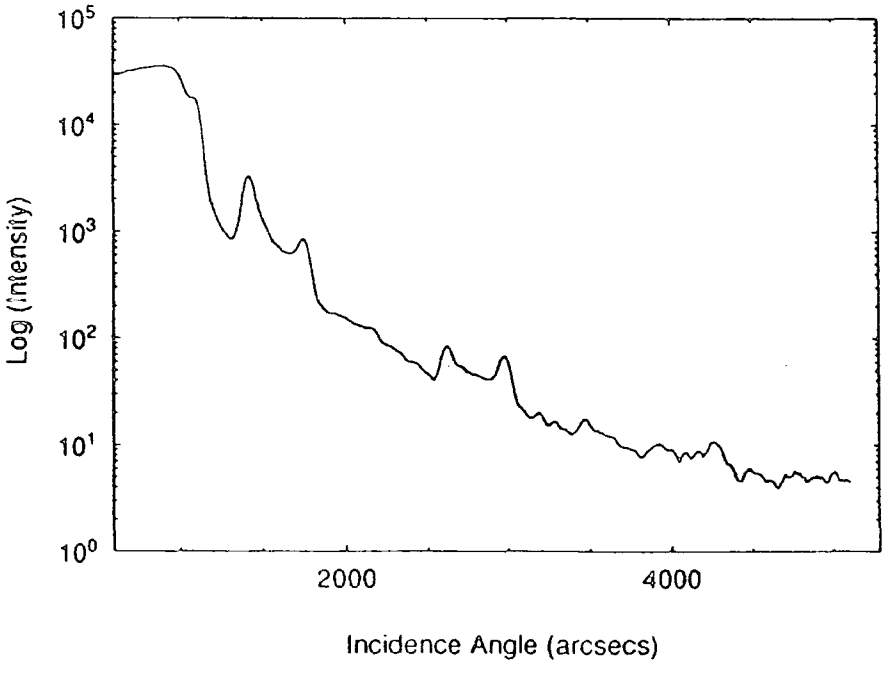


Figure 8.10(b) : GIXR profile of annealed ap1316 sample.

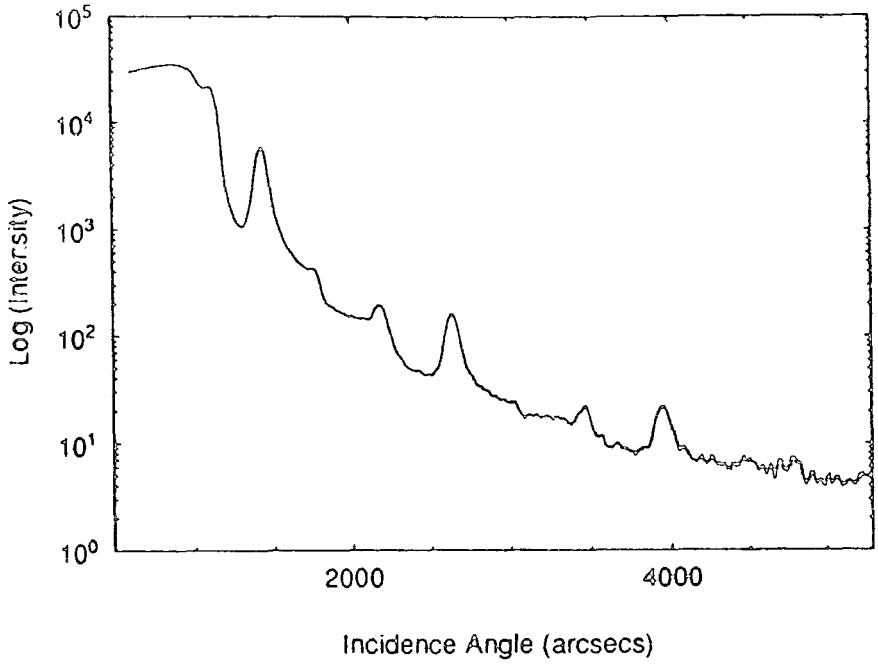


Figure 8.10(c) : GIXR profile of annealed ap1314 sample.

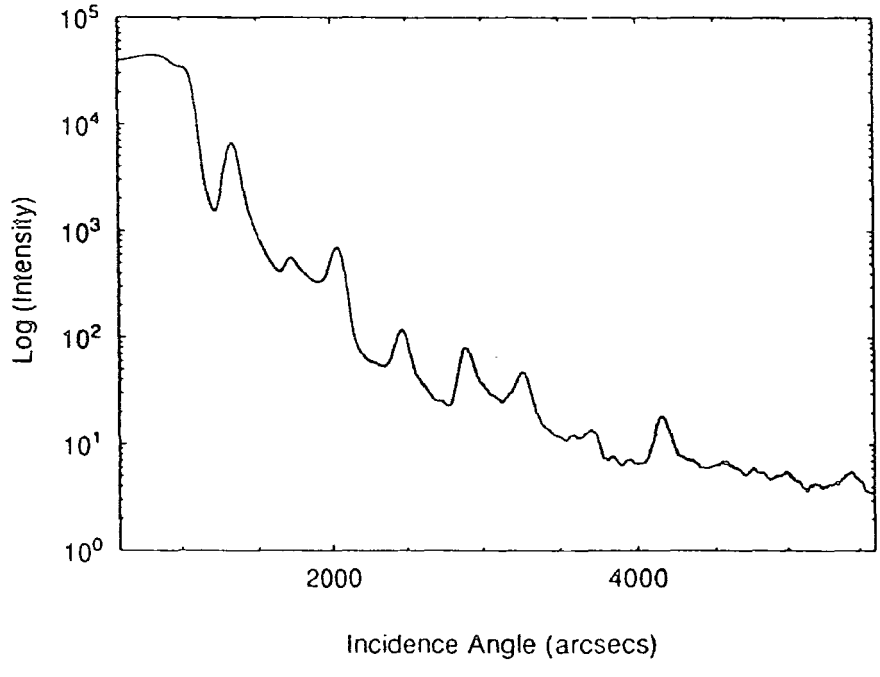


Figure 8.10(d) : GIXR profile of annealed ap1315 sample.

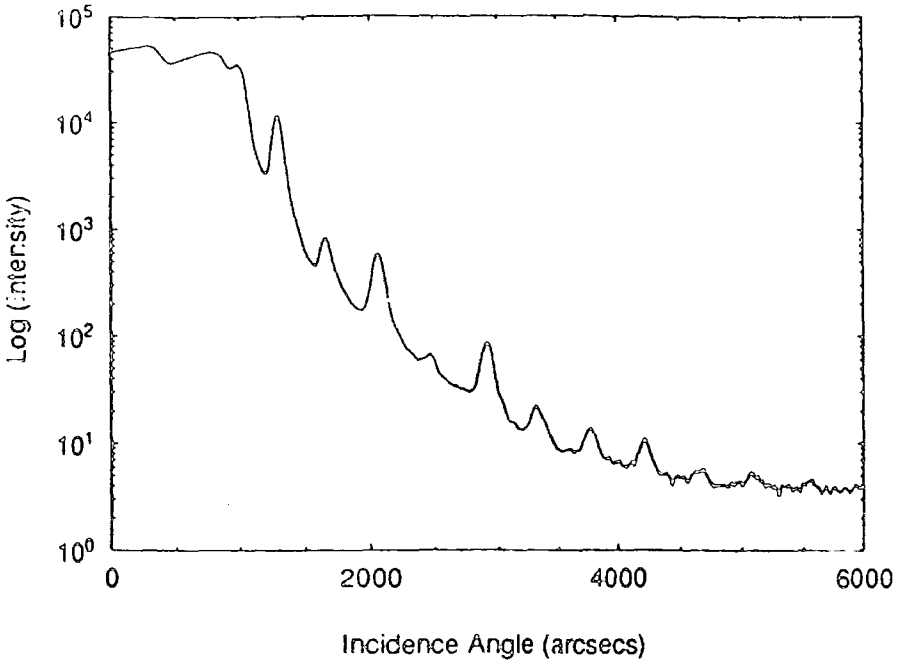


Figure 8.10(e) : GIXR profile of annealed ap1313 sample.

of diffusion is expected to be small. Schaffler[26] et al, who used SIMS to study diffusion in $Si\backslash Si_xGe_{1-x}$ heterostructures, employed an annealing time of 1000 seconds and found significant diffusion only became visible at 950°C, at which point the superlattice becomes a homogeneously doped $Si_xGe_{1-x}$ alloy[27].

Inspection of fig.8.10 shows that the effect of the modulation envelope upon the annealed data is more pronounced, implying that both layer thicknesses are well defined. Si atoms have a higher mobility than the heavier Ge atoms[28] and it is expected that as the sample is heated then Si rushes into and out of the $Si_xGe_{1-x}$ layer. This is accompanied by a small amount of Ge diffusion out of the $Si_xGe_{1-x}$ layer with the net result that the effective interfaces containing the $Si_xGe_{1-x}$ are pushed outwards. Hence, to model the annealed data increased values for the $Si_xGe_{1-x}$ layer thicknesses (and a thinner Si layer size) are needed. The effect of diffusion upon the GIXR profile will be particularly significant for high Ge content samples, the relative difference in electron density between the Si and $Si_xGe_{1-x}$ layers being large in these cases. To match the experimental GIXR profiles for samples ap1315 and ap1313, linearly graded layers of (2.4±0.3) nm, either side of the $Si_{1-x}Ge_x$ layer, are necessary. In effect, the simulation model structure now contains a superlattice period with four layers, as detailed in Table 8.4.

| | | | |
|---|---|---|---|
| | | Si Cap | 10 nm |
| { | %Ge : 0→(1-x) | $Si_xGe_{1-x}$ | 2.4nm |
| 5x{ | | $Si_xGe_{1-x}$ | 8 nm |
| { | %Ge : (1-x)→0 | $Si_xGe_{1-x}$ | 2.4nm |
| { | | Si | 24 nm |
| | | Si (001) Substrate | |

Table 8.4 : Sample structure used to simulate GIXR profiles of annealed $Si\backslash Si_{1-x}Ge_x$ superlattices.

As the Ge atoms are now spread over a larger volume a corresponding adjustment to the Ge fraction in the $Si_{1-x}Ge_x$ layer must be made. Simulated plots, incorporating the parameters in Table 8.5, for the two high Ge content samples are

shown in fig.8.11. The good fit provided by assuming linearly graded layers is further confirmed by simulation of the double crystal diffraction data in fig.8.12, which shows the double crystal rocking curve from the annealed ap1316 specimen. This sample (%Ge~20.6 in the pre-annealed state) has not relaxed (unlike ap1313), and superlattice peak structure is still present in the rocking curve of the annealed structure. An excellent fit to the diffraction data is obtained by assuming the same parameters as in the best fit to the GIXR data (Table 8.5).

| Sample | Si Layer Thickness (nm) | $Si_xGe_{1-x}$ Layer Thickness (nm) | $Si \rightarrow Si_xGe_{1-x}$ Roughness (nm) | $Si_xGe_{1-x} \rightarrow Si$ Roughness (nm) |
|---|---|---|---|---|
| ap1313 | 16.6 ± 0.3 | 10.8 ± 0.3 | 0.5 ± 0.2 | 0.5 ± 0.2 |
| ap1315 | 18.9 ± 0.3 | 9.7 ± 0.3 | 0.5 ± 0.2 | 0.5 ± 0.2 |

Table 8.5 : Sample parameters for annealed Si /$Si_xGe_{1-x}$ superlattices as determined by GIXR.

As atoms diffuse in and out of the $Si_xGe_{1-x}$ layer the long range roughness of the $Si_xGe_{1-x} \rightarrow Si$ interface will be "washed" out, leaving behind only the short term roughness or grading to affect the reflectivity profile. This is borne out by simulation where use of a (0.5±0.2) nm roughness at both interfaces provides the best fit to the experimental data. Any attempt to assign one of the interfaces with a larger roughness results in a detectable difference between the simulated and experimental plots, supporting the conclusion that the long range, periodic thickness variation has been masked by diffusion effects.

The above example demonstrates well one of the chief advantages of the GIXR technique - the ability to probe interface morphology at the sub-nanometre level, a capability which is further utilised in the following section.

## 8.6 GIXR Characterisation Of Magnetic Multilayers

Perhaps one of the most striking effects that interface roughness has on a systems properties occurs in the case of magnetic multilayers. The performance of these

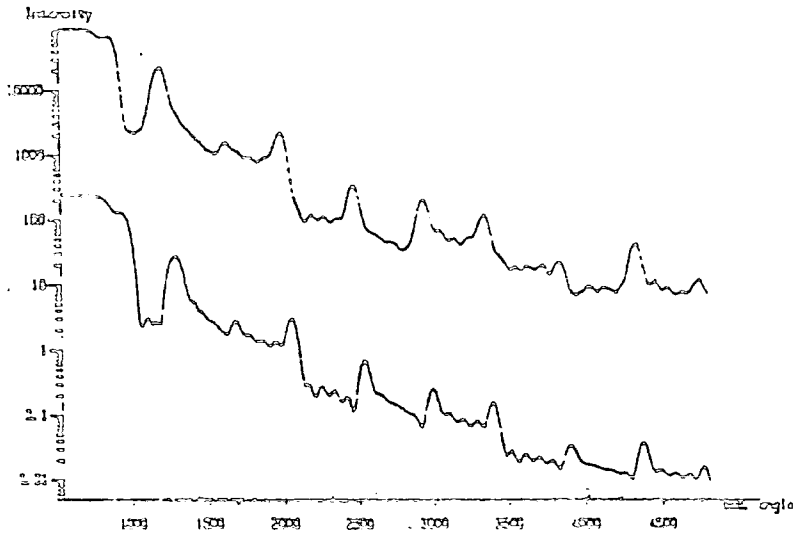

(a) ap1315

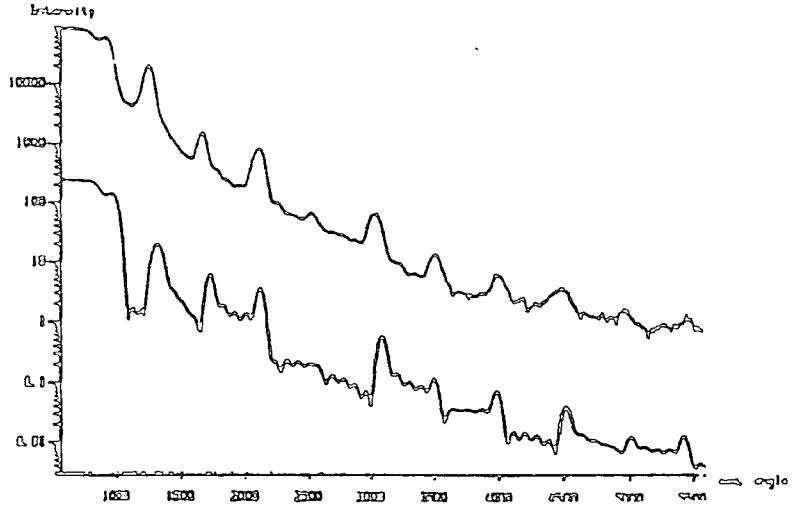

(b) ap1313

Figure 8.11 : Specular GIXR profiles of the two annealed high Ge content $Si_{1-x}Ge_x$ samples. The best fit simulations, incorporating the parameters in Table 8.4 are displayed as the lower curves in each plot.

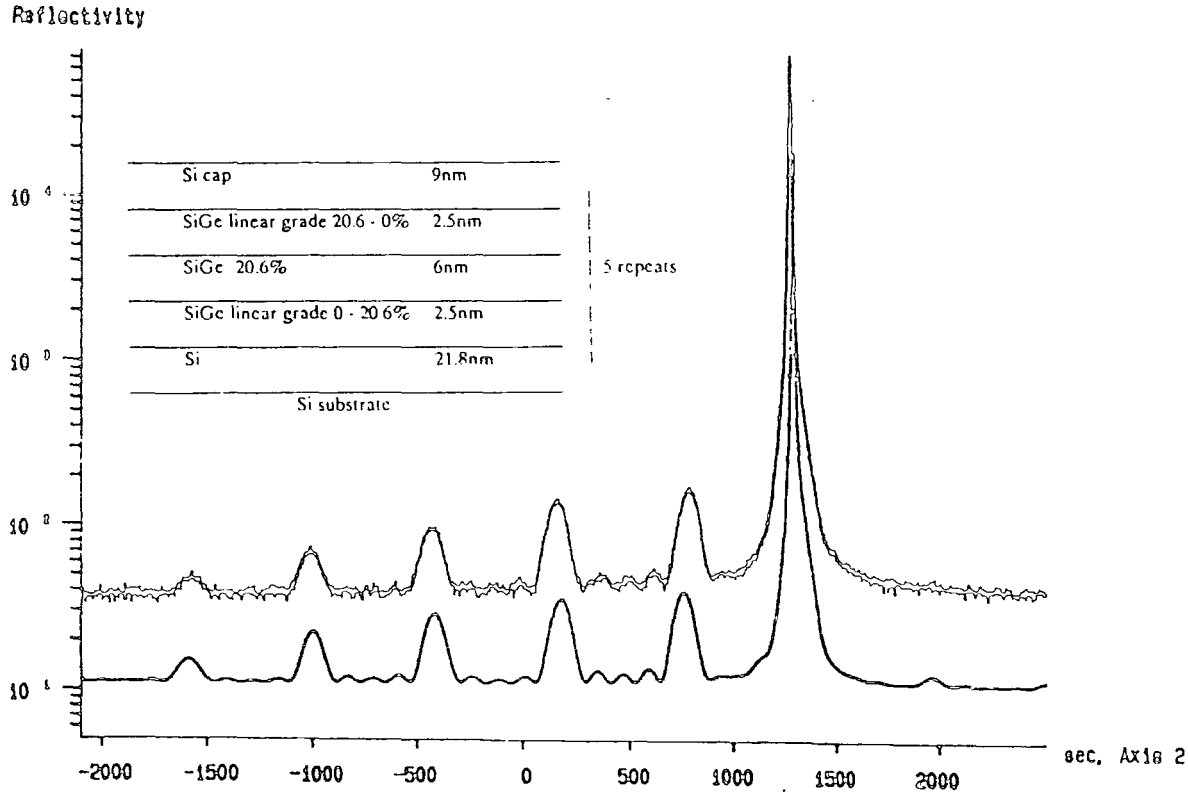


Figure 8.12 : (004) DCD Rocking Curve of the annealed ap1316 sample. The best fit simulation, incorporating the parameters shown inset, is the lower curve.

devices, discussed in Chapter 1, utilises the occurrence of the Giant Magneto Resistance (GMR) effect in the fabrication of high density magnetic recording media. To recap, Parkin[29] has catalogued the occurrence of oscillatory indirect magnetic exchange coupling in a large number of systems, concluding that this is a general phenomenon. The sign of the exchange coupling in a magnetic multilayer system is found to oscillate with variation in the non-magnetic spacer layer thickness, a maximum magnetoresistance being found for layer spacings corresponding to antiferromagnetic coupling. There is growing evidence that the magnitude of the GMR in these multilayers is sensitive to the roughness of the interfaces of the component layers[30]. This effect appears to be independent of the antiferromagnetic exchange coupling which governs the non-magnetic spacer-layer thickness at which GMR is observed[31]. Whether interface roughness increases or decreases the GMR is still a matter of contention. Research by Fullerton[30] et al. concluded that the GMR is larger when the low angle peaks in x-ray diffraction become broader and less intense, implying that the magnetoresistance is enhanced by the presence of interface roughness. This finding is at odds with work carried out by Takanashi[32] et al. who report, also from x-ray diffraction analysis, that the magnetoresistance increases with decreasing interface roughness. In attempting to explain the discrepancy between their result and that of Fullerton et al., Takanashi points out that it is unreasonable to estimate the degree of interface roughness exclusively from low angle x-ray diffraction analysis, as peak broadening is determined mainly by the irregularity of the multilayer period, rather than interface roughness due to lattice uncertainty and compositional mixing. For multilayers grown using different methods large variations in the GMR have been discovered. In Co-Cu multilayers grown by magnetic sputtering a room temperature magnetoresistance of 65% has been reported[31]. Similar films grown by MBE show a magnetoresistance maximum at the same value of non-magnetic layer (Cu) thickness, but the room temperature magnetoresistance is only a few percent. As the interface morphology, which is strongly influenced by the growth technique used, is thought to affect the GMR then characterisation of the multilayer interfaces by GIXR would thus be of obvious benefit.

The purpose of the following work is to investigate the interfacial structure of a variety of magnetic multilayers. Of particular interest is the analysis of samples fabricated using different growth methods and whether or not the interfacial roughness possesses distinctive features (which will affect the magnetic

properties). Demonstration GIXR experiments have been performed on three magnetic multilayer structures, the Au/Co, Ni/C and Fe/Cr systems. Initially, GIXR specular scans were recorded in order to gauge the quality of information available from magnetic multilayers and these results are presented below.

### 8.6.1 Specular GIXR Profiles

The Au/Co samples studied were grown by MBE at the University of Leeds by Dr. M.Walker. The specular GIXR scan, recorded on the Bede GXR1, for a Au/Co multilayer is shown in fig.8.13(a). The reflectivity profile shows several low order Bragg peaks with Kiessig fringes clearly visible between peaks. One feature of the Au/Co (and Ni/C) system is the large difference in electron density between the magnetic and non-magnetic components, resulting in high contrast Kiessig fringes. The quality of the top surface of this MBE grown sample is demonstrated in fig. 8.13(b), which shows the product of the measured intensity (minus detector background) and fourth power of the scattering angle plotted against incidence angle. Out to an incidence angle of almost four degrees (a scattering angle of eight degrees) the data remains almost parallel to the abscissa, indicating an extremely flat top surface of the film. The GIXR scan for a second Au-Co multilayer is displayed in fig.8.14(a). This sample consists of an eight period superlattice of alternate Au and Co layers, grown on a (011) oriented GaAs substrate, with a Ge buffer layer and thin Au layer between the superlattice and substrate. Measurement of the positions of the observed Bragg peaks determines the superlattice period while the total stack thickness is obtained from the Kiessig fringe spacing. The Bragg and Kiessig fringe positions are satisfactorily modelled by the use of the parameters in Table 8.6. The simulated profile, incorporating these parameters, is shown in fig.8.14(b). While the angular positions of peaks in the simulated profile correspond well to those in the experimental data, the amplitude of the Kiessig fringes, in particular, is significantly greater in the simulated case, where perfectly flat, abrupt interfaces are presumed. In order to model the size of interference fringes observed in the experimental case, a roughness of 0.7 nm is required at each of the Au and Co interfaces and a relatively large roughness of 1.5 nm at the upper surface of the Ge buffer layer. A simulated fit to the recorded data, incorporating the effects of roughness, is displayed in fig.8.14(c). While the fit between experimental and simulated GIXR profiles is now very good, for large scattering angles the experimental Kiessig

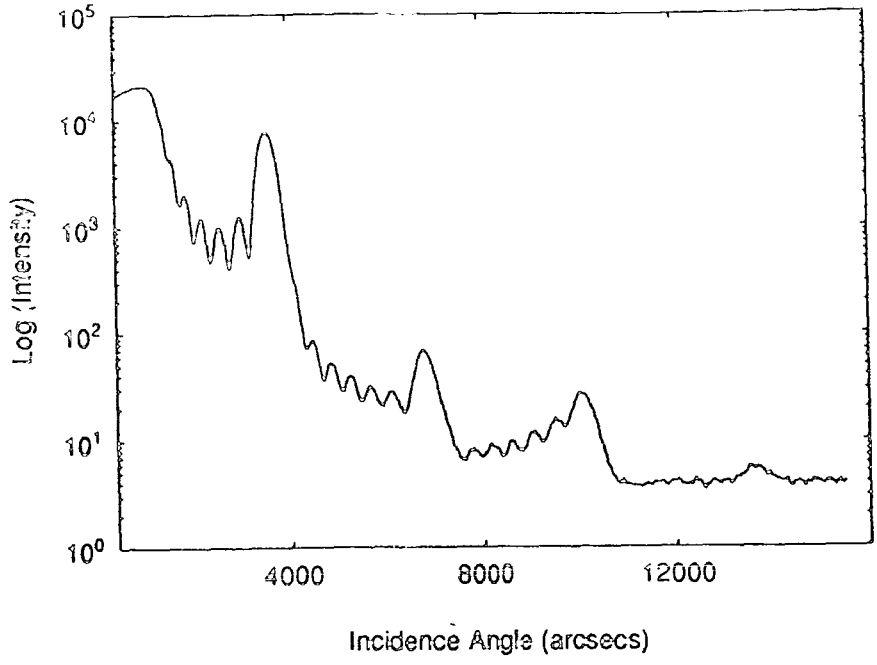


Figure 8.13(a) : Specular GIXR scan of an MBE grown Au/Co magnetic multilayer. The excellent Kiessig fringe visibility and presence of several low order Bragg peaks demonstrates excellent sample quality.

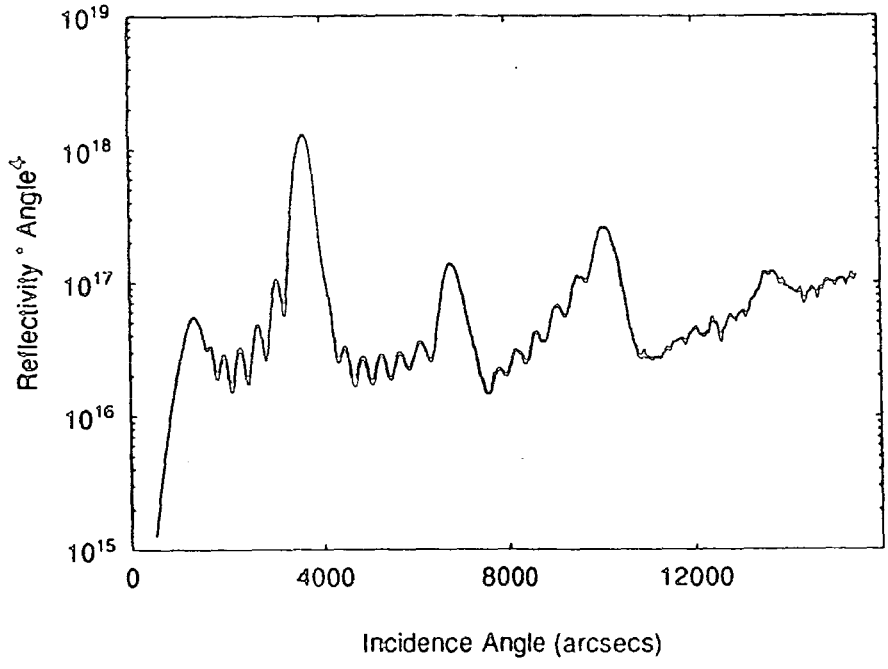


Figure 8.13(b) : The specular GIXR signal shown in Fig.8.13(a), multiplied by a factor of $\phi^4$ (after subtraction of the constant detector background). The fact that the data remains almost parallel to the abscissa indicates an extremely flat top surface.

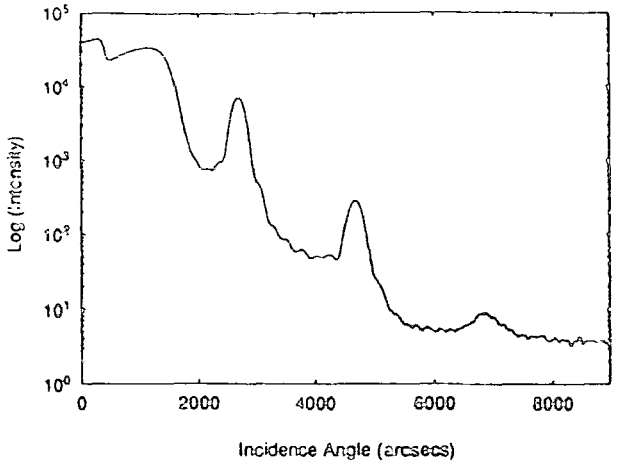


(a) Experimental (specular) GIXR data from a second Au/Co magnetic multilayer.

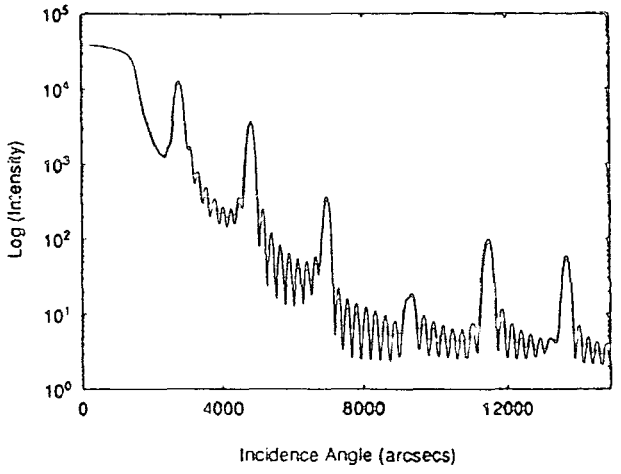


(b) Attempt at simulating data in (a) using parameters given in Table 8.6 No roughness is assigned to the multilayer interfaces.

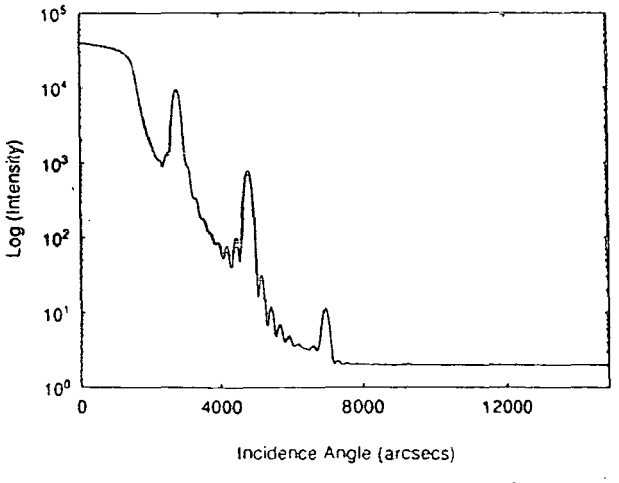


(c) Simulation of data in (a), using parameters in Table 8.6 Roughnesses of 1.5 nm at the Ge interface and 0.7 nm elsewhere are required to match peak intensities.

Figure 8.14(a-c) : Experimental and simulated GIXR profiles of a Au/Co multilayer.

fringes have lower contrast and the third order Bragg peak is broadened, an effect attributed to a small amount of random dispersion in the superlattice period.

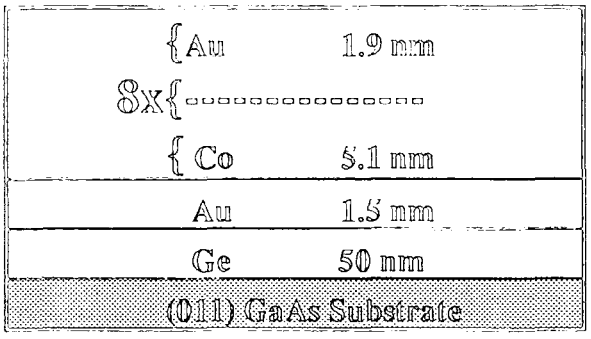


Table 8.6 : Simulated parameters for the GIXR profile in figure 8.14(b).

The MBE growth technique is recognised as being capable of growing thin layered samples to monolayer precision. This is well demonstrated by the above specular reflectivity profiles of the Au/Co multilayer samples which contain a wealth of structural information. However, MBE is not the only growth method used to produce multilayer samples and fig.8.15 shows the specular GIXR profile of a multilayer grown using sputtering techniques. This sample, a 10 period Ni/C multilayer, grown by M.Player and I.H.Munro of Aberdeen University, has a total thickness of 37.4 nm and multilayer period of 3.7 nm. As in the case of Au/Co, the consistency of the multilayer period and the large difference in electron density between the two types of component layers, results in the presence of several low order Bragg peaks and high contrast of the GIXR interference fringes. The high quality of the multilayer is confirmed by comparison with REFS simulations, which indicate relatively small values for r.m.s. roughness of 0.3 nm on the glass substrate and 0.5 nm on the multilayer interfaces.

Not all multilayer structures yield reflectivity curves with such excellent fringe and Bragg peak structure. Fig.8.16 shows the specular GIXR scan from a 20 period, sputtered Fe/Cr multilayer system. Due to the proximity of these 3d elements in the Periodic Table, contrast of Kiessig fringes is poor. While some interference fringes are observable, only one low order Bragg peak is recorded and the quality of the data is much worse in this instance. To match the overall fall of intensity and magnitude of the solitary Bragg peak, a relatively large top surface roughness of 2 nm is required. It should be remembered that REFS models roughness in the

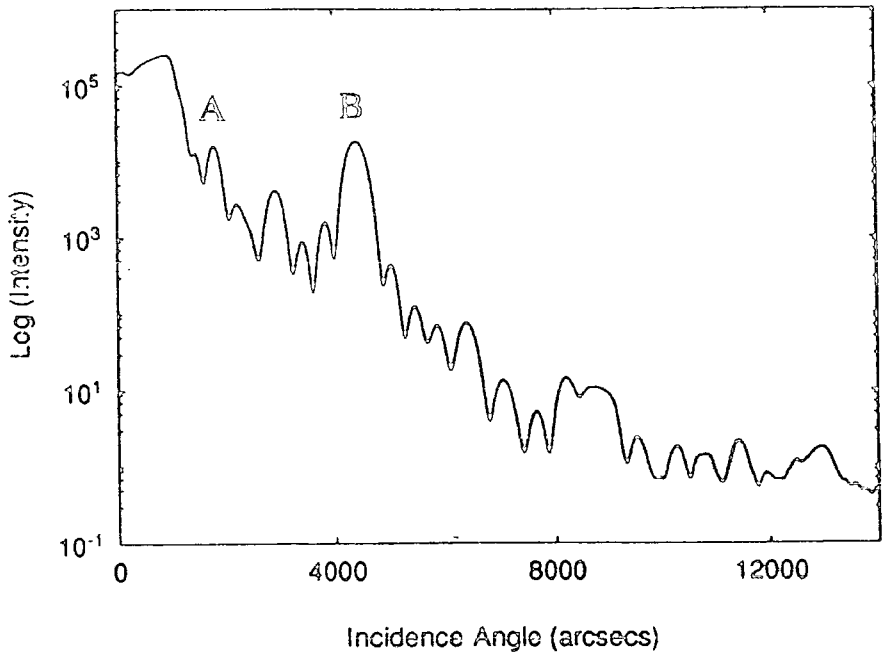


Figure 8.15 : Specular GIXR scan of a 10 period, sputtered Ni/C multilayer.

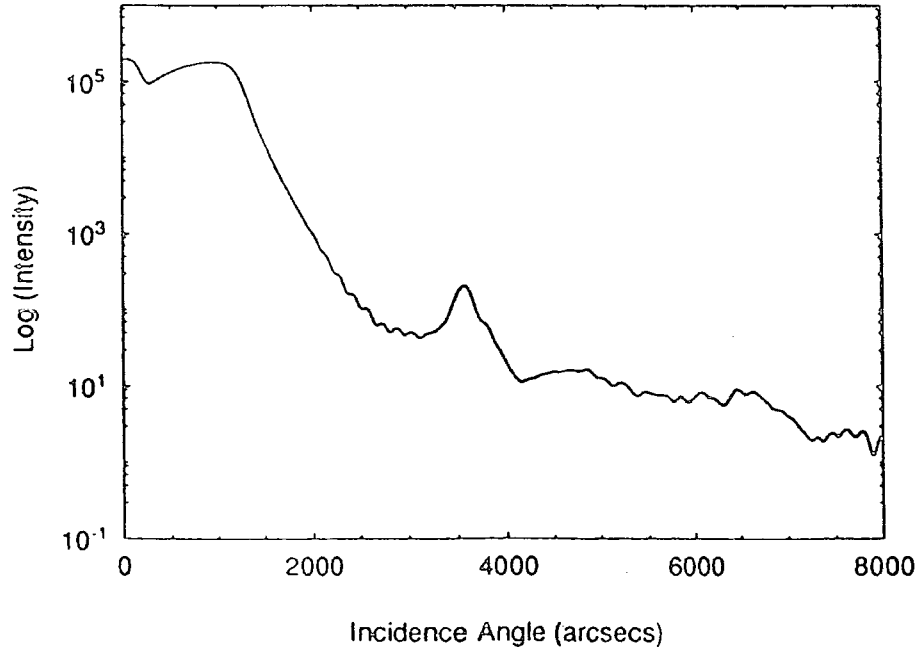


Figure 8.16 : Specular GIXR scan of a 20 period, sputtered Fe/Cr multilayer.
Note the poor quality of the reflectivity profile.

form of a density gradient, and this large value for top surface roughness probably arises from oxidation of the near surface layers (resulting in a significant density gradient in this region) rather than a large variation in the interface position (i.e. genuine "roughness"). Although values for the total stack thickness and Fe/Cr superlattice period may be obtained from angular positions of interference fringes and Bragg peaks, it should be noted that the quality of the data in fig.8.16 is insufficient to unambiguously determine the roughness of buried interfaces.

Specular data has thus been shown to give quantitative (in the case of Au/Co and Ni/C) and qualitative (in the case of Fe/Cr) information on interface structure. However, it should be stressed that collection of the specular signal does not allow us to distinguish between "true" roughness (i.e. variation of the interface position) and compositional intermixing. A specular GIXR scan detects both as a change in electron density only and cannot separate the two components. This problem can be solved by collecting the diffuse scatter in a GIXR experiment.

## 8.7 Diffuse Scatter In GIXR Experiments

Collection of GIXR data in the specular mode allows rapid characterisation of a sample via fitting of a model structure, generated using the theory of Parratt (Ref. 6, Chapter II), to the experimental profile. The effect of surface roughness is to not only reduce the specular reflectivity but also to introduce an off specular or diffuse contribution to the scattering. While specular reflectivity is sensitive to interface roughness, no information on the roughness length scale is provided nor is the technique capable of distinguishing between genuine (random) interface roughness and interdiffusion. A number of workers[33,34,35] have demonstrated that collection and analysis of the diffuse scatter in a GIXR experiment is capable of solving these problems. Methods of collecting diffuse scatter in reflectivity techniques were discussed in Chapter IV, where the easiest way to describe the scattering is to visualise it in reciprocal space. Essentially diffuse scatter techniques are similar to triple crystal diffraction methods, except here we are studying the scatter around the (000) reciprocal lattice point and a narrow slit in front of the detector acts as a low resolution analyser. Single diffuse scans are carried out by either rocking the sample only for a fixed detector position (equivalent to moving transversely in reciprocal space), or by carrying out a coupled $\theta$-$2\theta$ scan with an offset from the true specular position (equivalent to

moving vertically, or longitudinally, in reciprocal space). The use and interpretation of diffuse scanning has been developed by, amongst others, Vinogradov[36], Harada[37] and Sinha[38]. The intensity of diffuse scatter, $I_d$, measured in an experiment is related to the incident beam intensity, $I_0$, by equation (8.3),

$$I_d = I_0 \frac{\Delta\Omega}{A}\left(\frac{d\sigma}{d\Omega}\right)_d \tag{8.3}$$

where A is the area of the x-ray beam and $\Delta\Omega$ the solid angle subtended by the detector at the sample. By modelling the surface roughness with a Gaussian height distribution, the expression for the diffuse scattering from a single, rough surface has been written in the distorted wave Born approximation (DWBA) by Sinha[38] as,

$$\left(\frac{d\sigma}{d\Omega}\right)_d = \frac{A\left|k_0^2(1-n^2)\right|^2}{16\pi^2}\frac{e^{-q_z^2\sigma^2}}{q_z^2}|T(\alpha)|^2|T(\beta)|^2\iint(e^{q_z^2C(x,y)}-1)e^{(iq_x x+iq_y y)}dxdy \tag{8.4}$$

with $k_0$ the incident wave vector, n the refractive index, $\sigma$ the r.m.s. surface roughness. The factors $T(\alpha)$ and $T(\beta)$ represent Fresnel transmission coefficients for wave vectors with incidence angles, $\alpha$, and exit angles, $\beta$, respectively, as shown in fig.8.17. Two important results arise from this expression for the diffusely scattered radiation. Whenever $\alpha$ or $\beta$ make the critical angle with the sample surface, then the factors $T(\alpha)$ and $T(\beta)$ have maximum values and peaks occur in the diffuse scatter, a phenomena first discovered by Yoneda[39], after whom these peaks (or "wings") are known. Secondly, the magnitude of diffuse scatter is seen to depend upon a factor C(x,y), which is the correlation function between height fluctuations along the interface. If z(0) and z(x,y) describe the random heights at points 0 and (x,y) on the interface then C(x,y) gives the correlation, or lack of independence, of these random interface heights. Alternatively, C(x,y) expresses the probability that identical surface heights will be found at a separation r on the interface, where $r^2 = (x^2 + y^2)$. A general form of C(x,y) is given by equation (8.5).

$$C(x,y) = \langle z(0)z(x,y)\rangle = \sigma^2 \exp(-(r/\xi)^{2h}) \tag{8.5}$$

where $\xi$ is known as the roughness correlation length and $0 < h < 1$. For multilayer samples it has been found that a correlation can exist between the

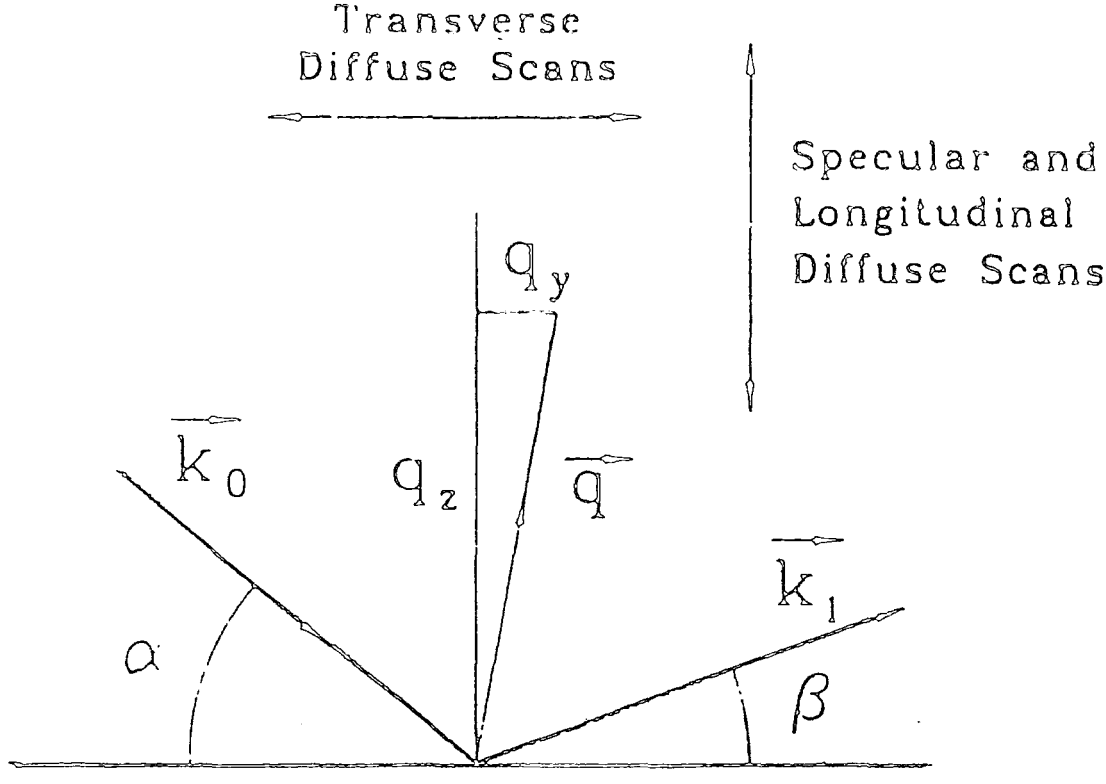


Figure 8.17 : Schematic reciprocal space diagram for scattering experiments. Specular scans correspond to $q_y$=0. After Sinha[34].

roughness profiles from *neighbouring* interfaces. Here, the correlation function between height fluctuations on interfaces i and j has been expressed by Sinha[38] as equation 8.6.

$$C_{i,j}(x,y) = \left\langle z_i(0) z_j(x,y) \right\rangle = \sigma^2 \exp\left[ \left( -\frac{(x^2+y^2)^{\frac{1}{2}}}{\xi} \right)^{2h} \right] \qquad (8.6)$$

At the specular condition, the diffuse scatter increases for increasing $\xi$ and decreasing h. If no correlation exists between the interface heights at *different* interfaces, then the correlation function vanishes and the diffuse scattering is the incoherent superposition of the roughness scattering from each interface. If there is some correlation between roughness at different interfaces, then the function $C_{i,j}(x,y)$ is finite for even well separated points, and the roughness is said to be correlated, or conformal. This point is further discussed in the following sections.

### 8.7.1. Diffuse GIXR Studies Of High Ge Content $Si_{1-x}Ge_x$ Superlattices

Of course, one material system which exhibited coherency in the interface structure was the Si/ $Si_{1-x}Ge_x$ system, analysed in Section 8.4.1.. For high Ge fractions (>0.4), the interface roughness was identified as having two components, one a short range roughness of 0.5 nm present at both interfaces in the pre-annealed and annealed samples, and a second long range periodic thickness variation of 0.9 nm present at the $Si_{1-x}Ge_x \rightarrow Si$ interface in the high Ge content pre-annealed samples. Longitudinal diffuse scans, collected by a carrying out a coupled $\theta/2\theta$ scan with an initial sample offset, are shown in fig.8.18(a) for the pre-annealed ap1313 sample (57% Ge). These show that, far away from the specular ridge and outside the region affected by the instrument function, the diffuse scatter is peaked at positions corresponding to the Bragg condition for the superlattice period. This peaking of the diffuse scatter around Bragg peaks has been observed previously in AlAs/GaAs and W/C[40] superlattices. Just as the specular superlattice peak is clearly recognised as arising from the constructive interference of the coherent scattering from the component layers, then the localisation of the strong diffuse scatter around the Bragg peaks indicates coherency in the diffuse component also. This coherency is attributed to the presence of correlated or conformal roughness in the sample structure[35,38,40,41]. For the annealed ap1313 sample a similar longitudinal

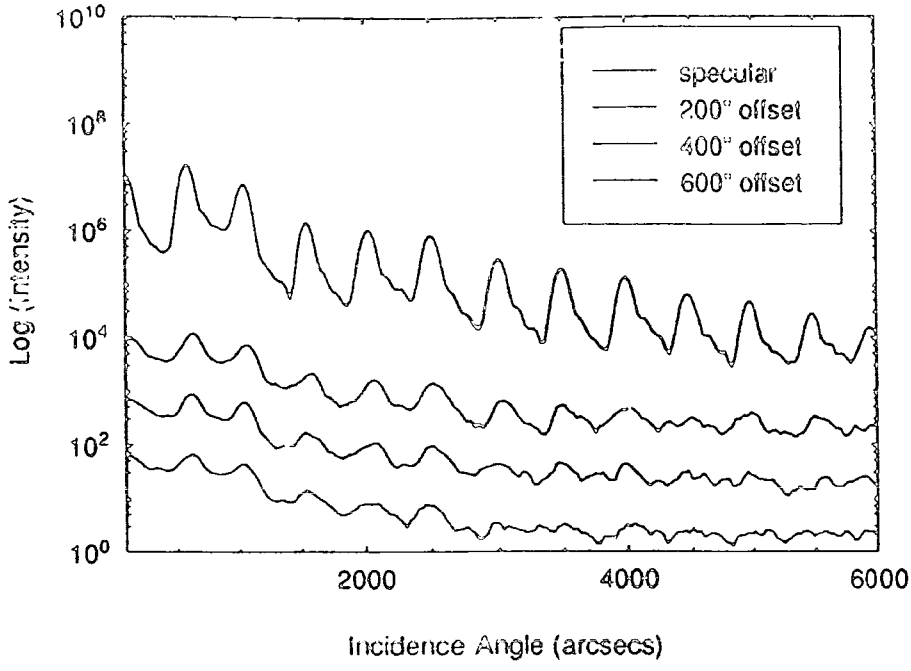


Figure 8.18(a) : Longitudinal diffuse scans from the pre-annealed ap1313 sample.

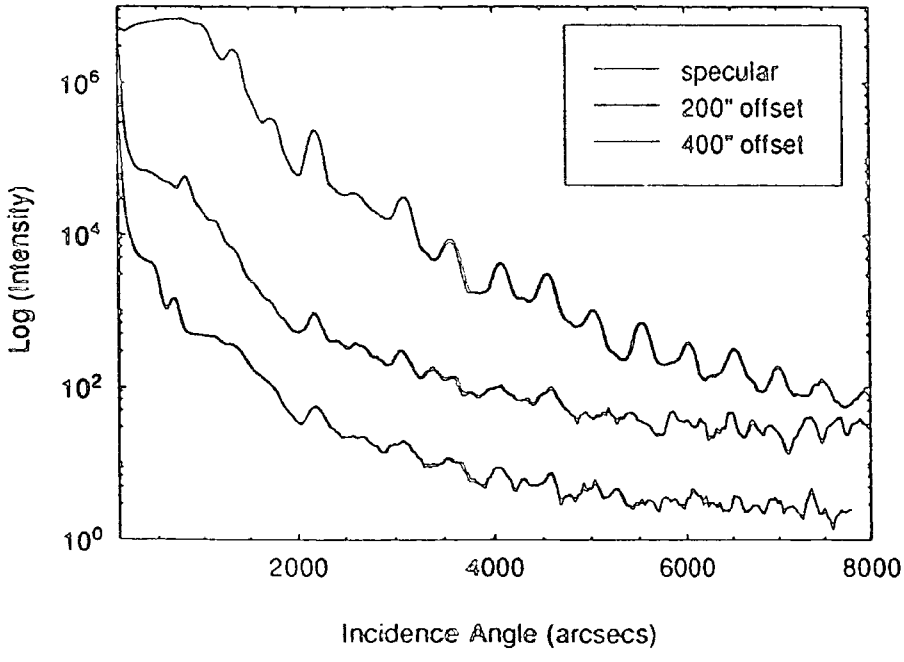


Figure 8.18(b) : Longitudinal diffuse scan from the annealed ap1313 sample.

diffuse scan, fig.8.18(b), shows that the structure in the diffuse scatter quickly dies away as the distance from the specular ridge is increased. For an initial sample offset of 400" from the specular (i.e. $\theta/2\theta$) condition, the structure in the longitudinal GIXR profile disappears. This can be attributed to the loss of the long range "correlated" roughness by diffusion at the interfaces of the annealed sample.

The longitudinal scans in fig.8.18(a), represent "slices" of the sample scatter offset from, but parallel to, the specular ridge. By recording a series of such longitudinal scans, for a variety of different initial sample offsets, a psuedo three dimensional map of the sample diffuse scatter can be obtained (fig.8.19). This shows that transverse to the specular ridge (clearly identified as running down the $\theta=2\theta$ line), "bars" of diffuse scatter can be seen, originating from the base of the specular Bragg peaks. These give further evidence for the presence of conformal roughness in the pre-annealed sample.

The loss of conformality upon annealing is also demonstrated by scanning pependicular to the specular ridge. Transverse scans from the pre-annealed ap1313 sample are shown in fig.8.20(b,c). The asymmetry of the intensity distribution in these scans (i.e. the gradient in the diffuse intensity going from left to right) results from a smaller sample area being illuminated as the incidence angle is increased. In section 8.5 it was noted that peaks (or Yoneda wings) occur when the angles $\alpha$ or $\beta$ make the critical angle with the surface. As well as the appearance of the Yoneda wings, subsidiary peaks, indicated by the arrows, are noted midway between the specular peak and the Yoneda wings (fig.8.20(b,c)). These peaks appear when the angles, $\alpha$ and $\beta$, are such as to satisfy a superlattice Bragg condition, and their existence has been reported in other multilayer systems[38]. These diffuse scatter "Bragg peaks" appear because of the "order" in the interface roughness of the pre-annealed ap1313 sample. The transverse scans shown in fig8.20(b,c) were carried out centred around the points A,B,C and D in the specular profile (fig.8.20(a)). Similar transverse diffuse scans from the annealed sample, fig.8.21(a,b,c), do not exhibit these subsidiary peaks, the conformal roughness of the interfaces having been destroyed by the thermal treatment.

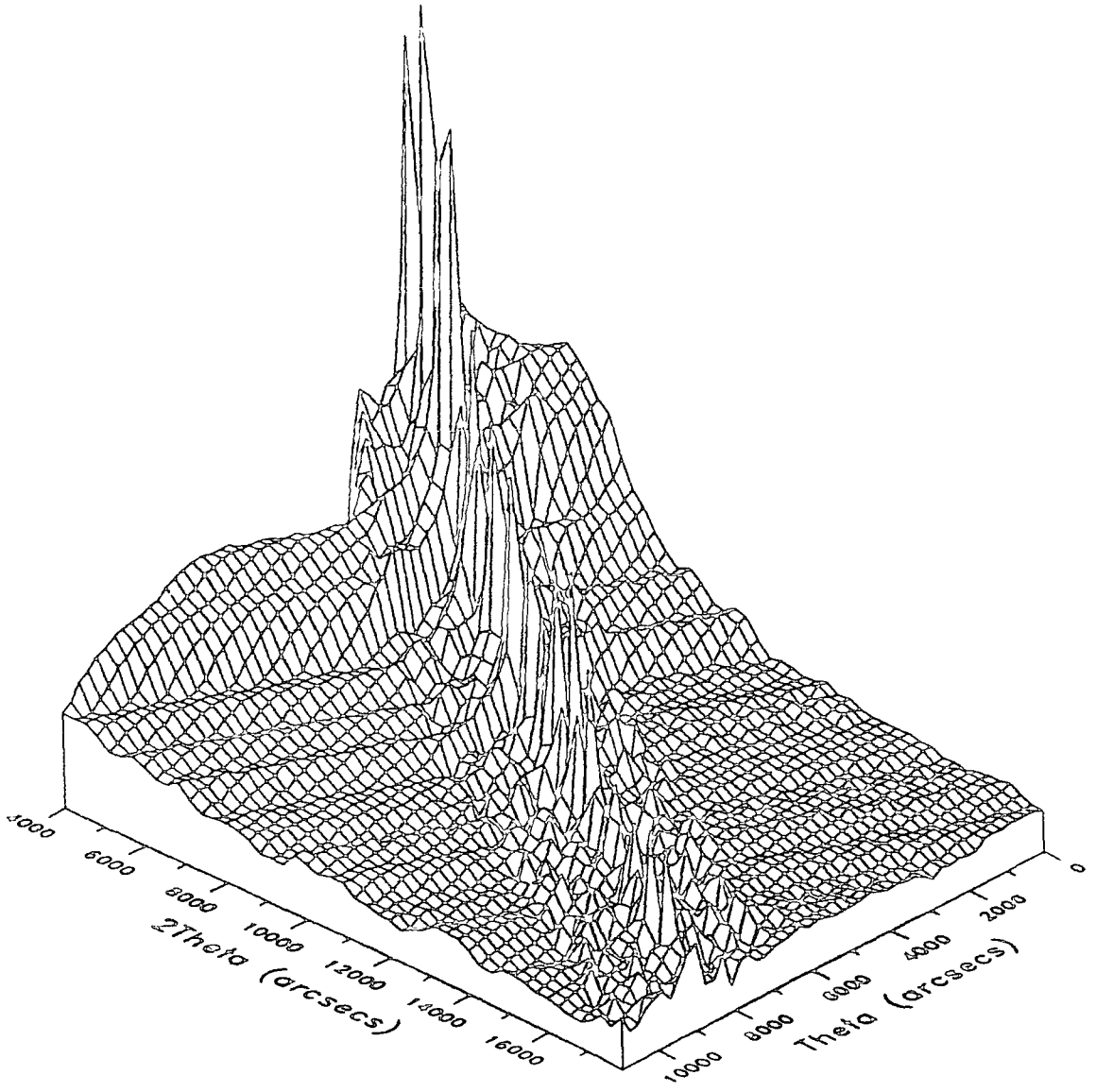


Figure 8.19 : Pseudo 3-d plot of the scatter from the pre-annealed ap1313 sample. The data was collected as a series of longitudinal scans.

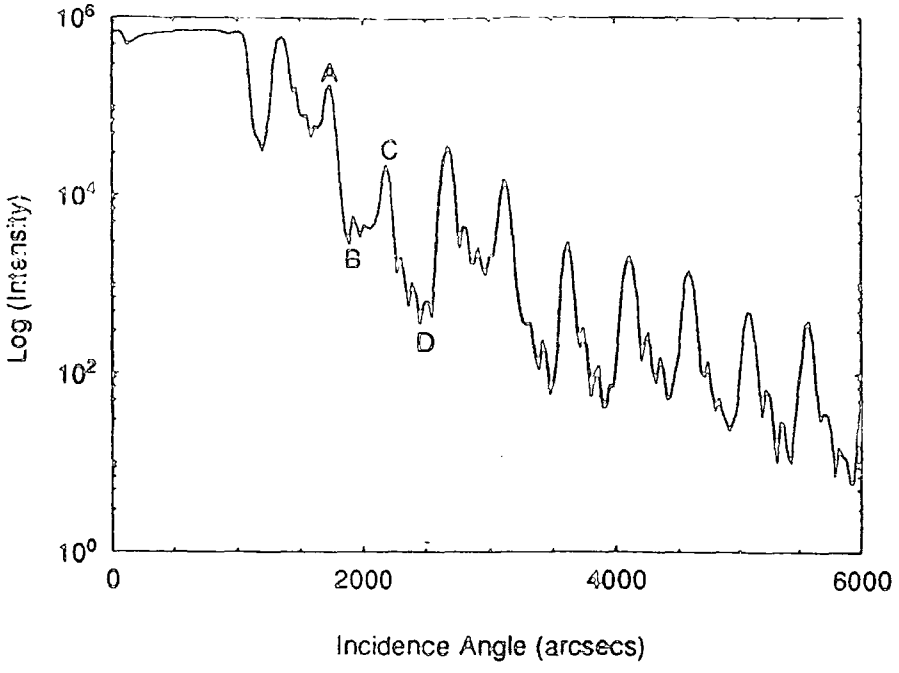


Figure 8.20(a) : Specular scan data from pre-annealed ap1313 sample. The transverse scans shown below were carried out centred on the points A,B,C and D.

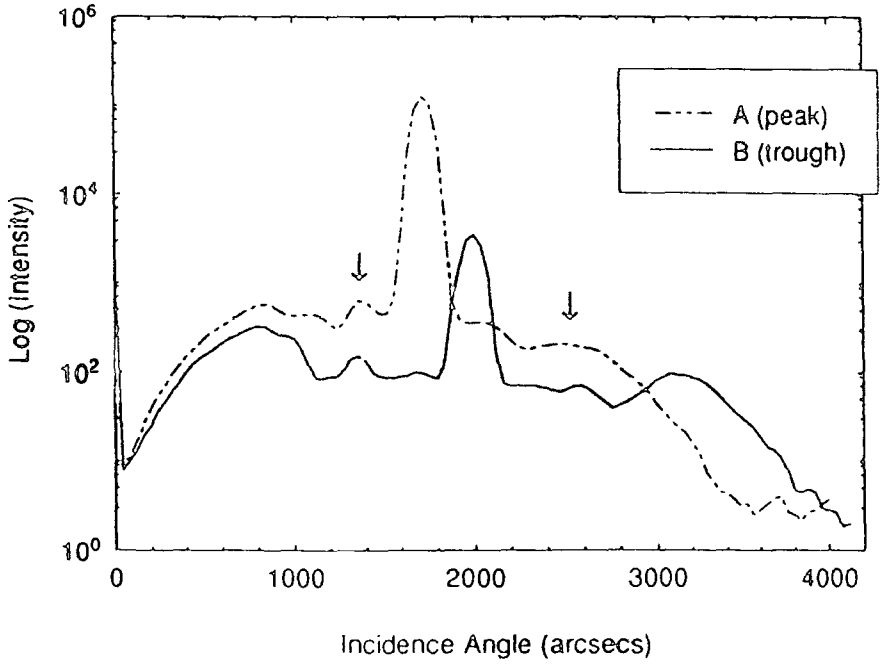


Figure 8.20(b) : Transverse scans for pre-annealed ap1313 sample, carried out at the points A and B in fig.8.20(a).

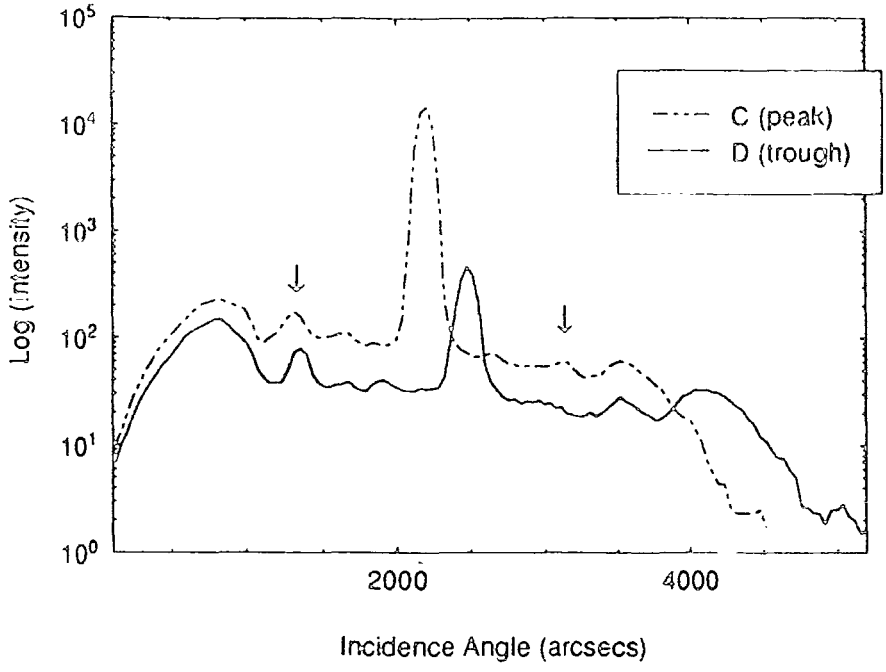


Figure 8.20(c) : Transverse scans for pre-annealed ap1313 sample, carried out at the points C and D in fig.8.20(a).


Figure 8.21(a) : Specular scan data from annealed ap1313 sample. The transverse scans shown below were carried out centred on the points A,B,C and D.

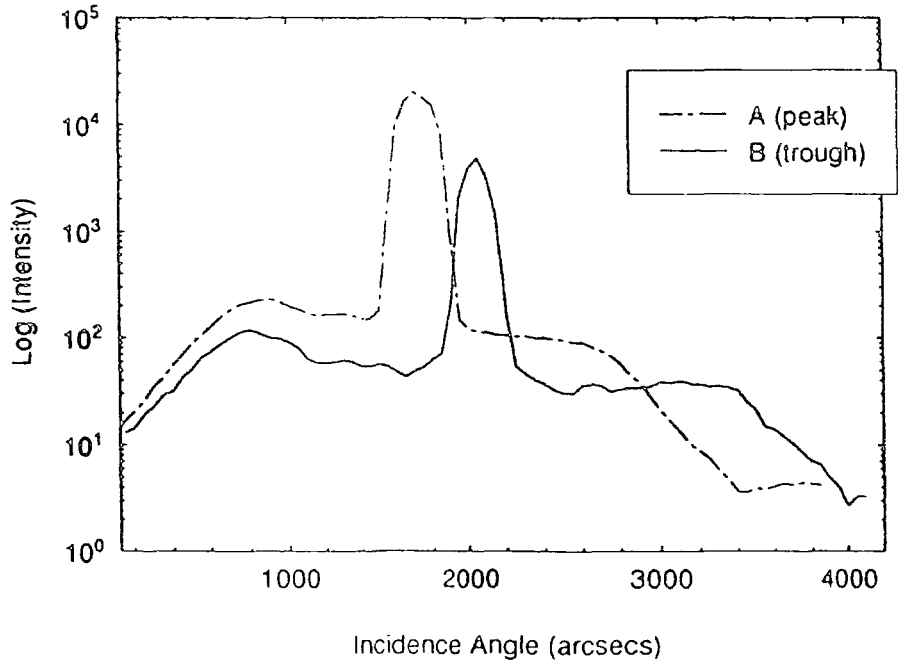


Figure 8.21(b) : Transverse scans for annealed ap1313 sample, carried out at the points A and B in fig.8.21(a).

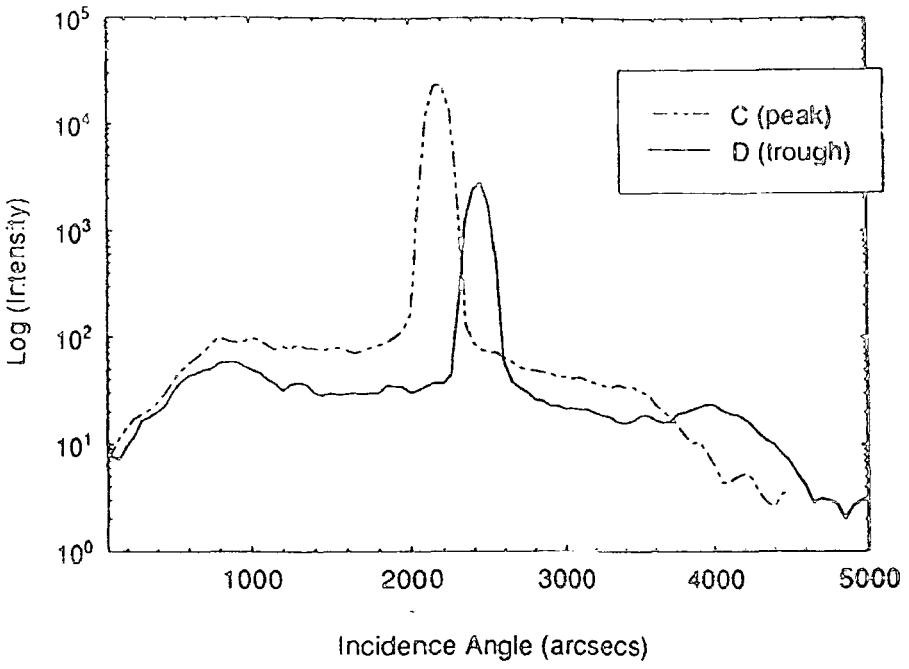


Figure 8.21(c) : Transverse scans for annealed ap1313 sample, carried out at the points C and D in fig.8.21(a).

### 8.7.2 Diffuse GIXR Studies Of Magnetic Multilayers

Figure 8.15 showed the specular scan from a 10 period Ni-C sputtered multilayer, of total thickness 37.4 nm and multilayer period 3.7 nm. Transverse diffuse scatter experiments were carried out at positions A and B, marked on fig.8.15. Despite the specular intensity at these two positions being similar there is a remarkable difference in the magnitude and distribution of the diffuse scatter (fig.8.22). Around the Bragg peak (position B) the diffuse scatter extends over an angular range of some 8000" while the diffuse scatter at position A is significant only close to the specular peak. This behaviour suggests that, as for the pre-annealed ap1313 sample, conformal roughness exists through the multilayer structure. This conformal roughness occurs when a particular interface roughness pattern, adopted by the bottom layer in a superlattice structure, is replicated by subsequent layers grown on top as the multilayer structure is fabricated. Hence, there will be a correlation between height fluctuations on different interfaces, introducing vertical periodicity in the roughness profile. The measured diffuse intensity will then show structure as a function of $q_z$ similar to the specularly reflected x-rays, as a result of the coherent addition of diffuse scatter from each interface.

As interface roughness has such a significant bearing on the properties of metallic multilayers it is of great interest to know if conformal roughness is present in other multilayers. Fig.8.23 is a pseudo-three dimensional contour map of the scatter from the Au/Co multilayer system described in Table 8.5, and whose specular GIXR profile is shown in fig.8.14(a). This data was recorded as a set of transverse scans with the three dimensional grid generated by feeding the scan data into the Golden Software program SURFER. The second Bragg peak can be clearly identified in the scattering map with a large bar of diffuse scatter running through the Bragg peak, transversely to the specular ridge. This extended ridge of diffuse scatter is spectacular evidence for the presence of conformal roughness in the Au/Co multilayer system.

Although the work presented in this chapter is from a limited number of multilayer samples, it seems highly probable that conformal roughness exists in all multilayer samples. The diffuse scatter from multilayer interfaces can thus be separated into two components, that arising from conformal (correlated) roughness and genuine (random) interface roughness. This has important implications for the analysis of

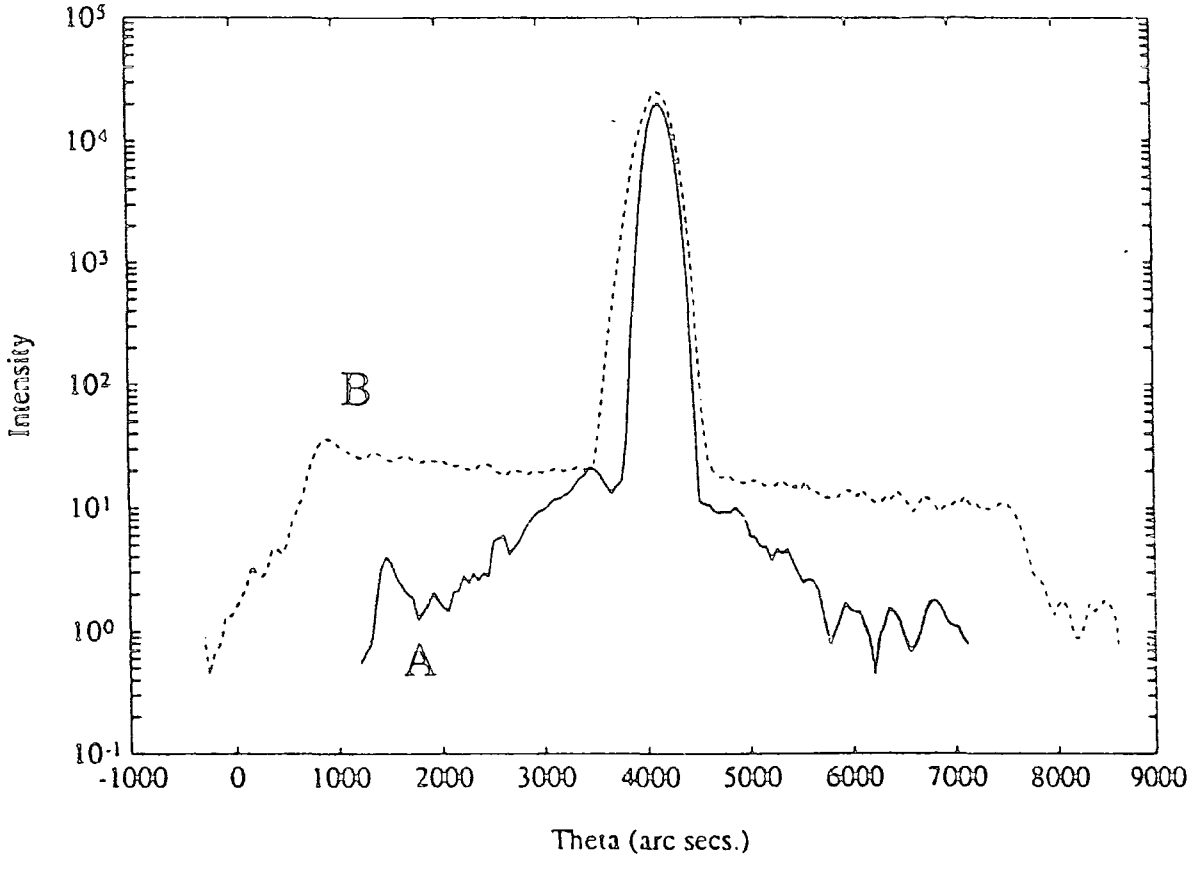


Figure 8.22 : Transverse diffuse scans of the Ni/C multilayer, carried out at positions A (Kiessig fringe peak) and position B (low order Bragg peak), as indicated on Fig.8.15

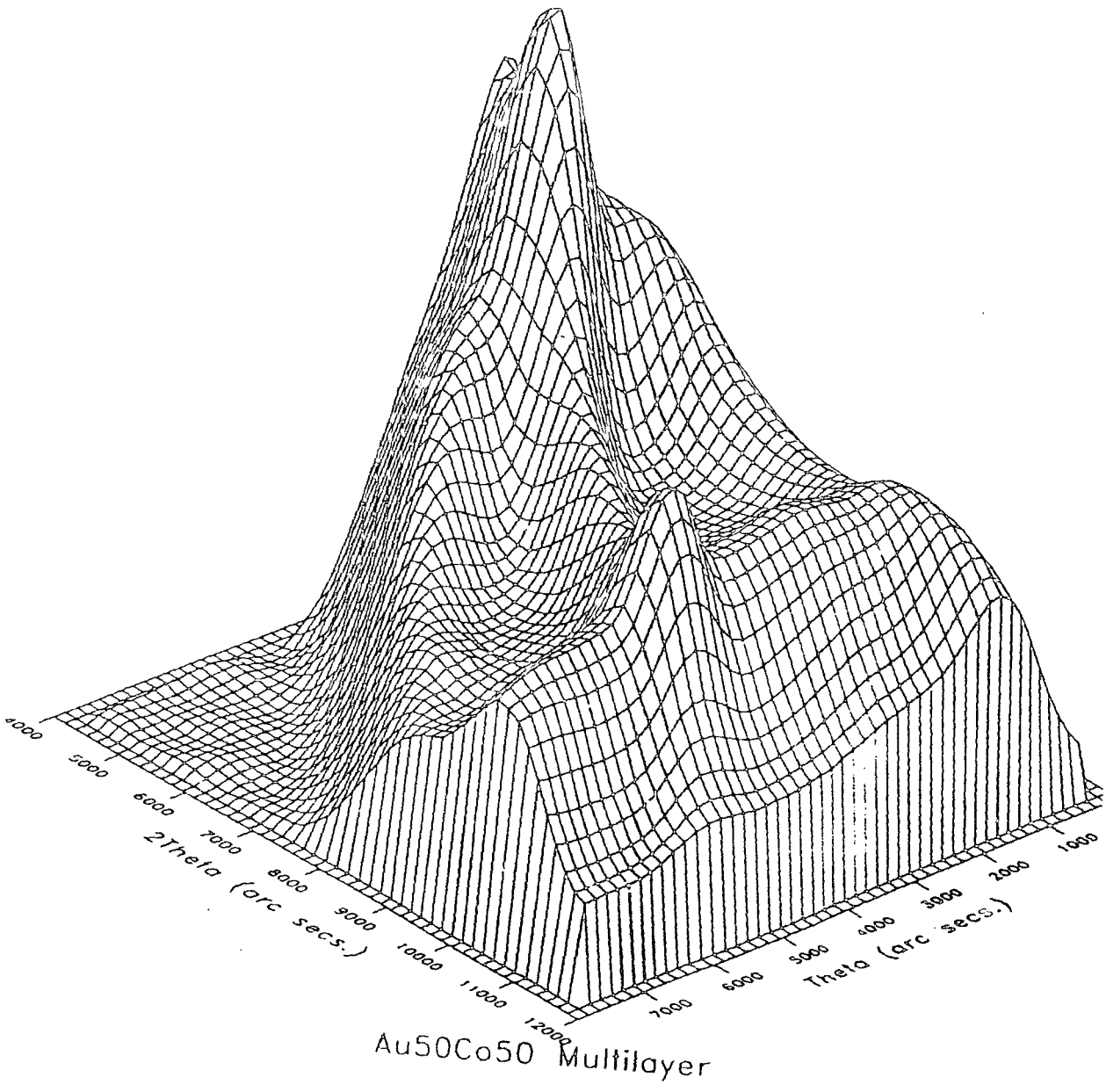


Figure 8.23 : Pseudo three dimensional plot of the scatter from a Au/Co multilayer. Note the strong bars of diffuse scatter transverse to the specular ($\theta/2\theta$) ridge.

magnetic multilayers where the interface roughness is believed to affect the magnetic properties of the sample. At present, it is not known if the magneto-resistive behaviour is affected by the conformal or random roughness (or both). The present study has demonstrated that collection of diffuse scatter in GIXR experiments can be used to establish whether conformal roughness exists or not within a particular specimen. By analysing a series of samples, originating from different growth techniques, it should be possible, by combining GIXR and magneto-resistance measurements, to establish how (or if) the presence of conformal roughness affects the properties of the magnetic multilayer.

## 8.8 Conclusions

The GIXR technique, in conjunction with a simulation program, has been used to characterise complicated multilayer structures, yielding valuable information on the interfacial roughness. Double crystal diffraction and GIXR have been used to measure the layer compositions, thicknesses and roughnesses of $Si/Si_{1-x}Ge_x$ superlattices. For structures with $x < 0.3$ the roughness at both types of interface had an r.m.s. value of $(0.5 \pm 0.3)$ nm. For higher Ge content samples the two types of interface were found to have differing values of roughness. The roughness at the $Si_{1-x}Ge_{1-x} \rightarrow Si$ interface has a long range periodic thickness variation in addition to the short range roughness present at the other interface, a conclusion confirmed by TEM analysis. Upon annealing for one hour at 850°C, the GIXR technique is shown to suffer no loss in sensitivity. The effect of thermal processing is to destroy the long range roughness at the $Si_{1-x}Ge_x \rightarrow Si$ interface, an effect attributed to the diffusion of Si and Ge atoms across the interface. Diffuse scattering measurements on the pre-annealed ap1313 sample (57% Ge), reveal structure in the diffuse scatter, with peaks in intensity of the diffuse component at the same angular position as the specular Bragg peaks. The presence of subsidiary peaks in transverse diffuse scans, midway between the specular peak and Yoneda wings is reported for a pre-annealed $Si \setminus Si_{0.43}Ge_{0.57}$ superlattice. These diffuse scatter "Bragg peaks" are further evidence for the presence of correlated or conformal roughness in the pre-annealed sample. For the annealed ap1313 sample, where diffusion effects have "washed" out the long range periodic roughness, the extension of diffuse scatter transverse to the specular ridge is small, confirming the loss of correlation between height fluctuations on different interfaces.

The potential of the GIXR technique for the analysis of interfaces in magnetic multilayers is demonstrated. High quality specular data can be collected from both MBE grown and sputtered multilayers, where a large difference exists in the electron density of the two elemental species. For 3-d, 3-d systems (i.e. Fe/Cr) the near matching of electron densities, together with oxidation of the top surface, results in it being more difficult to collect good specular GIXR data. By collecting the diffuse scatter transverse to low order Bragg peaks, the existence of conformal roughness has been strikingly demonstrated in the Ni/C and Au/Co magnetic multilayer systems.

# Chapter IX

## Conclusions And Suggestions For Further Work

This thesis has applied high resolution x-ray diffraction and x-ray reflectivity techniques to the analysis of semiconducting and magnetic materials. Traditionally, double crystal diffractometry (DCD) has been extensively used in the analysis of single crystal specimens. The techniques of triple crystal diffractometry (TCD) and grazing incidence x-ray reflectivity (GIXR) have not found such widespread use, possibly because of the lack of commercial instruments available which are based around these characterisation methods. The work presented in this thesis has shown that TCD and, particularly with regard to employment in a production environment, GIXR, provide complementary information to the DCD technique, which can of great use in the study of growth mechanisms.

Chapter V discussed techniques of DCD data reduction from HEMT structures which would allow layer thickness to be automatically extracted using Fourier transform methods. To obtain a clear Fourier transform the substrate peak must be excluded from the region analysed. The visibility of the Fourier peaks is further enhanced by normalising the data to an "average" envelope, in order to increase the contrast of thickness fringes, and applying an autocorrelation to increase the visibility of periodic components relative to the background noise. This method of data manipulation has been successful in producing Fourier transforms with clear, distinct peaks. The drawback with Fourier analysis of HEMT diffraction data is that there is often insufficient modulation information for individual frequencies (and hence layer thicknesses) to be resolved. In this instance, observed Fourier peaks correspond to "average" layer thicknesses. While this is unfortunate, the technique may still be of some use in a mass production context if methods of calibrating the Fourier data can be achieved. Where a particular sample structure is repeatedly grown, then the expected position of the "average" layer thickness can be calculated. The Fourier analysis technique could then be applied as a "pass/fail" step in quality assurance.

Chapter VI discussed a technique for the absolute lattice parameter measurement of single crystals. The method uses a triple crystal diffractometer with motorised $2\theta$ circle motion and the ability for fine, precise rocking of the analyser crystal. One of the advantages of this technique is that the set-up procedure and experimental method are very similar to those followed in a conventional triple crystal experiment. Hence, absolute lattice

parameter measurements could be carried out routinely prior to the triple crystal analysis of specimens, with only a small amount of time required to switch from one experiment to the other. Exemplary measurements on (horizontal Bridgman) GaAs and LEC grown InAs crystals yield lattice constants of 5.65424±0.00006Å and 5.65388±0.00018Å (GaAs), and 6.05864±0.00006Å (InAs). While two of these values have an absolute precision around 1 part in $10^5$, the absolute traceability of the technique is around 2 parts in $10^5$.

In Chapter VII, TCD was applied to the analysis of three material systems, namely; the $Hg_{1-x}Mn_xTe$ on GaAs, the $Cd_{1-x}Hg_xTe$ on CdTe/$Cd_{1-x}Zn_xTe$ and the low temperature grown GaAs systems. By mapping the diffuse scatter in reciprocal space the extent of lattice mosaicity (i.e., tilting) and dilation can be obtained. TCD and double crystal topography studies of $Hg_{1-x}Mn_xTe$ on GaAs reveal that layer material grown by the direct alloy growth (DAG) method has a mosaic structure with a typical sub-grain size of (130±5)μm. Material grown by the interdiffused multilayer process (IMP) is shown to be single crystal by double crystal x-ray topography. TCD studies of $Cd_{1-x}Hg_xTe$ grown by LPE on (vertical Bridgman) CdTe and $Cd_{0.96}Zn_{0.04}Te$ substrates show that higher crystalline quality layers are obtained for the $Cd_{0.96}Zn_{0.04}Te$ substrates. For both substrate types the layer perfection increases with layer thickness although the quality of the layer is always inferior to that of the substrate. The major contribution to rocking curve widths is from mosaicity of the samples, a result supported by the defect selective etching studies of Watson (Ref. 34, Chapter VII). Contrary to reports in the literature (e.g., Ref. 35, Chapter VII), it appears (from both etching studies and TCD) that the substrate dislocation density is not preserved in the layer material. However, substrates analysed by other workers have a higher initial dislocation density than those used in this study, and a "critical" dislocation density may exist above which residual lattice strain is entirely relieved by threading dislocations. Below this critical value, some lattice strain remains which may be relieved by some dislocation-multiplication process (i.e., the half loop mechanism), with the net result of a larger dislocation density being observed in the layer than in the substrate. In order to test this hypothesis, etching and triple crystal studies should be conducted on a series of $Cd_{1-x}Hg_xTe$ layers grown on substrates with a range of dislocation densities.

TCD analysis of low temperature grown GaAs (by the MBE and ALE methods) reveals that layers grown on GaAs substrates at low temperatures (200°C) exhibit a larger lattice parameter than that of bulk GaAs. This is attributed to the deposition of an As-rich GaAs

layer. If the growth temperature is increased to 300°C then ALE grown layers are deposited with a relatively perfect crystal structure. In general, for layers deposited at the same temperature by MBE and ALE, then the more perfect layers are grown by the ALE technique. Annealing of the high defect content samples (i.e., those grown at 200°C) significantly improves the crystalline quality of the GaAs layer. This may be attributed to the annihilation of misfit dislocations during the thermal treatment.

Chapter VIII used the GIXR technique in the analysis of $Si/Si_xGe_{1-x}$ superlattices and metallic multilayer samples. The reflectivity technique is shown to be capable of measuring layer thickness to within 1Å for particular data sets. The method is particularly suited for the measurement of very thin layer thicknesses in the region 10Å to 2000Å. Perhaps the most attractive feature of GIXR is its capability to measure top surface and interfacial roughness (and separate the two). GIXR has been used to characterise $Si/Si_xGe_{1-x}$ superlattices with material parameters obtained by matching experimental profiles to simulated plots. In this way, superlattice layer thickness has been measured accurate to ±3Å. GIXR has revealed that the two different types of interface in the high Ge content $Si/Si_xGe_{1-x}$ superlattices (the $Si \rightarrow Si_xGe_{1-x}$ and the $Si_xGe_{1-x} \rightarrow Si$ interfaces) have different roughness values, the $Si_xGe_{1-x} \rightarrow Si$ interface being rougher, a result which has been confirmed by TEM. The reason for this growth pattern is not understood and it is recommended that a further series of $Si/Si_xGe_{1-x}$ superlattice be grown (under a variety of growth conditions) and analysed by GIXR. These structures may also be grown with and without buffer layers in order to investigate the effects of layer strain.

The analysis of magnetic multilayers by GIXR reveals that peaks in the diffuse scatter occur at the Bragg condition for the 1-D artificial lattice formed by the multilayered sample. These peaks are believed to arise from conformal roughness of the layer interfaces, i.e., that a correlation exists between the interfacial roughness profiles of different layers. Maxima in the diffuse scatter at Bragg peaks are also discovered for the high Ge content $Si/Si_xGe_{1-x}$ superlattices. The phenomena of conformal roughness is believed to be a general property of multilayered samples, although further diffuse GIXR studies on more multilayered and superlattice specimens is required if this is to be confirmed.

## Chapter 1 References


1 Moss S.J. and Ledwith A, *The Chemistry Of The Semiconductor Industry*, Chapman and Hall, New York (1987).

2 Mullin J.B., Heritage R.J., Holliday C.H. and Straughan B.W., J. Cryst. Growth, 34, 281 (1968).

3 Gatos H.C. and Lavine M.C., J. Electrochem. Soc., 104, 427 (1960).

4 Kao K.C. and Hockham G.A., Proc. IEEE, 13, 1151 (1961).

5 Payne D.N. and Gambling W.A., Electron. Lett., 11, 176 (1975).

6 Horiguchi M. and Osanai H., Electron. lett., 12, 310 (1976).

7 Miya T., Terunuma Y., Hosaka T. and Miyashita T., Electron. lett., 15, 106 (1979).

8 Bell T.E., IEEE Spectrum (Dec.), 38 (1983).

9 Okamoto K., Edahiro T., Kawana A. and Miya T., Electron. Lett., 15(22), 729 (1979).

10 Agrawal G.P. and Dutta N.K., *Long Wavelength Semiconductor Lasers*, Van Nostrand, New York (1986).

11 Gunshor R.L., Kolodziejski L.A., Nurmikko A.V. and Otsuka N., Ann. Rev. Mat. Sci., 18, 325 (1988).

12 Sze S.M., *Semiconductor Devices - Physics and Technology*, McGraw Hill, New York (1985).

13 Jaros M., *Physics and Applications of Semiconductor Devices*, McMillan (1991).

14 McGuire T.R and Potter R.I., IEEE Trans. Magn., 11, 1018 (1975).

15 Thompson D.A., Romankiw L.T. and Mayadas A.F., IEEE Trans. Magn., 11, 1039 (1975).

16 Heremans J., J. Phys. D: Appl. Phys., 26, 1149 (1993).

17 Baibach M.N., Broto J.M., Fert A., Nguyen Van Dau F., Petroff F., Etienne P., Creuzet G., Friedrich A. and Chazelas J., Phys. Rev. Lett., 61, 2472 (1988).

18 Mosca D.H., Petroff F., Fert A., Schroeder P.A., Pratt W.P. Jr. and Loloee R., J. Mag. Magn. Mat., 94, L1-L5 (1991).

19 Nakajima K., Komiya S., Akita K., Yamaoka T. and Ryuzun O., J. Electrochem. Soc.,127, 1568 (1980).

20 Logan R.A., Prog. Cryst. Growth Charac., 12, 215 (1986).

21 Nagai H., Prog. Cryst. Growth Charac., 12, 271 (1986).

22 Takahashi S. and Nagai H., J. Cryst. Growth, 51, 502 (1981).

23 Besomi P., Wilson R.B., Wagner W.R. and Nelson R.J., J. Appl. Physics, 54, 535 (1983).

24 Chatterjee A.K., Faktor M.M., Lyons M.H. and Moss R.H., J. Cryst. Growth, 56, 591 (1982).

25 Stringfellow G.B., Semicond. & Semimetals, 22, 209 (1985).

26 Nelson A.W., Moss R.H., Spurdens P.C., Cole S. and Wong S., Br. telecom Technol. J., 4, 85 (1986).

27 Davies G.J. and Andrews D.A., Br. Telecom. Technol. Jour., 3(2), 59 (1985).

28 Vogdjani N., Lamarchand A. and Paradan M., J. Phys. Colloq. C5, 43, 339 (1982).

29 Tokumitsu E., Kudoo Y., Konagai M. and Takabaski K., J. Appl. Phys., 55, 3163 (1984).

30 Tsang W.T., Appl. Phys. Lett., 45, 1234 (1984).

31 Ming L.Yu., J. App. Phys., 73(2), 716 (1993).

32 Usui A., Proc. of the IEEE, 80(10), 1641 (1992).

33 Suntola T., Mat. Sci. Report, 4, 261 (1989).

34 Honoré L.R.J.P., Private Communication.

35 Ohring M., *The Materials Science Of Thin Films*, Academic Press (1992).

36 Griesche J., Enderlein R. and Schikora D., Phys. Stat. Sol. (a), 109, 11 (1988).

37 Olsen G.H and Smith R.T., Phys. Stat. Sol. (a), 31, 739 (1975).

38 Halliwell M.A.G., Adv. In X-ray Analysis, 33, 61 (1990).

39 Matthews J.W. and Blakeslee A.E., J. Cryst. Growth, 27, 118 (1974).

40 Andersson T.G., Chen Z.G., Kulakous V.D., Uddin A. and Vallin T.J., Appl. Phys. Lett., 51, 10 (1987).

41 Mikkelson J.C. and Boyce J.B., Phys. Rev. Lett., 49(19), 1412 (1982).

42 Fukui T., Jap. J. App. Phys., 23(4), L208 (1984).

43 Hornstra J. and Bartels W.J., J. Cryst. Growth, 44, 518 (1978).

44 Davidenkov N.N., Sov. Phys. Solid State, 2, 2595 (1961).

45 Chu S.N.G., Macrander A.T., Strege K.E. and Johnson W.D., J. Appl. Phys., 57, 249 (1985).

46 Hill M.J., PhD. Thesis, University Of Durham (1985).

47 Shaffner T.J., Scan. Elect. Microscop., 1, 11 (1986).

48 Maissel L.I. and Glang R., *Handbook of Thin Films Technology*, McGraw Hill, New York (1970).

49 Tolansky S., *Multiple Beam Interference Microscopy Of Metals*, Academic Press, London (1970).

50 Maissel L.I. and Francombe M.H., *An Introduction To Thin Films*, Gordon and Breach, New York (1973).

51 Cooney R.P. and Mahoney M.R., *Advances In Infra-Red And Raman Spectroscopy*, Edited by Clark R.J.H. and Hester R.E., Heyden, London, (1982).

52 Creighton J.A., *Spectroscopy At Surfaces*, Edited by Clark R.J.H. and Hester R.E., Wiley, Chichester (1988).

53 Chang K.H., Bhattacharya P.K. and Gibala R., J. Appl. Phys., 65(9), 3391 (1989).

54 Alavi K., Petroff P., Wagner W.R. and Cho A.Y., J. Vac. Sci. & Technol., B1(2), 146 (1983).

55 Carey K.W., Appl. Phys. Lett., 46, 89 (1985).

56 Schaus C.F., Shealy J.R., Eastman L.F., Cooman B.C., and Carter C.B., J. Appl. Phys., 59(2), 678 (1986).

57 Dupius R.D., Bean J.C., Brown J.M., Macrander A.T., Miller R.C. and Hopkins L.C., J. Electron. Mat., 16(1), 69 (1987).

58 Orton J.M., Fewster P.F., Gowers J.P., Dawson P., Moore K.J., Dobson P.J., Curling C.J., Foxon C.T., Woodbridge K., Duggan G. and Ralph H.I., Semicond. Sci. & Technol., 2, 597 (1987).

59 Asher S., Adv. In X-ray Anal., 31, 53 (1988).

60 Smith K.K., Thin Solid Films, 84, 171 (1981).

61 Goetz K.H., Bimberg D., Jürgensen H., Selders J., Solomonov A.V., Glinskii G.F. and Razeghi M., J. Appl. Phys., 54(8), 4543 (1983).

62 Rivière J.C., *Surface Analytical Techniques*, Clarendon Press, Oxford (1990).

63 Feldman L.C., *Fundamentals Of Surface And Thin Film Analysis*,Elsevier Science Publishing Co., New York (1986).

64 Tanashiro Y., Takayanagi K. and Yagi K., J Microscopy, 142, 211 (1986).

65 Lehmpfuhl G. and Uchida Y., Ultramicroscopy, 26, 177 (1988).

66 Benninghoven A.W., Rudenauer F.G. and Werner H.W., *Secondary Ion Mass Spectometry - Basic Concepts, Instrumental Aspects, Applications and Trends*, Wiley, New York (1987).

67 Degreve F., Thorne N.A. and Lang J.M., J. Mat. Sci., 23, 4181 (1988).

68 Bird J.R. and Williams J.S., *Ion Beams For Materials Analysis*, Academic Press, Sydney (1989)

69 Chu W.K., Mayer J.W., Nicolet M.A., Buck T.M., Amsel G. and Eisen F., Thin Solid Films, 17, 1 (1963).

## Chapter III References


1 Teo B.K. and Joy D.C., *EXAFS Spectroscopy*, Plenum Press, London (1981).

2 Prinz R. and Konigsberger D., *X-Ray Absorption: Principles and Techniques of EXAFS, SEXAFS and XANES*, J.Wiley, New York, (1968).

3 Margaritondo G., *Introduction To Synchrotron Radiation*,Oxford Univ. Press (1988).

4 Pomerantz M., Thin Solid Films, 152, 165 (1987).

5 Névot L. and Croce P., Rev. Phys. Appl., 15, 761 (1980).

6 Parratt L.G., Phys. Rev., 95(2), 359 (1954).

7 Compton A.H. and Allison S.K., *X-Rays In Theory And Experiment*, McMillon (1936).

8 Nevot L. and Croce P., Rev. Phys. Appl., 15, 761 (1980).

9 Sinha S.K., Sirota E.B., Garoff S. and Stanley H.B., Phys. Rev. B, 38, 2297 (1988).

10 Pynn R., Phys. Rev. B, 45, 602 (1992).

11 Cowley R.A. and Ryan T.W., J. Phys. D: Appl. Phys., 20, 61 (1987).

12 James R.W., *The Optical Principles of the Diffraction of X-Rays*, Bell, London (1948).

13 Warren B.E., *X-Ray Diffraction*, Addison Wesley (1969).

14 Cullity B.D., *Elements Of X-Ray Diffraction*, Addison-Wesley (1969).

15 McKie D. and McKie C., *Essentials Of Crystallography*, Blackwell (1986).

16 Darwin C., Phil. Mag., 27, 315 and 675 (1914).

17 Ewald P.P., Ann. Physik., 49, 117 (1916).

18 Laue M. Von, Acta. Cryst., 5, 619 (1952).

19 Zachariasen W.H., *Theory of X-Ray Diffraction in Crystals*, Wiley, New York (1945).

20 Pinsker Z.G., *Dynamical Scattering of X-Rays in Crystals*, Springer-Verlag, Berlin (1978).

21 Batterman B.W. and Cole H., Rev. Mod. Phys., 3, 681 (1964).

22 Authier A., *Advances in Structure Research by Diffraction Methods*, Ed. Brill and Mason, 3, 1 (1970).

23 Hart M., *Characterisation of Crystal Growth Defects by X-Ray Methods*, Ed. Tanner and Bowen, London, Plenum Press, 216 and 483 (1980).

24 Tanner B.K., *X-ray Diffraction Topography*, Pergamon Press (1976).

25 Segmüller A., Noyan I.C. and Speriosu V.S., Prog. Cryst. Growth & Charac., 18, 21 (1989).

26 Petrashen P.V., Sov. Phys. Solid State, 17, 1882 (1976).

27 Hill M.J., Tanner B.K., Halliwell M.A.G. and Lyons M.H., J.Appl. Cryst., 18, 446 (1985).

28 Bensoussan S., Malgrange C. and Sauvage-Simkin M., J. Appl. Cryst., 20, 222 (1987).

29 Fewster P.F. and Curling C.J., J. Appl. Phys., 62, 4154 (1987).

30 Takagi S., J. Phys. Soc. Japan, 26, 1239 (1969).

31 Taupin D., Bull. Soc. Fr. Mineral Crystallog., 87, 469 (1964).

## Chapter III References


1 Hart M., J. Cryst. Growth, 55, 409 (1981).

2 Compton A.H., Rev. Sci. Instrum., 2(7), 365 (1931).

3 Hart M., J. Cryst. Growth, 55, 409 (1981).

4 Schwarzchild M.M., Phys. Rev., 32, 162 (1928).

5 Allison S.K. and Williams J.H., Phys.Rev., 35, 1476 (1930).

6 Allison S.K., Phys. Rev., 41, 1 (1932).

7 Compton A.H. and Allison S.K., *X-Rays In Theory And Experiment*, MacMillon (1936).

8 Du Mond J.W.M., Phys. Rev., 52, 872 (1937).

9 Tanner B.K., *X-Ray Diffraction Topography*, Pergamon Press (1976).

10 Pinsker Z.G., *Dynamical Scattering Of X-Rays In Crystals*, Springer-Verlag, Berlin (1978).

11 Pietsch U. and Borchard W., J. Appl. Cryst., 20, 8 (1987).

12 Yoshimura J., J. Appl. Cryst., 17, 426 (1984).

13 Xu S. and Li R., J. Appl. Cryst., 21, 213 and 218 (1988).

14 Renninger M. Von., Acta. Cryst., 8, 597 (1955).

15 Cowley R.A., Acta. Cryst., A43, 825 (1987).

16 Ryan T.W., PhD. Thesis, University of Edinburgh (1986).

17 Nakayama K., Hashizume H., Miyoshi A., Kikuta S. and Kohra K., Z. Naturforsch,A28, 632 (1973).

18 Tanner B.K., Adv. X-Ray Analy., 33,1 (1990).

19 Du Mond J.W., Phys. Rev. 52, 872 (1937).

20 Beaumont J.H. and Hart M., J. Phys. E: Sci. Inst., 7, 823 (1974).

21 Bartels W.J., J. Vac. Sci. & Tech., B1(2), 338 (1983).

22 Slusky S.E.G. and Macrander A.T., J. Appl. Cryst., 20, 522 (1987).

23 Bonse U. and Hart M., Appl. Phys. Lett., 7, 238 (1965).

24 Fewster P.F., J. Appl. Cryst., 22, 64 (1989).

25 Loxley N., Bowen D.K. and Tanner B.K., Proc. Mat. Res. Soc. (Symp. J.), (1990).

## Chapter IV References


1 Miles S.J., PhD. Thesis, University Of Durham (1989).

2 Turnbull A.G., PhD. Thesis, University Of Durham (1992).

3 Tanner B.K., *X-Ray Diffraction Topography*, Pergamon Press (1976).

4 Tanner B.K. and Bowen D.K., J. Cryst. Growth, 126, 1 (1993).

5 Bartels W.J. and Nijman W., J. Cryst. Growth, 44, 518 (1978).

6 Wang X.R., Chi X.Y., Zheng H., Miao Z.L., Wang J., Zhang Z.S. and Jin Y.S., J. Vac. Sci. & Tech., B6(1), 34 (1988).

7 Hart M., *Characterisation of Crystal Growth Defects by X-ray Methods*, edited by Tanner B.K. and Bowen D.K., Plenum Press, 483 (1980).

8 Fewster P.F., J. Appl. Cryst., 18, 334 (1985).

9 Tanner B.K., Chu X. and Bowen D.K., Proc. Mat. Res. Soc., 69, 191 (1986).

10 Halliwell M.A.G., Inst. Phys. Conf. Ser., 60(5), 271 (1981).

11 Tanner B.K. and Bowen D.K (Editors), *Characterisation Of Crystal Growth Defects By X-Ray Methods*, Plenum, New York (1980).

12 Hart M., Science Progress, Oxford, 56, 429 (1968).

13 Yoshimura J., Miyazaki T., Wada T., Kohra K., Hosaka M., Ogawa T. and Taki S., J. Cryst. Growth, 46, 691 (1979).

14 Jones G.R., Young I.M., Cockayne B. and Brown G.T., *Microscopy Of Semiconducting Materials*, Inst. Phys. Conf. Ser., 60, 265 (1981).

15 Bond W.L. and Andrus J., Am. Mineralogist, 37, 622 (1952).

16 Bonse U. and Kappler E., Z. Naturforsch, 13a, 348 (1958).

17 Petroff J.F., Sauvage M., Riglet P. and Hashizume H., Phil. Mag. A, 42, 319 (1980).

18 Bak-Misuik J., Gronkowski J., Hartwig J. and Wierzchowski W., Phys. Stat. Sol. A, 99, 345 (1987).

19 Barnett S.J., Brown G.T and Tanner B.K., *Microscopy Of Semiconducting Materials*, Inst. Phys. Conf. Ser., 87, 615 (1987).

20 Barnett S.J., Tanner B.K. and Brown G.T.,Proc. Mat. Res. Soc., 41, 83 (1985).

21 Renninger M. Von, Acta Cryst.,8, 597 (1955).

22 Stevenson A.W., Wilkins S.W., Harada J., Kashiwagura N., Oshima K. and Sakata M., Acta Cryst., A44, 828 (1988).

23 Lucas C.A., Hatton P.D., Bates S., Ryan T.W., Miles S.J. and Tanner B.K., J. Appl. Phys., 63, 1936 (1988).

24 Ryan T.W., Hatton P.D., Bates S., Watt M., Sotomayor-Torres C., Claxton P.A. and Roberts J.S., Semicond. Sci. & Technol., 2, 241 (1987).

25 Lomov A.A., Zaumseil P. and Winter U., Acta Cryst., A41, 223 (1985).

26 Charniy L.A., Morozov A.N., Bublik V.T., Scherbachev K.D., Stepantsova I.V. and Kaganer V.M., J. Cryst. Growth, 118, 163 (1992).

27 Iida A. and Kohra K., Phys. Stat. Sol. (a), 51, 533 (1979).

28 Loxley N., Monteiro A., Cooke L., Bowen D.K. and Tanner B.K., Proc. Mat. Res. Soc., 240, 219 (1992).

29 Sinha S.K., Physica B., 173, 25 (1991).

## Chapter V : References


1 Jeong J., Schilesinger T.E. and Milnes A.G., J. Cryst. Growth 87, 265 (1988).

2 Baümbach T., Rhan H. and Pietsch U., Phys. Stat. Sol. (a) 109, K7 (1988).

3 Ferrari C. and Franzosi P., J. Appl. Phys. 65 (4), 1544 (1989).

4 Batterman B.W. and Hilderbrandt G., Acta. Cryst. A24, 150 (1968).

5 Bartels W.J. and Nijman W., J. Cryst. Growth 44, 518 (1978).

6 Macrander A.T. and Strege K., J. Appl. Phys. 59, 442 (1986).

7 Bensoussan S., Malgrange C., Sauvage-Simkin M., N'Guesson K. and Gibart P., J. Appl. Cryst. 20, 222 (1987).

8 Bocchi C., Ferrari C., Franzosi P.,Fornuto G., Pellegrino S. and Taiariol F., J. Electron. Mat. 16, 245 (1987).

9 Wie C.R., J. Appl. Phys. 65 (6), 2267 (1989).

10 Prilepskii M.V. and Sukhodreva J.M., Phys. Chem. Mech. Surf. 3 (1), 188 (1985).

11 Tanner B.K. and Halliwell M.A.G., Semicond. Sci. & Tech. 3, 967 (1988).

12 Miles S.J., PhD. Thesis, University Of Durham (1989).

13 Macrander A.T., Lau S., Strege K. and Chu S.N.G. (1988), Appl. Phys. Letts. 52(23), (1985).

14 Cooley P.M and Tukey J.W., Mathematics Of Computation, 19, 297 (1965).

15 Hecht E., "*Optics*", 2nd Edition, 250 (1987).

16 Ramirez R.W., *The FFT:Fundamentals and Concepts*, Prentice Hall International Inc. (1985).

## Chapter VI References


1 Bond W.L., Acta Cryst., 13, 330 (1960).

2 Willoughby A.F.W., and Driscoll C.M.H., J. Mat. Sci., 6, 1389 (1971).

3 Hart M., J. Cryst. Growth, 55, 409 (1981).

4 Turnbull A.G., PhD. Thesis, University of Durham (1992).

5 Estop E., Izreal A. and Sauvage M., Acta. Cryst., A32, 627 (1976).

6 Sajovec F., Wolf R., Fattah A., Bickmann K., Wenzl H., Nagel G., Rüfer H., Tomzig E. and de Bièvre P., Phys. Stat. Sol. (a), 122, 139 (1990).

7 Morozov A.N. and Bublik V.T., J. Cryst. Growth, 75, 497 (1986).

8 Biggin S. and Dingley D.J., J. App. Cryst., 10, 376 (1977).

9 Helmer R.G., Heath R.L., Putnam M. and Gipson D.H., Nucl. Instr. Methods, 57, 46 (1967).

10 Buras B., Staun Olsen J., Gerward L., Selsmark B. and Lindegaard-Andersen A., Acta. Cryst., A31, 327 (1974).

11 Bordas J., Glazer A.M., Howard C.J., and Bourdillon A.J., Phil. Mag.,35, 311 (1977).

12 Fukumori T., Futagami K. and Matsunaga K., Jap. J. App. Phys., 21(10), 1525 (1982).

13 Bowen D.K. and Tanner B.K, submitted to J. Appl. Crystall.

14 Bowen D.K., Tanner B.K., Hudson J.M., Pape I., Loxley N. and Tobin S., submitted to Adv. In X-Ray Analysis.

15 Fatemi M., J. Crystal Growth., 96, 316 (1989).

16 Häusermann D. and Hart M., J. Appl. Cryst., 23, 63 (1990).

17 Deslattes R.D., Kessler E.G., Sauder W.C. and henins A., Ann. Phys., 129, 378 (1980).

18 Buschert R.C., Meyer A.J., Stuckey Kauffman D. and Gotwals J.K., J. Appl. Cryst., 16, 599 (1983).

19 Fewster P.F., J. Appl. Cryst., 15, 275 (1982).

20 Hornstra J. and Bartels W.J., J. Cryst. Growth, 44, 513 (1978).

21 Pietsch U. and Borchard W., J. Appl. Cryst., 20, 8 (1987).

22 Bearden J.A., Rev. Mod. Phys., 39, 78 (1967).

23 Fukumori T. and Futagami K., Jap. J. App. Phys., 27(3), 442 (1988).

24 Windisch D. and Becker P., Phys. Stat. Sol. (a), 118, 379 (1990).

25 Usuda K., Yasuami S., Higashi Y., Kawata H. and Ando M., Jap. J. App. Phys., 29, L210 (1990).

26 Giesecke G. and Pfister H., Acta. Cryst., 11, 369 (1958).

27 Ferrari C., Bruni M.R., Martelli F. and Simeone M.G., J. Cryst. Growth, 126, 144 (1993).

## Chapter VII References


1 Furdyna J.K., J. Appl. Phys., 64, R29 (1988).

2 Rogalski A., Infrared Phys., 31, 117 (1991).

3 Delves R.T. and Lewis B., J. Phys. Chem. Solids, 24, 549 (1963).

4 Clifton P.A., Brinkman A.W. and Al-Allak H.M., Semicond. Sci.&Tech., 5, 1067 (1990).

5 Funaki M., Lewis J.E., Hallam T.D., Chaorong L., Halder S.K., Brinkman A.W. and Tanner B.K., Semicond. Sci. & Technol., 8, S200 (1993).

6 Hallam T.D., Halder S.K., Hudson J.M., Li C.R., Funaki M., Lewis J.E., Brinkman A.W. and Tanner B.K., J. Phys. D.:Appl. Phys., 26, A161-A166 (1993).

7 Keir A.M, Barnett S.J., Giess J., Walsh T.D. and Astles M.G., Appl. Surf. Sci., 50, 103 (1991).

8 Hallam T.D., Tanner B.K., Funaki M., Brinkman A.W., - *to be published in Proc. Mat. Res. Soc. (1993).*

9 Irvine S.C., Tunnicliffe J. and Mulline J.B., Mater. Lett., 2, 305 (1984).

10 Tunnicliffe J., Irvine S.J.C., Dosser O.D. and Mullin J.B., J. Cryst. Growth, 68, 245 (1984).

11 Funaki M., Brinkman A.W., Hallam T.D. and Tanner B.K., App. Phys. Lett (1993).

12 Hallam T.D., Private Communication.

13 Farrow R.F.C., Schetzina J.F. and Cheung J.T. (Editors) , Proc. Mat. Res. Soc., 90 (1987).

14 Matare H.F., *Defect Electronics In Semiconductors*, Wiley-Interscience, USA, 145 (1971).

15 Yamamoto T., Miyamoto Y. and Tanikawa K., J. Cryst. growth, 72, 270 (1985).

16 Miyamoto Y., Sakai H. and Tanikawa K., *Proc. of the Society of Photo-Optical Instrumentation Engineers*, edited by I.J.Spiro, 572, 115 (1985).

17 Brossat T., Azema A., Botineau J. and Raymond F., SPIE, 588, 111 (1985).

18 Chow D.H., McCaldin J.O., Bonnefoi A.R., McGill T.C., Sou I.K., Faurie J.P., Shirland F.A. and Wu O.K., J. Vac. Sci. & Tech., A6, 2728 (1988).

19 Sakamoto K. and Okabe Y., Jap. J. Appl. Phys., 25, 444 (1986).

20 Craid D., Opt. Commun., 68, 69 (1988).

21 Tarry H.A., Electron. Lett., 22, 416 (1986).

22 Zucca R., Bajaj J. and Blazejewski E.R., J. Vac. Sci. & Tech., A6, 2728 (1988).

23 Andersson T and Lundqvist S., Opt. Quantum Electron., 19, 313 (1987).

24 Alebdra A., Orsal B., Valenza M., Linares C., Pichard G., Meslage J. and Boisrobert C., Ann. Telecomm., 43, 117 (1988).

25 Mottet S., Viallet J.E., Boisrobert C. and Scavennec A., Ann. Telecomm., 7-8, 365 (1988).

26 Noreika A.J., Farrow R.F.C., Shirland F.A., takei W.J., Greggi J. Jr., Wood S. and Choyke W.J., J. Vac. Sci. & Technol., A4, 2081 (1986).

27 Roussille R., Amingual D., Boch R., Destefanies G.L. and Tissot J.L., Appl. Phys. Lett., 44, 679 (1984).

28 Thompson J., Woodhouse K.T. and Dineen C., J. Cryst. growth, 77, 452 (1986).

29 Edwall D.D., Gertner E.R. and Tennant W.E., J. Appl. Phys., 55, 1543 (1984).

30 Yoshikawa M., Ueda S., Maruyama K. and Takigawa H., J. Vac. Sci. & Technol., A3, 153 (1985).

31 Woolhouse G.R., Magee T.J., Kawayoshi H.A., Leung C.S.H. and Ormond R.D., J. Vac. Sci. & Technol., A3, 83 (1985).

32 Szilagyi A. and Grimbergen M.N., J. vac. Sci. & Technol., A4, 2200 (1986).

33 Dean B.E., Johnson C.J., McDevitt S.C., Neugebauer G.T., Sepich J.L., Dobbyn R.C., Kuriyama M., Ellsworth J., Vydyanath H.R. and Kennedy J.J., J. vac. Sci. & Technol., 9(3), 1840 (1991).

34 Watson C.C.R., PhD.Thesis, University Of Durham (1993).

35 Yoshikawa M., J. Appl. Phys., 63, 1533 (1987).

36 Matthews J.W. and Blakeslee A.E., J. Crystal Growth, 27, 118 (1974).

37 Fitzgerald E.A., Watson G.P., Proano R.E., Ast D.G., Kirchener P.D., Pettit G.D. and Woodall J.M., J. Appl. Phys., 65, 2220 (1989).

38 Smith F.W., Calawa A.R., Chen C.L., Manfra M.J. and Mahoney L.J., IEEE Electron. Device Lett., 9, 77 (1988).

39 Lin B.J., Kocot C.P., Mars D.E. and Jaeger R., IEEE Trans. Electron. Devices, ED-9, 46 (1988).

40 Yin L.W., Hwang Y., Lee J.H., Kolbas R.M., Trew R.J. and Misra U.K., IEEE Electron. Device Lett., EDL-11, 561 (1990).

41 Van Exter M., Fattinger C. and Grischkowsky D., App. Phys. Lett., 55, 337 (1989).

42 J.N., Liliental-Weber Z., Yau W.F. and Weber E.R., Phys. Rev. Letters, 66, 3079 (1991).

43 Kaminska M., Liliental-Weber Z., Weber E.R., George T., Kortright J.B., Smith F.W., Tsaur B.Y. and Calawa A.R., Appl. Phys. Letters, 54, 1881 (1989).

44 Warren A.C., Woodall J.M., Freeouf J.L., Grischkowsky D., McInturff D.T., Melloch M.R. and Otsuka N., App. Phys. Lett., 57, 1531 (1990).

## Chapter VIII References


1 Loxley N., Monteiro A., Cooke L., Bowen D.K. and Tanner B.K., Proc. Mat. Res. Soc., 240, 219 (1992).

2 Rabedeau T.A., Tidswell I.M. and Pershan P.S., App. Phys. Lett., 59, 26 (1991).

3 Krol A., Resat H., Sher C.J., Woronick S.C., Ng W., Kao Y.H., Cole T.L., Green A.K., Lowe-Ma C.K., Nee T.W. and Rehn V., J. App. Phys., 69(2), 949 (1991).

4 Akhsakhalyan A.D., Fraerman A.A., Platonov Yu.Ya., Polushkin N.I. and Salaschenko N.N., Thin Solid Films, 207, 19 (1992).

5 Sanyal M.K., Sinha S.K., Huang K.G. and Ocko B.M., Phys. Rev. Letters, 66(5), 628 (1991).

6 Braslau A., Pershan P.S., Swislow G., Ocko B.M. and Als-Nielsen J., Phys. Rev. A, 38(5), 2457 (1988).

7 Von Kiessig H., Ann. Physik, 10, 715 and 769 (1931).

8 Sakurai K. and Iida A., Adv. In X-Ray Anal., 35, PAGE NO. (1992).

9 Wormington M., Bowen D.K. and Tanner B.K, Proc. Mat. Res. Soc.,238, 119 (1992).

10 Nevot L and Croce P., Rev. Phys. Appl., 15, 761 (1980).

11 Pynn R., Phys. Rev. B, 45, 602 (1992).

12 Stearns D.G., J. Appl.. Phys., 65(2), 491 (1989).

13 Stearns D.G., J. Appl. Phys., 71(9), 4286 (1992).

14 Beckmann P. and Spizzichino A., *The Scattering Of Electromagnetic Waves From Rough Surfaces*, Pergamon Press (1963).

15 Tanner B.K., Miles S.J., Bowen D.K., Hart L. and Loxley N., Proc. Mat. Res. Soc., 208, 345 (1991).

16 Spirkl W. et al., *To be published*

17 Powell A.R., Bradler J., Thomas C.R., Kubiak R.A., Bowen D.K., Wormington M. and Hudson J.M., Proc. Mat. Res. Soc., 238, 653 (1992).

18 Jain S.C. and Hayes W., Semicond. Sci. & Tech., 6, 547 (1991).

19 Kasper E., Surface Science, 174, 630 (1986).

20 Mendez E.E. and Von Klitzing K., *Physics And Applications Of Quantum Wells And Superlattices*, NATO ASI Series B: Physics Vol. 170 (1987).

21 Phillip H.R. and Taft E.A., J. App. Phys., 53, 5224 (1982).

22 Blunt R., *Private Communication* (1991).

23 Friess E., Schorer R., Eberl K. and Abstreiter G., J. Vac. Sci. Technol. B, 9(4), 2045 (1991).

24 Born M. and Wolf E., *Principles Of Optics*, 51, Pergamon Press, Oxford (1970).

25 Timbrell P.Y., Baribeau J.M., Lockwood D.J. and McCaffrey J.P., J. App. Phys., 67(10), 6292 (1990).

26 Schaffler F., Herzog H.J., Jorke H. and Kasper E., J. Vac. Sci. Technol. B, 9(4), 2039 (1991).

27 Schaffler F, and Jorke H., App. Phys. Lett., 58(4), 397 (1991).

28 Brugger H., Friess E., Abstreiter G., Kasper E. and Kibbel H., Semicond. Sci. &Technol., 3, 1166 (1988).

29 Parkin S.S.P., Phys. Rev. Lett, 67, 3598 (1991).

30 Fullerton E.E., Kelly D.M., Guimpel J., Schuller J.K. and Bruynseraede Y., Phys. Rev. Lett. 68, 859 (1992).

31 Parkin S.S.P., Li Z.G. and Smith D., Appl. Phys. Lett., 58, 2710 (1991).

32 Takanashi K., Obi Y., Mitani Y. and Fujimori H., J. Physical Soc. Japan, 61(4), 1169 (1992).

33 Steyerl A., Malik S.S and Iyengar L.R., Physica B, 173,47 (1991).

34 Sinha S.K., Physica B, 174, 499 (1991).

35 Sinha S.K., Sirota E.B., Garoff S. and Stanley H.B., Phys. Rev. B, 38(4), 2297 (1988).

36 Vinogradov A.V., Zorev N.N., Kozhevnikov S.I., Sagitov S.I. and Tur'yanskil A.G., Sov. Phys. JETP, 67(8), 1631 (1988).

37 Harada J., Acta. Cryst., A48, 764 (1992).

38 Sinha S.K., Physica B., 173, 25 (1991).

39 Yoneda Y., Phys Rev., 131(5), 2010 (1963).

40 Savage D.E., Kleiner J., Phang Y.H., Jankowski T., Jacobs J., Kariotis R. and Lagally M.G., J. App. Phys., 69, 1411 (1991).

41 Clemens B.M, Bain J.A., Payne A.P., Hufnagel T.C. and Brennan S.M., Proc. Mat. Res. Soc., Vol. 239, 475 (1992).

# Appendix A

## MATLAB Program for FFT Analysis Of HEMT Double Crystal Diffracton Rocking Curves

Chapter V described a program which used Fast Fourier Transform (FFT) analysis to extract the harmonic components (and hence thickness information) from HEMT double crystal rocking curve data. The program is written using the MATLAB data manipulation software package, designed by Cambridge Controls, and comprises one "core" routine with several sub-routines (one of which is written in Pascal). This "core" routine is known as "fastft.m" and is written in the MATLAB language. To start the program the fasft.m routine is called by typing "fastft" from within the MATLAB package. It should be noted that a pre-requisite for the successful running of the MATLAB program is that the computer should be fitted with a numerical co-processor. The various sub-routines called from within fastft.m are:

| | | |
|---|---|---|
| loadfile.pas | - | a Pascal routine which strips the"header" from rocking curves recorded using the Bede DCC control software. The angular and countrate information is passed to the MATLAB program in the form of a matrix called TEMP.DAT. |
| sg.m | - | a MATLAB routine which applies a Savitsky-Golay smooth to the data stored in TEMP.DAT. This routine was written by Dr. Simon Cockerton of Bede Scientific Instruments Ltd. (to whom due acknowledgement is given). |
| trimdata.m | - | a MATLAB routine which "windows" out a user-specified region of a data set. |
| logonly.m | - | a MATLAB routine which takes the log of the smoothed, windowed data. |
| normal.m | - | this MATLAB routine "normalises" the rocking curve by fitting an envelope to the raw data and dividing one by the other. |
| peakfind.m | - | a MATLAB routine which detects the peaks in a data set. |
| splinfit.m | - | a MATLAB routine which fits a cubic spline to the peaks detected by the peakfind routine. |

fftplot.m — a MATLAB routine which converts from Fourier space to the (layer) thickness regime.

The code listings for each of these routines is given below.

fastfft.m

```
format long e;
clear;
!del *.met;
!dir *.x*;
% loadfile in from as-saved Bede DCC format
!loadfile;
%apply Savitsky-Golay smooth
sg;
a=TEMP(1:N-8);
i=MDATA;
clear TEMP;
[p,N]=size(a);
step=a(2)-a(1);
step=fix(abs(step));
disp(' ');
semilogy(a,i);
xlabel('Angle (arc secs.)');
ylabel('Log(intensity)');
pause;
%"window" out substrate peak
trimdata;
%ask user if "logonly" or "normalise" method is to be followed
m=input('(logonly) or (normal)ise :  ','s');
eval(m);
%subtract d.c. background
average=mean(real(i));
i=i-average;
plot(A,i);
title('Smoothed, windowed, logged data - dc level removed');
pause;
%apply auto-correlation
i=xcorr(i,i);
plot(i);
title('Auto-Correlated Data');
pause;
disp(' Carrying out Fast Fourier Transform ... ');
F=fft(i);
[N,p]=size(F);
```

```
F=F.*conj(F);
phi=0;
thetab=33.034;
thetab=thetab*pi/180;
x=(1/step)*(0:(N/2)-1)/N;
t=x*(3600*180/pi)*1.54*sin(thetab+phi)/(sin(2*thetab));
disp('Ready to plot FFT - choose range for x-axis:');
fftplot;
```

loadfile.pas (Pascal routine)

```
program loadfile;

var
  f, t : text;
  i    : integer;
  filename : string[14];
  line : string[80];

begin
    writeln('Name of file to be analysed : ');
    read(filename);
    writeln(' Loading data file ...');
    assign(f,filename);
    reset(f);
    assign(t,'temp.dat');
    rewrite(t);
     repeat
      readln(f,line);
     until line='Position   Count';
    while not Eof(f) do
      begin
         readln(f,line);
         writeln(t,line);
      end;
    close(t);
end.
```

sg.m

```
disp('Carrying out a Savitzky-Golay smooth to the data file.');
disp('Please wait ....');
load TEMP.DAT;
N=LENGTH(TEMP(:,2));
```

```
NDATA=TEMP(:,2);
NDATA=NDATA+1;
M=N-8;
for I=2:9;
J=I-1;
NP(I)=NDATA(J);
end
for I=1:M;
J=I+8;
for K=1:8;
KA=K+1;
NP(K)=NP(KA);
end
NP(9)=NDATA(J);
NSUM=59*NP(5)+54*(NP(4)+NP(6))+39*(NP(3)+NP(7))+14*(NP(2)+NP(8))-
21*(NP(1)+NP(9));
MDATA(I)=NSUM/231;
end
```

trimdata.m

```
disp('Select section of data to be analysed.');
amin=input('Minimum angle : ');
amax=input('Maximum angle : ');
A=[ ];
newi=[ ];
for j=1:N,
        if a(j) > amin,
          if a(j) < amax,
          A=[A;a(j)];
         newi=[newi;i(j)];
          end
        end
end
i=newi;
clear newi;
semilogy(A,i);
title('Section of data selected');
xlabel('Angle (arc secs.)');
ylabel('Intensity');
pause;
end
```

logonly.m

```
[N,p]=size(A);
disp(' ');
disp('Taking log of data');
disp(' ');
i=log10(i);
```

normal.m

```
[N,p]=size(A);
%find peaks in data
peakfind;
i=log10(i);
Q=log10(Q);
%form "envelope" by fitting cubic spline to peaks detected
splinfit;
a=A;
%second chance to window data
trimdata;
```

peakfind.m

```
backgrnd=1;
sd=sqrt(backgrnd);
e=input('No. of standard deviations : ');
dist=input('Peak search criteria (no. points away)? ');
sample=input('Graph Comment? ','s');
title1=[sample,' : "o" - peak positions'];
P=[A(1)];
Q=[i(1)];
for j=(dist+1):N-(dist),
        if i(j) > (backgrnd+(e*sd)-backgrnd-(e*sd)),
            if i(j) > i(j-1),
                if i(j) > i(j+1),
                    if i(j) > i(j-(dist)),
                        if i(j) > i(j+(dist)),
                        P=[P;A(j)];
                        Q=[Q;i(j)];
                        end
                    end
                end
            end
        end
end
```

```
P=[P;A(N)];
Q=[Q;i(N)];
semilogy(A,i,P,Q,'o');
title(title1);
xlabel('Angle (arc secs.)');
ylabel('Intensity');
pause;
clear backgrnd e sd j;
end
```

splinfit.m

```
Qi=spline(P,Q,A);
plot(A,i,A,Qi,'o');
title('Cubic spline fit to the data');
pause;
%divide envelope by raw data
i=Qi./i;
plot(A,i);
xlabel('Theta (arc secs.)');
title('Normalised data');
pause;
```

fftplot.m

```
tmin=input('Min. of thickness range = ');
tmax=input('Max. of thickness range = ');
fstep=((3600*180)/(step*pi))*1.541*sin(thetab+phi)/(N*sin(2*thetab));
plot(t((tmin/fstep):(tmax/fstep)),F((tmin/fstep):(tmax/fstep)))
xlabel('Thickness (Angstroms) ');
ylabel('Fourier Amplitude');
pause;
disp('To replot FFT - type "fftplot".');
end
```

The program flow is as follows:

a) the user runs the routine fastft.m from within MATLAB.

b) the data is read in by loadfile.pas and stored in a matrix called TEMP.DAT.

c) the data is transferred to the routine sg.m, where a Savitsky-Golay smooth is applied. The angular and countrate data are now stored in two separate vectors (a and i, respectively).

d) the user may now window out a particular section of the rocking curve data (i.e., the InGaAs layer peak) by defining minimum and maximum values of angle.

At this point the user is given the option of following the "logonly" or the "normalise" method for data reduction (see Chapter V). The choice is made by typing either "logonly" or "normal" at the appropriate prompt. If the logonly method is chosen, the log of the processed data is taken. For the normalise method, peaks in the diffraction profile are detected and a cubic spline fitted through the peak positions identified. The raw data is then divided by the "envelope" generated by this cubic spline fitting procedure. The user is then given one more option to "window" the processed region, so that any glitches which may have occured at the extrema of the data, as a result of the spline fitting procedure, may be eliminated. Whichever method is chosen, the program flow will then continue as follows:

e) the d.c. level is subtracted (so that the data is centred about zero).

f) an autocorrelation is applied.

g) a Fast Fourier Transform is applied.

h) the data is plotted as (Fourier amplitude) v (layer thickness).

Finally, the user is given the option of re-plotting the final graph within specified maximum and minimum angular values.

At each stage in the program, a record of any graph plotted can be made by inserting the line

meta *filename1.ext*

immediately after any command which plots a graph to the screen (where *filename1.ext* is the name of the file to be generated). This command will generate a MATLAB meta-file which can be converted to a postscript file (for subsequent plotting) by the command,

gpp \dps *filename1.ext filename2.ext*

Here, *filename2.ext* is the name to be assigned to the postscript file.